

# Università degli Studi di Salerno

Dipartimento di Chimica e Biologia “Adolfo Zambelli”



PhD Thesis in Chemistry

XXXI Ciclo

## *Synthesis and Properties of New Macrocyclic Derivatives*

Tutor:

**Prof. Carmine Gaeta**

Ph.D. Student

**Paolo Della Sala**

8800100019

Coordinatore:

**Prof. Gaetano Guerra**

**Academic Year 2017-2018**



*“The only easy day was yesterday”*

Navy SEALs's motto



<b>1</b>	<b>Introduction</b>	<b>7</b>
1.1	Supramolecular Chemistry	7
1.2	Macrocycles in Supramolecular Chemistry	18
<b>2</b>	<b>Supramolecular Properties of Larger Resorcin[6]arene Macrocycles</b>	<b>22</b>
2.1	Synthesis of Larger Resorcinarenes: An Overview	22
2.2	Solid State Self-Assembly of Resorcin[6]arene	26
2.3	Synthesis of a Tetrasulfate-Resorcin[6]arene Cavitand	34
2.4	Biomolecular Recognition with Larger Resorcin[6]arene Derivatives	48
<b>3</b>	<b>Synthesis of New CycloParaPhenylene Macrocycles and Studies of Their Properties</b>	<b>63</b>
3.1	Carbon Nanobelt and Carbon Nanohoops: An Overview	63
3.2	Application of [n]CPPs	73
3.3	Tuning Cycloparaphenylene Host Properties by Chemical Modification	76
3.4	Synthesis, Optoelectronic and Supramolecular Properties of a CPP-Calix[4]arene Hybrid Host	90
3.5	New Optoelectronic Applications of CycloParaPhenylene Derivatives	103
3.6	A [8]CPP Derivative as Emitter in Triplet-Triplet Annihilation Upconversion	105
3.7	CPP-Based Luminescent Solar Concentrator	120

<b>4</b>	<b>Experimental Section</b>	<b>130</b>
4.1	General Section	130
4.2	Solid State Self-Assembly of Resorcin[6]arene	132
4.3	Synthesis of a Tetrasulfate-Resorcin[6]arene Cavitand	135
4.4	Biomolecular Recognition with Larger Resorcin[6]arene Derivatives	139
4.5	Tuning Cycloparaphenylene Host Properties by Chemical Modification	152
4.6	Synthesis, Optoelectronic and Supramolecular Properties of a CPP-Calix[4]arene Hybrid Host	180
4.7	A [8]CPP Derivative as Emitter in Triplet-Triplet Annihilation Upconversion	200
4.8	CPP-Based Luminescent Solar Concentrator	217

# 1 Introduction

## 1.1 Supramolecular Chemistry

Supramolecular chemistry<sup>1</sup> is a multidisciplinary branch of the chemistry that study the systems constituted by molecules or ions held together by secondary interactions.

The expression “Supramolecular Chemistry” has been coined for the first time by Jean-Marie Lehn in 1978 and defined as the “... *chemistry of molecular assemblies and of the intermolecular bond*”.<sup>1</sup> Furthermore, this field can be divided in two categories: **host-guest chemistry**,<sup>2</sup> in which the aim is the design of host molecules able to complex in a specific way, appropriate guests (generally smaller molecules or ion - Figure 1a), and the **self-assembly**<sup>3</sup> processes that explore the spontaneous and reversible association of two or more molecules to form an aggregate<sup>3a</sup> in solution or in the solid state (Figure 1b).

Both, the host-guest chemistry and the self-assembly processes are deriving inspiration from the natural systems, where numerous examples of supramolecular phenomena are known.<sup>1</sup>

---

<sup>1</sup> Lehn, J.-M., *Supramolecular Chemistry*, VCH, Weinheim, Germany, 1995; Lehn, J.-M. *Angew. Chem. Int. Ed. Engl.* **1988**, *27*, 89-112.

<sup>2</sup> Cram D. J. *Angew. Chem. Int. Ed. Engl.* **1988**, *27*, 1009-1020.

<sup>3</sup> (a) Swiegers, G. F., “Self-Assembly: Terminology”, in *Encyclopedia of Supramolecular Chemistry*, Steed J. W. and Atwood, J. L. (Eds), Marcel Dekker, New York, NY, USA, 2004, pp. 1263-1269; (b) Hamilton, T. D. and MacGillivray, L. R., “Self-Assembly in biochemistry” in *Encyclopedia of Supramolecular Chemistry*, Steed J. W. and Atwood, J. L. (Eds), Marcel Dekker, New York, NY, USA, 2004, pp. 1257-1262.

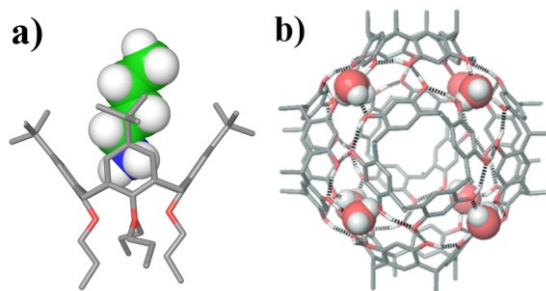


**Figure 1:** Example of: **a)** molecular recognition of the *n*-butylammonium guest with the tetrapropoxy-*p*-*tert*-butylcalix[4]arene host; <sup>4</sup> **b)** Self-assembly of six resorcin[4]arene molecules and 8 water molecules to form the hexameric capsule reported by Atwood<sup>5</sup> in 1997.

Learning the lesson from natural processes and taking inspiration from them, in the last decades, artificial systems have been designed able to mimic the majority of their performances. Thus, the selective recognition of substrates by natural receptors (e.g.: enzymes) has inspired the host-guest chemistry. Regarding the self-assembly processes, useful informations have been obtained by studying the natural systems such as the DNA.<sup>3b</sup>

### 1.1.1 The Self-Assembly

The **self-assembly phenomena**,<sup>6</sup> is defined as “*The spontaneous and reversible association of two or more*

<sup>4</sup> Talotta, C.; Gaeta, C.; Neri, P. *J. Org. Chem.* **2014**, 79, 9842–9846.

<sup>5</sup> MacGillivray, L. R. and Atwood, J. L. *Nature* **1997**, 389, 469-472.

<sup>6</sup> a) Hof, F.; Craig, S. L.; Nuckolls, C.; Rebek, J. Jr.; *Angew. Chem. Int. Ed.* **2002**, 41, 1488–1508 and reference cited therein. b) Rebek, Jr. J.; *In Hydrogen-Bonded Capsules: Molecular Behavior in Small Spaces*, World Scientific Pub Co Inc, 2015.

components to form a larger, non-covalently bound aggregate".<sup>3,4-7</sup>

As representative example, the resorcin[4]arene macrocycle **1** assembles both, in the solid state<sup>5</sup> and in solution<sup>8</sup> in the presence of water, to form a cage (hexameric capsule) constituted by 6 macrocycles **1** and 8 water molecules, sealed by 60 (O-H...O) hydrogen bonds. The internal volume of 1375 Å<sup>3</sup> is large enough to encapsulate 6-8 molecules of CHCl<sub>3</sub> or benzene (Figure 2).<sup>5</sup>

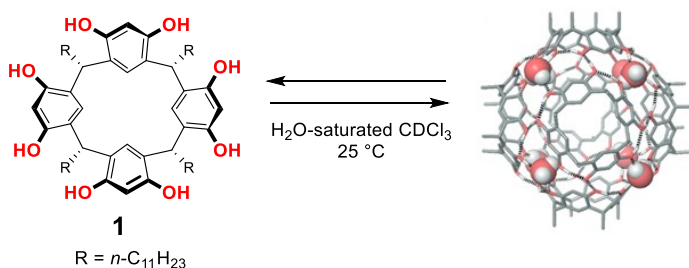


**Figure 2:** Self-assembly of the hexameric resorcinarene capsule.<sup>5,8</sup> (Right) In the tube model of the hexameric capsule the undecyl chains and H-atoms have been removed for clarity, while bridged H<sub>2</sub>O molecules are represented as CPK model.

In the last decade, many reports in the field of supramolecular catalysis have shown that the resorcinarene hexameric capsule is able to catalyze chemical reactions.<sup>9</sup> Like an enzymatic active site, the inner cavity of the hexameric capsule is able to host selectively the substrates, and by virtue of the confinement effect they can react, leading to the formation of intermediates

<sup>7</sup> Steed, J.W.; Turner, D. R.; Wallace, K. J. in *Core concepts in Supramolecular Chemistry and Nanochemistry*, Chapter 1, WILEY, West Sussex - UK, 2007.

<sup>8</sup> Avram, L. and Cohen, Y. *J. Am. Chem. Soc.* **2002**, *124*, 15148-15149.

<sup>9</sup> (a) Catti, L.; Zhang, Q.; Tiefenbacher, K. *Chem. Eur. J.* **2016**, *22*, 9060-9066. (b) La Manna, P.; Talotta, C.; Floresta, G.; De Rosa, M.; Soriente, A.; Rescifina, A.; Gaeta, C.; Neri, P. *Angew. Chem. Int. Ed.* **2018**, *57*, 5423-5428.

and transition states stabilized by secondary interactions with the capsule.<sup>9a</sup>

## 1.1.2 The Host-Guest Chemistry and the Principles of the Molecular Recognition

Hosts are defined as synthetic structures which are able to bind, in a selective way (molecular recognition), smaller molecules or ions (guests) by means secondary interactions such as, dipole-dipole, hydrogen-bond, electrostatic, hydrophobic and Van der Waals interactions (Figure 3).

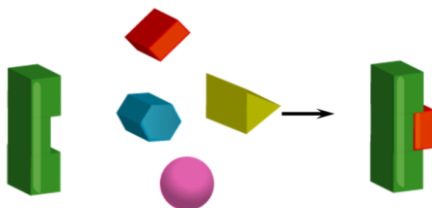
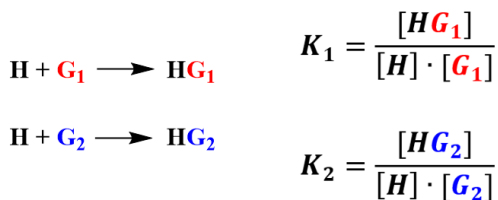


**Figure 3:** Molecular recognition. In green the host while the smaller elements represent the guests.

The formation of a host-guest complex is an equilibrium process defined by an association constant:



The selectivity is the ratio of the association constants  $K_1/K_2$ , for the host  $H$ , binding two guest  $G_1$  and  $G_2$ .<sup>10</sup>

The specificity of binding of the natural enzymes toward their substrates has inspired the design of artificial hosts for the molecular recognition of anions, cations and neutral guests. The origin of the specificity of the natural enzymes can be explained using the *Lock and Key* analogy proposed by Emil Fischer in 1894.<sup>11</sup>

This model compares the enzyme to a lock (host) and substrate to a key (guest), thus the interaction between them is driven by geometric (size and shape) and electronics complementarities between both the binding sites.

Daniel Koshland, half a century later, introduced the *Induced Fit* model - according which, conformational changes can occur in the enzymatic active site in order to facilitate the binding of the substrate (Figure 4): "... the flexibility of a "hand in glove", which included Fisher's idea of a fit but added the flexibility concept".<sup>12</sup>

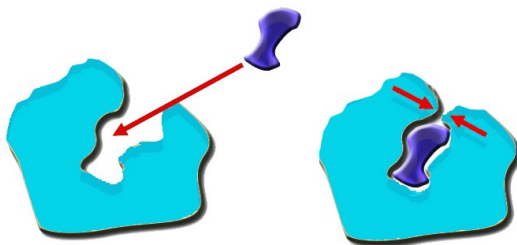


**Figure 4:** Induced Fit model representation - The enzyme (blue) binds substrate (purple) upon an adaptive conformational change.

---

<sup>10</sup> Hamilton, A. D. in *Comprehensive Heterocyclic Chemistry*, Pergamon Press, 1984.

<sup>11</sup> Fischer, H. E. *Berichte der deutschen chemischen Gesellschaft* **1894**, 27, 298-2993.

<sup>12</sup> Koshland, D. E. Jr. *Angew. Chem. Int. Ed. Engl.* **1994**, 33, 2375-2378.

In order to reach a higher recognition between host and guest, some crucial factors must be taken into account during the design of new hosts:

- **Complementarity:** As in the lock and key model, a high recognition is related to the steric (shape and size) and electronic complementarity (positive/negative charges, H-bonds donor/acceptor, etc.) between the interacting surfaces. Some examples of complementarity are reported in Figure 5a and 5b. In particular in Figure 5a,<sup>13</sup> is illustrated the recognition of  $K^+$  by the 18-crown-6 host, in which the spherical cation fits into the circular cavity of the host. The Figure 5b, shows the recognition of the nitrate anion by means the  $C_3$ -symmetrical host designed by Anslyn.<sup>14</sup> The perfect steric and electronic complementarity between host and the anionic guest affords a high selectivity.

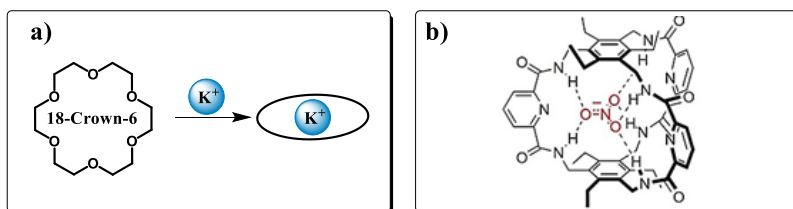


**Figure 5.** Steric and electronic complementarity: **a)** Spherical recognition of  $K^+$  with the 18-Crown-6 and, **b)** Recognition of a trigonal planar anion (nitrate) with the  $C_3$ -symmetrical host of Anslyn.<sup>14</sup>

<sup>13</sup> Atwood, J. L. and Steed, J. W. in *Encyclopedia of Supramolecular Chemistry*, CRC Press, 2004.

<sup>14</sup> Bisson, A. P.; Lynch, V. M.; Monahan, M. K. C.; Anslyn, E. V. *Angew. Chem. Int. Ed.* **1997**, *36*, 2340-2342.

- **Large contact area between host and guest and multiple interactions sites.** If the host is able to wrap around the guest, then more secondary interactions can be established and more stable is the resulting complex (Figure 6).

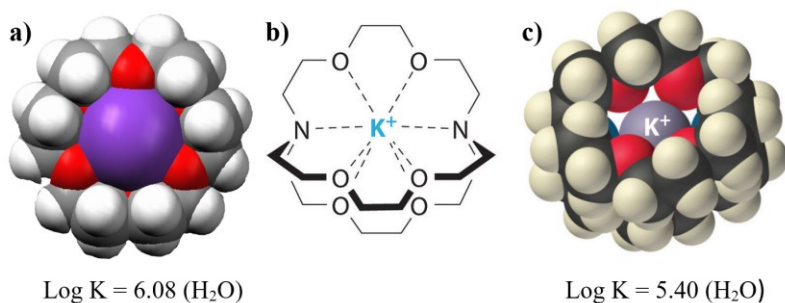


**Figure 6.** Large contact area between host and guest: **a)** CPK-model of the  $\text{K}^+$  18-crown-6 complex where part of the cation surface (purple) is left open and accessible to the solvent ; **b)** Chemical drawing of  $\text{K}^+$  2,2,2-cryptand and, **c)** CPK-model of the  $\text{K}^+$  2,2,2-cryptand in which the 2,2,2-cryptand is able to wrap around  $\text{K}^+$  guest.

- **Preorganization:** it is the ability of the host and guest to interact between them without making significant conformational changes (Figure 7). Indeed, citing<sup>15</sup> the paradigm of the molecular recognition of Cram : “*the more highly hosts and guests are preorganized for binding and low solvation prior to their complexation, the more stable will be their complexes*”.<sup>2,15</sup>

<sup>15</sup> Cram, D. J. *Angew. Chem., Int. Ed. Engl.*, **1986**, 25, 1039-1134. Cram, D. J. *Science* **1988**, 240, 760-767.

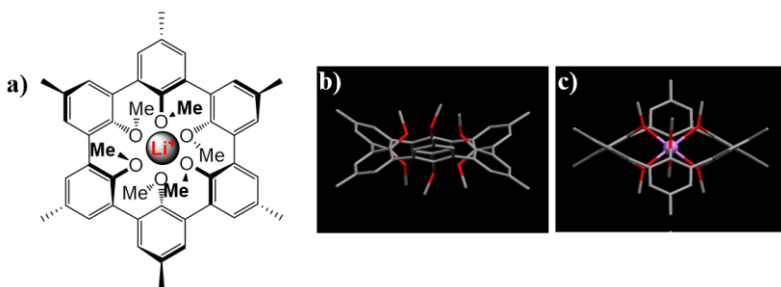


**Figure 7.** Preorganization: **a)** Structure of the  $\text{Li}^+$   $\subset$  Spherand complex studied by Cram; **b)** side-view of the spherand free and **c)** side-view of the  $\text{Li}^+$   $\subset$  spherand.

Another interesting aspect related to the preorganization of the host is the so called “**macrocycle effect**” which plays a fundamental role for the thermodynamic stability of the host-guest complexes.<sup>16</sup>

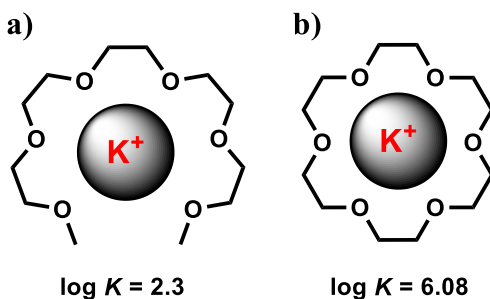


**Figure 8.** The macrocycle effect: **a)**  $\text{K}^+$   $\subset$  Podand complex and **b)**  $\text{K}^+$   $\subset$  [18]-Crown-6 (right).

Comparison between the association constant values for the formation of two complexes in Figure 8 shows clearly that the  $\text{K}^+$   $\subset$  [18]-crown-6 is significantly more stable than the  $\text{K}^+$   $\subset$  podand (pentaethyleneglycol) complex (Figure 8). In accord with the macrocyclic effect: “*Host systems that are more preorganized into a large cyclic shape form more stable*

<sup>16</sup> Cabiness, D. K. and Margerum, D. W. *J. Am. Chem. Soc.* **1969**, *91*, 4092-4093.

complexes as there is no energetically unfavorable change in conformation in order to bind a guest.”<sup>17</sup> In fact, during the formation of the  $K^+ \subset$  podand (pentaethyleneglycol) complex a conformational change of the podand must occur in order to adapt its shape (and binding site) around to the  $K^+$  guest (from open to close conformation, Figure 9a), as a result a great loss of degrees of freedom will occur ( $\Delta S < 0$ ).

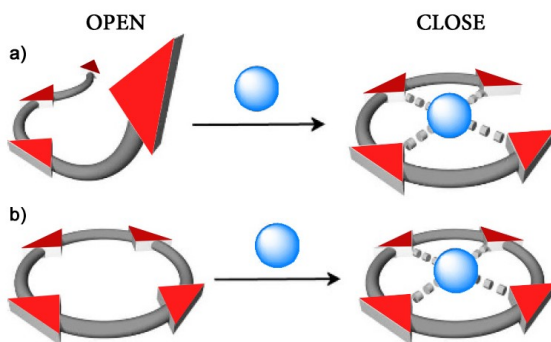


**Figure 9** : a) Not preorganized ligand (as podand) ; b) preorganized macrocyclic structure.

Differently the cyclic [18]-crown-6 in Figure 8, shows a binding site already preorganized for the complexation of the guest (close conformation, Figure 9b), and consequently the  $\Delta S$  of binding is much less and hence more favorable. Analogously the enthalpic contribution is more favorable to the formation of the  $K^+ \subset$  [18]-crown-6 complex. In fact, the free podand (Figure 8) adopts a linear conformation (open conformation, Figure 9a) in solution in order to minimize the electrostatic repulsion between the electrons lone-pairs on oxygen atoms. In the open conformation, the donor atoms of a podand are also

<sup>17</sup> Steed, J.W.; Turner, D. R.; Wallace, K. J. in *Core concepts in Supramolecular Chemistry and Nanochemistry*, Chapter 1, WILEY, West Sussex - UK, 2007.

more accessible to the solvent molecules for the solvation (Figure 9a). Consequently, in order to adopt a close conformation during the complexation of the cation, the podand must overcome the unfavorable electrostatic repulsion between the electrons lone pairs and, also, a great amount of energy must be paid in order to break the interactions with the solvent. Differently, the cyclic host [18]-crown-6 already adopts a close conformation in which the electrostatic repulsion between the lone pairs have been overcome during the synthesis, in addition the binding site of a macrocyclic hosts is less accessible for the solvation.

In conclusions, based on these considerations we can conclude that the macrocyclic structures form more stable host-guest complexes with respect to the analogous podands (linear derivatives). For this reason, to date, many efforts have been focused on design and synthesis of new macrocyclic derivatives for their application in supramolecular processes. Thus, in the last decade, appealing macrocyclic structures have been reported which showed amazing supramolecular properties: pillar[n]arene<sup>18</sup>, calix[n]tetrolarenes<sup>19</sup>, bambu[n]suril<sup>20</sup>, oxatub[n]arene<sup>21</sup>, zorbarene<sup>22</sup>,

---

<sup>18</sup> Ogoshi, T.; Kanai, S.; Fujinami, S.; Yamagishi, T.; Nakamoto, Y. *J. Am. Chem. Soc.* **2008**, *130*, 5022-5023.

<sup>19</sup> Zafrani, Y. and Cohen, Y. *Org. Lett.* **2017**, *19*, 3719-3722.

<sup>20</sup> Svec, J.; Necas, M.; Sindelar, V. *Angew. Chem. Int. Ed. Engl.* **2010**, *49*, 2378-2381.

<sup>21</sup> Jia F.; He, Z.; Yang, L. P.; Pan, Z. S.; Yi, M.; Jiang, R. W.; Jiang, W. *Chem. Sci.*, **2015**, *6*, 6731- 6738.

<sup>22</sup> Tran, A. H.; Miller, D. O.; Georghiou, P.E. *J. Org. Chem.* **2005**, *70*, 1115-1121.

biphen[*n*]arenes<sup>23</sup>, cycloparaphenylene<sup>24</sup> and cyclophenacenes<sup>25</sup> - Figure 10.

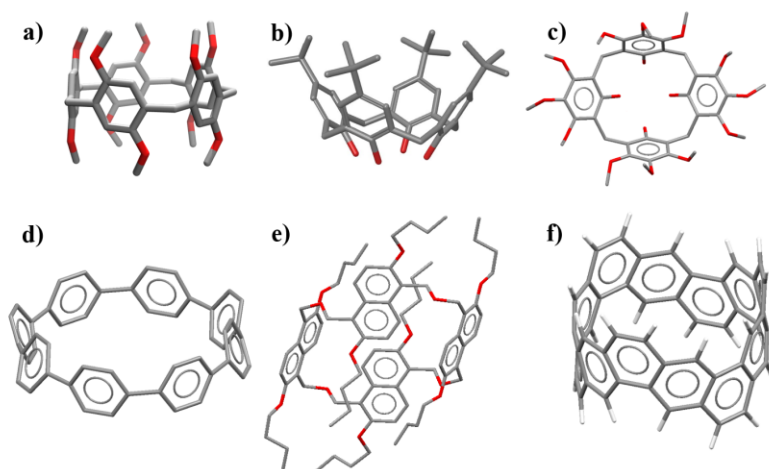


**Figure 10:** a) Pillar[5]arene, b) Calix[4]arene, c) Calix[4]tetrolarenes, d) [8]Cycloparaphenylene, e) Oxatub[4]arene and f) Cyclophenacenes.

These macrocyclic hosts have shown interesting recognition abilities toward cations,<sup>26</sup> anions<sup>27</sup> and neutral molecules of clinical<sup>28</sup> and environmental interests.<sup>29</sup>

<sup>23</sup> Chen, H.; Fan, J.; Hu, X.; Ma, J.; Wang, S.; Li, J.; Yu, Y.; Jia, X.; Li, C.; *Chem. Sci.*, **2015**, *6*, 197- 202.

<sup>24</sup> Jasti, R.; Bhattacharjee, J.; Neaton, J. B.; Bertozzi, C. R. *J. Am. Chem. Soc.* **2008**, *130*, 17646-17647.

<sup>25</sup> Povie, G.; Segawa, Y.; Nishihara, T.; Miyauchi, Y.; Itami, K. *Science*, **2017**, *356*, 172-175.

<sup>26</sup> a) Yang, L.P.; Lu, S.B.; Valkonen, A.; Pan, F.; Rissanen, K.; Jiang W. *Beilstein J. Org. Chem.* **2018**, *14*, 1570–1577.

<sup>27</sup> a) Busschaert, N.; Caltagirone, C.; Rossom, W. V.; Gale, P. A. *Chem. Rev.* **2015**, *115*, 8038-8155. b) Gale, P. A.; Howe, E. N. W.; Wu, X. *Chem* **2016**, *1*, 351-422.

<sup>28</sup> Ma; X. And Zhao, Y. *Chem. Rev.* **2015**, *115*, 7794–7839.

<sup>29</sup> a) Dsouza, R. N.; Pischel, U.; Nau, W. M. *Chem. Rev.* **2011**, *111*, 7941–7980. b) Albelda, M. T.; Frias, J. C.; Garcia-Espana, E.; Schneider, H-J. *Chem. Soc. Rev.* **2012**, *41*, 3859-3877.

## 1.2 Macrocycles in Supramolecular Chemistry

The macrocyclic hosts show a central cavity (binding site) able to bind complementary guests through secondary interactions. As previously discussed, cyclic hosts are more preorganized and consequently form more stable host-guest complexes with respect to the linear podand analogues. However, the macrocycle flexibility provides kinetic support to the complexation by facilitating access of the guest to the central cavity. <sup>6</sup> Thus, for the design of new macrocyclic hosts, needs to find the right balance between complementarity/rigidity and flexibility of the cyclic backbone. At this regard, an excellent example is the lariat-ether host reported in Figure 11, which can be considered as a cryptand analogous with a three-dimensional binding site. Differently, by the cryptand hosts, the lariat-ethers (Figure 11) show a more favorable kinetic of binding thanks to the flexibility of the pendant side arm, at which is associated the preorganization of the central crown-like binding site.

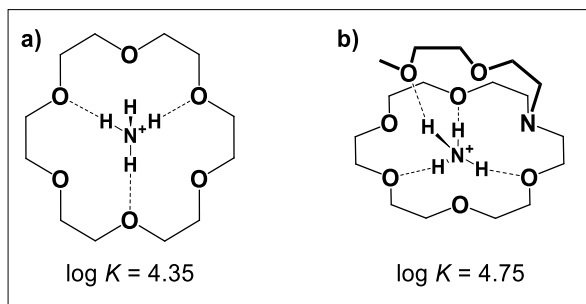


**Figure 11:**  $\text{NH}_4^+ \subset [18]\text{crown-6}$  and  $\text{NH}_4^+ \subset$  lariat-ether.

Historically, the efforts of the scientists have been directed toward the study of cyclophane<sup>13,17,30</sup> macrocycles because of their synthetic and conformational versatility. The term cyclophane includes the bowl-shaped molecules constituted by bridged aromatic ring. The presence of aromatic units (e.g.: benzene, naphthalene) ensures the easy functionalization of the macrocycles and consequently the synthesis of hosts with novel features and properties - Figure 12.

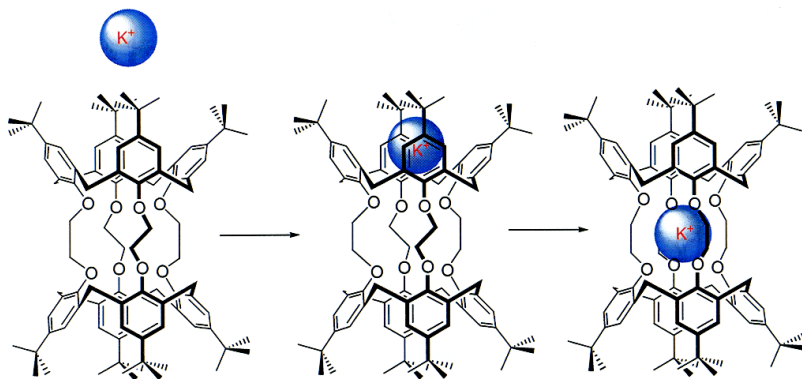


**Figure 12:** Calix[4]tubes proved highly selective for complexation of potassium over all group I metal cations.<sup>31</sup>

A central role in supramolecular chemistry has been played by the resorcinarene<sup>30c</sup> and calixarene<sup>30b,c</sup> macrocycles which constituted useful scaffolds for the synthesis of hosts with

<sup>30</sup> (a) Diederich, F. N. *Cyclophanes*; Royal Society of Chemistry: London, 1991; (b) Gutsche, C. D. *Calixarenes, An Introduction*; Royal Society of Chemistry: Cambridge, UK, 2008; (c) Neri P, Sessler J. L., Wang M.-X., (Eds.), *Calixarenes and Beyond*, Springer, Dordrecht, 2016; (d) Ogoshi, T. in *Monographs in Supramolecular Chemistry - Pillararenes*, Chapter 1, RSC, Cambridge - UK, 2016; (e) Cram, D. J.; Cram J. M. in *Container Molecules and Their Guests*, Monographs in Supramolecular Chemistry; Stoddart, J. F. Ed; Royal Society of Chemistry: Cambridge, 1994.

<sup>31</sup> Matthews, S. E.; Schmitt, P.; Felix, V.; Drew, M. G. B.; Beer, P. D. *J. Am. Chem. Soc.* **2001**, *124*, 1341-1353.

interesting supramolecular properties. Taking inspiration from them, in the last decades, novel macrocycles (e.g.: pillar[n]arenes<sup>30d</sup> and coronarenes<sup>32</sup>) have been designed and synthesized which have shown even more innovative supramolecular properties.

### 1.2.1 Resorcin[n]arenes

Resorcin[n]arenes<sup>30e</sup> (or calix[n]resorcinarenes) are compounds synthesized starting from resorcinol in the presence of aldehydes under acidic conditions. Vogel and Niederl, first in 1940,<sup>33</sup> reported the elucidation of the structure of the “*crystalline condensation product of acetaldehyde with resorcinol*”,<sup>33</sup> the authors reported that: “*the crystalline condensation products seem to possess a similar structural pattern as the porphyrins obtainable in pyrrole-carbonyl compounds condensations, but possessing benzene instead of “pyrrole”*”.<sup>33</sup> In 1968, Nilson<sup>34</sup> for the first time reported an X-ray structure of a resorcin[4]arene obtained by condensation of resorcinol with benzaldehyde, while in 1980, Högberg<sup>35</sup> reported the synthesis of two stereoisomeric resorcinarene derivatives starting from acetaldehyde and resorcinol and their conformational characterization in solution by dynamic NMR spectroscopy.<sup>35</sup> In this context, the stereoselective synthesis of the resorcinarene derivatives in  $C_{4v}$  isomers (Scheme 1),

---

<sup>32</sup> Wang, M. X. *Sci. China Chem.* **2018**, *61*, 993-1003.

<sup>33</sup> Niederl, J. B. and Vogel, H. J. *J. Am. Chem. Soc.* **1940**, *62*, 2512-2514.

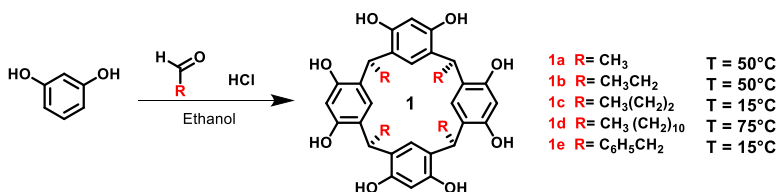
<sup>34</sup> Nilson, B. *Acta Chem. Scand.* **1968**, *22*, 732-747.

<sup>35</sup> Högberg, A. G. S. *J. Org. Chem.* **1980**, *45*, 4498-4500.

reported by D. J. Cram in 1988,<sup>36</sup> has constituted a milestone for the success and the diffusion of these macrocycles.

### 1.2.1.1 Synthesis of resorcin[*n*]arenes: the synthesis of Cram<sup>36</sup>

Tetrameric derivative **1** is the most studied and can be easily obtained under mild conditions, generally using a plethora of aliphatic or aromatic aldehydes and HCl in ethanol as solvent - Scheme 1.



**Scheme 1:** Synthesis of the resorcin[4]arene derivatives developed by Cram.<sup>36</sup>

The resorcin[4]arene derivatives in Scheme 1 are obtained in high yields, ranging from 60 to 88 % after crystallization from ethanol.<sup>36</sup>

<sup>36</sup> Tunstad, L. M.; Tucker, J. A. Dalcanele, E.; Weiser, J.; Bryant, J. A.; Shermann, J. C.; Helgeson, R. C.; Knobler, C. B.; Cram, D. J. *J. Org. Chem.* **1989**, *54*, 1305-1312.

## 2 Supramolecular Properties of Larger Resorcin[6]arene Macrocycles

The first aim of this PhD project has been encouraged by a recent result reported by our group,<sup>37</sup> and regarding the study of an improved synthetic procedure for the synthesis of the large resorcin[6]arene macrocycle **3** in Figure 13.<sup>37</sup> The new synthetic procedure, has paved the way to the possibility to study the supramolecular properties of the resorcin[6]arene macrocycle, until this moment left unexplored in literature.

### 2.1 Synthesis of Larger Resorcinarenes: An Overview

As concerns the study and the supramolecular applications of the resorcinarene macrocycles, the attention has been principally focused on the resorcin[4]arene (Scheme 1 and Figure 13), which has constituted a useful platform for building more elaborated synthetic hosts.<sup>30e</sup> In macrocyclic chemistry, many attentions have been devoted to the design and synthesis of new macrocycles. Naturally, the study of resorcin[*n*]arene macrocycles with a number of resorcinol rings > 4 (*larger*, Figure 16) could pave the way for the synthesis of supramolecular systems with new and intriguing recognition or self-assembly properties.

---

<sup>37</sup> Della Sala, P.; Gaeta, C.; Navarra, W.; Talotta, C.; De Rosa, M.; Brancatelli, G.; Geremia, S.; Capitelli, F.; Neri, P. *J. Org. Chem.* **2016**, *81*, 5726-5731.

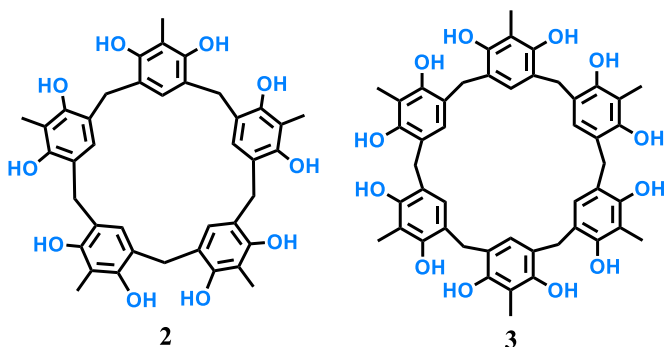


**Figure 13:** Larger resorcin[ $n$ ]arenes ( $n > 4$ ).

Differently from tetrameric derivatives in Scheme 1, the larger cyclo-adducts (Figure 13) **2** and **3** have been scarcely investigated owing their poor solubility in common organic solvents.<sup>38,39</sup>

The first synthesis of the larger resorcinarenes **2** and **3** (Figure 13), has been published by Konishi<sup>38</sup> and coworkers, which reported the formation of **3**, by reaction of 2-methylresorcinol with 1,3,5-trioxane in the presence of ethanol as solvent and aqueous concentrated HCl as catalyst and for short reaction times (3 h at reflux instead of 12-24 h reported for the tetramers in Scheme 1). The authors reported that the purification of **3** was difficult, due to the poor solubility of the resorcin[6]arene **3** in common organic solvents. The lack of solubility of **3** was attributed to the presence of free OH groups, thus<sup>38</sup> the crude reaction mixture was before acylated with propionic anhydride and successively purified.

<sup>38</sup> a) Konishi, H.; Ohata, K.; Morikawa, O.; Kobayashi, K. *J. Chem. Soc., Chem. Commun.* **1995**, 309-310. b) Konishi, H.; Nakamura, T.; Ohata, K.; Kobayashi, K.; Morikawa, O. *Tetrahedron Lett.* **1996**, *37*, 7383-7386.

In these reports,<sup>38</sup> Konishi and coworkers, demonstrated that the formation of the resorcin[5]arene **2** and resorcin[6]arene **3** was obtained under kinetic conditions: for short reaction time, while after equilibration for longer reaction time the tetramer, resorcin[4]arene, was the favored product.<sup>38</sup>

Interestingly, Sherman<sup>39</sup> and coworkers obtained the larger resorcinarene **2** and **3** by reaction of 2-methylresorcinol with diethoxymethane in the presence of aqueous concentrated HCl as catalyst and ethanol as solvent. Accordingly with the results previously reported by Konishi's group,<sup>38</sup> Sherman and coworkers<sup>39</sup> showed that the larger resorcinarene **2** and **3** were formed in good yields for short reaction time (30 min at 60 °C).<sup>39</sup> Analogously to the results reported by Konishi,<sup>38</sup> the purification of the larger resorcinarene **2** and **3** was difficult because of poor solubility of derivatives, in fact, by quoting the authors:<sup>39</sup> "*Moreover, it is far easier to purify the cavitated mixture than to isolate the different resorcinarene products and bridge them separately*", thus after 30 minutes at 60 °C the reaction was quenched and the crude reaction mixture was directly treated with CH<sub>2</sub>BrCl in the presence of base to give the cavitands **4** and **5** (Figure 14).<sup>39</sup>

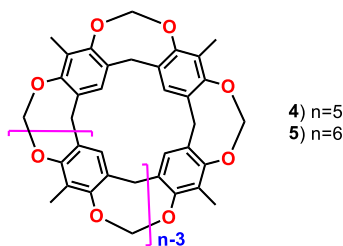
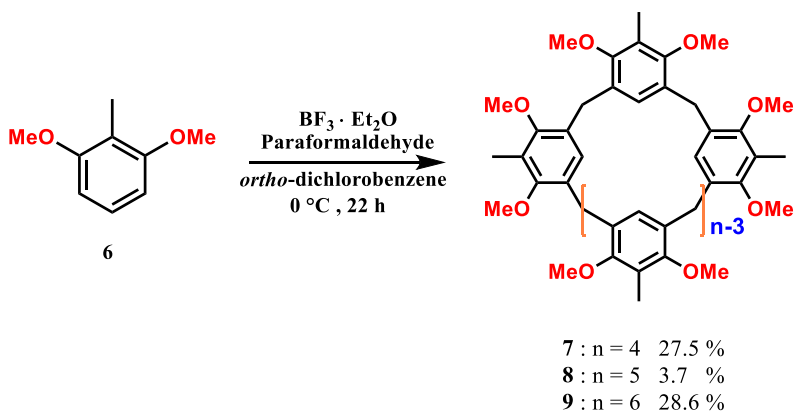


**Figure 14:** Larger [5,6]cavitands reported by Shermann.<sup>39</sup>

<sup>39</sup> Naumann, C.; Roman, E.; Peinador, C.; Ren, T.; Patrick, B. O.; Kaifer, A. E.; Shermann, J. C. *Chem. Eur. J.* **2001**, 7, 1637-1645.

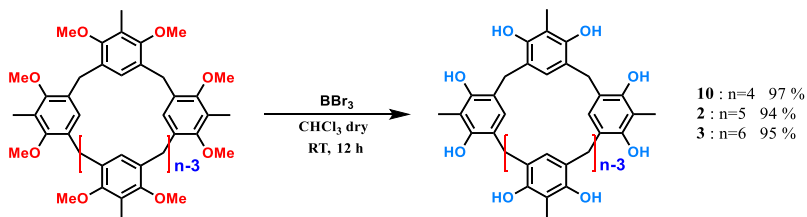
Thus, the results reported by Konishi<sup>38</sup> and Shermann<sup>39</sup> indicated that the presence of masked OH groups in larger resorcinarene macrocycles plays a crucial role for their solubility in organic solvents, making their work-up procedures easier. On the basis of these results<sup>38,39</sup> our group has reported in 2016<sup>37</sup> an improved procedure for the synthesis of larger resorcin[5,6]arene by using 1,3-dimethoxy-2-methylbenzene **6** as starting material, with the aim to directly obtain larger resorcinarenes with masked OH functions (Scheme 2), in order to improve both purification procedures and synthetic efficiency.



**Scheme 2:** Synthesis of derivatives **7**, **8** and **9**.<sup>37</sup>

In details our results<sup>37</sup> showed that, by treatment of 1,3-dimethoxy-2-methylbenzene **6** with paraformaldehyde in *ortho*-dichlorobenzene as the solvent and  $\text{BF}_3$  at  $0\text{ }^\circ\text{C}$ , the resorcin[5]arene **8** and the resorcin[6]arene **9** were obtained in 3.7 and 28.6 % of yield (Scheme 2). Interestingly, under the conditions reported in Scheme 2 the resorcin[6]arene **9** was the most abundant product. Thanks to the good solubility of the derivatives **8** and **9** in common organic solvent, their

purification was performed by chromatographic column. Successive treatment of **9** with  $\text{BBr}_3$  afforded to the synthesis of resorcin[6]arene **3** in quantitative yields (Scheme 3).



**Scheme 3:** Synthesis of derivatives **10**, **2** and **3**.

Very recently, Atwood and coworkers reported a novel procedure of purification of the *C*-ethylresorcin[6]arene which was separated from its tetrameric homologous, through the formation of co-crystals with 1-(2-pyridylazo)-2 naphthol<sup>40</sup> or 4,4'-bipyridine<sup>41</sup> in alcoholic solvents.

## 2.2 Solid State Self-Assembly of Resorcin[6]arene<sup>42</sup>

There are a great deal of examples in which resorcinarene based systems are involved in molecular recognition, biomimetic catalysis, gas storage and drug delivery.<sup>43</sup> In

<sup>40</sup> Jiang, S.; Patil, R. S.; Barnes, C. L.; Atwood, J. L. *Cryst. Growth Des.* **2017**, *17*, 2919-2922.

<sup>41</sup> Jiang, S.; Patil, R. S.; Barnes, C. L.; Atwood, J. L. *Cryst. Growth Des.* **2017**, *17*, 4060-4063.

<sup>42</sup> Brancatelli, G.; Geremia, S.; Gaeta, C.; Della Sala, P.; Talotta, C.; De Rosa M.; Neri, P. *CrystEngComm* **2016**, *18*, 5045-5049.

<sup>43</sup> a) Harrowfield, J.; Koutsantonis, G. In *Calixarenes in the Nanoworld*; Vicens, J.; Harrowfield, J.; Baklouti, L.; Eds. Springer: Netherlands, **2007**.

addition, resorcinarenes and cavitands are useful scaffolds to develop novel molecular containers (or cages).<sup>44</sup> In fact, as it is well known, resorcin[4]arene derivatives, form self-assembled capsules (Figure 2) in which the aromatic cavity is isolated from the external environment and offers a binding pocket for the inclusion of complementary guests.<sup>45</sup> The confinement of molecules into the capsule stabilizes reactive species<sup>46</sup> promote chemical reactions through the confinement of reactants and catalysts inside the inner space of the capsules.<sup>9,47</sup>

Atwood in 1997,<sup>44c</sup> showed that the self-assembly of six resorcin[4]arene molecules and 8 water molecules to form the hexameric capsule occurs in the solid state (Figure 2). The X-ray structure of the hexameric capsule in Figure 2 resembles a cube with six resorcinarene molecules located on the sides and eight water molecules as the corners in a chiral structure, sealed by 60 (O-H...O) H-bonds. Thus, an octahedral-shaped cavity was formed with an internal volume of 1375 Å<sup>3</sup> that can host about 6-8 molecules of chloroform or benzene. The pioneering work of Atwood<sup>44c</sup> prompted us to study the solid-state self-assembly properties of the larger resorcin[6]arene macrocycle

---

b) Hoskins, C.; Papachistout, A.; Ho, T. M. H.; Crtis A. D. M. *J. Nanomed. Nanotechnol.* **2016**, *7*, 1-7 and reference cited therein.

<sup>44</sup> (a) Cram, D. J.; Cram J. M. in *Container Molecules and Their Guests*, Monographs in Supramolecular Chemistry; Stoddart, J. F. Ed; Royal Society of Chemistry: Cambridge, 1994. (b) Ajami, D.; Liu, L.; Rebek, J. Jr. *Chem. Soc. Rev.* **2015**, *44*, 490–499. (c) MacGillivray, L. R.; Atwood, J. L. *Nature* **1997**, *389*, 469–472

<sup>45</sup> Mecozzi, S. and Rebek, Jr. *J. Chem. Eur. J.* **1998**, *4*, 1016-1022.

<sup>46</sup> a) Cram, D. J.; Tanner, M. E.; Thomas, R. *Angew. Chem., Int. Ed. Engl.* **1991**, *30*, 1024-1027. b) Korner, S. K.; Tucci, F. C.; Rudkevich, D. M.; Heinz T.; Rebek, J. *Chem. Eur. J.* **2000**, *6*, 187–195.

<sup>47</sup> Zarra, S.; Wood, D. M.; Roberts, D. A.; Nitschke, J. R. *Chem. Soc. Rev.* **2015**, *44*, 419-432.

**3**, which has been synthesized exploiting the synthetic procedure recently reported by us.<sup>37</sup>

## 2.2.1 Solid-state Assembly of a Resorcin[6]arene in Twin Molecular Capsules<sup>42</sup>

Crystals of **3** were obtained by slow evaporation from a solution of toluene/ethyl acetate. X-ray analysis revealed that in the solid state the resorcin[6]arene **3** adopts a pinched cone conformation<sup>42</sup> (Figure 15a) which is defined by two trimeric 3/4 cone-like sub-cavities - (highlighted in blue and yellow in Figure 14a) almost perpendicular to each other as reported by Ugozzoli for calix[6]arene.<sup>48</sup>

Superimposition between the pinched cone conformations of *p*-*tert*-butylcalix[6]arene (blue in Figure 15 b) and resorcin[6]arene (violet in Figure 15 b) shows their similarity, with a low root-mean-square deviation value of 0.578 Å.

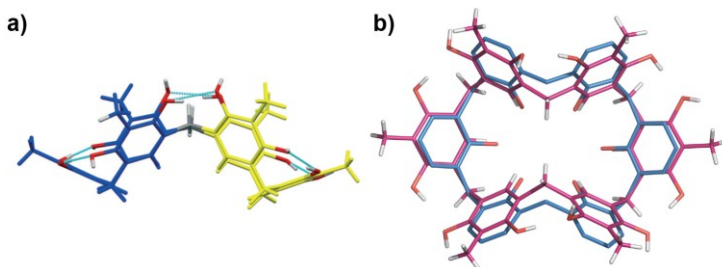


**Figure 15:** a) Side view of pinched-cone conformation of **3** with the two subcavities highlighted. b) Superimposition between the pinched conformation of **3** (violet) and *p*-*tert*-butylcalix[6]arene (blue).

<sup>48</sup> Ugozzoli, F. and Andreetti, G. D. *J. Incl. Phenom. Mol. Recognit. Chem.* **1992**, *13*, 123-126.

Surprisingly, in the solid state, two units of resorcin[6]arene **3** self-assemble in a molecular capsule (Figure 16a) in which two resorcinarene molecules are facing each other. The capsule is sealed by two square-arrays of intra and intermolecular hydrogen bonds between the OH groups of two macrocycles (Figure 16a-c). Close inspection of the structure of the capsule in Figure 16a revealed that two trimeric 3/4 cone-like cavities of each resorcin[6]arene are facing each other to form two pockets (twin capsules), each of which includes solvent molecules (Figure 17), toluene and ethyl acetate.

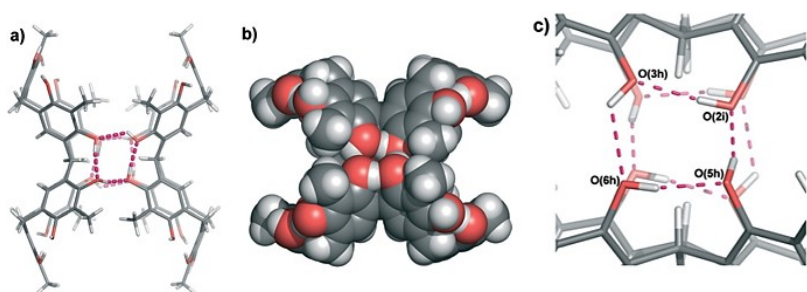


**Figure 16:** a) Side view of the solid-state structure of the capsule; b) CPK model of capsule; c) Detailed view of the square pattern of H-bonds.<sup>42</sup>

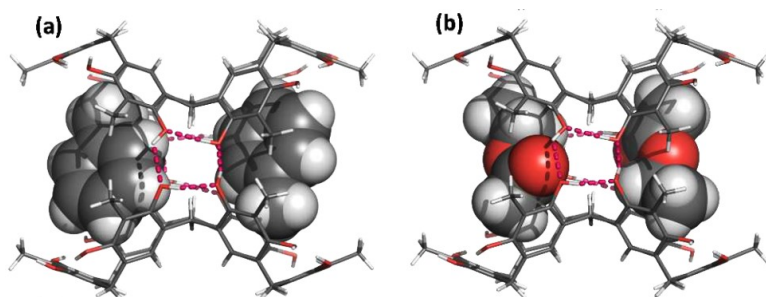


**Figure 17:** Encapsulation of toluene a) and ethyl acetate b) guest molecules in the molecular capsule.<sup>42</sup>

Toluene molecules establish  $\pi\cdots\pi$  stacking interactions with the aromatic walls of the container and two  $\text{ArCH}_2\text{-H}\cdots\pi$  interactions, the first one between the methyl group of the toluene and the aromatic wall of the macrocycle, and the second one between an aromatic CH group of toluene and an Ar group of the host (Figure 17a). Ethyl acetate is held in place by  $\text{CH}_3\cdots\pi$  interaction and weak H-bond between the carbonyl oxygen atom and the OH group of resorcin[6]arene - Figure 17b.

For each pocket of the molecular capsule, an average volume of void space of  $252 \text{ \AA}^3$  was calculated by using VOIDOO software (see Experimental Section) - Figure 18. Volumes of toluene and ethyl acetate guests (VG) were also calculated with the same program, and resulted  $96$  and  $85 \text{ \AA}^3$ , respectively.

In the field of synthetic receptors, a single value parameter, the Packing Coefficient (PC),<sup>44</sup> was introduced by Rebek and Mecozzi to simplify the assessment of complex stability for host-guest systems. It was found that the optimal PC value, defined as the ratio between the volume of the guest over the void volume of the receptor cavity, ranging from 46 to 64 % ( $0.55 \pm 0.09$  (55%)), in the liquid state when weak intermolecular interactions (dispersion forces, van der Waals interactions) are presents.

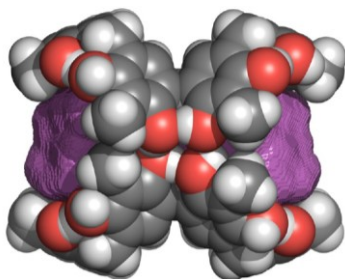


**Figure 18:** Surfaces of the voids available in the solid-state structure of the capsule (purple).

This simple rule has been validated in a large number of synthetic host-guest systems in solution and has been also extended to biological receptors.

Thus, by the volumes data calculated by VOIDOO, we have estimated a PC of  $96/252 = 0.38$  and  $86/252 = 0.34$  for the solid-state inclusion of toluene and ethyl acetate, respectively, into the pockets of the molecular capsule.

Finally, the view along the *c*-axis showed the presence of parallel rows of resorcin[6]arene capsules linked by intermolecular H-bonds between the OH groups of adjacent resorcin[6]arene units (Figure 19).

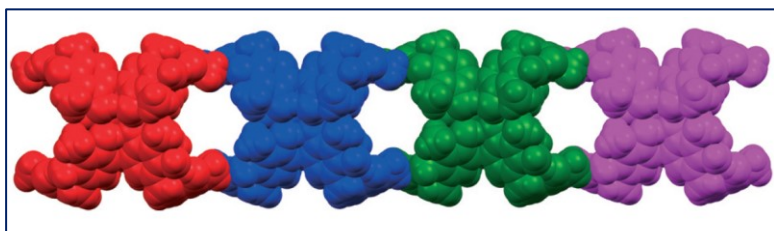


**Figure 19:** View of the one-dimensional self-assembly of molecular capsules along the *c*-axis.

In order to investigate the role played by the solvent in the solid-state self-assembly of the resorcin[6]arene molecules, we have performed a slow crystallization by DMF, a very strong competitor solvent for hydrogen bonding. In fact, the dimerization of **3** in the presence of DMF as crystallization solvent does not occur. X ray diffraction analysis shows the **3** adopts again a pinched cone conformation stabilized through six intramolecular H-bonds (Figure 20a).

Crystallization solvent has been included in crystalline lattice and six intermolecular hydrogen bonds are formed between the DMF molecules and OH groups of the resorcin[6]arene

molecules (Figure 20a). Each column arrangement of resorcin[6]arene (Figure 20b) runs parallel to the *b*-axis and is flanked by two other equivalent columns whose resorcinarenes cavities are oriented in the opposite direction - Figure 20b.

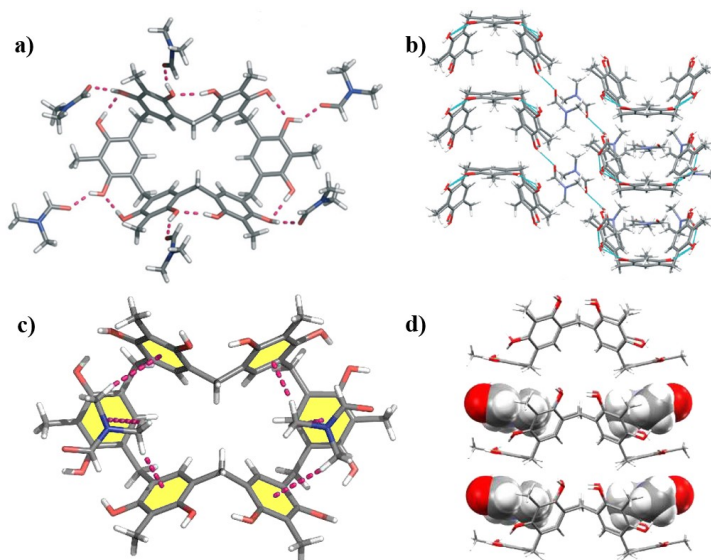


**Figure 20:** a) Resorcin[6]arene is surrounded by six DMF molecules interacting through intermolecular H-bonds; b) Columnar assembly of **3** viewed along the *b*-axis; c) CH $\cdots$  $\pi$  interactions between the DMF guest molecules and the aromatic walls of host; d) Stacking of **3** and guest DMF molecules along the *b*-axis.

The columnar arrangements of **3** along the *b*-axis in Figure 20 b present voids between the stacked resorcinarenes which are filled with DMF molecules (Figure 20 c and 20 d) that establish C-H $\cdots$  $\pi$  interactions (Figure 20c) with the aromatic walls of **3** (C-H $\cdots$  $\pi$  distances ranging from 3.474(2) to 3.987(2) Å).

Crystallographic data for both capsular derivatives were reported in Table 1.

**Table 1:** Crystal structure informations.

	<b>3</b> (Toluene/Ethyl Acetate)	<b>3</b> (DMF)
CCDC code	CCDC 1458015	CCDC 1458012
Empirical formula	C <sub>48</sub> H <sub>48</sub> O <sub>12</sub> , 0.5(C <sub>7</sub> H <sub>8</sub> ), 0.5(C <sub>4</sub> H <sub>8</sub> O <sub>2</sub> ), C <sub>4</sub> H <sub>8</sub> O <sub>2</sub>	C <sub>48</sub> H <sub>48</sub> O <sub>12</sub> , 6 (C <sub>3</sub> H <sub>7</sub> N O)
Formula weight	995.08	1255.43
Temperature (K)	100(2) K	100(2) K
Wavelength (Å)	0.7000	0.7000
Crystal system	Triclinic	Monoclinic
space group	<i>P</i> -1	<i>P</i> 2 <sub>1</sub> / <i>c</i>
<i>a</i> (Å)	11.91(1)	29.012(1)
<i>b</i> (Å)	14.88(1)	7.058(2)
<i>c</i> (Å)	16.83(1)	32.683(1)
$\alpha$ (°)	70.96(2)	90
$\beta$ (°)	87.2(1)	105.991(3)
$\gamma$ (°)	71.42(2)	90
<i>V</i> (Å <sup>3</sup> )	2668(3)	6433.4(18)
<i>Z</i> , $\rho_{\text{calc}}$ (Mg·m <sup>-3</sup> )	2, 1.239	4, 1.296
$\mu$ (mm <sup>-1</sup> )	0.085	0.090
<i>F</i> (000)	1058	2688
Data collection $\theta$ range	1.263-25.000	2.455°- 30.017°
Refl. collected / unique	48563 / 14544	56892 / 19593
Refinement method	FMLS on F <sup>2</sup>	FMLS on F <sup>2</sup>
Data / restraints / parameters	9245 / 13 / 744	18107 / 0 / 841
GOF	1.092	1.190
<i>R</i> <sub>1</sub> indices [ <i>I</i> >2 $\sigma$ ( <i>I</i> )]	0.1053	0.0760
<i>wR</i> <sub>2</sub> indices [ <i>I</i> >2 $\sigma$ ( <i>I</i> )]	0.2673	0.2001
<i>R</i> <sub>1</sub> indices (all data)	0.1087	0.0772
<i>wR</i> <sub>2</sub> indices (all data)	0.2730	0.2007

In conclusion,<sup>42</sup> single crystals of the resorcin[6]arene macrocycle were obtained from a toluene/ethyl acetate solution and from a DMF solution. Two different crystal structures were achieved from different solvents and in both crystal forms, **3** adopts a pinched cone conformation (Table 1), very similar to that reported for the *p*-*tert*-butylcalix[6]arene.<sup>48</sup> The pinched cone of the resorcin[6]arene **3** was stabilized by intramolecular H-bonds between OH groups. The crystal structure analysis of the triclinic form reveals that in the solid state the resorcin[6]arene assembles in a twin molecular capsule able to host toluene and ethyl acetate solvent molecules.

## 2.3 Synthesis of a Tetrasulfate-Resorcin[6]arene Cavitand <sup>49</sup>

### 2.3.1 Resorcin[4]arene-based Cavitand: An Overview

Cavitands are macrocyclic hosts with enforced cavities and designed to preorganize the resorcin[4]arene cavity by blocking the interconversion between the different conformations (Figure 21). <sup>50</sup>

Generally, resorcin[4]arene cavitands are obtained by bridging the OH groups with appropriate spacers, such as, methylene,<sup>39</sup> phosphonate,<sup>51</sup> thiophosphonate <sup>52</sup> and quinoxaline.<sup>53</sup>

In its pioneering work,<sup>54</sup> Cram for the first time reported the synthesis of resorcin[4]arene-based cavitands and the study of their conformational and supramolecular properties. Cram and coworkers highlighted the fundamental role played by bridges of different nature and length on the conformational mobility, shape, depth and recognition ability of this class of

---

<sup>49</sup> Gaeta, C.; Della Sala, P.; Talotta, C.; De Rosa M.; Soriente, A.; Brancatelli, G.; Geremia, S.; Neri, P. *Org. Chem. Front.* **2016**, *3*, 1276-1280.

<sup>50</sup> Cram, D. J. *Science* **1983**, *219*, 1177-1183.

<sup>51</sup> Menozzi, D.; Pinalli, R.; Massera, C.; Maffei, F.; Dalcanale, E. *Molecules* **2015**, *20*, 4460-4472.

<sup>52</sup> Pinalli, R.; Suman, M.; Dalcanale, E. *Eur. J. Org. Chem.* **2004**, 451-462.

<sup>53</sup> Cram, D. J.; Choi, H. J.; Bryant, J. A.; Knobler, C. B. *J. Am. Chem. Soc.* **1992**, *114*, 7748-7765 and reference cited therein.

<sup>54</sup> Cram, D. J.; Karbach, S.; Kim, H.-E.; Knobler, C. B.; Maverick, E. F.; Ericson, J. L.; Helgeson, R. C. *J. Am. Chem. Soc.* **1988**, *110*, 2229-2237.

compounds.<sup>54</sup> Cram showed clearly that the introduction of methylene bridges between the proximal OH groups of **1** (Figure 21), led to the formation of a cavitand **11** (Figure 21) which was able to host appropriate guests complementary to its cavity, such as CH<sub>2</sub>Cl<sub>2</sub>.<sup>54</sup>

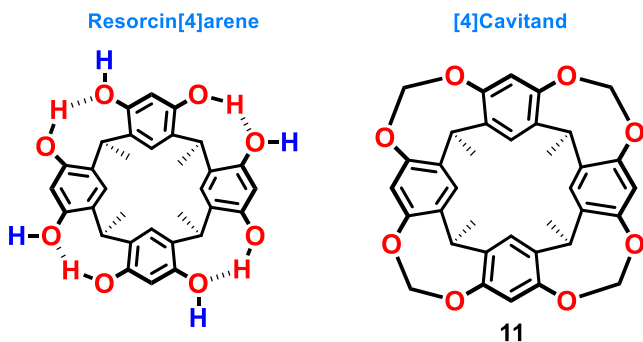


**Figure 21:** Structural difference between resorcinarenes and cavitand.

Rebek<sup>55</sup> reported in 1998 a novel class of cavitand named Velcrand<sup>56</sup> (**12** in Figure 22), which exhibit amazing supramolecular abilities as concerns the self-assembling in dimeric capsules and the molecular recognition and catalysis.<sup>57</sup>

In details the cavitand **12** is able to dimerize in a cylindrical capsule **12·12** driven by the formation of eight bifurcate H-bond interactions between self-complementary imide groups.<sup>6, 46b</sup>

<sup>55</sup> Heinz, T.; Rudkevich, D. M.; Rebek, J. Jr. *Nature* **1998**, *394*, 764-766.

<sup>56</sup> Tucci F. C.; Rudkevich, D. M.; Rebek, J. Jr. *J. Chem. Eur. J.* **2000**, *6*, 1007-1017 and reference cited therein.

<sup>57</sup> Mosca, S.; Yu, Y.; Rebek Jr, J. *Nature Protocol*, **2016**, *11*, 1371-1387.

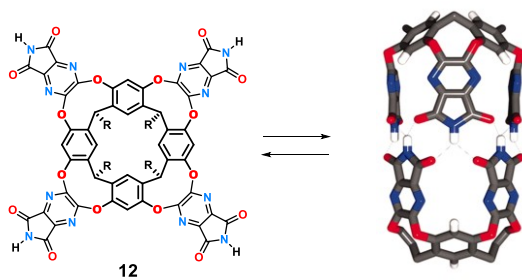


**Figure 22:** Tetraimide cavitaand **12** and its self-assembling in dimeric capsule sealed by 8 bifurcated H-bonds.<sup>55</sup>

Remarkable examples of cavitaands have been reported by Dalcanale and coworkers<sup>56,57</sup> which were able to bridge two vicinal hydroxyl groups of **1** with phosphonate and thiophosphonate groups (derivatives **13** and **14** in Figure 23).<sup>51,52</sup>

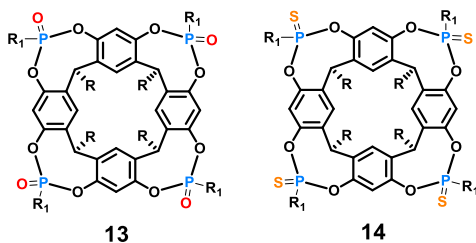


**Figure 23:** Phosphonate and thiophosphonate cavitaands developed by Dalcanale's group.<sup>51,52</sup>

Tetraphosphonate resorcin[4]arene cavitaands<sup>51</sup> show recognition abilities toward *N*-methylated ammonium guests by virtue of H-bonding and dipole-dipole interactions between P=O groups of **13** and the ammonium function of the guest.<sup>58</sup> The recognition abilities of tetraphosphonate cavitaands toward ammonium and alcohol guests have been exploited in gas sensing and cantilever-based chemical sensors (Figure 24).

<sup>58</sup> Maffei, F.; Betti, P.; Genevese, D.; Montalti, M.; Prodi, L.; De Zorzi, R.; Geremia, S.; Dalcanale, E. *Angew. Chem.* **2011**, *123*, 4750 – 4753.

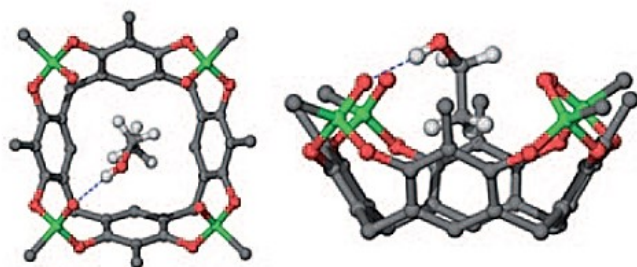


**Figure 24:** Top and side views of the crystal structures of the derivative **EtOH C-13**.<sup>58</sup>

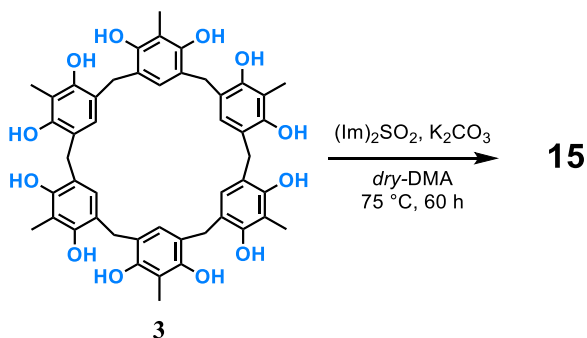
The studies on resorcinarene-based cavitands, reported to date in the literature, are focused on tetramer, while limited information have been reported on larger resorcin[6]arene. These considerations led me to develop a new topic, regarding the synthesis of a resorcin[6]arene cavitand in which the proximal OH groups are bridged with sulfate groups (R-SO<sub>2</sub>-R). The sulfate-bridge (R-SO<sub>2</sub>-R) can be considered as a supramolecular interacting group thanks to its H-bonds acceptor abilities and its inherent polarity. This project was also inspired by the diaryl sulfates synthetic route reported recently by Shi.<sup>59</sup>

### 2.3.2 Synthesis of Tetrasulfate Resorcin[6]arene Cavitand and NMR Investigation<sup>49</sup>

The treatment of **3** with *N,N'*-sulfuryldiimidazole [(Im)<sub>2</sub>SO<sub>2</sub>] and K<sub>2</sub>CO<sub>3</sub> in dry *N,N*-dimethylacetamide at 75 °C for 60 h, gave bridged derivative **15** in 30 % yield, after purification on silica gel – Scheme 4.<sup>49</sup> MALDI FT-ICR mass analysis shows

<sup>59</sup> Guan, B.-T.; Lu, X.-Y.; Zheng, Y.; Yu, D.-G.; Wu, T.; Li, K.-L.; Li, B.-J.; Shi, Z.-J. *Org. Lett.* **2010**, *12*, 396.

a monoisotopic peak at 1087.0895  $m/z$  attributable to  $[M+Na]^+$  of a tetrasulfate-bridged derivative (calculated: 1087.0888).



**Scheme 4:** Synthesis of **15**.

The structure assignment of the  $(\text{SO}_4)_4$ -bridged **15** was based on spectral  $^1\text{H}$  and  $^{13}\text{C}$  NMR data. Structural information can be related at just one of three possible  $(\text{SO}_4)_4$ -bridged derivatives namely, 1,2,4,5-tetra-bridged **15**, 1,2,3,4-tetra-bridged **15'**, and 1,2,3,5-tetra-bridged **15''** - Figure 25.

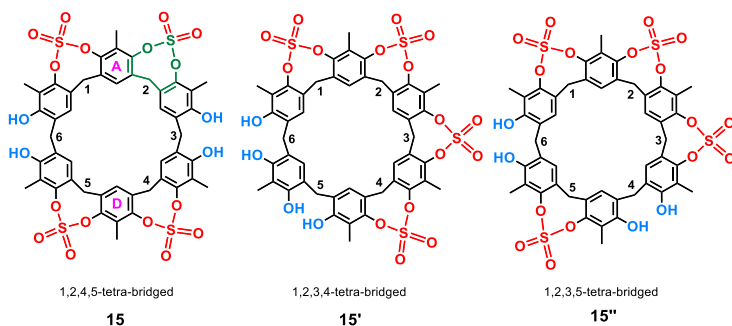


**Figure 25:** The three possible regioisomers of a tetrasulfate-bridged resorcin[6]arene **15**.

The  $^1\text{H}$  NMR spectrum of **15** at 403 K (400 MHz, TCDE) - Figure 26, show the presence of two broad  $\text{ArCH}_2\text{Ar}$  singlets at 4.05 and 3.94 ppm, in 2:1 ratio, two  $\text{ArCH}_3$  singlets at 2.29

and 2.42 ppm (2:1 ratio), and finally two *ArH* signals in 2:1 ratio at 7.30 and 7.33 ppm. This  $^1\text{H}$  NMR spectrum was only compatible with the symmetry of the 1,2,4,5-bridging pattern of **15** in Figure 25.

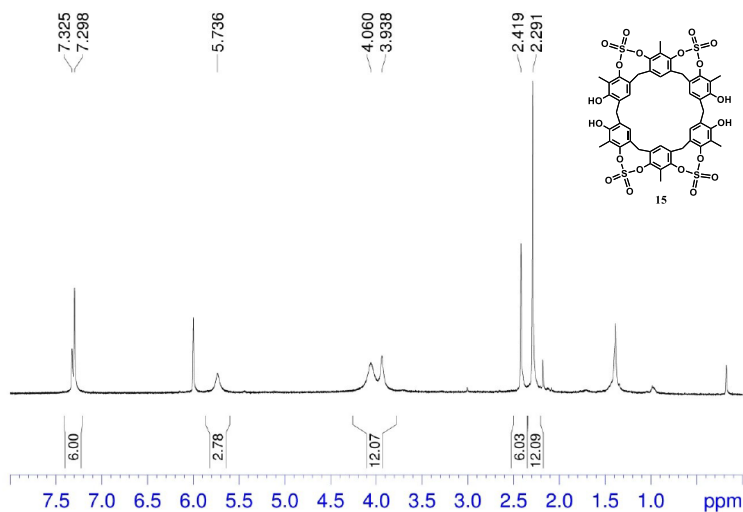


**Figure 26:**  $^1\text{H}$  NMR spectrum of **15** (TCDE, 600 MHz, 403 K).

Surprisingly, VT NMR study shows that the cooling at 298 K (TCDE, 400 MHz) caused the freezing of two conformational isomers of **15**.

In fact,  $^1\text{H}$  NMR spectrum of **15** at 298 K in Figure 27a and 2D COSY spectrum in Figure 27f, showed clearly that two independent sets of  $\text{ArCH}_2\text{Ar}$  AX systems were present. In Figure 27a we marked in blue three AX systems in a 1 : 1 : 1 ratio, attributable to the conformer **15a** (in Figure 28d,e), while the second one in which two AX systems in a 2 : 1 ratio, (blue in Fig. 27a) are attributable to the conformer **15b** (Figure 28a,c). Integration of the corresponding  $^1\text{H}$  NMR signals evidenced a 50/50 ratio for the two conformers **15a** and **15b**.

As concerns the conformer **15b** (Figure 28a,c), the presence of two methylene AX systems at 4.51/3.70 (8H) and 3.90/3.14 (4H) ppm in a 2:1 ratio (COSY spectrum, Figure 27f), suggested a conformation in which were presents two orthogonal symmetry planes bisecting the aromatic rings A and D of **15** (Figure 25) and the methylene bridges 3 and 6 in Figure 25. A Monte Carlo conformational search (MM3 force field, CHCl<sub>3</sub> as solvent) suggested the conformation **15b** in Figure 28a,b as the lowest energy structure compatible with these <sup>1</sup>H NMR signal pattern. In this conformation (Figure 28a,b) the resorcin[6]arene adopts again a pinched cone conformation and the four 8-membered SO<sub>4</sub>-rings (Figure 28a,c) adopt a boat-chair conformation (the boat-chair shape is highlighted in red in Figure 28c), in analogy to the known 6H,12H-dibenzo[d,g][1,3]dioxocine ring.<sup>60</sup>

As concerns the conformer **15a**, the presence of three ArCH<sub>2</sub>Ar AX systems at 4.55/3.75, 3.62/4.22 and 4.14/3.28 ppm in a 1:1:1 ratio (COSY spectrum, in Figure 27f), is compatible with the presence of only one symmetry plane bisecting the aromatic rings A and D of **15** in Figure 25. A Monte Carlo conformational search (MM3 force field, CHCl<sub>3</sub> as solvent) suggested the conformation **15a** in Figure 28d as the lowest energy structure compatible with these <sup>1</sup>H NMR signal patterns. In this conformer, the resorcin[6]arene backbone adopts a pinched cone conformation with two adjacent 8-membered SO<sub>4</sub>-rings (Figures 28d,f), in a distorted-boat conformation (the distorted boat-shape of the 8-membered ring is highlighted in red in Figure 28f). Such distorted-boat

---

<sup>60</sup> (a) Wöhnert, J.; Brenn, J.; Stoldt, M.; Aleksiuik, O.; Grynszpan, F.; Thondorf, I.; Biali, S. E. *J. Org. Chem.* **1998**, 63, 3866-3871.

conformation was already reported in calixarene derivatives containing 6H,12H-dibenzo[d,g][1,3]dioxocine rings.<sup>61</sup>

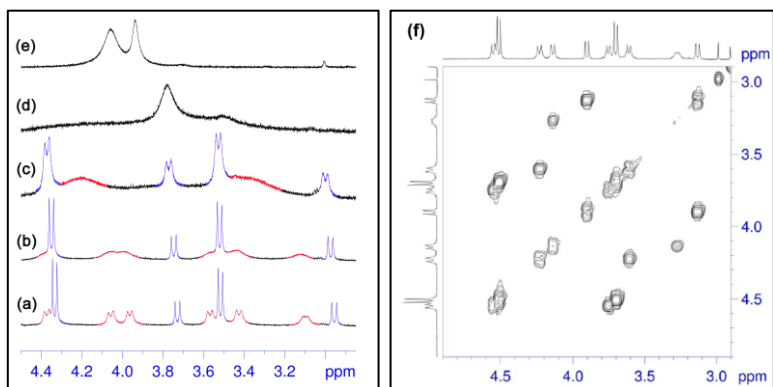


**Figure 27:** Methylene region of the  $^1\text{H}$  NMR spectrum (400 MHz, TCDE) of **15** at: (a) 298 K; (b) 313 K; (c) 333 K; (d) 363 K; (e) 403 K. (f) Expansion of 2D COSY spectrum (TCDE, 600 MHz, 298 K) of derivative **15**.

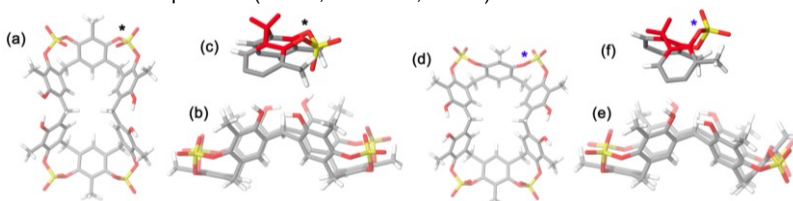


**Figure 28:** Lowest energy conformations (Monte Carlo conformational search, MM3,  $\text{CHCl}_3$  as solvent) of: **a)** top view of **15b**; **b)** side view of **15b**; **c)** particular of the boat-chair conformation<sup>60</sup> of the 8-membered ring bearing the sulfate bridge; **d)** top view of **15a**; **e)** side view of **15a**; **f)** particular of the distorted boat conformation<sup>61</sup> of the 8-membered rings bearing sulfate bridge in **15a**.

High temperature  $^1\text{H}$  NMR data show a coalescence for  $\text{ArCH}_2\text{Ar}$  AX systems of **15a** and **15b** at 333 and 363 K (400 MHz), respectively. From these data an energy barrier of 15.4

<sup>61</sup> (a) Troisi, F.; Gaeta, C.; Neri, P. *Tetrahedron Lett.* **2005**, *46*, 8041- 8046.

and 16.5 kcal/mol was calculated<sup>62</sup> for the conformational interconversion of **15a** and **15b**, respectively.

In solution the conformational ratio **15a/15b** is affected by the nature and polarity of the solvent. Thus, while in TCDE a 1:1 ratio was found, in CD<sub>3</sub>CN the symmetrical pinched conformation **15b**, in which the four 8-membered sulfate rings adopt a boat-chair conformation, is favored - Figure 28 - with respect to **15a** (at 298 K) with a 98/2 ratio (measured by <sup>1</sup>H NMR signal integration).

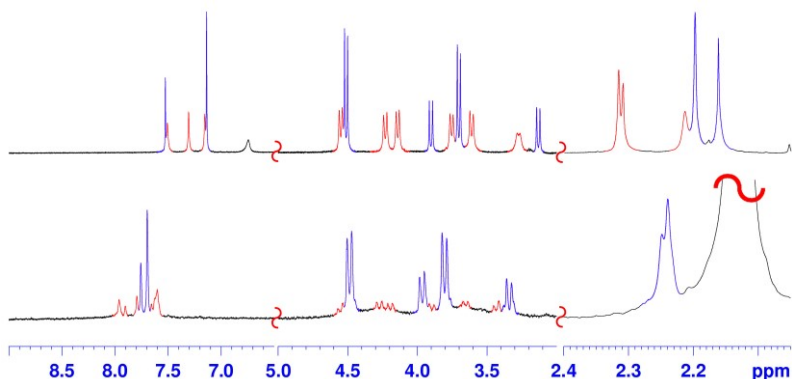


**Figure 29:** Significant portions of the <sup>1</sup>H NMR spectra of: (top) **15** in TCDE (298 K, 600 MHz); (bottom) **15** in CD<sub>3</sub>CN (298 K, 600 MHz). Marked in blu and in red the <sup>1</sup>H NMR signals of the conformer **15b** and **15a** respectively.

Probably, the regular pinched conformation **15b** in solution is templated by the acetonitrile solvent molecules that can occupy its two sub-cavities establishing secondary interactions.

This assumption was corroborated by the inspection of the solid-state structure of **15** obtained by X-ray analysis of a crystals formed by slow evaporation of an acetonitrile solution

<sup>62</sup> Kurland, R. J.; Rubin, M. B.; Wise, M. B. *J. Chem. Phys.* **1964**, *40*, 2426-2431.

of **15** Figure 28f. – In the solid state the cavitand **15** adopts a pinched cone conformation in which the four 8-membered sulfate rings adopt a boat-chair conformation<sup>60,61</sup> - Figure 30. The central free OH groups establishes intramolecular H-bond (with an O...O distance of 2.7 Å) that stabilize the pinched conformation - Figure 30b. Interestingly, in the solid state, two acetonitrile molecules are included into the two sub-cavities of the pinched cone conformation of **15** where establish weak hydrogen-bond interactions C-H...O=S between the methyl group of the CH<sub>3</sub>CN and oxygen atom of the sulfate bridge (Figures 30a,d) with an average C-H...O=S distance of 3.32 Å and an average C-H...O=S angle of 147.5 Å.

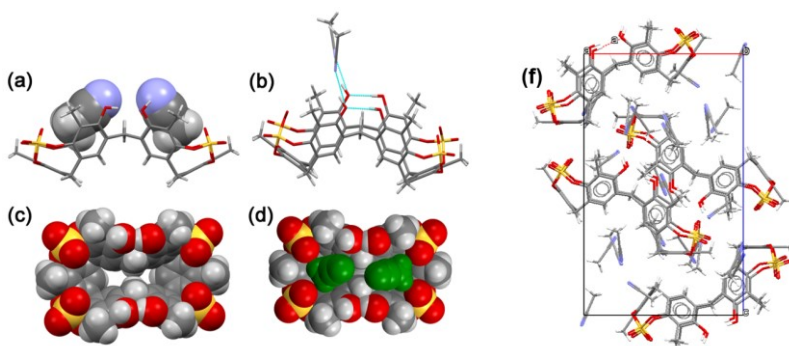


**Figure 30:** X-ray structure of tetrasulfate-resorcin[6]arene cavitand **15**.

In addition, the methyl groups of CH<sub>3</sub>CN are involved in C-H... $\pi$  interactions with the aromatic rings of **15** with an average distance C-H... $\pi^{\text{centroid}}$  of 3.55 Å.

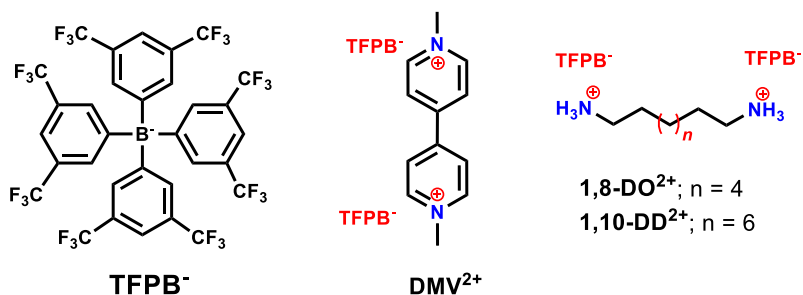
Crystallographic data of derivative **15** was reported in Table 2.

**Table 2:** Crystal structure informations.

	Derivative 15
CCDC code	CCDC 1485235
Empirical formula	C <sub>48</sub> H <sub>40</sub> O <sub>20</sub> , S <sub>4</sub> 7(C <sub>2</sub> H <sub>3</sub> N)
Formula weight	1352.42
Temperature (K)	100 K
Wavelength (Å)	0.7000
Crystal system	Monoclinic
space group	<i>P</i> 21/ <i>n</i>
<i>a</i> (Å)	13.909(4)
<i>b</i> (Å)	20.264(2)
<i>c</i> (Å)	22.762(2)
$\alpha$ (°)	90(2)
$\beta$ (°)	91.41(3)
$\gamma$ (°)	90(2)
<i>V</i> (Å <sup>3</sup> )	6414(2)
<i>Z</i> , $\rho_{\text{calc}}$ . (Mg·m <sup>-3</sup> )	4, 1.401
$\mu$ (mm <sup>-1</sup> )	0.217
F(000)	2825
Data collection $\theta$ range	5.021-27.499

### 2.3.3 Molecular Recognition Ability

We investigate through NMR techniques the molecular recognition ability of the cavitand **15** toward di-cationic guests such as **1,8-DiammoniumOctane** (1,8-DO<sup>2+</sup>), **1,10-DiammoniumDecane** (1,10-DD<sup>2+</sup>), and **DiMethylViologen** (DMV<sup>2+</sup>), as Tetrakis[3,5-bis(triFluoromethyl)Phenyl]Borate TFPB<sup>-</sup> salts - Figure 31.<sup>63</sup>

**Figure 31:** Guests tested toward derivative 15.

<sup>63</sup> Gaeta, C.; Troisi, F.; Neri, P. *Org. Lett.* **2010**, *12*, 2092–2095.

$^1\text{H}$  NMR titrations were carried out in acetonitrile- $d_3$ , where the regular pinched **15b** was the most abundant conformer (98/2 ratio **15b/15a**), by increasing the [guest]/[host] ratio while keeping constant the host concentration at about 0.001 mol/L. In all instances, the host signals were observed as averaged single resonances because of the fast exchange on the NMR timescale between the free and bound state.

The addition of TFPB salt of 1,8- $\text{DO}^{2+}$  to a solution of host **15** caused a downfield shift of its NMR signals, indicative of the inclusion of the guest inside the aromatic cavity of **15**. In accord, molecular mechanics calculations revealed that in 1,8- $\text{DO}^{2+} \subset \mathbf{15}$  complex the guest is linked to **15** via a two-point double-hydrogen bonding between  $\text{NH}_3^+$  and  $\text{SO}_4$  groups, while the host exhibits a regular pinched cone conformation - Figure 34b.

The Job's plot for **15** toward 1,8- $\text{DO}^{2+}$  showed a maximum at a mole fraction of 0.5, thus indicating a 1:1 binding stoichiometry - Figure 32b.

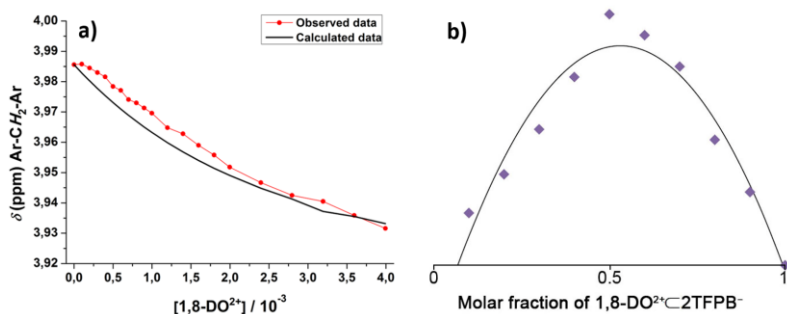


**Figure 32:** a) Plot of the observed downfield chemical shift of the ArCH<sub>2</sub>Ar of **15** as a function of added 1,8- $\text{DO}^{2+}$ ; b) Job's Plot experiment for the 1,8- $\text{DO}^{2+} \subset \mathbf{15}$  complex.

Likewise, a titration experiment was performed with TFPB salt of **1,10-DD**<sup>2+</sup> but no appreciable interaction could be detected by NMR spectroscopy. Probably because of its length, **1,10-DD**<sup>2+</sup> cannot form the two-point double-hydrogen bonding interaction with the sulfate bridges of **15**.

Finally, titration and Job's plot with TFPB salt of **DMV**<sup>2+</sup> was performed - Figure 33. The formation of **DMV**<sup>2+</sup>⊂**15** complex was unequivocally confirmed by the base peak at 625.1068 m/z (calcd. 625.1070) in the MALDI-FT-ICR mass spectrum in accordance with the molecular formula of the complex - Figure 34a.

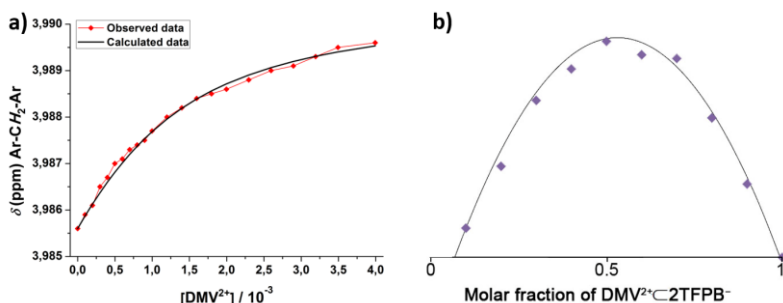


**Figure 33:** a) Plot of the observed downfield chemical shift of the ArCH<sub>2</sub>Ar of **15** as a function of added **DMV**<sup>2+</sup>; b) Job's Plot experiment for the **DMV**<sup>2+</sup>⊂**15** complex.

A close inspection of the energy-minimized (OPLS force field) structure of **DMV**<sup>2+</sup>⊂**15** complex reveals that the positive N-atoms of the guest are in close contact with SO<sub>4</sub> bridges of **15** (average distance N<sup>+</sup>⋯O=S of 3.5 Å) to establish ion-dipole interactions - Figure 34c. Association constants were calculated to both guests through nonlinear regression analysis<sup>64</sup> and a value of 600 M<sup>-1</sup> was calculated for the formation of **1,8-DO**<sup>2+</sup>⊂**15** complex and 1200 M<sup>-1</sup> for **DMV**<sup>2+</sup>⊂**15** complexes.

<sup>64</sup> Hirose, K. in *Analytical Methods in Supramolecular Chemistry*, ed. Schalley, C. A. Wiley-VCH, Weinheim, 2007.

In conclusion we have reported the first example of resorcin[6]arene-based cavitand. Sulfate bridges play a double role, both, as structural element for the preorganization of the larger resorcin[6]arene macrocycle and as functional supramolecular interacting groups.

The structure of the tetrasulfate-cavitand **15** was assigned by 1D and 2D NMR studies. In addition, the recognition abilities of the tetrasulfate-cavitand toward diammonium guests were investigated by standard NMR methods and high-resolution mass spectrometry.

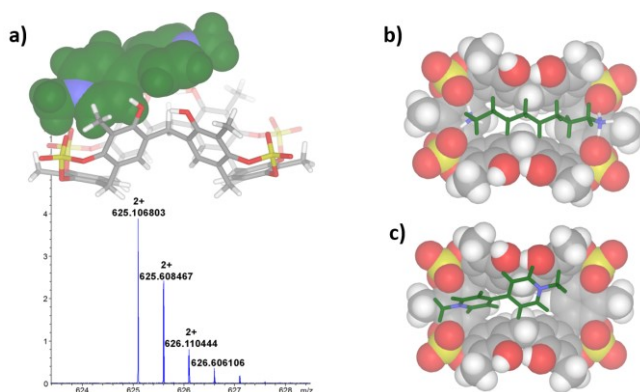


**Figure 34:** a) Significant portion of the HR MALDI FT-ICR mass spectrum of the  $\text{DMV}^{2+} \cdot \mathbf{15}$  complex showing the isotopic envelop with a  $\Delta$  spacing of 0.5 m/z; b) Minimized structures (molecular mechanics calculations, OPLS force field) of  $1,8\text{-DO}^{2+} \cdot \mathbf{15}$  and c) of  $\text{DMV}^{2+} \cdot \mathbf{15}$ .

As predicted, the sulfate-bridges play a crucial role in the interaction with 1,8-diammoniumoctane cation via a two-point double-hydrogen bonding between the ammonium groups and the sulfate bridges.

The resorcin[6]arene cavitand is also able to bind the dimethylviologen cation by means of ion-dipole interactions and high-resolution mass spectrometry prove the formation of host-guest complex.

## 2.4 Biomolecular Recognition with Larger Resorcin[6]arene Derivatives

65

### 2.4.1 Biomolecular Recognition with Macrocyclic Derivatives

Recently, many efforts have been focused on the study of the interactions between macrocyclic derivatives and biological druggable targets.<sup>66</sup> The principal aim of these studies is the design of macrocyclic compounds active as anti-cancer agents. In a pioneering work, Hamilton and co-workers<sup>67</sup> reported that calixarene derivatives bearing peptide-functions, were able to inhibit the tumor growth and angiogenesis *in vivo*, thanks to their selective binding to PDGF growth factor. Interestingly, the results of Hamilton and co-workers, also, showed a lack of toxicity of the calixarene framework *in vivo* biological tests. De Mendoza<sup>68</sup> and co-workers synthesized a calixarene derivative bearing cationic tetramethylguanidinium groups and showed that this macrocyclic derivative was able to interact selectively with the tetrameric protein p53TD-R337H mutant through hydrophobic interactions, ion pairing, and hydrogen bonding. Neri<sup>69</sup> and co-workers, obtained significant results in

---

<sup>65</sup> Manuscript in Preparation.

<sup>66</sup> Peczuh, M. W. and Hamilton, A. D. *Chem. Rev.* **2000**, *100*, 2479–2493.

<sup>67</sup> Blaskovich, M. A.; Lin, Q.; Delarue, F. L.; Sun, J.; Park, H. S.; Coppola, D.; Hamilton, A. D.; Sebt, S. M. *Nat. Biotechnol.* **2000**, *18*, 1065–1070.

<sup>68</sup> Gordo, V. Martos, E. Santos, M. Menendez, C. Bo, E. Giralt, J. de Mendoza *Proc. Natl. Acad. Sci. USA* **2008**, *105*, 16426–16431.

<sup>69</sup> M. G. Chini, S. Terracciano, R. Riccio, G. Bifulco, R. Ciao, C. Gaeta, F. Troisi, P. Neri, *Org. Lett.* **2010**, *12*, 5382–5385.

the inhibition of the histone deacetylase inhibitors (HDACis) by calix[4]arene derivatives bearing amido-functions, and by molecular docking they showed that, van der Waals interactions between the large hydrophobic groups at the exo rim of the calixarene derivatives and the four external hydrophobic pockets on the enzyme surface were essential for the stabilization of the HDAC-calixarene complex. More recently, the same authors reported the inhibition of the PDI enzyme, by a calix[4]arene derivative bearing acetamido functions at the upper rim.<sup>70</sup>

Macrocyclic derivatives such as calixarenes and resorcinarenes, thanks their synthetic versatility, can be functionalized with a variable number of functions through which they can establish multiple interactions with biomolecular targets affording to efficient inhibition of druggable targets.

## 2.4.2 Multivalent Effect

Many natural systems establish multiple simultaneous interactions to perform their task efficiently. Starting from this idea, new types of molecules are developed, called **Multivalent Systems**, that can bind a biomolecular guest through multiple and non-covalent interactions. This is an interesting and alternative approach to the traditional lock/key strategy to access new selective and potent inhibitors.<sup>71</sup>

---

<sup>70</sup> Tommasone, S.; Talotta, C.; Gaeta, C.; Margarucci, L.; Monti, M.C.; Casapullo, A.; Macchi, B.; Prete, S. P.; De Araujo, A. L.; Neri, P. *Angew. Chem. Int. Ed.* **2015**, *54*, 15405-15409.

<sup>71</sup> a) Gouin, S. G. *Chem. Eur. J.* **2014**, *20*, 11616-11628. b) Baldini, L.; Casnati, A.; Sansone, F.; Ungaro, R. *Chem. Soc. Rev.* **2007**, *36*, 254–266.

Generally, a multivalent system is composed by *recognition units* which are generally constituted by a known inhibitor of a druggable biomolecular target (blu in Figure 35), a *central core* (gray sphere in Figure 35) and appropriate spacers.

We can define the “valency” as the number of *recognition units* for a given compound. The high number of interactions result in an improved specificity and thermodynamic and kinetic stability compared to a simple monovalent interaction. Therefore, multivalent systems show affinity enhancement compared to the corresponding monovalent ligand. This behavior is called “multivalent effect”.<sup>72</sup>

In order to quantify the multivalent effect, we can define the *relative inhibitory potencies* - RP (**R**elative **P**otency) - given by the ratio of the IC<sub>50</sub> (half maximal inhibitory concentration) values of the monovalent unit and that of the multivalent compounds.

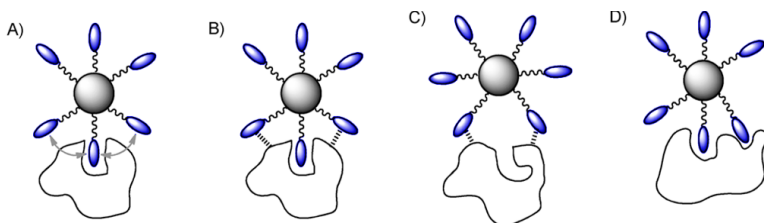


**Figure 35:** Possible binding modes in multivalent systems. **a)** Statistical rebinding, **b)** multiple non-specific interaction, **c)** secondary interactions between ligand and sterically encumbered substrate and **d)** clustering.

The second parameter is related to the affinity enhancement - **RP/n** – and it is defined as the ratio between RP and the number

---

<sup>72</sup> a) Lundquist, J. J.; Toone, E. J. *Chem. Rev.* **2002**, *102*, 555-578. b) Mammen, M.; Choi, S. K.; Whitesides, G. M. *Angew. Chem. Int. Ed.* **1998**, *37*, 2754-2794.

of interacting units. We observe a multivalent effect when  $RP/n \gg 1$ .

In multivalent systems, play a crucial role the design of scaffolds bearing multiple recognition units in order to develop new and more efficient inhibitor.<sup>73</sup> Macrocycles, such as calixarenes and resorcinarenes are a suitable choice, because they can be functionalized with a variable number of recognition units. Examples of calixarene-based multivalent systems<sup>74</sup> have been reported by Ungaro and coworkers.<sup>75</sup>

### 2.4.3 Multivalent Systems for the Inhibition of Glycosidases

Tumors are associated with a variety of structural alterations in the size and composition of the carbohydrates of glycoconjugates on the tumor cell surface.<sup>76</sup> The *N*-linked oligosaccharides on the cancer cell surfaces are larger and highly-branched. Oligosaccharide synthesis occurs in the endoplasmic reticulum, and is a process controlled by glycosidase enzymes. Naturally the glycosidases are involved in the malignant transformation of cells, and consequently specific glycosidases inhibitors may be promising candidates

---

<sup>73</sup> Fulton, D. A. and Stoddart, J. F. *Bioconjugate Chem.* **2001**, *12*, 655-672.

<sup>74</sup> Sansone, F.; Baldini, L.; Casnati A.; Ungaro, R. *New J. Chem.* **2010**, *34*, 2715-2728.

<sup>75</sup> Marra, A.; Scherrman, M.; Dondoni, A.; Casnati, A.; Minari, P.; Ungaro, R. *Angew. Chem. Int. Ed.*, **1994**, *33*, 2479-2481.

<sup>76</sup> Dennis, J. W Changes in glycosylation with malignant transformation and tumor progression, in *Cell Surface Carbohydrates and Cell Development*, ed. Fukada, M. **1991**, CRC Press, Boca Ration, USA, pp 161-194

for cancer chemotherapy.<sup>77</sup> The use of glycosidase inhibitors to prevent the formation of aberrant *N*-Linked oligosaccharides through the inhibition of druggable-glycosidases has emerged as a promising frontier for identifying new therapeutic strategy against cancer.

Golgi  $\alpha$ -mannosidase II (GMII) enzyme plays a central role in the mammalian *N*-glycosylation pathway, which constitutes a crucial step in the formation of mature glycans. The active site of GMII includes a Zn atom as part of the catalytic systems (Figure 36).

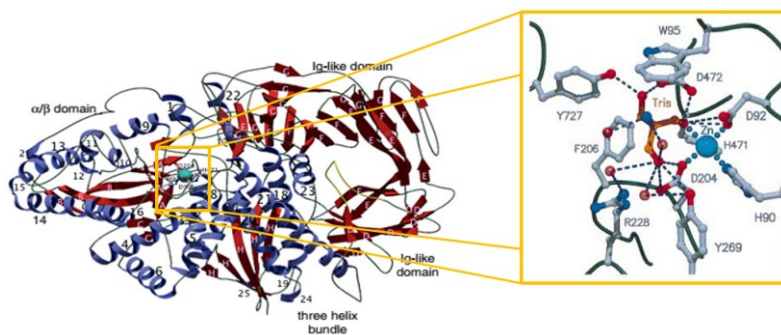


**Figure 36:** X ray structure of dGMII and magnification of catalytic site.

Natural pyrrolidine-based iminosugar as the 1,4-dideoxy-1,4-imino-D-arabinitol (**DAB-1**), extracts by *Angylocalyx boutiqueanus*, - Figure 37, has shown excellent inhibition properties toward  $\alpha$ -glucosidase II and Golgi-mannosidases I and II.

<sup>77</sup> a) Compain, P. and Martin, O. R. in *Iminosugars: from Synthesis to Therapeutic Applications*, Wiley VCH: New York, **2007**. b) Asano, N.; Oseki, K.; Kizu, H.; Matsui, K.; *J. Med. Chem.* **1994**, *37*, 3701-3706.

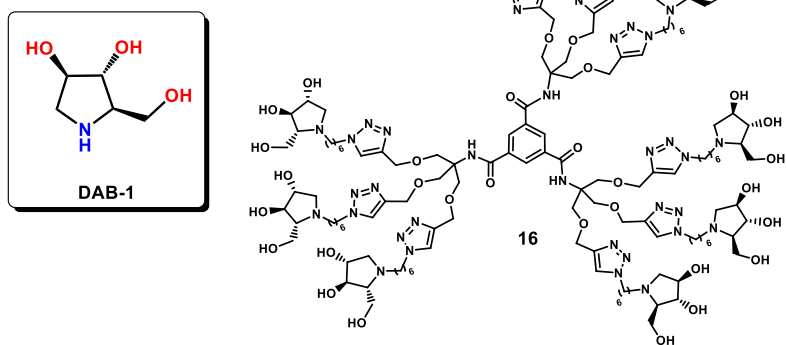


**Figure 37:** Multivalent system synthesized by Prof. Cardona.<sup>78</sup>

Recently, Cardona and coworker have reported the multivalent system **16**, (Figure 37) bearing nine **DAB-1** units which shows a very high RP/n value of 1520.<sup>78</sup>

These results prompted us to consider the design of a resorcin[6]arene-based multivalent system for the inhibition of glycosidase. Since, the introduction of a unit **DAB-1** on each OH group of the resorcin[6]arene **3** could lead to the synthesis of a multivalent system bearing 12 recognition units **DAB-1**.<sup>79</sup> On the basis of these considerations, in collaboration with Prof. Francesca Cardona of University of Florence, we have developed the new resorcin[6]arene-based multivalent derivative bearing **DAB-1** units in Figure 38.

The synthetic strategy is based on the CuAAS cycloaddition between the azide **17** (synthesized by Cardona's group) and the

<sup>78</sup> Mirabella, S.; D'Adamio, G.; Matassini, C.; Goti, A.; Delgado, S.; Gimeno, A.; Robina, I.; Moreno-Vargas, A. J.; Sestak, S.; Jiménez-Barbero, J.; Cardona, F. *Chem. Eur. J.* **2017**, *23*, 14585-14596.

<sup>79</sup> Soomro, Z. H.; Cecioni, S.; Blanchard, H.; Praly, J.; Imberty, A.; Vidal, S.; Matthews, S. E. *Org. Biomol. Chem.* **2011**, *9*, 6587-6597.

resorcin[6]arene derivative **20** bearing propargyl groups - Figure 38 .

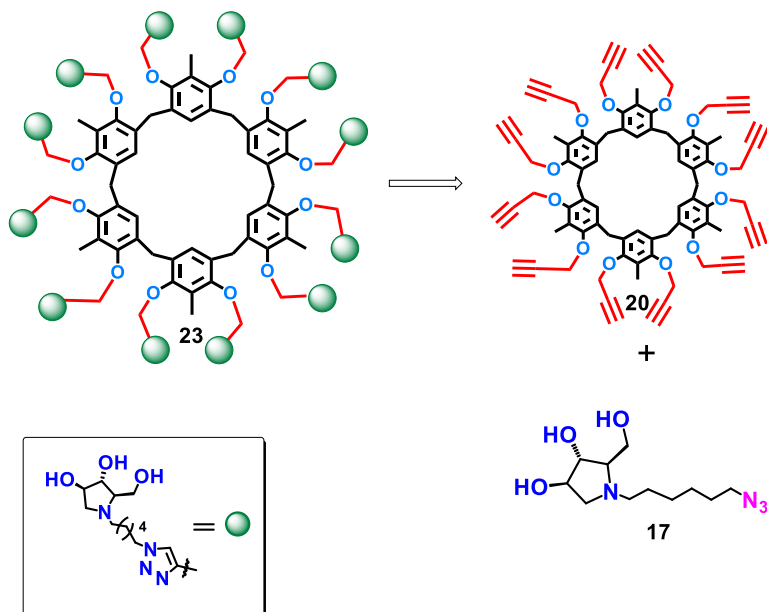


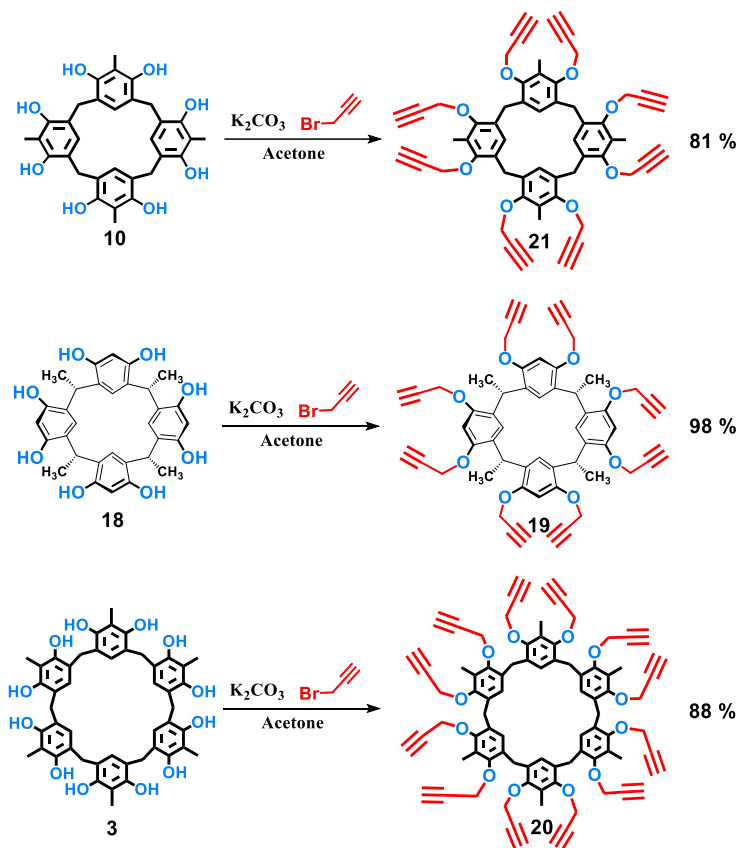
**Figure 38:** Catalytic strategy for obtaining the multivalent resorcin[6]arene-based system **23**.

In addition, resorcin[4]arene-based imminosugars **22** and **24** at lower valence (eight) were synthesized in order to compare their biological activities with that of the derivative **23**. Finally, biological assays were performed by Sergej Sesták from Institute of Chemistry, Center for Glycomics of Slovak Academy of Sciences.

#### 2.4.4 Synthesis and Characterization

In the first step, derivatives **10**, **18** and **3** were alkylated using propargyl bromide and potassium carbonate as base and all the derivatives were obtained with a good yield - Scheme 5.

$^1\text{H}$  NMR spectrum of derivative **21** (acetone- $d_6$ , 400 MHz, 298 K) shows a doublet at 4.48 ppm attributable to  $\text{OCH}_2$  and a triplet for  $\text{C}\equiv\text{CH}$  H-atom at 3.04 ppm ( $J=3.2$  Hz).



**Scheme 5:** Synthesis of derivative **19**, **20** and **21**.

The singlet at 3.89 ppm, attributable to  $\text{ArCH}_2\text{Ar}$  groups, is the proof of the fast rotation of the aromatic rings through the annulus and of the high conformational mobility of the macrocycle at room temperature - Figure 39a.

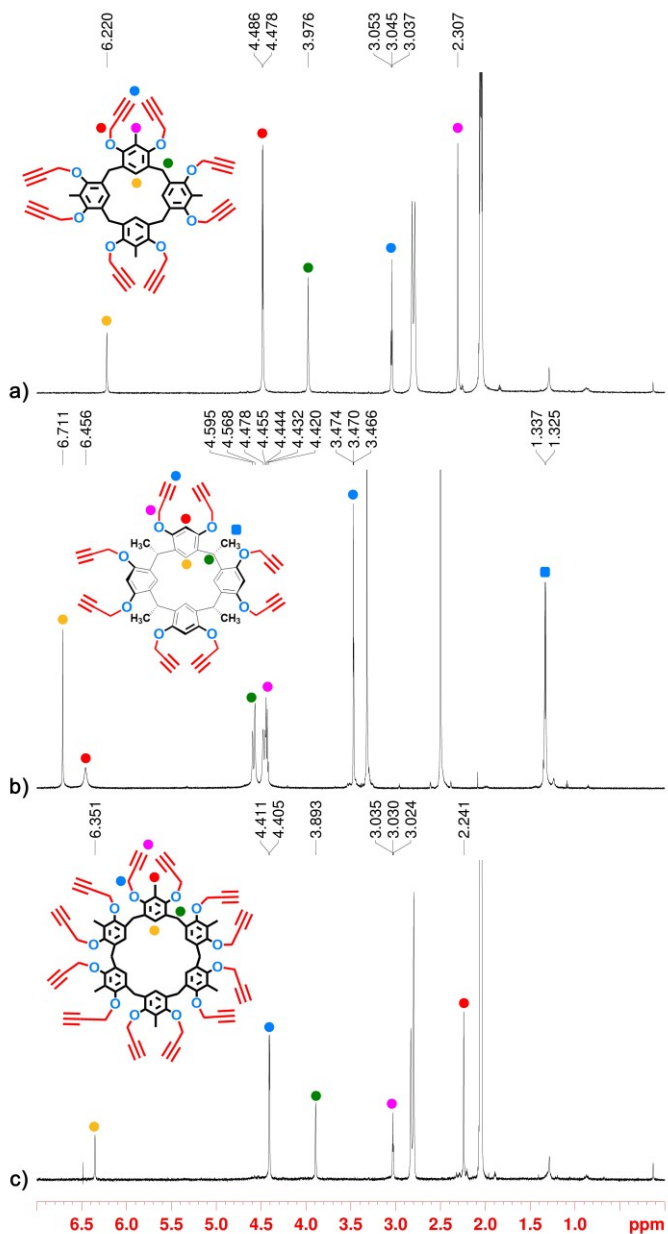


**Figure 39:**  $^1\text{H}$  NMR spectra of: a) Derivative 21 (acetone- $d_6$ , 400 MHz, 298 K), b) Derivative 19 (DMSO, 600 MHz, 298 K) and c) Derivative 20 (acetone- $d_6$ , 300 MHz, 298 K).

Likewise, derivative **20** (acetone- $d_6$ , 300 MHz, 298 K) shows a doublet at 4.40 ppm for  $OCH_2$ , a triplet at 3.03 ppm for  $C\equiv CH$  ( $J=1.8$  Hz) and finally at 3.89 ppm the singlet attributable to  $ArCH_2Ar$  - Figure 39c.

In accord with the spectroscopic data reported in literature for **19**,<sup>80</sup> the  $^1H$  NMR spectrum of derivative **19** (DMSO, 600 MHz, 298 K) shows a doublet at 4.58 ppm for the  $ArCH(CH_3)Ar$  that is partially overlapped with the  $OCH_2$  signals at 4.44 ppm. At 1.33 ppm we observe a doublet attributable to  $CHCH_3$  while the triplet at 3.47 ppm is attributable to the  $C\equiv CH$  ( $J=2.4$  Hz) group- Figure 39b.

A High-Resolution MALDI Fourier-Transform ion cyclotron resonance (MALDI-FT-ICR) mass spectrum shows a monoisotopic ion peak for the derivative **18** at  $m/z$  849.3492 [ $M+H^+$ ] (calculated: 849.3422) and for derivative **20** at  $m/z$  1273.5121 [ $M+H^+$ ] (calculated: 1273.5097).

Derivatives **22**, **23** and **24** were obtained by reaction of the corresponding propargylated resorcinarene derivatives with the azide **17** in the presence of  $CuSO_4$ , ascorbic acid in THF/ $H_2O$  in ACE tube and irradiate with microwave at 80° C for 45 min - Scheme 6.

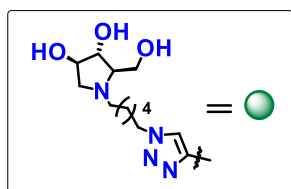
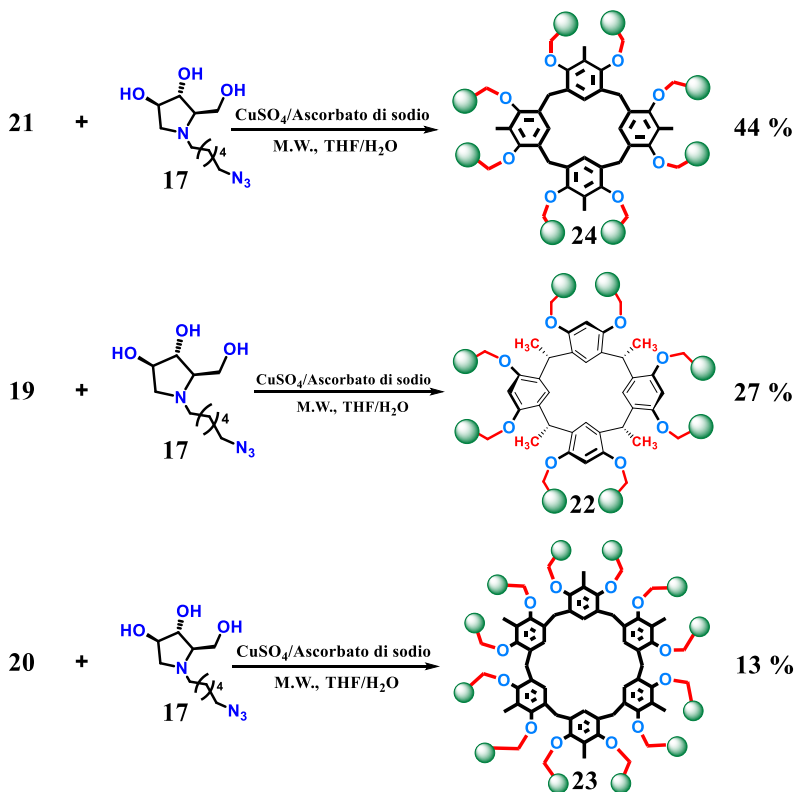
The purification of the derivatives thus obtained, was performed through column chromatography on silica gel using an ammonia solution in MeOH as liquid phase in order to eliminate Cu(I) that could interfere with biological essays.

$^1H$  NMR of **24** ( $CD_3OD$ , 600 MHz, 298 K) - Figure 40- shows a singlet at 7.78 ppm attributable to the triazole cycle and two

---

<sup>80</sup> Liu, W.; Yang, H.; Wu, Wenbo; Gao, H.; Xu, S.; Guo, Q.; Liu, Y.; Xu, S.; Cao, S.; *J. Mater. Chem. C*; **2016**, *4*, 10684-10692.

signals attributable to the diastereotopic  $CH_2$  at 2.81 and 2.32 ppm (see 2D-HSQC in experimental detail). Alkyl chain signals can be assigned through 2D COSY at 1.47, 1.29 (32 H), 1.86 and 4.34 ppm - Figure 41.



**Scheme 6:** Synthesis of glycoconjugates **22**, **23** and **24**.

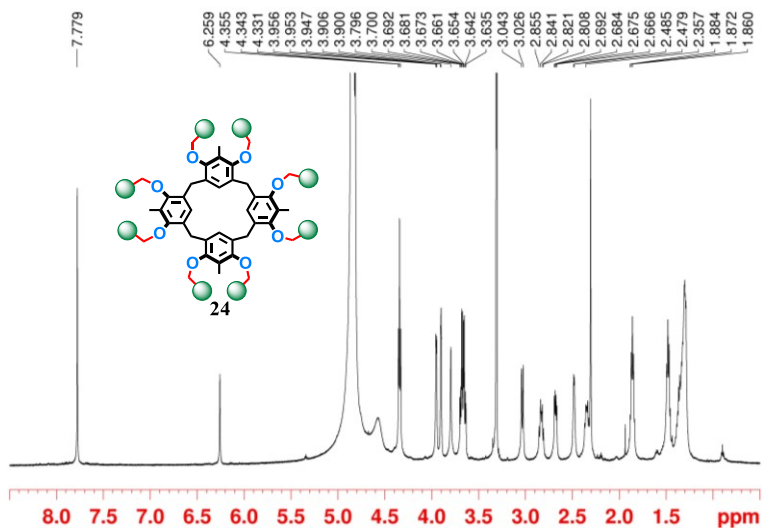


**Figure 40:**  $^1\text{H}$  NMR spectrum of derivative **24** ( $\text{CD}_3\text{OD}$ , 600 MHz, 298K).

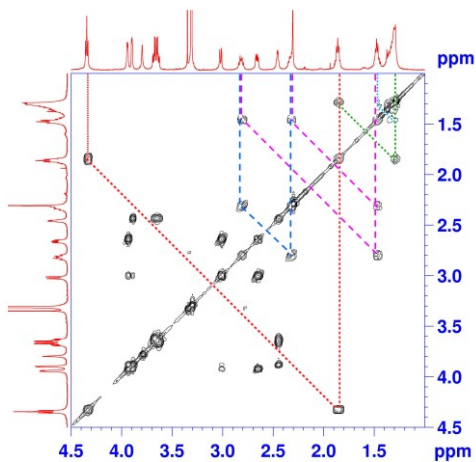


**Figure 41:** Magnification of 2D COSY spectrum of derivative **24**. Signals of coupling between  $\text{CH}_2$  of alkyl chain were marked ( $\text{CD}_3\text{OD}$ , 600 MHz, 298K).

MALDI FT-ICR mass spectrum of **24** shows a peak for  $[\mathbf{24}+\text{H}]^+$  at  $m/z$  2915.6992 (calculated: 2915.6991) that confirms the molecular formula of **24**. MALDI FT-ICR

investigation after and before the chromatographic purification shows clearly the the elution of the sample of **24** with an ammonia solution in MeOH is effective in removing  $\text{Cu}^+$ . Mass spectrum performed before of the purification - Figure 42a - exhibits four isotopic patterns attributable to  $[\mathbf{24}+\text{H}^+]$ ,  $[\mathbf{24}+\text{Na}^+]$ ,  $[\mathbf{24}+\text{K}^+]$  and  $[\mathbf{24}+\text{Cu}^+]$  species.<sup>81</sup> After purification we can observe only the peaks of the  $[\mathbf{24}+\text{H}^+]$ ,  $[\mathbf{24}+\text{Na}^+]$  and  $[\mathbf{24}+\text{K}^+]$  complexes - Figure 42b. For the derivative **24** a specific rotation value of  $\alpha = -21.0^\circ$  ( $c = 4.1 \text{ mg/l}$  in metanol) was measured.

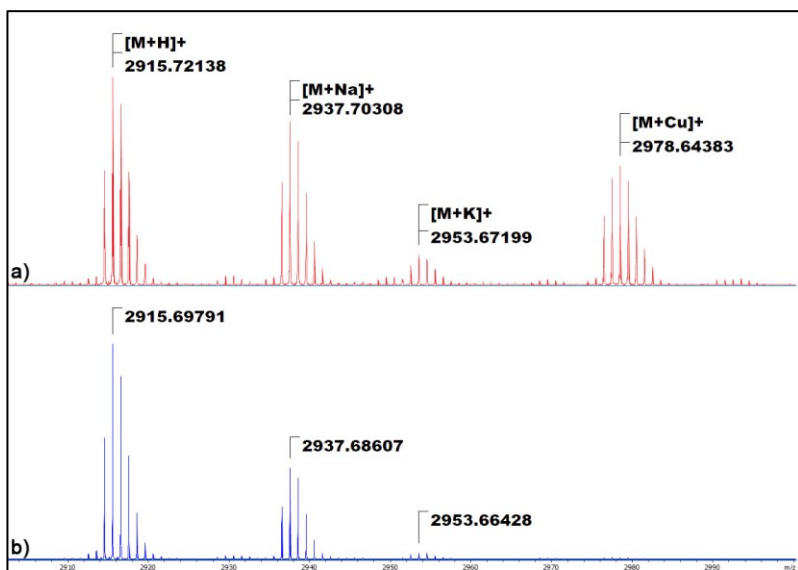
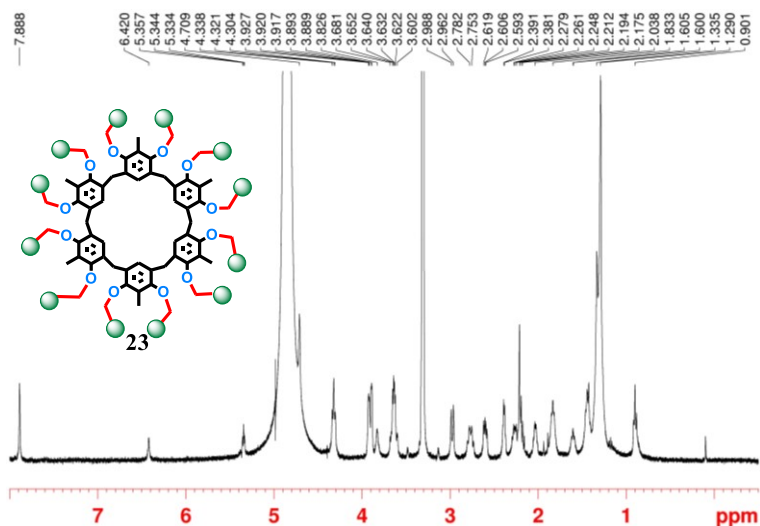


**Figure 42:** Portions of MALDI FT-ICR of derivate **24** **a)** before purification and **b)** after purification purification through chromatography column performed with ammonia solution in MeOH.

<sup>81</sup> FT-ICR mass investigation have a detection threshold at nM concentration.

$^1\text{H}$  NMR ( $\text{CD}_3\text{OD}$ , 600 MHz, 298K) of derivative **23** is reported in Figure 43. MALDI FT ICR spectrum of **23** shows a monoisotopic signal [**23**+ $\text{Na}^+$ ] at  $m/z$  4395.5286 (calculated: 4395.5910). A specific rotation value of  $\alpha=-33.50^\circ$  was measured for **23** ( $c = 1.9$  mg/l in metanol).



## 2.4.5 Biological Assays

Biological tests were performed toward three  $\alpha$ -mannosidases and particularly Jack Bean  $\alpha$ -mannosidase (**JBMan**), Golgi  $\alpha$ -mannosidase (**GMII**) and lysosomal  $\alpha$ -mannosidases (**LManII**) and two glucosidases:  $\alpha$ -Glucosidase and Amyloglucosidase.

For each enzyme was calculated the relative potency (rp) and relative potency per active unit (rp/n) and the values are reported in Table 3 and 4.

**Table 3:** IC<sub>50</sub>, rp and rp/n values measured for α-Mannosidases.

<b>α-Mannosidases</b>							
		<b>JBMan</b>		<b>GMIib</b>		<b>LManII</b>	
<b>Compound</b>	<b>Valency</b>	<b>IC<sub>50</sub></b>	<b>rp (rp/n)</b>	<b>IC<sub>50</sub></b>	<b>rp (rp/n)</b>	<b>IC<sub>50</sub></b>	<b>rp (rp/n)</b>
<b>DAB-1</b>	1	1300	-	175	-	2450	-
<b>24</b>	8	14.5	88 (11)	5.3	33 (4.1)	865	2.8 (0.35)
<b>23</b>	12	3.8	342 (29)	1.7	103 (8.6)	523	4.7 (0.4)
<b>22</b>	8	5.3	248 (31)	3.7	47 (6)	173	14 (1.8)

**Table 4:** IC<sub>50</sub>, rp and rp/n values measured for Glucosidases.

<b>Glucosidases</b>					
		<b>α-Glucosidase</b>		<b>Amyloglucosidase</b>	
<b>Compound</b>	<b>Valency</b>	<b>IC<sub>50</sub></b>	<b>rp (rp/n)</b>	<b>IC<sub>50</sub></b>	<b>rp (rp/n)</b>
<b>DAB-1</b>	1	153	-	8	-
<b>24</b>	8	29.3	5.2 (0.65)	0.31	26 (3.3)
<b>23</b>	12	15.3	10 (0.8)	0.2	41 (3.4)
<b>22</b>	8	10.8	14 (1.8)	0.38	21 (2.7)

The results reported in Tables 3 and 4 evidence that all the resorcinarene derivatives have a good inhibitory activity. The most important result regards the high selectivity of the derivatives **22-24** toward **GMIib** mannosidase with respect to **LManII**, as expressed for both IC<sub>50</sub> and rp/n values: this selectivity plays a crucial role for anti-cancer applications. Both **JBMn** and **GMIib** are prone to accept multivalent inhibitors, in fact RP/n values are large in both cases. Finally, the multivalent resorcin[6]arene derivative **23** gave an, very promising, IC<sub>50</sub> value toward GMIib of 1.7 μM.

# 3 Synthesis of New CycloParaPhenylene Macrocycles and Studies of Their Properties

## 3.1 Carbon Nanobelt and Carbon Nanohoops: An Overview

An ancient and fascinating challenge in macrocyclic chemistry is the synthesis of carbon nanobelts and carbon nanohoops (Figure 44).<sup>82</sup> Belt and hoop-like macrocycles are constituted by fully conjugated  $\pi$  systems that possess electronics and optical features of interest for applications in organic electronics and photonics.<sup>83</sup>

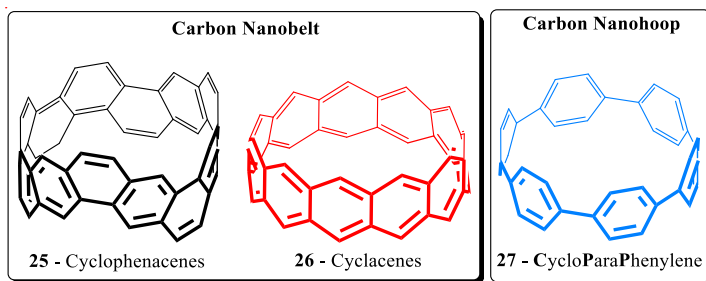


**Figure 44:** Examples of Carbon Nanohoop and Carbon Nanobelt.

<sup>82</sup> Iyoda, M.; Kuwatani, Y.; Nishinaga, T.; Takase, M.; Nishiuchi, T. in *Fragments of Fullerenes and Carbon Nanotubes*, Petrukhina, M. A.; Scott, L. T. Eds.; Wiley, **2012**.

<sup>83</sup> Tahara, K. and Tobe, Y. *Chem. Rev.* **2006**, *106*, 5274-5290.

Belt-shaped macrocycles (Figure 44 - derivatives **25** and **26**) are constituted by fused benzene rings, and initially were of interest as synthetic challenge.<sup>84</sup> Thus, as example given, the cyclacene (Figure 44), the shortest belt segment of zigzag CNTs, was only theorized in literature in 1954.<sup>85</sup> Many scientists have attempted the synthesis of the cyclacenes, among them, Stoddart,<sup>86</sup> Schlüter,<sup>87</sup> and Cory,<sup>88</sup> but unsuccessfully. Analogously, Vögtle<sup>89</sup> proposed a nanobelt (Vögtle's belt), which can be considered as a segment of armchair CNTs, and analogously to cyclacene, the Vögtle's belt has never been synthesized. Very recently, in an impressive work, Itami<sup>25</sup> and coworkers has reported the synthesis of a macrocyclic carbon nanobelt, constituted by a closed loop of fully fused edge-sharing benzene rings. The nanobelt **25** has been obtained by iterative Wittig reactions followed by a nickel-mediated aryl-aryl coupling reaction. In the last decade,<sup>90</sup> many attentions have been devoted to the synthesis of macrocyclic carbon nanorings, in which arene rings are linked by single bonds. Among, the carbon nanorings, the [**n**]CycloParaPhenylenes ([**n**]CPPs, Figure 44) are fully conjugate macrocycles constituted by *n* para-linked benzene

---

<sup>84</sup> a) Eisenberg, D.; Shenhar, R.; Rabinovitz, M. *Chem. Soc. Rev.* **2010**, 39, 2879-2890. b). Tahara, K. and Tobe Y. *Chem. Rev.* **2006**, 106, 5274-5290.

<sup>85</sup> Heilbronner, E. *Helv. Chim. Acta* **1954**, 37, 921-935.

<sup>86</sup> Kohnke, F. H.; Slawin, A. M. Z.; Stoddart, J. F.; Williams, D. J. *Angew. Chem. Int. Ed. Engl.* **1987**, 26, 892-894.

<sup>87</sup> Standera, M. and Schlüter, A. D. in *Fragments of Fullerenes and Carbon Nanotubes*, Petrukhina, M. A.; Scott, L. T. Eds.; Wiley, **2012**., pp. 343-366

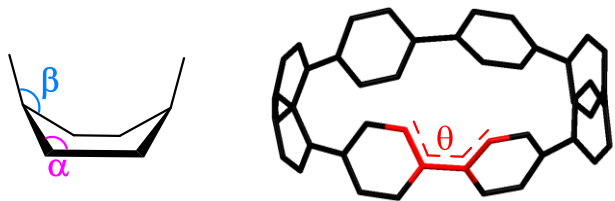
<sup>88</sup> Cory, R. M.; McPhail, C. L.; Dikmans, A. J.; Vittal, J. J. *Tetrahedron Lett.* **1996**, 37, 1983-1986.

<sup>89</sup> Vögtle, F.; Schroder, A.; Karbach, D. *Angew. Chem. Int. Ed. Engl.* **1991**, 30, 575-577.

<sup>90</sup> Segawa, Y.; Yagi, A.; Matsui, K.; Itami, K. *Angew. Chem. Int. Ed.* **2016**, 55, 5136-5158.

units.<sup>91</sup> The cyclic structure of CPPs induces a high energy strain in these macrocycles. As shown by DFT calculations at the B3LYP/6-31G(d) level of theory,<sup>92</sup> a dramatic increase of energy strain was calculated as the diameter of CPP decreases. For example, [12]CPP has an energy strain approximately of 4 kcal mol<sup>-1</sup> for aryl ring, while [5]CPP (the smallest of the series) has a 24 kcal mol<sup>-1</sup> of energy strain for aromatic ring. The structural parameters,  $\alpha$ ,  $\beta$  and  $\theta$  angles represented in Table 5, are indicative of the strain of the CPP derivatives:  $\alpha$  and  $\beta$  values decrease as the dimensions of the CPPs become larger, while the torsion angle  $\theta$  increases as the CPP become larger, until to reach similar values to those of the linear *p*-polyphenylenes.<sup>93</sup>

**Table 5:** Calculated bending and torsional angles for CPPs.<sup>94</sup>



The figure shows two chemical structures. On the left is a small CPP ring with two angles labeled:  $\alpha$  (pink) and  $\beta$  (blue). On the right is a larger CPP ring with a torsion angle labeled  $\theta$  (red).

[n] CPP	6	8	10	12	14	16	18	20
$\alpha$	12.5	9.3	7.3	6.1	5.2	4.6	4.0	3.6
$\beta$	18.0	13.7	11.1	9.3	8.0	6.9	6.3	5.6
$\theta$	27.4	30.7	32.7	33.4	34.4	35.0	34.9	35.1

<sup>91</sup> Darzi, E. R.; Jasti, R. *Chem. Soc. Rev.* **2015**, *44*, 6401-6410 and reference cited therein.

<sup>92</sup> Segawa, Y.; Omachi, H.; Itami, K. *Org. Lett.* **2010**, *12*, 2262-2265.

<sup>93</sup> Segawa, Y.; Fukazawa, A.; Matsuura, S.; Omachi, H.; Yamaguchi, S.; Irle, S.; Itami, K. *Org. Biomol. Chem.* **2012**, *10*, 5979-5984.

The structural size-depending properties, previously summarized, are closely interconnects with the optoelectronic features of CPP derivatives. As shown in Figure 45, the right balance between the bending and torsional effects influences the HOMO-LUMO energy gap of CPPs.<sup>94</sup>

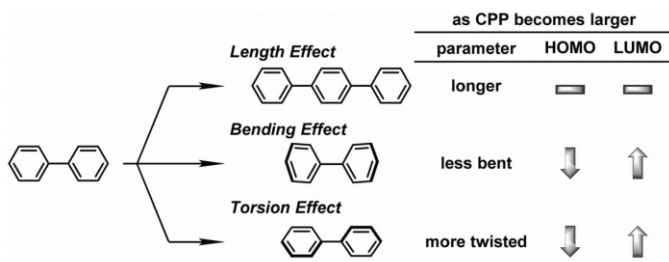


**Figure 45:** Contribution of the structural effects on HOMO(LUMO energy levels).<sup>91</sup>

As CPP becomes larger, then the HOMO-LUMO energy gap increases as result of the stabilization of the HOMO level and destabilization of the LUMO level: *vice versa*, CPPs show a narrowing of the HOMO-LUMO gap as the number of benzene units  $n$  decreases, as shown in Figure 46.

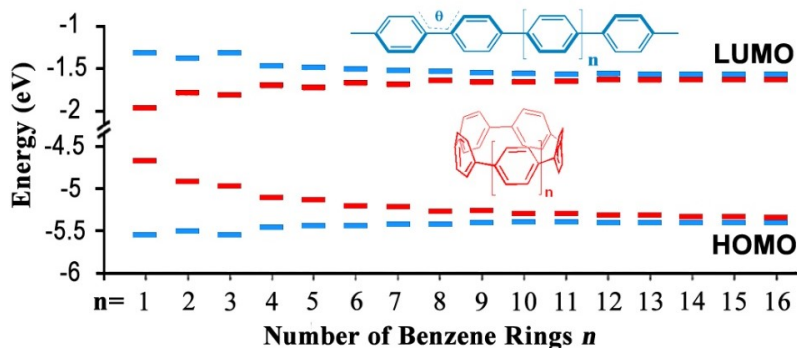


**Figure 46:** Comparison of the HOMO-LUMO band-gap between the CPPs and the linear paraphenylenes.<sup>91</sup>

<sup>94</sup> Lewis, S. E. *Chem. Soc. Rev.* **2015**, *44*, 2221-2304.

Differently, the linear paraphenylenes show a narrowing of the HOMO-LUMO gap as  $n$  (Figure 46, blu) and conjugation length is increased, as reported in Figure 54.<sup>84</sup> It is clear that, these aspects influence the optoelectronic properties of CPP macrocycles. In details, regarding the optical properties, the [5-12]CPPs have a common absorption maximum between 335–340 nm (Figure 47).

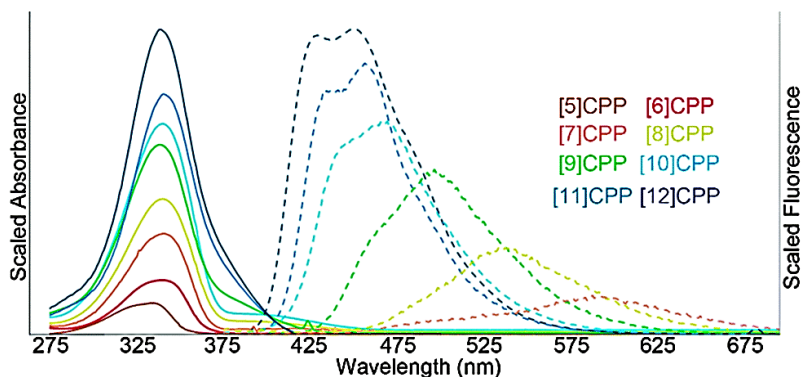


**Figure 47:** Absorption spectra (full line) and fluorescence spectra (dashed line) of [5-12]CPPs.<sup>91</sup>

In fact, as reported,<sup>95</sup> the HOMO–LUMO optical transitions in CPPs are Laporte forbidden because of the conservation of orbital symmetry for the centrosymmetric CPPs (Figure 48). In details, the absorbance maxima for all [n]CPPs derivatives are almost identical and have been attributed to degenerate HOMO-1 to LUMO or HOMO-2 to LUMO transitions, and HOMO to LUMO+1 or HOMO to LUMO+2 transitions.

<sup>95</sup> Adamska, L.; Nayyar, I.; Chen, H.; Swan, A. K.; Oldani, N.; Fernandez-Alberti, S.; Golder, M.R.; Jasti, R.; Doorn, S. K.; Tretiak, S. *Nano Lett.* **2014**, *14*, 6539-6546.

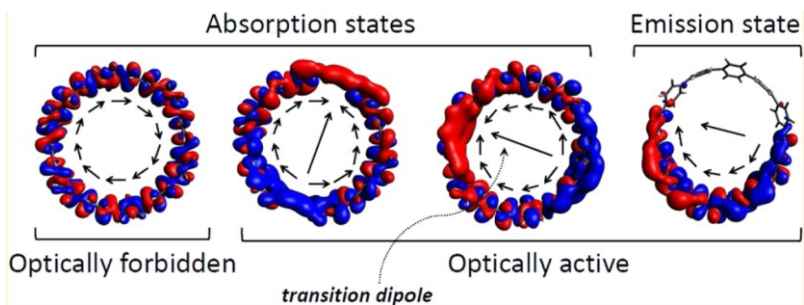


**Figure 48:** Representation of orbital distribution of transition density. The black arrows represent transition dipole moment.<sup>95</sup>

Fluorescence spectra are red-shifted when CPP become smaller while no fluorescence is observed for [6] and [5]CPPs - Figure 47. In addition, as reported in Table 6 the quantum efficiency decreases as the CPP macrocycle become smaller. These observations have been explained performing time-dependent density functional theory studies (TD-DFT). In detail, because of a violation of the Frank-Condon principle, the relaxation from  $S_2$  and  $S_3$  states to  $S_1$  state occurs.

**Table 6:** Summary of experimental photophysical properties for [5]–[12]CPP<sup>91</sup>

[n]CPP	Diameter (nm)	Absorbance (nm)	Fluorescence (nm)	Stoke Shift (nm)	Fluorescence Quantum Yield	Extinction coefficient ( $M^{-1} cm^{-1}$ )
5	0.67	335	--	--	--	$5.7 \cdot 10^4$
6	0.79	340	--	--	--	N.A.
7	0.95	340	587	247	0.007	$6.9 \cdot 10^4$
8	1.1	340	533	193	0.1	$1.0 \cdot 10^5$
9	1.2	340	494	154	0.38	$1.2 \cdot 10^5$
10	1.4	338	466	128	0.65	$1.3 \cdot 10^5$
11	1.5	340	458	118	0.73	$1.3 \cdot 10^5$
12	1.6	339	450	111	0.81	$1.4 \cdot 10^5$

Interestingly, in larger [n]CPPs (with  $n > 7$ ) the  $S_1$  state breaks the symmetry of the ground state - Figure 48 - causing emission to the  $S_0$  state and consequently a decreasing quantum

efficiency and redshifting fluorescence from [12]CPP to [7]CPP were observed. In smaller [5 and 6]CPPs the S<sub>1</sub> state conserves the symmetry of the ground state and so emission to the S<sub>0</sub> state doesn't occur and no fluorescence is observed.

### 3.1.1 Synthesis of Cycloparaphenylenes

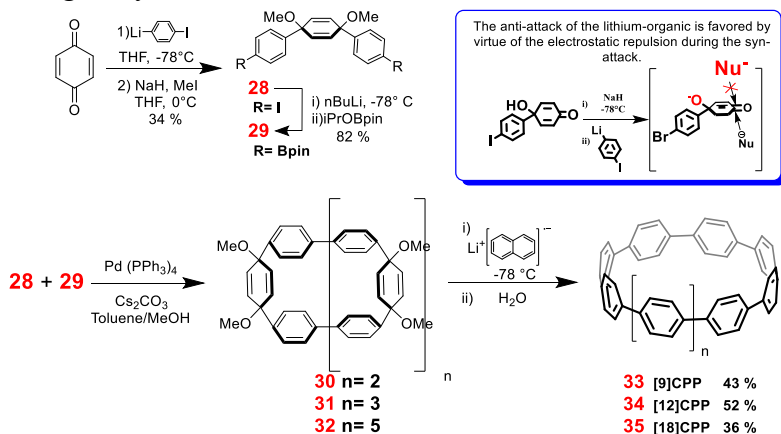
As previously discussed, the [*n*]CPPs derivatives are highly curved nanostructures which suffer of a high level of strain and consequently the direct macrocyclization from linear paraphenylenes has never been observed.<sup>96</sup> Consequently, the synthetic strategies adopted for the synthesis of CPPs, by Justi, Yamago and others,<sup>96</sup> provide for macrocyclization between rigidly-curved elements<sup>96</sup> as masked benzene rings and successive aromatization of the macrocyclic precursors. On this basis, the first syntheses of CPPs - Scheme 10 - has been reported by Jasti and Bertozzi in 2008.<sup>24</sup> In the synthesis of Jasti and Bertozzi (Scheme 7), the key intermediate is the rigidly-curved derivative **28**, incorporating the 3,6-syn-dimethoxy-cyclohexa-1,4-diene unit as a masked benzene: in fact the diene was aromatized after the macrocyclization by treatment with sodium naphthalide.<sup>96</sup>

Derivative **28** was obtained by double addition of monolithium reagent (obtained from 1,4-diiodobenzene) at 1,4-benzoquinone. Diiodide **28** was transformed in diboronate **29** and subsequently, hemicyclic derivatives **28** and **29** was coupled through Suzuki-Miyaura cross-coupling to give three macrocycles: **33**, **34** and **35** constituted by nine, twelve and eighteen units respectively. Treatment with sodium naphthalide (that was found to be an excellent solution to

---

<sup>96</sup> Hirst, E. S. and Jasti R. *J. Org. Chem.* **2012**, *77*, 10473-10478.

reduce oxidized cyclic compounds) gave final CPP derivatives with good yields.<sup>24</sup>



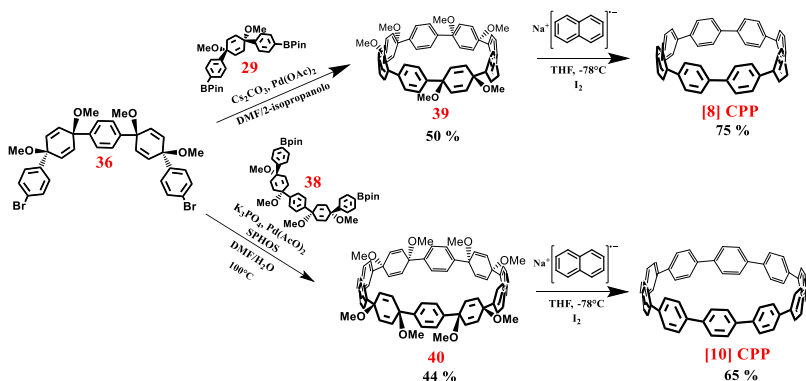
**Scheme 7:** Jasti synthetic route.<sup>24</sup>

The discovery of an efficient route to obtain CPP derivatives, gave a new thrust to improve this procedure and to discover of new ones. Similarly, were synthesized selectively [7-12] CPP.<sup>97</sup> In 2012 Jasti reported a cheaper gram-scale synthesis of [8] and [10] CPPs - Scheme 8.<sup>98</sup>

In the gram-scale synthesis of Jasti,<sup>87</sup> a crucial role is played by derivative **36** which can be synthesized in large quantities. Derivative **36** (bears two cyclohexadiene rings) was reacted with **29** to give macrocycle **39** with 50 % of yield. Likewise, diboronate **38** (obtained from **36**) was coupled to give derivative **40** with 44% of yield. In order to minimize the cost of production, Pd(OAc)<sub>2</sub> has been used as catalyst for the cross-coupling macrocyclization. Finally [8]CPP and [10]CPP was obtained in 75% and 65% of yield respectively in reductive aromatization reaction.

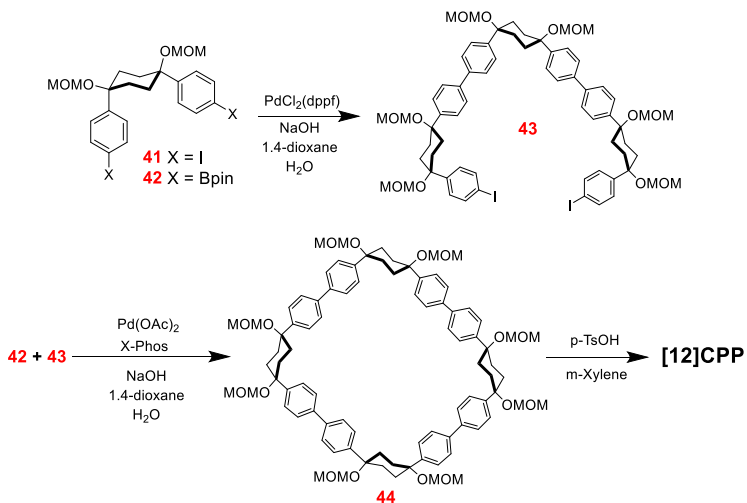
<sup>97</sup> Darzi, E. R.; Sisto, T. J.; Jasti, R. *J. Org. Chem.* **2012**, *77*, 6624-6628.

<sup>98</sup> Xia, J.; Bacon, J. W.; Jasti, R. *Chem. Sci.* **2012**, *3*, 3018-3021.



**Scheme 8:** Gram-Scale synthesis of [8] and [10]CPP reported by Jasti.<sup>98</sup>

In 2009 Itami and co-workers have investigated the synthesis of [12]CPP.<sup>99</sup>



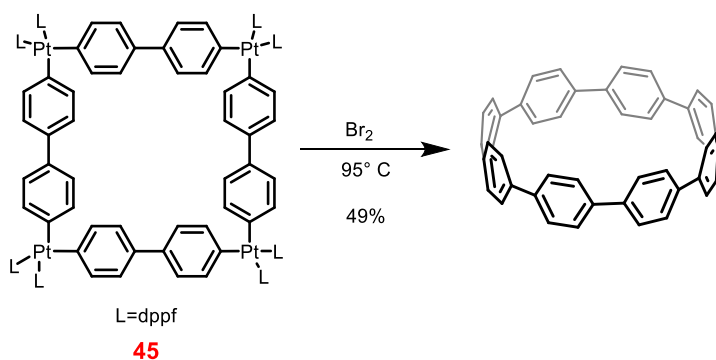
**Scheme 9:** Itami synthetic route.<sup>99</sup>

<sup>99</sup> Takaba, H.; Omachi, H.; Yamamoto, Y.; Bouffard, J.; Itami, K. *Angew. Chem., Int. Ed.* **2009**, 48, 6112-6116.

Synthetic strategy is based on the use of *cis*-cyclohexane-1,4-diyl units - Scheme 9. Derivatives **43** and **44** was obtained through Suzuki-Miyaura cross-coupling and final aromatization reaction was performed by microwave with *p*-toluenesulfonic acid.

Finally, in 2010 Yamago achieved the first selective synthesis for [8]CPP, the smallest cycloparaphenylene at the time. Differently from two previously strategies, Yamago reduce the synthetic step through directly formation of tetranuclear platinum complex **45** - Scheme 10.<sup>100</sup>

Reductive elimination reaction gave [8]CPP with 49 % of yield but with disadvantages of limited scalability. Similar strategy can be performed in order to obtain [8]-[13] CPP in selective way.<sup>101</sup>



**Scheme 10:** Yamago synthetic route.<sup>100</sup>

<sup>100</sup> Yamago, S.; Watanabe, Y.; Iwamoto, T. *Angew. Chem. Int. Ed.* **2010**, *49*, 757–759.

<sup>101</sup> Iwamoto, T.; Watanabe, Y.; Sakamoto, Y.; Suzuki, T.; Yamago, S. *J. Am. Chem. Soc.* **2011**, *133*, 8354-8359.

## 3.2 Application of [n]CPPs

### 3.2.1 Seeds for Carbon Nanotubes

Carbon nanotubes (CNTs) are intriguing materials that showed interesting features in different fields (electronics, optics, material science, etc.) and many efforts have been devoted to study them.<sup>102</sup>

Carbon nanotubes can be divided on the base of three fundamental parameters: i) diameters, ii) number of walls and iii) chirality, respectively show in Figure 49 in a, b and c. The difference in optoelectronic properties of these materials is closely relate to these structural properties.<sup>103</sup>

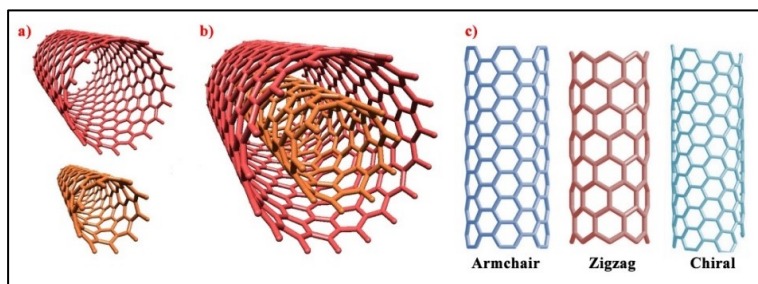


**Figure 49:** Different structural properties of carbon nanotubes.

CPPs can be seen as the shortest cyclic unite of armchair carbon nanotube and on this basis the scientists have envisioned a template synthesis of single-walled of CNT starting by CPPs.<sup>104</sup>

---

<sup>102</sup> Jasti, R. and Bertozzi, C. R. *Chem. Phys. Lett.* **2010**, 494, 1-7.

<sup>103</sup> Petrukhina, M.A. and Scott, L. T. in *Fragments of fullerenes and carbon nanotubes*, Chapter 11, WILEY, West Sussex - UK, **2011**.

<sup>104</sup> Omachi, H.; Nakayama, T.; Takanishi, E.; Segawa, Y.; Itami, K. *Nature Chemistry* **2013**, 5, 572-576.

In 2013 Itami published the elongation of carbon nanotube starting from [12]CPP through Chemical Vapor Deposition and using ethanol like carbon source - Figure 50. The authors showed that the lack of perfect diameter and chirality is limited, and the scalability of the process can be improved.<sup>97</sup>

In 2016 Jasti explored the Dies-Alder reaction as new strategy to elongate carbon nanotube starting by perylene-incorporated CPP derivatives using nitroethylene which acts as a masked acetylene equivalent.<sup>105</sup>

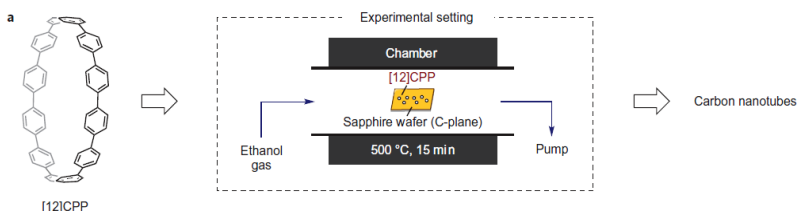


**Figure 50:** Schematic presentation of the elongation experiments to obtain CNT starting from [12]CPP. The reaction plate was placed in the heated chamber at 500 °C for 15 minutes with a flow of ethanol gas.<sup>104</sup>

### 3.2.2 Molecular Recognition Abilities of [n]CPPs

The appealing structure of the [n]CPP macrocycles and their optoelectronic properties are of interest for their applications as host in molecular recognition processes. The  $\pi$ -electron rich aromatic cavity of CPPs should interact with a wide range of substrates to give very interesting supramolecular phenomena. The first example was reported by Yamago in 2011<sup>106</sup> in which

<sup>105</sup> Jackson, E.P.; Sisto, T. J.; Darzi, E. R.; Jasti, R. *Tetrahedron* **2016**, *72*, 3754-3758.

the molecular recognition ability of different size CPPs toward Buckminsterfullerene were investigated. NMR investigation revealed the high selectivity of [10]CPP toward Fullerene C60 and fluorescence titration allowed the calculation of the association constant.<sup>106</sup> Solid state investigation shown a peapod structure where the guest was hosted inside the cavity of CPP through  $\pi$ - $\pi$  interactions with the  $\pi$ -electron rich aromatic cavity of the CPP host- Figure 51a.<sup>62</sup>

Similarly, was studied the complexation of the Fullerene-C70 with the [11]CPP.

X ray studies show clearly that in the C70 $\subset$ [11]CPP complex the CPP host adopts a peapod structure in which the nanoring is distorted owing induced-fit phenomenon - Figure 51b.<sup>107</sup>

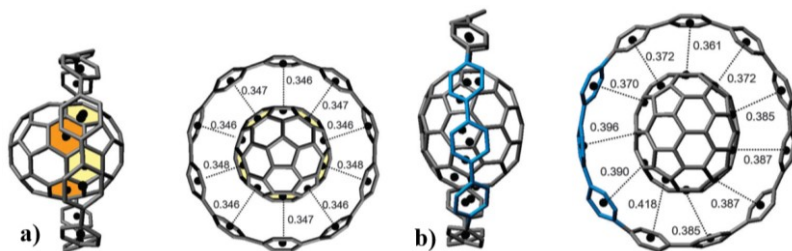


**Figure 51:** Peapod structures of **a)** C60  $\subset$  [10]CPP and **b)** C70  $\subset$  [11]CPP.<sup>106,107</sup>

<sup>106</sup> Iwamoto, T.; Watanabe, Y.; Sadahiro, T.; Haino, T.; Yamago, S. *Angew. Chem. Int. Ed.* **2011**, *50*, 8342-8344.

<sup>107</sup> Iwamoto, T.; Watanabe, Y.; Takaya, H.; Haino, T.; Yasuda, N.; Yamago, S. *Chem. Eur. J.* **2013**, *19*, 14061-14068.

### 3.3 Tuning Cycloparaphenylene Host Properties by Chemical Modification<sup>108</sup>

Cycloparaphenylenes was discovered in 2008 and they are excellent candidates for applications in nanoelectronics and photonics. Poorly investigated are the molecular recognition ability of these macrocycles. Fullerene C<sub>60</sub> and C<sub>70</sub> was studied recently,<sup>106,107</sup> but at the date, there isn't informations regarding the recognition abilities of CPPs toward small organic molecules. Among the guests of interest in supramolecular chemistry, the ammonium organic cations<sup>109</sup> play a pivotal role for the synthesis of interpenetrated architectures<sup>110</sup> and molecular machines.<sup>111</sup> Prompted by these considerations, and with the aim to obtain a CPP host for the recognition of pyridinium guests, a topic of this PhD project has been devoted to the synthesis of CPP derivative **46**, bearing an electron-rich 1,4-dimethoxybenzene ring, which is well

---

<sup>108</sup> Della Sala, P.; Talotta, C.; Caruso, T.; De Rosa M.; Soriente, A.; Neri, P.; Gaeta, C. *J. Org. Chem.* **2017**, *82*, 9885–9889.

<sup>109</sup> Lupo, F.; Capici, C.; Gattuso, G.; Notti, A.; Parisi, M. F.; Pappalardo, A.; Pappalardo, S.; Gulino, A. *Chem. Mater.* **2010**, *22*, 2829–2834.

<sup>110</sup> De Rosa, M.; Talotta, C.; Gaeta, C.; Soriente, A.; Neri, P.; Pappalardo, S.; Gattuso, G.; Notti, A.; Parisi, M. F.; Pisagatti, I. *J. Org. Chem.* **2017**, *82*, 5162–5168.

<sup>111</sup> a) Bruns C. J.; Stoddart, J. F. *The Nature of the Mechanical Bond: From Molecules to Machines, First Edition*. John Wiley & Sons: **2017**. b) Feringa, B. L. (Nobel Lecture). *Angew. Chem. Int. Ed.* **2017**, *56*, 11060–11078. c) Sauvage, J.-P. (Nobel Lecture). *Angew. Chem. Int. Ed.* **2017**, *56*, 11080–11093. d) Stoddart, J. F. (Nobel Lecture). *Angew. Chem. Int. Ed.* **2017**, *56*, 11094–11125. e) Leigh, D. A. *Angew. Chem. Int. Ed.* **2016**, *55*, 14506–7441. f) Balzani, V.; Venturi, M.; Credi, A., *Molecular Devices and Machines: A Journey Into the Nano World*. Wiley-VCH: **2003**

known<sup>111</sup> for its affinity toward pyridinium guests, and to the study of its recognition properties.<sup>97</sup>- Figure 52.

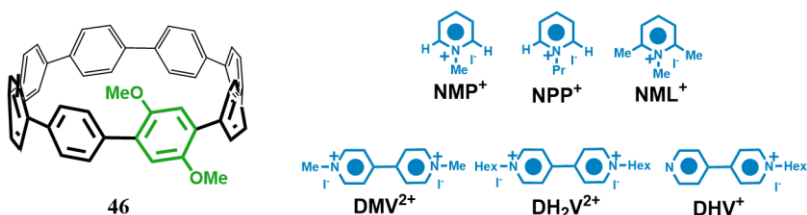


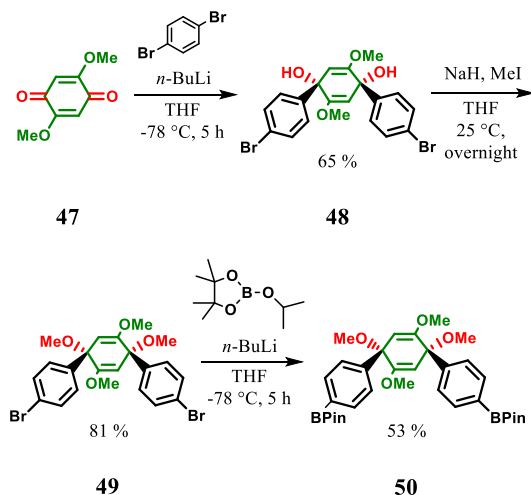
**Figure 52:** Derivative 1,4-DMB-[8]CPP **46** and organic cationic guests investigated in this work.

### 3.3.1 Synthesis and Characterization of 1,4-DMB-[8]CPP

The synthesis of the [8]CPP derivative **46** incorporating a 1,4-dimethoxybenzene unit (1,4-DMB-[8]CPP, Figure 52) was obtained through a modification of the gram-scale synthesis of CPPs reported by Jasti.<sup>98</sup> Diboronic pinacol ester **50** incorporating the 1,4-dimethoxycyclohexa-1,4-dienyl unit was synthesized through the synthetic scheme outlined in Scheme 11.

2,5-dimethoxy-(1,4)-benzoquinone (**47**), commercially available, was allowed to react with mono aryl-lithium derivate (obtained by 1,4-dibromobenzene) to give derivative **48** with 65 % of yield. Hydroxyl groups of **48** was protected by methylation performed with MeI and NaH to give the derivative **49**. Finally, this compound was treated with *n*-BuLi in dry THF and isopropyl pinacol borate at -78 °C to give, after chromatographic purification the derivative **50** in 53 % of yield. Suzuki-Miyaura cross-coupling between the dibromide

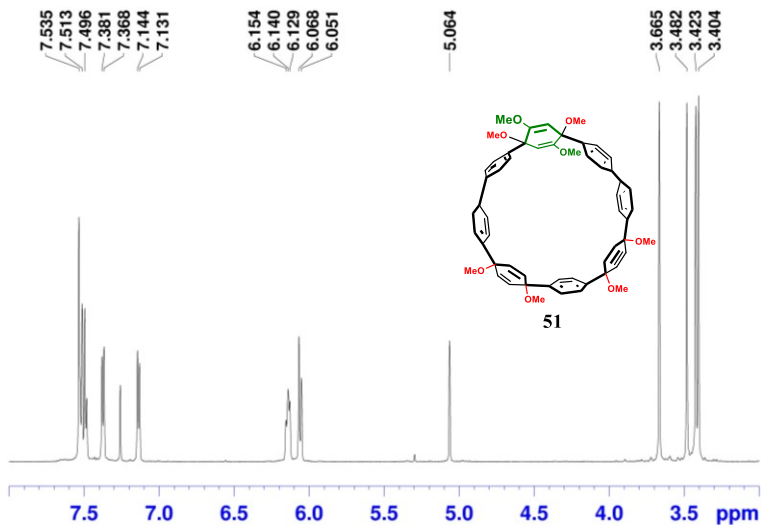
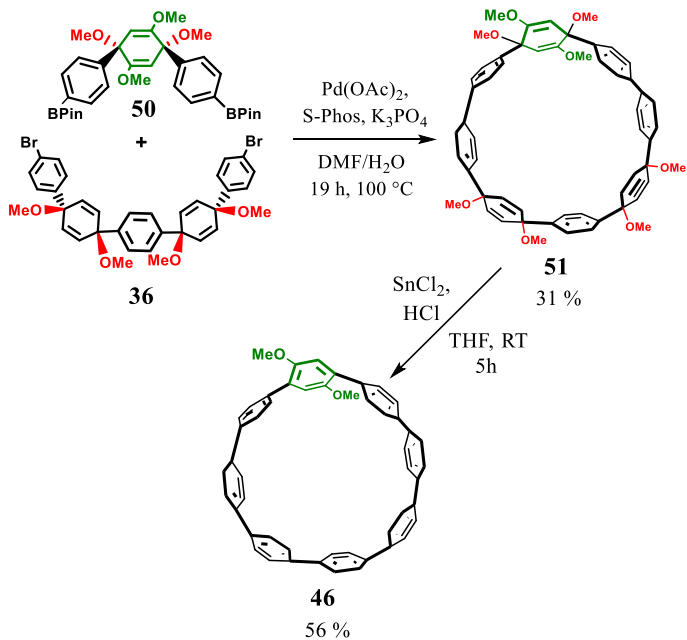
**36** and the diboronic pinacol ester **50** afforded to the macrocycle **51** in 31% yield - Scheme 12.



**Scheme 11:** Synthesis of diboronic pinacol ester **50**.

MALDI-FT-ICR mass spectrum exhibits an molecular ion peak of  $[M]^+$  at  $m/z$  668.2708 (calculated: 668.2710) in accord with the molecular formula of **51**.

$^1\text{H}$  NMR spectrum of **51** in Figure 53 ( $\text{CDCl}_3$ , 600 MHz at 298 K) shows four singlets attributable to the OMe groups between 3.40 and 3.66 ppm and a  $\text{C}=\text{CH}$  singlet for the 1,4-dimethoxycyclohexa-1,4-dienyl unit of **51** at 5.06 ppm. Between 6.05 and 6.15 ppm can be observed the vinyl protons of the cyclohexyl moieties and finally the aromatic signals of **51** were detected between 7.13 and 7.53 ppm. FT-ICR mass spectrum shows a monoisotopic peak of  $[M+\text{Ag}]^+$  at  $m/z$  961.2859 (calculated: 961.2870).



Derivative **51** was reduced with SnCl<sub>2</sub> and HCl in degassed THF to give the CPP **46** in 56% yield - Scheme 15.

<sup>1</sup>H NMR spectrum of **46** - Figure 54 - (CDCl<sub>3</sub>, 600 MHz at 298 K) shows the loss of three OCH<sub>3</sub> singlets of the cyclohexadienyl unit. One singlet was present at 3.73 ppm attributable to the OMe group of **46**, which correlated in the HSQC spectrum with a carbon resonance at 57.1 ppm.

The aromatic protons of the 1,4-dimethoxybenzene unit resonated as a singlet at 6.83 ppm. A careful interpretation of the DQF-COSY spectrum showed the presence of an AB system at 7.41 and 7.59 ppm ( $J = 8.7$  Hz) attributable to the benzene ArH rings adjacent to the substituted 1,4-DMB-unit.

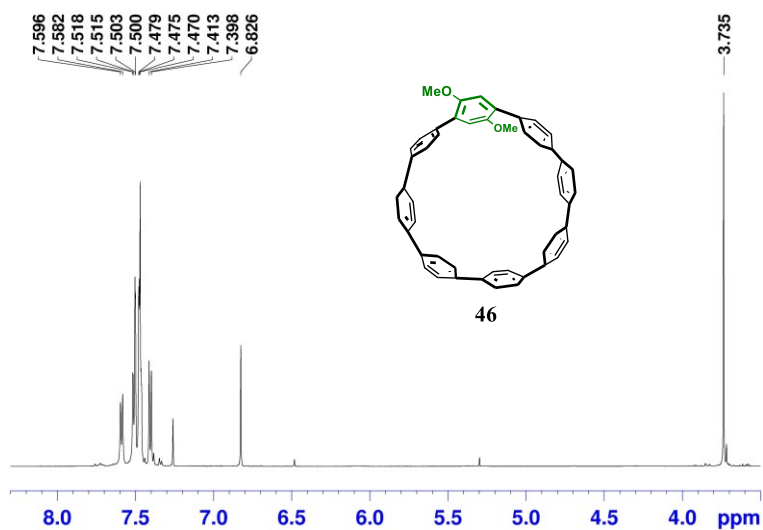


**Figure 54:** <sup>1</sup>H NMR spectrum of derivative **46** (CDCl<sub>3</sub>, 600 MHz, 298K).

<sup>1</sup>H VT NMR experiments - Figure 55 - showed a broadening of AB system previously described upon lowering the temperature, with a coalescence at 223 K. Below 223 K, two AX systems emerged, attributable to a/b and a'/b' protons in Figure 55b, in accordance with a slowdown of the rotation

around the benzene-benzene bonds. The analysis of the  $^1\text{H}$  VT and  $^{13}\text{C}$  NMR spectra of **46** is in accordance with its dissymmetric structure of **46** due to the presence of a  $C_2$ -axis passing through the substituted ring and the distal benzene unit.

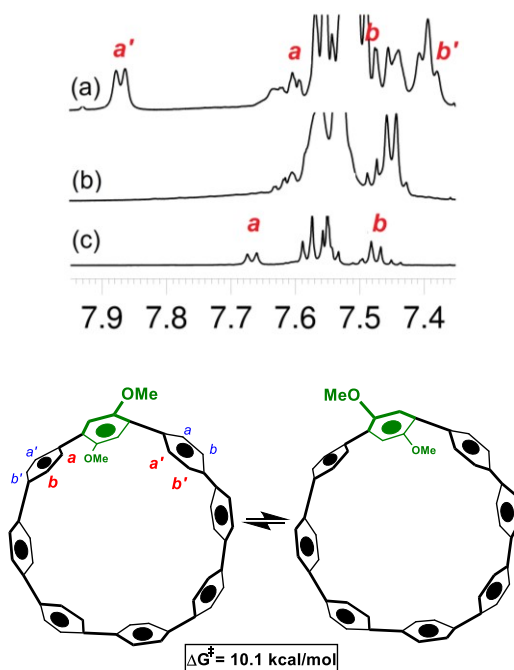


**Figure 55:** (right)  $T > 223$  K rapid isomerization process with respect to the NMR time scale (600 MHz):  $a = a'$  and  $b = b'$ .  $T < 223$  K, slow isomerization with respect to the NMR time scale,  $a \neq a'$  and  $b \neq b'$ . (left) Aromatic region of the  $^1\text{H}$  NMR spectrum of **46** (600 MHz,  $\text{CD}_2\text{Cl}_2$ ) at **a**) 183 K, **b**) 223 K, and **c**) 298 K

Derivative **46** is free from stereogenic carbon atoms and its chirality arises from the nonplanar structure which loses symmetric planes because of the para-relationship between the two methoxy groups.<sup>112</sup> Notably, as evidenced in Figure 55, the rapid rotation with respect to the NMR time scale (600 MHz)

<sup>112</sup> E. L. Eliel, S. H. Willen in *Stereochemistry of Organic Compounds*, Wiley, New York, 1994.

around the biphenyl bonds affords to a fast isomerization of **46**. From the coalescence temperature of 223 K ( $T_c$ ), an energy barrier <sup>113</sup> of 10.1 kcal/mol was deduced for this isomerization process (with the equation reported below).

$$\Delta G_c^\ddagger = aT_c \left[ 9.972 + \log \left( \frac{T_c}{\sqrt{\Delta v^2 + 6J^2}} \right) \right]$$

Finally, a close inspection of the DFT optimized structure of **46** at the B3LYP/6-31G(d,p) level of theory shows an average dihedral angle of 33° between the substituted 1,4-DMB ring and the adjacent benzene rings, while a torsion angle of 30° was found for the other biphenyl bonds of the CPP hoop.

### 3.3.2 Optoelectronic Features of **46**

Optoelectronic characterization of **46** was performed through cyclic voltammetry and UV-Vis and fluorescence spectroscopy.

In the first instance, cyclic voltammetry measurements were performed using

CH<sub>2</sub>Cl<sub>2</sub> as solvent and TBAP as the electrolyte.

All measured potentials were referenced to the platinum quasi-reference electrode potential which has been calibrated with the ferrocene/ferrocenium (Fc/ Fc<sup>+</sup>) redox couple. Derivative **46** showed an oxidation half-wave at a potential of 0.50 V, lower than that 0.59 V reported for [8]CPP (Figure 56a).

The UV-Visible spectrum of **46** shows the absorbance maximum at  $\lambda_{\text{abs}} = 340$  nm and a coefficient of molar extinction

---

<sup>113</sup> Kurland, R. J.; Rubin, M. B.; Wise, W. B. *J. Chem. Phys.* **1964**, *40*, 2426-2431.

of  $\epsilon_{340} = 57\,000\text{ M}^{-1}\text{ cm}^{-1}$ , five times greater than the [8]CPP. Fluorescence maximum at  $\lambda_{\text{em}} = 542\text{ nm}$ , with quantum yield  $\Phi = 0.42$  (quinine sulfate as standard), a value higher than that reported for [8]CPP ( $\Phi = 0.10$ ) (Figure 56b).

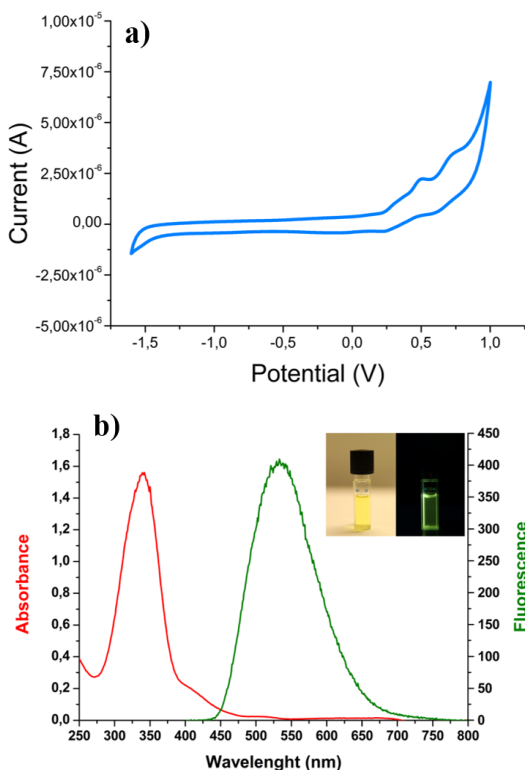


**Figure 56:** a) Cyclic voltammetry of **46** (vs Fc/Fc<sup>+</sup>); b) Absorbance (red line) and fluorescence (green line) spectra of **46** in  $\text{CH}_2\text{Cl}_2$  ( $\lambda_{\text{exc}} = 340\text{ nm}$  and  $\epsilon_{340} = 57\,000\text{ M}^{-1}\text{ cm}^{-1}$ ). Inset: photographs of **46** at sunlight and after irradiation at 365 nm in  $\text{CH}_2\text{Cl}_2$ .

### 3.3.3 Pyridinium Guest Recognition

As it is well known, the electron-rich 1,4-dimethoxybenzene moiety exhibits a natural affinity for the  $\pi$ -electron poor guests such as pyridinium cations.<sup>108a</sup> Therefore, in order to evaluate

the recognition abilities of **46** toward pyridinium guests we have performed 1D and 2D NMR and HR-MS studies of complexation (Figure 57).<sup>108a</sup>

When a CDCl<sub>3</sub> solution of *N*-methylpyridinium (NMP<sup>+</sup>) was titrated with **46**, a dramatic shielding of the <sup>1</sup>H NMR signals of the guest was observed (Figure 57a-d).

A fast complexation equilibrium between NMP<sup>+</sup> and **46** was observed, with respect to the NMR timescale (600 MHz, 298 K), and consequently the <sup>1</sup>H NMR signals of NMP<sup>+</sup> (in red in Figure 57b-d) were observed as averaged single resonances between the free and complexed form of NMP<sup>+</sup> ( $\delta_{\text{observed}} = X_{\text{free}} \delta_{\text{free}} + X_{\text{complex}} \delta_{\text{complex}}$ ).

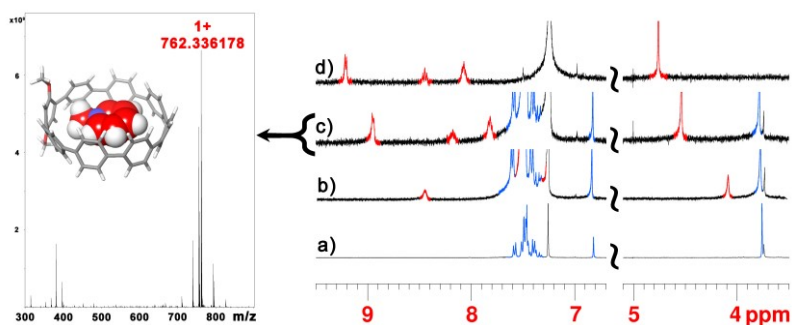


**Figure 57:** (Left) HR MALDI FT ICR spectrum of a 1:1 mixture of **46** and NMP<sup>+</sup>I<sup>-</sup>. (Right) <sup>1</sup>H NMR spectra (600 MHz, 298 K, CDCl<sub>3</sub>) of **a)** **46** (0.003 M); **b)** **46** in the presence of an excess of NMP<sup>+</sup>I<sup>-</sup>; **c)** 1:1 mixture of **46** and NMP<sup>+</sup>I<sup>-</sup>; **d)** NMP<sup>+</sup>I<sup>-</sup>.

In details, the <sup>1</sup>H NMR signals of the NMP<sup>+</sup> guest in red in Figure 57a-d, were up-field shifted upon addition of CPP **46**, to indicate the inclusion of the guest inside the aromatic cavity of CPP. The high-resolution mass spectrum of the 1:1 host guest mixture showed a molecular ion peak at *m/z* 762.3361 (calculated:762.3367) attributable to the NMP<sup>+</sup>⊂**46** complex (Figure 57).

In order to define the stoichiometry of the  $\text{NMP}^+\text{C}46$  complex we have performed a 2D-DOSY NMR experiment between **46** and  $\text{NMP}^+$ . By close inspection of the DOSY spectrum of the 1:1 mixture (15 mM in Figure 58b) of **46** and  $\text{NMP}^+$ , a coefficient diffusion of  $5.77 \pm 0.05 \times 10^{-10} \text{ m}^2/\text{s}$  was calculated for the  $\text{NMP}^+\text{C}46$  complex.<sup>108a</sup>

From the diffusion coefficient of the  $\text{NMP}^+\text{C}46$  complex and by using the Stokes-Einstein<sup>114</sup> equation, a hydrodynamic radius  $R_h(\text{exp}) = 7.08 \text{ \AA}$  was obtained. This result is in a good accord with the hydrolytic radius estimated through DFT optimized structure of complex that showed a value of  $R_h(\text{calculated}) = 8.66 \text{ \AA}$ .

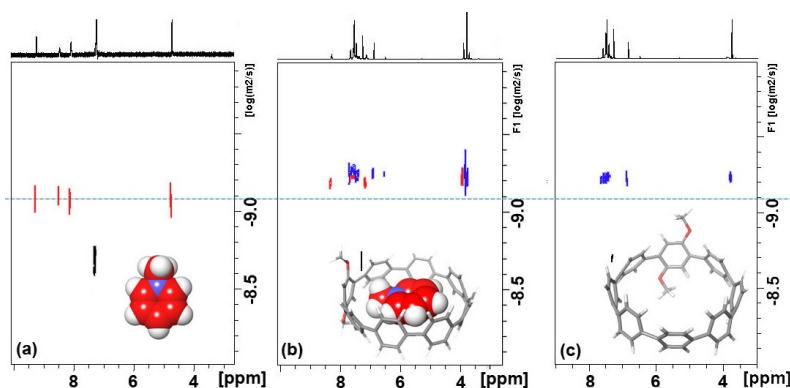


**Figure 58:** 2D-DOSY spectra (600 MHz,  $\text{CDCl}_3$ , 298 K) of **a**)  $\text{NMP}^+\text{I}^-$  (15 mM); **b**) 1:1 mixture of  $\text{NMP}^+\text{I}^-$  and derivative **46** (15 mM each one); and **c**) derivative **46** (15 mM).

In addition, comparison between the DOSY spectra in Figure 58, confirms the formation of the  $\text{NMP}^+\text{C}46$  complex.

Analogously, when a solution of *N*-propylpyridinium iodide ( $\text{NPP}^+$ ) - Figure 59b- and *N*-methyllutidinium ( $\text{NML}^+$  in Figure

<sup>114</sup>  $R = k_B T / 6\pi\eta D$ , where  $k_B$  is the Boltzmann constant,  $T$  is the absolute temperature, and  $\eta$  is the viscosity of  $\text{CDCl}_3$  at 298 K, 0.542 cP)

59c) in  $\text{CDCl}_3$  were titrated with **46**, similar shielding of the guest  $^1\text{H}$  NMR signals were observed. Association constant values for the formation of the complexes were obtained through nonlinear regression analysis<sup>71</sup> of the NMR titration data for a 1:1 stoichiometry. The binding isotherms for each guest are reported in Figure 59.

The  $\text{NMP}^+ \subset \mathbf{46}$  complex shows an apparent association constant of  $2200 \text{ M}^{-1}$  (error <15%), a value higher than that calculated for  $\text{NPP}^+ \subset \mathbf{46}$  and  $\text{NML}^+ \subset \mathbf{46}$  of  $1950 \text{ M}^{-1}$  and  $800 \text{ M}^{-1}$  respectively (Figure 59).

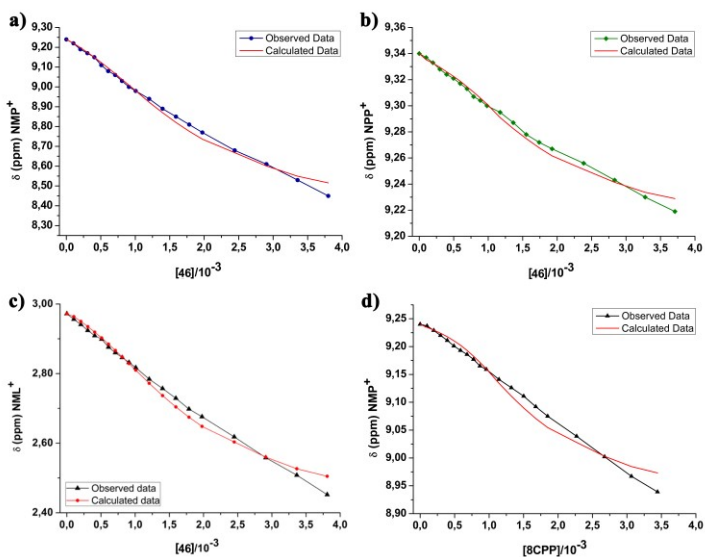


**Figure 59:** a) Plot of the observed (blue) and calculated (red) upfield shift of the  $^1\text{H}$  NMR signals of  $\text{NMP}^+$  as a function of  $[\mathbf{46}]$ ; b) Plot of the observed (green) and calculated (red) upfield  $^1\text{H}$  NMR chemical shift of the *o*-ArH of  $\text{NPP}^+$  as a function of  $[\mathbf{46}]$ ; c) Plot of the observed (black) and calculated (red) upfield  $^1\text{H}$  NMR chemical shift of the methyl of  $\text{NML}^+$  as a function of  $[\mathbf{46}]$ ; d) Plot of the observed (black) and calculated (red) upfield  $^1\text{H}$  NMR chemical shift of the *o*-ArH of  $\text{NMP}^+$  as a function of  $[\mathbf{8}]\text{CPP}$ .

In order to compare the recognition abilities of **46** with those of the native  $[\mathbf{8}]\text{CPP}$  we have studied the complexation of

NMP<sup>+</sup> guest with [8]CPP by NMR titration experiments. A CDCl<sub>3</sub> solution of NMP<sup>+</sup>I<sup>-</sup> was titrated with [8]CPP<sup>56</sup> and an apparent association constant value of 700 M<sup>-1</sup> was found for the formation of the NMP<sup>+</sup>⊂[8]CPP complex, a value significantly lower than that obtained for the complexation of NMP<sup>+</sup> guest with **46** (Figure 59d).

When dimethylviologen guest DMV<sup>2+</sup>, dihexylviologen guest DH<sub>2</sub>V<sup>2+</sup> and hexylviologen DHV<sup>+</sup> were added to a CDCl<sub>3</sub> solution of derivative **46**, no hint of interaction was detected by <sup>1</sup>NMR spectroscopy.

DFT calculations, at the B3LYP/6-31G(d,p) level of theory using Grimme's dispersion corrections (IOp(3/124 = 3)),<sup>115</sup> suggests that the electron-rich 1,4-dimethoxybenzene moiety in **46** plays a central role in the complexation of NMP<sup>+</sup> guest.

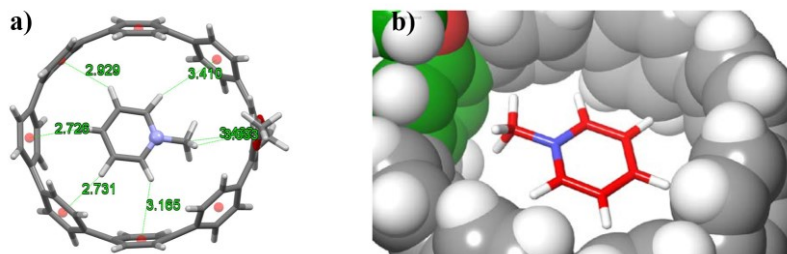


**Figure 60:** C-H... $\pi$  centroid distances for the NMP<sup>+</sup>⊂**46** complex

In fact, the DFT model of NMP<sup>+</sup>⊂**46** complex in Figure 60 suggest the presence of a cation... $\pi$  interaction between N<sup>+</sup> of the guest and the 1,4-dimethoxybenzene moiety of **46** with a distance N<sup>+</sup>... $\pi^{\text{centroid}}$  of 4.9 Å and seven C-H... $\pi$  interactions (Figure 60a).

<sup>115</sup> Grimme, S. *J. Comput. Chem.* **2006**, *27*, 1787–1799.

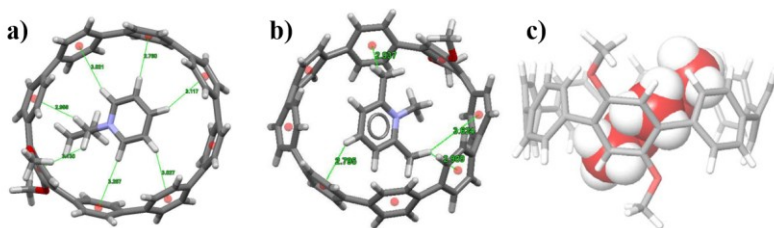


**Figure 61:** a) C-H $\cdots\pi$  centroid distances for the NPP $^+$ ⊂**46** complex; b) and c) C-H $\cdots\pi$  centroid distances for the NML $^+$ ⊂**46** complex

Finally, the DFT-optimized model obtained for the NML $^+$ ⊂**46** complex reveals an oblique orientation - Figure 61b - of the guest inside the cavity of macrocycle, the complex was stabilized through three C-H $\cdots\pi$  interactions between the NML $^+$  guest and host **46**.

In summary, the complexation phenomenon was highlighted through fluorescence technique. When a solution of host (constant throughout the titration) was titrated with NMP $^+$  guests, a quenching of the fluorescence of **46** was observed - Figure 62a.

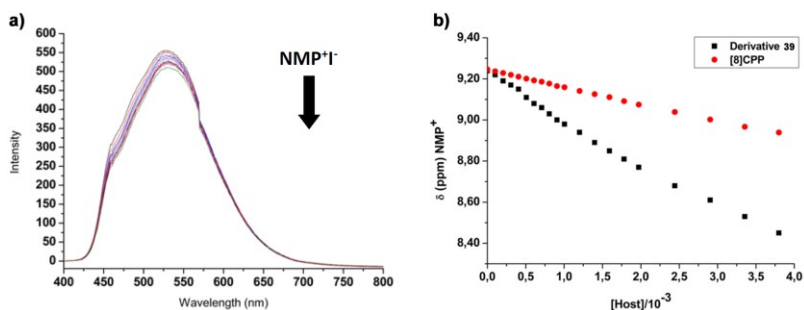


**Figure 62:** a) Fluorescence spectra of **46** ( $1.00 \times 10^{-5}$  mol L $^{-1}$ ,  $\lambda_{exc} = 340$  nm) in the presence of NMP $^+$ I $^-$  in CH $_2$ Cl $_2$ . The concentrations of NMP $^+$ I $^-$  are 0.0 – 50 ( $\times 10^{-5}$  mol L $^{-1}$ ) from the top to the bottom. b) Plots of  $\delta$  for *o*-ArH of NMP $^+$  as a function of the concentration of **46** (■) and [8]CPP (●).

In conclusion, we have reported the synthesis of a [8]CPP derivative incorporating an electron-rich 1,4-dimethoxybenzene ring. This is the first example of substituted CPP derivative reported in literature able to recognize pyridinium guests. Owing to the presence of the 1,4-dimethoxybenzene ring a fine-tuning of the binding abilities of **46** toward pyridinium guests was obtained with respect to the native [8]CPP macrocycle - Figure 62b. In accordance, DFT calculations show that the close steric fitting between the pyridinium guest and the rigid aromatic cavity of **46** allows the formation of stabilizing cation $\cdots\pi$  interactions and C-H $\cdots\pi$  interactions between host and guest. This information could open new perspectives for the design of CPP hosts with intriguing recognition properties.

## 3.4 Synthesis, Optoelectronic and Supramolecular Properties of a CPP-Calix[4]arene Hybrid Host <sup>116</sup>

### 3.4.1 Hybrid Calix[4]arene Hosts: An Overview

Calixarenes are considered as a versatile platform for developing macrocyclic hosts with novel and intriguing supramolecular features.<sup>117</sup> Among the calixarene hosts, a main role has been played by the hybrid systems which are composed by calixarene skeleton and portion of different macrocyclic hosts (crown-ethers,<sup>118</sup> spherands,<sup>119</sup> resorcinarene<sup>120</sup> and calixpyrrole<sup>121</sup>) installed at the upper or lower rim.

The hybrid systems combine the supramolecular features of both the hosts, as example given, recently, Sessler and coworkers,<sup>128</sup> reported a hybrid host in which the

---

<sup>116</sup> Della Sala, P.; Talotta, C.; Capobianco, A.; Soriente, A.; De Rosa, M.; Neri, P.; Gaeta, C. *Org. Lett.* **2018**, *20*, 7415–7418.

<sup>117</sup> a) Gaeta, C.; Talotta, C.; Farina, F.; Teixeira, F. A.; Marcos, P. A.; Ascenso, J. R.; Neri, P. *J. Org. Chem.* **2012**, *77*, 10285–10293. b) Gaeta, C.; Talotta, C.; Margarucci, L.; Casapullo, A.; Neri, P. *J. Org. Chem.* **2013**, *78*, 7627–7638.

<sup>118</sup> Ghidini, E.; Ugozzoli, F.; Ungaro, R.; Harkema, S.; Abu El-Fadl, A.; Rehinoudt, D. N.; Ugozzoli, F.; *J. Am. Chem. Soc.* **1990**, *112*, 6979–6983.

<sup>119</sup> Dijkstra, P. J.; Brunink, J. A. J.; Bugge, K.-E.; Reinhoudt, D. N.; Harkema, S.; Ungaro, R.; Ugozzoli, F.; Ghidini, E. *J. Am. Chem. Soc.* **1989**, *111*, 7567–7575.

<sup>120</sup> Galán, A.; Escudero-Adán, E. C.; Frontera, A.; Ballester, P. *J. Org. Chem.* **2014**, *79*, 5545–5557.

<sup>121</sup> Kim, S. K.; Sessler, J. L.; Gross, D. E.; Lee, C.-H.; Kim, J. S.; Lynch, V. M.; Delmau, L. H.; Hat, B. P. *J. Am. Chem. Soc.* **2010**, *132*, 5827–5836.

calix[4]pyrrole was fused with a calix[4]arene macrocycle. The hybrid hosts in Figure 63, combine the anion recognition abilities of the calix[4]pyrrole with the cation recognition abilities of the calix[4]arene, in order to perform ion pair recognition.

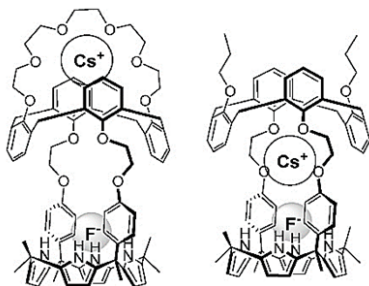


**Figure 63:** Hybrids Calix[4]arene-Calix[4]pyrrole developed by Sessler

Among the hybrid calixarene hosts, the calix-crown synthesized by Asfari<sup>122</sup> is used by U. S. Department of Energy to extract cesium from process wastewater and to stabilizing dangerous materials (Figure 64).<sup>123</sup>

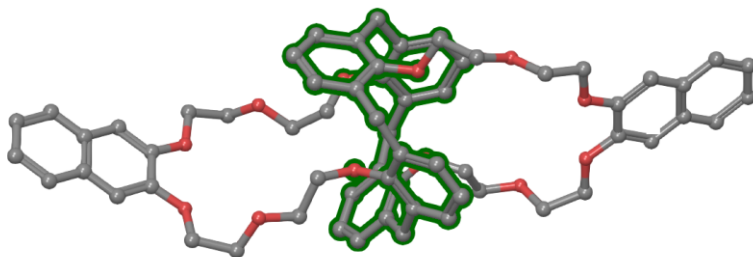


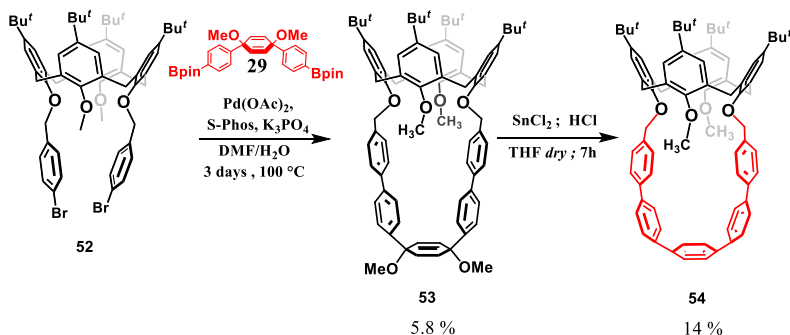
**Figure 64:** Ball-and-stick representations of calix[4]arene bearing two crown ethers moiety. Green highlight calix[4]arene scaffold in 1,3-alternate conformation.

<sup>122</sup> Asfari, Z.; Wenger, S.; Vicens, J. *Supramol. Sci.* **1994**, *1*, 103–110.

<sup>123</sup> Duncan, N. C.; Roach, B. D.; Williams, N. J.; Bonnesen, P. V.; Rajbanshi, A.; Moyer, B. A. *Sep. Sci. Technol.* **2012**, *47*, 2074–2087

As discussed previously, the CPP macrocycles possess interesting optoelectronic properties. Prompted by these considerations, we have envisioned to combine the optoelectronic properties of CPPs with the recognition abilities of the calixarene moiety. Thus, a topic of this Ph.D work has been devoted to the design and synthesis of the CPP-Calix[4] hybrid system **54** reported in Scheme 13 and to study its recognition and optoelectronic properties.

### 3.4.2 Synthesis and Characterization<sup>116</sup>



**Scheme 13:** Synthesis of derivative **54**.<sup>116</sup>

The main step for the synthesis of **54**, is the Suzuki-Miyaura cross-coupling between the known<sup>24</sup> derivative **29** incorporating a cyclohexa-2,5-diene moiety as masked benzene ring, and the bis[*p*-bromobenzyloxy]-calix[4]arene derivative **52**, to give the precursor **53** which has been aromatized to **54** by treatment with SnCl<sub>2</sub> or sodium naphthelide. The macrocyclization between **52** and **29** has been performed in DMF/H<sub>2</sub>O as solvent in the presence of *S*-Phos, K<sub>3</sub>PO<sub>4</sub> and Pd(AcO)<sub>2</sub>. After mixing for 3 d at 100 °C, the derivative **53** was isolated by chromatographic column in

5.8 %<sup>124</sup> of yield. The HR MALDI-FT-ICR mass spectrum of derivative **53** showed a molecular ion peak  $[M+Na]^+$  at  $m/z$  1167.6645 (calculated:1167.6473).<sup>116</sup>

The <sup>1</sup>H NMR (600 MHz, TCDE, 373 K) spectrum in Figure 65 of **53** shows overlapped aromatic signals attributable to the CPP-bridge between 7.36 and 7.54 ppm (16 H), while the calixarene aromatic signals appeared as broad singlets at 6.53 ppm and 6.93 ppm. Regarding the cyclohexadienyl ring of **53**, a broad signal was detected at 6.00 ppm. At 4.66 ppm was presents a broad signal attributable to the OCH<sub>2</sub> protons, while the two broad signals at 3.97 and 3.13 ppm was attributable to methylene bridge of the calix-skeleton. The two singlets at 3.13 and 3.14 were attributable to OCH<sub>3</sub> groups.<sup>116</sup>

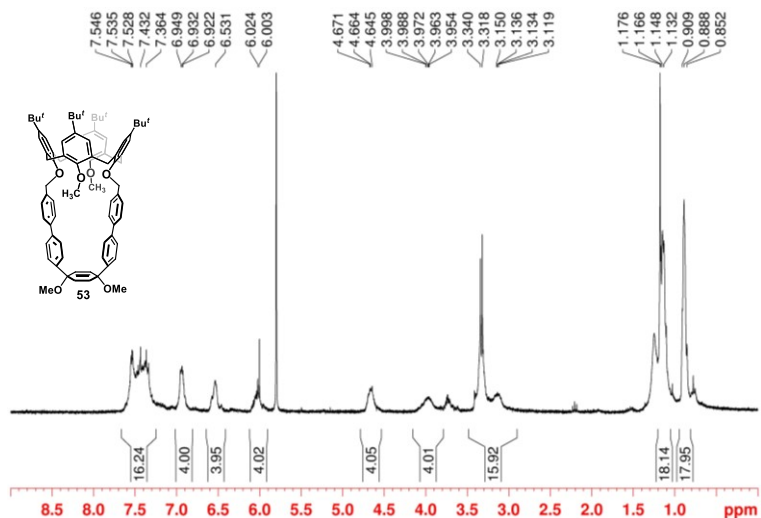


**Figure 65:** <sup>1</sup>H NMR spectrum of **53** (TCDE, 600 MHz, 373 K).

<sup>124</sup> The low yields reported in some CPPs synthesis are due to high strain associated with the CPP macrocycles, see refs 24, 96 and 108.

Finally, at 0.88 and 1.15 ppm, two singlets were attributable to the *tert*-butyl group of calixarene.

The reductive aromatization of **53** with SnCl<sub>2</sub> in the presence of HCl and THF as the solvent, for 7 h, gave **54** in 14 % of yield - Scheme 13.

The reliability of the results was proved by MALDI-FT-ICR mass spectrum (obtained using cationization agent NaTFA) that showed molecular ion peaks [M+Na]<sup>+</sup> at m/z 1105.6147 (calculated: 1105.6105).<sup>116</sup>

To confirm the structural assignment of **54** we performed a MALDI-CID MS/MS. The CID mass spectrum of sodiated **54** [54+Na]<sup>+</sup> exhibits an interesting fragmentation behavior, which is in accord with the loss of the CPP-bridge related to a homolytic dissociation of two OCH<sub>2</sub>-CPP bonds. While, the collisional activation of the sodiated **54** [54+Na]<sup>+</sup> generates exclusively <sup>t</sup>BuC[4](OMe)<sub>2</sub>(O·)<sub>2</sub>@Na<sup>+</sup> at m/z 697.421760 (calculated: 697.422731; accuracy = 1.40 ppm). Similar results were obtained performing MALDI-CID MS/MS studies in presence of LiTFA (Figure 66).

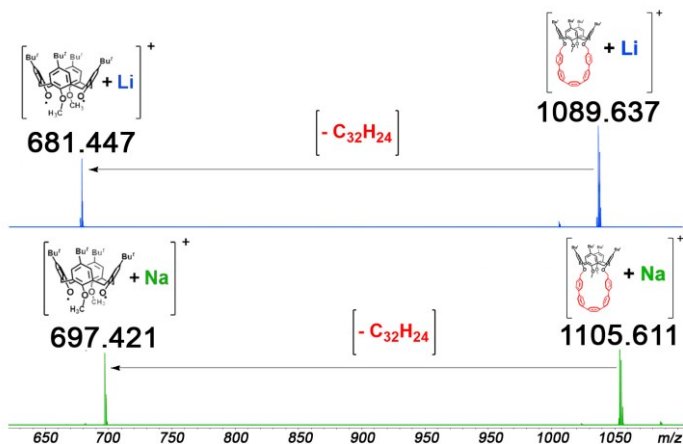


**Figure 66:** HR MALDI-FT-ICR-CID mass spectrum of **54** in the presence of cationization agent NaTFA (bottom) and LiTFA (top).

The  $^1\text{H}$  NMR spectrum of **54** (600 MHz,  $\text{CDCl}_3$ , 393K), shows broad  $\text{ArCH}_2\text{Ar}$  signals, to prove of the high conformational mobility of two anisole rings of **54** (Figure 69) owing to the OMe *through-the-annulus* passage - Figure 67.

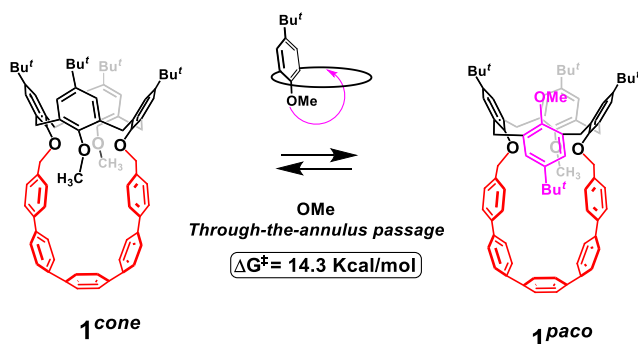


**Figure 67:** Cone-Paco interconversion due to the *through-the-annulus* passage.

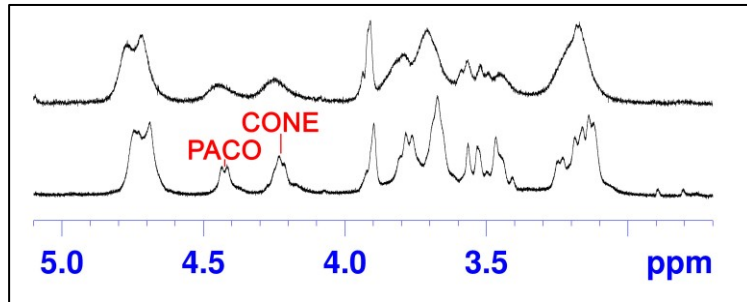


**Figure 68:** Methylene regions of the  $^1\text{H}$  NMR spectra (600 MHz,  $\text{CDCl}_3$ ) of **54** at: (down) 253K; (top) 298K.

Low temperature experiment shows that at 253 K, the  $\text{ArCH}_2\text{Ar}$  signals decoalesced in two AX systems assignable to two conformations of **54**, namely, the cone and partial cone (paco) conformation, frozen out in the NMR time scale (Figure 68).

$^1\text{H}$  NMR signals integrations shows that the cone and paco conformation of derivative **54** exist in 46 and 54 %, respectively. Increasing the temperature, the  $^1\text{H}$  NMR spectrum (TCDE 300 MHz) shows a coalescence for the methylene bridges signals at 323 K. A complete sharpening of the  $^1\text{H}$  NMR signals of **54** was observed at 393 K, due to fast  $\text{OCH}_3$  through-the-annulus passage. An energy barrier of 14.3 kcal/mol was calculated for this conformational process.<sup>14</sup> In the end, the  $^1\text{H}$  NMR spectrum of **54** at 393 K (TCDE, 300 MHz), exhibits an  $\text{ArCH}_2\text{Ar}$  AX system at 4.05/3.21 ppm, an  $\text{OCH}_2$  singlet at 4.66 ppm and an  $\text{OCH}_3$  singlet at 3.34 ppm (Figure 69).

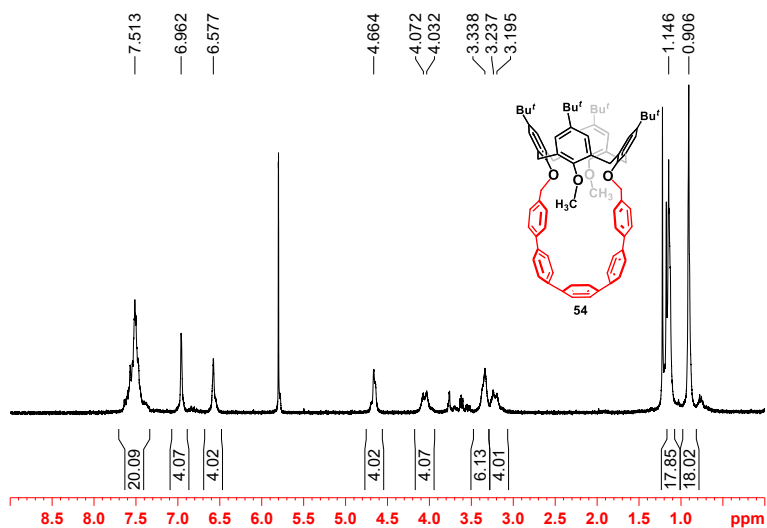
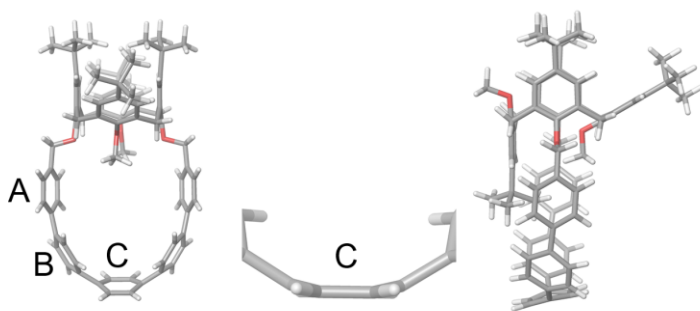


Figure 69:  $^1\text{H}$  NMR spectrum of **54** (TCDE, 600 MHz, 393 K).

### 3.4.3 DFT Investigation and Optoelectronic Features of the Hybrid CPP-Calix[4] derivative<sup>116</sup>

The cone and partial cone conformation of **54** were optimized at B3LYP/6-31G(d) level of theory including solvent (dichloromethane) effects, which were modeled through the polarizable continuum model (PCM). B3LYP computations found the partial cone conformation are more stable than the cone conformation by less than 0.4 kcal/mol. Therefore, cone and paco can be view as almost isoenergetic conformations in line with NMR results, finding two relevant conformers.

A careful analysis of the optimized structure of partial cone conformer of **54** – Figure 70 – revealed the presence of stabilizing C–H··· $\pi$  interactions<sup>125</sup> between the *tert*-butyl group of the inverted aromatic ring with the CPP-bridge. Indeed, a C–H··· $\pi$  interaction was found in the paco conformation between OCH<sub>3</sub> group and the distal inverted anisole ring of **54**.



**Figure 70:** DFT-optimized structures of **54** in: (left) cone-conformation; (middle) detail of the benzene ring C; (right) partial-cone conformation.

<sup>125</sup> Suezawa, H.; Ishihara, S.; Umezawa, Y.; Tsuboyama, S.; Nishio, M. *Eur. J. Org. Chem.* **2004**, 4816–4822.

DFT-calculations indicate that CPP-bridge of **54** adopt an alternating zigzag conformation for both conformers. In detail a dihedral angle  $\theta$  of  $33^\circ$  was predicted between neighboring phenylene rings A

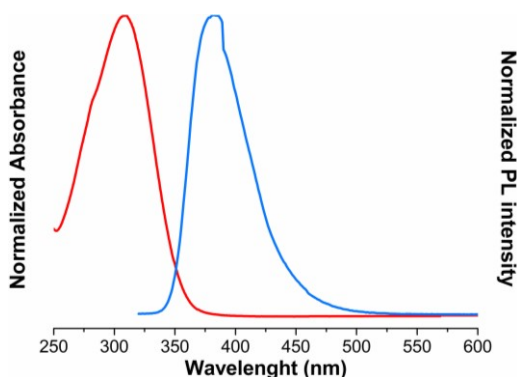


**Figure 71:** Absorption (red) and fluorescence (blue) spectra of derivative **54**.

and B - Figure 70 – very similar to that observed for [12]CPP ( $34^\circ$ ). Smaller value of torsion angle  $28^\circ$  was found between neighboring phenylene rings B and C - Figure 70 – very similar to that observed for smaller [6]CPP derivative. Finally, DFT investigation show a bending angle  $\alpha$  values of  $13.6^\circ$  for the benzene ring C (Figure 70) close to that found in [6]CPP while a softer deformation was observed for benzene rings B  $9.6^\circ$ .

In conclusion, the DFT structure of **54** in Figure 70 reveals that the CPP-bridge in **54** suffer a strain not uniformly distributed over the phenylene chain, but mainly located on the benzene ring C (Figure 70).

The CPP strain is also transmitted to the connected calixarene Ar rings which are consequently forced to be almost parallel in both cone and paco conformers (Figure 70).

The absorption spectrum of **54** - Figure 71, exhibits an intense and broad band, extending for ca 1.5 eV and peaked at 310 nm, ( $\epsilon_{310} = 35000 \text{ M}^{-1} \text{ cm}^{-1}$ ). Maximum absorption is considerably blue shifted with respect to the case of unsubstituted [n]CPPs. This behavior is predictable owing the disruption of conjugation system due to the insertion of the aliphatic units of

calixarene scaffold into the hoop of **54**. In agree with time dependent TDDFT computations the absorption band results from three optical transitions, falling at 346, 285 and 275 nm. In opposition with regular *n*CPPs where the  $S_1 \leftarrow S_0$  transition is forbidden, the HOMO  $\rightarrow$  LUMO excitation is optically allowed in **54** due to the loss of symmetry. An intense transition (predicted at 285 nm) consists of HOMO  $\rightarrow$  LUMO+1 and HOMO-4  $\rightarrow$  LUMO excitations. The last gives rise to a weak charge transfer from the benzene unit of the calixarene moiety to the CPP bridge. In addition, transition is predicted to occur at 275 nm, mainly HOMO  $\rightarrow$  LUMO+2 in character consistent with the shoulder observed at 280 nm.

Same conclusions are discovered for the cone conformation of **54** - Figure 72.

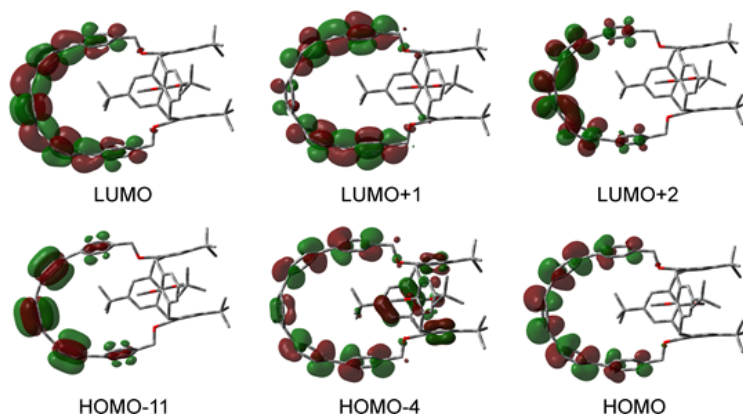


**Figure 72:** Isodensity surface plots of the frontier Kohn-Sham orbitals of the paco conformer of **54**.

The fluorescence spectrum of **54** (Figure 71) shows the maximum at 382 nm, significantly blue-shifted with respect to linear *p*-quinquephenyl derivatives, which shows maximum intensity at

344 nm.<sup>126</sup> The fluorescence quantum yield of **54** is  $\Phi = 0.26$  (using anthracene in EtOH as standard), value significantly lower than that reported for linear *p*-quinquephenyls,  $\Phi \approx 0.89$ ,<sup>126</sup> but far higher than that of [5]CPP, which show vanishing emission.<sup>127</sup>

### 3.4.4 Molecular Recognition Ability

The recognition ability of **54** toward  $\text{Li}^+$  and  $\text{Na}^+$  cations were studied through fluorescence studies. Titration experiment was performed adding  $\text{NaPF}_6$  or  $\text{LiPF}_6$  to a solution of **54** in  $\text{CHCl}_3/\text{CH}_3\text{CN}$  (9:1, v/v). Fluorescence intensity of **54** peaked at 382 nm progressively decreased as shown in Figure 73.

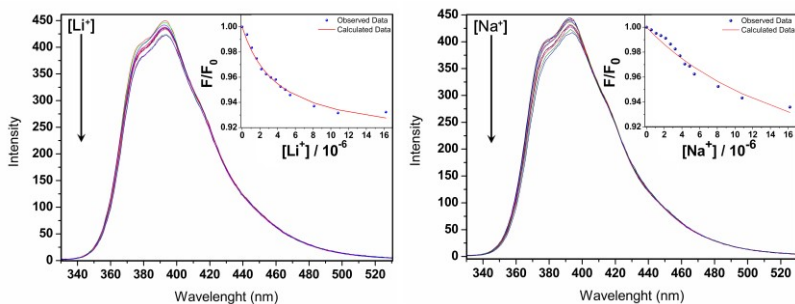


**Figure 73:** Fluorescence spectra of **54** (5.4  $\mu\text{M}$ ) upon addition of  $\text{PF}_6^-$  salts of  $\text{Li}^+$  (left) and  $\text{Na}^+$  (right) (0.1–3.0 equiv) in  $\text{CHCl}_3/\text{CH}_3\text{CN}$  (9:1, v/v).

The association constants found for  $\text{Na}^+ \cdot \text{54}$  and  $\text{Li}^+ \cdot \text{54}$  in a  $\text{CHCl}_3/\text{CH}_3\text{CN}$  (9:1, v/v) mixture were determined by curve fitting analysis of the fluorescence data.<sup>128</sup> The binding

<sup>126</sup> Nijegorodov, N. I.; Downey, W. S.; Danailov, M. B. *Spectrochim. Acta, Part A* **2000**, *56*, 783–795.

<sup>127</sup> Kayahara, E.; Patel, V. K.; Yamago, S. *J. Am. Chem. Soc.*, **2014**, *136*, 2284–2287.

<sup>128</sup> Thordarson, P. *Chem. Soc. Rev.* **2011**, *40*, 1305–1323.

constants values calculated for  $\text{Na}^+\text{c}54$  and  $\text{Li}^+\text{c}54$  complexes, are respectively,  $4.7 \cdot 10^4 \text{ M}^{-1}$  and  $2.5 \cdot 10^5 \text{ M}^{-1}$ . The calix[4]-CPP shows a pronounced affinity for  $\text{Li}^+$  cation with a  $\text{Li}^+/\text{Na}^+$  selectivity ratio of about 5.

Unlike by calixcrown and calixspherand hybrid calix-derivative, which exhibit a greater affinity for  $\text{Na}^+$  cation over  $\text{Li}^+$ ,<sup>126</sup> in the case of **54** this behaviour is reversed. In addition, when the solution of **54** was titrated with the larger  $\text{K}^+$  cation no hint of interaction between the host **54** and  $\text{K}^+$  (as  $\text{KPF}_6$ ) was detected by fluorescence titration. In summary, the thermodynamic stability of the  $\text{M}^+\text{c}54$  complexes follow the order  $\text{Li}^+ > \text{Na}^+$ , while  $\text{K}^+$  is not complexed.

DFT calculations at  $\text{B}_3\text{LYP}/6\text{-}31\text{G}(\text{d})$  level of theory suggest that the cationic guest is located near to the oxygen atoms at the lower rim of the calix-skeleton (Figure 74).

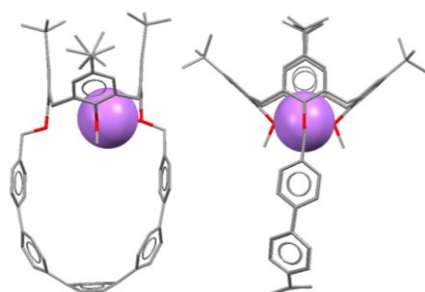


**Figure 74:** Different views of DFT-optimized structure of  $\text{Li}^+\text{c}54$ .

These data suggest that the size complementarity between host **54** and cationic guest plays a crucial role for the stability of the complexes. Probably, the small size of the CPP-bridge at the lower rim of **54**, and the conformational rigidity of the bridged calix-skeleton, does not allow the access of larger cations into its binding site. In addition, probably, also the cation $\cdots\pi$  interaction between the  $\text{Li}^+/\text{Na}^+$  cations and the aromatic CPP

bridge in **54** plays a special role for the stabilization of the  $\text{Li}^+ \subset \mathbf{54}$  complex. In conclusion, calix-CPP **54** shows an unexpected selectivity for the  $\text{Li}^+$  cation over  $\text{Na}^+$ , as a result of more favorable cation $\cdots\pi$  interactions of  $\text{Li}^+$  with the CPP-bridge and its better size-complementarity.

In conclusion we have reported a new interesting class of CPP-based hybrid host in which a cycloparaphenylene moiety was fused with the calix[4]arene skeleton. DFT conformational analysis reveals that derivative **54** presents a strain not uniformly distributed over the phenylene chain. Our studies show that the CPP-bridged calix[4]arene **54** combines perfectly the recognition abilities of the calix-skeleton with the optoelectronic features of CPP derivatives. Finally, Calix-CPP **54** shows a non-common  $\text{Li}^+$  selectivity due to a more favourable interaction between the cation and the aromatic rings of the CPP bridge.

### 3.5 New Optoelectronic Applications of CycloParaPhenylene Derivatives

In the last decade, the applications investigated for the CycloParaPhenylenes (CPPs) have been principally focused in the field of the templated synthesis of uniform single walled carbon nanotubes<sup>109</sup> and as supramolecular hosts for the recognition of fullerenes<sup>111,112</sup> and more recently of pyridinium guests.<sup>113</sup> In addition, the size-dependending optoelectronic properties of these macrocycles could be of interest in materials science for the synthesis of electronic, optical, and optoelectronic materials and devices. In this field, however, their real applications are limited. Recently, [10]cycloparaphenylene tetra alkoxy<sup>129</sup> derivatives were synthesized and their thin films were spin-coated showing absorption and fluorescence spectra almost similar to those in solution. The carrier transport properties of these thin films were almost identical to those of PCBM ([6,6]-Phenyl C<sub>61</sub> butyric acid methyl ester), which is used widely as an n-type active layer in bulk heterojunction photovoltaics. Regarding the optoelectronic materials, recently, a [4]cyclofluorene-based OLED<sup>130</sup> has been reported with a strong green band emission. Prompted by these considerations a topic of this PhD project has been focused on the study of new optoelectronic applications of CPP macrocycles. In details, in collaboration with the proff. Andrea Peluso and Amedeo Capobianco

---

<sup>129</sup> Kayahara, E.; Sun, L.; Onishi, H.; Suzuki, K.; Fukushima, T.; Sawada, A.; Kaji, H.; Yamago, S. *J. Am. Chem. Soc.* **2017**, *139*, 18480-18483.

<sup>130</sup> Liu, Y.-Y.; Lin, J.-Y.; Bo, Y.-F.; Xie, L.-H.; Yi, M.-D.; Zhang, X.-W.; Zhang, H.-M.; Loh, T.-P.; Huang, W. *Org. Lett.* **2016**, *18*, 172 – 175.

(Department of Chemistry and Biology, University of Salerno) has been investigated the light upconversion abilities of a new [8]CPP derivative, via triplet-triplet-annihilation process. In a different project, performed in collaboration with the prof. Luca Beverina (Università di Milano-Bicocca), has been investigated the use of CPP derivatives as organic fluorophores in the preparation of luminescent solar concentrators.

### 3.6 A [8]CPP Derivative as Emitter in Triplet-Triplet Annihilation Upconversion<sup>131</sup>

Upconversion is a photophysical process in which photons emission at higher energy (shorter wavelength) is observed upon excitation at lower energy. This phenomenon can be exploited in different applications, for converting low energy photons into light adequate for photovoltaic,<sup>132</sup> photocatalysis,<sup>133</sup> and bioimaging.<sup>134</sup>

One of the principal methods for the photon Up conversion is the Triplet-Triplet Annihilation process.

Qualitative Jablonski Diagram describe the TTA upconversion process between triplet sensitizer and annihilator - Figure 75.

This process is based on mixing in solution of an annihilator (triplet sensitizer) and of an emitter (triplet acceptor). The excitation energy is harvested by the first and the energy is transferred to the second via triplet-triplet energy transfer through a Dexter process.<sup>136</sup>

Subsequently, the emitter at the triplet excited state will collide with each other and produce the singlet excited state of the acceptor that finally can decay in ground state across radiative emissions.

---

<sup>131</sup> Della Sala, P.; Capobianco, A.; Caruso, T.; Talotta, C.; De Rosa, M.; Neri, P.; Peluso, A.; Gaeta, C. *J. Org. Chem.* **2018**, *83*, 220–227.

<sup>132</sup> Monguzzi, A.; Braga, D.; Gandini, M.; Holmberg, V. C.; Kim, D. K.; Sahu, A.; Norris, D. J.; Meinardi, F. *Nano Lett.* **2014**, *14*, 6644–6650.

<sup>133</sup> (a) Khnayzer, R. S.; Blumhoff, J.; Harrington, J. A.; Haefele, A.; Deng, F.; Castellano, F. N. *Chem. Commun.* **2012**, *48*, 209–211. (b) Ye, C.; Wang, J.; Wang, X.; Ding, P.; Liang, Z.; Tao, X. *Phys. Chem. Chem. Phys.* **2016**, *18*, 3430–3437.

<sup>134</sup> a) Zhao, J.; Ji, S.; Guo, H. *RSC Advances* **2011**, *1*, 937–950. b) Liu, Q.; Feng, W.; Yang, T.; Yi, T.; Li, F. *Nat. Protoc.* **2013**, *8*, 2033–2044.

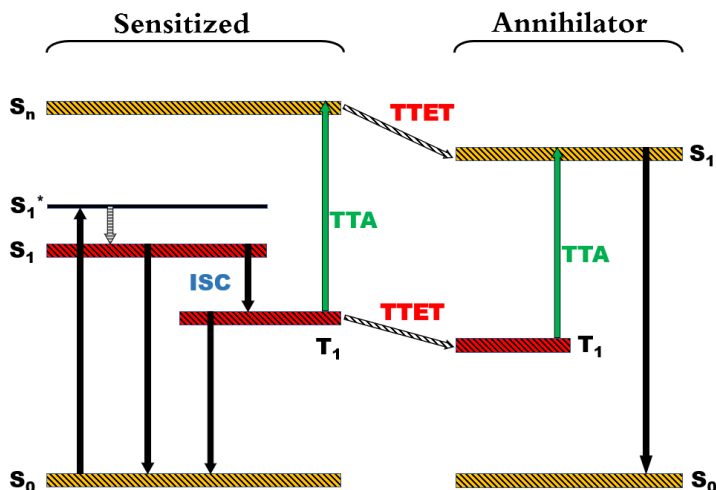


**Figure 75:** Jablonski Diagram for the TTA upconversion process.  $S_0$  is ground state energy,  $T_1$  is triplet state,  $S$  are the singlet states, **TTET** is triplet–triplet energy transfer, **TTA** is triplet triplet annihilation process and **ISC** in an intersystem crossing.

Among the most used pairs of annihilator-emitter there is palladium-porphine complex (PdOEP) and the 9,10-diphenyl anthracene (9,10-DPA)<sup>135</sup> that are cheaper and longtime investigated - Figure 92. Previously we have highlighted the excellent abilities of CPP macrocycles as emitter, exhibiting high fluorescence quantum yields. Thus, based on these considerations, we have envisioned of incorporate the 9,10-DPA unit into a [8]CPP skeleton **55** in order to obtain the first example of a CPP-based emitter in photon upconversion, thus widening the application fields of this class of compounds.

<sup>135</sup> (a) Kozlov, D. V.; Castellano, F. N. *Chem. Commun.* **2004**, 2860–2861. (b) Islangulov, R. R.; Lott, J.; Weder, C.; Castellano, F. N. *J. Am. Chem. Soc.* **2007**, *129*, 12652–12653. (c) Keivanidis, P. E.; Balushev, S.; Miteva, T.; Nelles, G.; Scherf, U.; Yasuda, A.; Wegner, G. *Adv. Mater.* **2003**, *15*, 2095–2098.

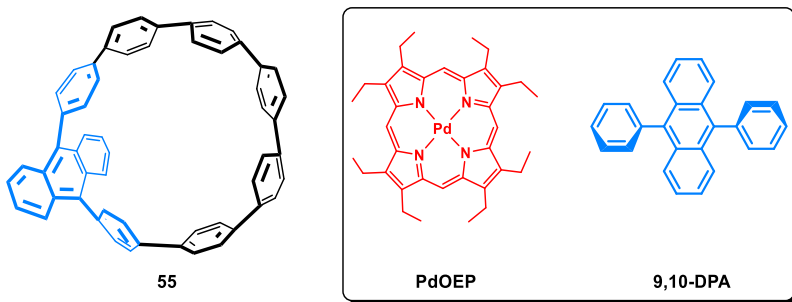
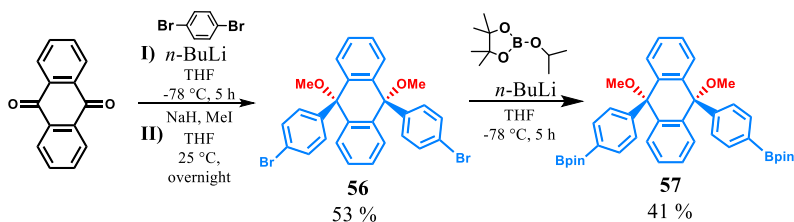


**Figure 76:** Derivative **55** synthesized and **PdOEP** and **9,10-DPA** involved in TTA-Upconversion.

### 3.6.1 Synthesis of Anthracene-Incorporated [8]CPP Derivative **55**<sup>131</sup>

The key step for the synthesis of CPP **55** is the macrocyclization between curved elements (Scheme 14), **36**<sup>98</sup> and **63**<sup>131</sup> bearing the 9,10-dimethoxy-9,10-dihydroanthracene curved-moiety as masked anthracene unit. While the derivative **36** has been previously reported by Jasti,<sup>98</sup> the synthesis of **57** is outlined in Scheme 14. 1,9-Anthraquinone was reacted with (4-bromophenyl) lithium to give the syn-diol, which was methylated to give the derivative **56** in 53 % of yield.

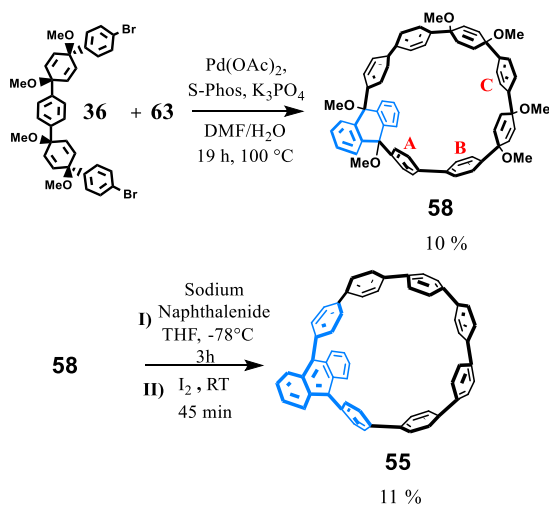


**Scheme 14:** Synthesis of diboronate **57**.

Derivative **56** was treated in anhydrous atmosphere with  $n$ -butyllithium and isopropyl pinacol borate for five hours. After

chromatography purification diboronate **57** was obtained in 41 % of yield - Scheme 14.

Macrocyclization between the known derivative **36** and **57** in the presence of Pd(OAc)<sub>2</sub>, *S*-Phos, and K<sub>3</sub>PO<sub>4</sub> in DMF/H<sub>2</sub>O, gave the macrocycle **58** in 10 % of yield- Scheme 15.



**Scheme 15:** Synthesis of derivative **55**.

The reliability of the results was proved by MALDI FT-ICR mass spectrum, which showed a molecular ion peak at  $m/z$  894.3895 (calculated: 894.3921).

The <sup>1</sup>H NMR - Figure 77 - spectrum of **58** (CDCl<sub>3</sub>, 600 MHz, 298 K) exhibited three singlets at 3.46, 3.41, and 3.15 ppm, in a 1:1:1 attributable to the OCH<sub>3</sub> groups. Regarding the cyclohexadienyl rings of **58**, an AB system was present at 6.03 and 6.11 ppm ( $J = 10.3$  Hz, 4H each), which correlated in the HSQC spectrum with two resonances at 133.0 and 133.5 ppm. Moreover, the <sup>1</sup>H NMR spectrum of **58** evidenced the presence of two AB systems at 7.44/7.38 ppm ( $J = 8.5$  Hz, 4H each) and 7.17/6.92 ppm ( $J = 8.5$  Hz, 4H each) attributable to the benzene

rings named **A** and **B** (Scheme 15). Finally, a singlet can be observed at 7.50 ppm attributable to ArH of ring **C** (4H).

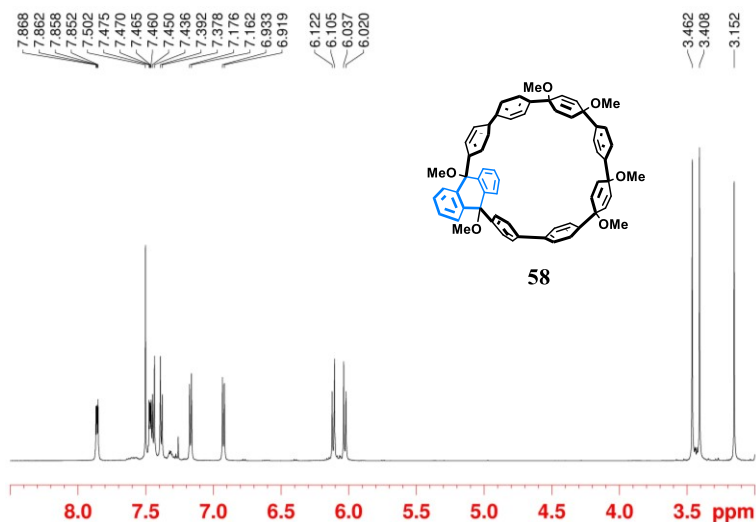


**Figure 77:**  $^1\text{H}$  NMR of derivative **58** ( $\text{CDCl}_3$ , 600 MHz, 298K).

Finally, the macrocycle **58** was aromatized by treatment with sodium naphthalenide at  $-78\text{ }^\circ\text{C}$  for 3 h in the dark, in degassed dry THF and followed by quenching with  $\text{I}_2$ , affording to the derivative **55** in 11 % yield.<sup>136</sup>

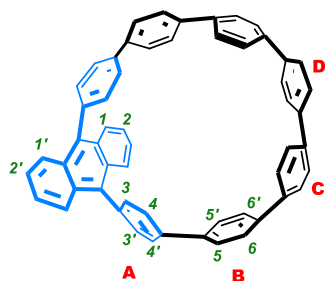


**Figure 78:** Structure of derivative **55**.

A close analysis of the  $^1\text{H}$  NMR - Figure 79 - and DQF-COSY - Figure 80 - spectra of derivative **55** in ( $\text{CDCl}_3$ , 600 MHz, 298 K) showed two distinct

<sup>136</sup> The low yields are common in the CPPs synthesis and are presumably due to high strain associated with the CPP macrocycles, see refs 24, 96 and 108

AA'BB' spin systems assignable to the ArH atoms 1/2 and 1'/2' - Figure 78 - of the anthracenyl unit. In details, the two AA'BB' systems were detected at 7.89/7.39 and 7.72/7.41 ppm as highlighted in DQF-COSY and correlated in the HSQC spectrum with four different carbon resonances at 127.72, 128.64, 127.64 and 127.12 ppm, respectively.

It's clear that the two peripheral benzene rings of the anthracenyl group in **55** are nonequivalent. This behavior is due at their different in/out orientation with respect to the macrocycle cavity, which implies a hindered rotation around  $\tau_1$  Figure 81a.

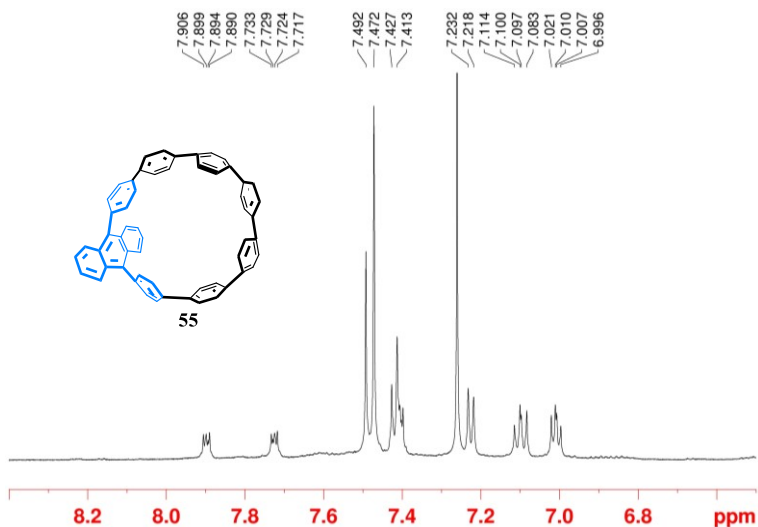


**Figure 79:** Significant portion of the <sup>1</sup>H NMR spectrum of **55** (600 MHz, CDCl<sub>3</sub>, 298 K).

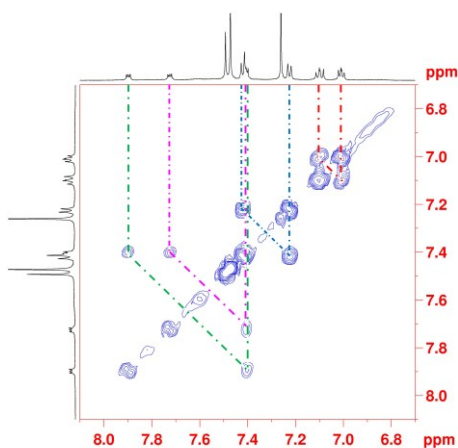


**Figure 80:** Significant portion of the DQF-COSY spectrum of **55** (600 MHz,  $\text{CDCl}_3$ , 298 K).

Because of this limited rotation, the benzene ring **A** (Figure 78), close to the anthracenyl group, adopts a tilted orientation, and the two 3/3' (and 4/4') protons become nonequivalent - Figure 79. Consequently, two AB systems were found in the  $^1\text{H}$  NMR spectrum of **55** for the *ortho*-coupled 3/4 and 3'/4' protons at 7.11/ 7.01 ( $J = 6.1$  Hz) and 7.00/7.08 ppm ( $J = 9.0$  Hz). VT  $^1\text{H}$  NMR experiments (400 MHz,  $\text{C}_2\text{D}_2\text{Cl}_4$ ) evidenced no hint of coalescence up to 393 K for the signals of anthracenyl unit and aromatic ring **A**.

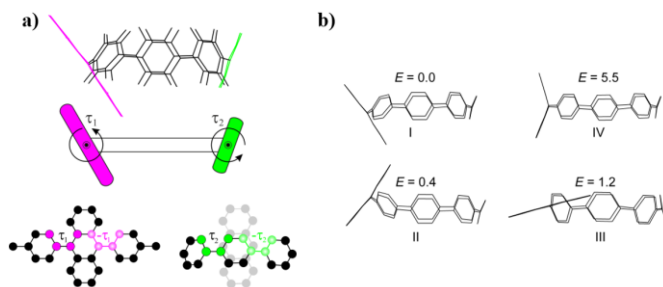


**Figure 81:** a) Schematic representation of **55** indicating the dihedral angle  $\tau_1$  and  $\tau_2$ . b) The most stable conformers of **55** and their relative energies ( $E / \text{kcal mol}^{-1}$ ).

In addition, the DQF-COSY spectrum of **55** shows the presence of another AB system at 7.42/7.23 ppm ( $J = 8.4$  Hz) of 5/6 H atoms attributable to ArH protons of **B** - Figure 78.

### 3.6.2 DFT conformational studies

DFT conformational studies and TD DFT analysis were performed in collaboration with the proff. Andrea Peluso and Amedeo Capobianco (Department of Chemistry and Biology, University of Salerno). The analysis of the 1D and 2D NMR spectra of **55**, suggest the presence of a plane of symmetry and consequently the geometry optimizations of derivative **55** were restricted to the  $C_s$  point group. For this purpose, we estimate the optimized potential energy profile along the Lagrangian variable  $\tau_1$ . Was fixed in each step two dependent dihedral angles and carry out an optimization of all the other nuclear coordinates.

A close inspection of conformational results obtained by DFT studies highlight the inclined orientation of anthracene unit. The most relevant conformers at RT exhibit an alternating zigzag conformation of the phenylene rings, with the dihedral angle between neighboring phenylene units being ca.  $28^\circ$ , close to the optimal value of  $30^\circ$  found for [n]CPP systems.

The dihedral angle  $\tau_1$  is almost  $60^\circ$  in both conformers **I** and **II**, reaching the expected value for free 9,10-DPA ( $\approx 77^\circ$ ) only in **III**. Deformation and bent angles showed a value of  $6.2$  and  $14.2^\circ$ , respectively, close to the values of  $9.3$  and  $13.7^\circ$  observed for  $\alpha$  and  $\beta$  in the phenyl rings of [8]CPP - Figure 81b. Different ways were taken to verify that all molecular conformations were assessed: (i) geometry optimizations by

scanning the  $\tau_2$  parameters and (ii) geometry optimizations starting from casual conformations. No additional minimum energy conformations were found.

### 3.6.3 Optoelectronic features

Derivative **55** was characterized through cyclic voltammetry, UV-Vis spectroscopy and fluorescence spectrophotometry and DFT calculation.

Voltammogram of **55** exhibits the first oxidation peak at 0.53 V vs Fc<sup>+</sup>/Fc redox couple, a similar value to that found for [8]CPP (0.59 V).

The first oxidation potential of the most stable conformer (**I**) is predicted to be at +0.52 V vs Fc<sup>+</sup>/Fc by (RO) CAM-B3LYP computations, in good agreement with the measured value.

Time dependent DFT studied performed using PCM-CAM-B3LYP/6-31+G\*\*<sup>137</sup> level of theory, predicts that the HOMO and LUMO of **55** are mainly localized on the anthracene unit. The predicted HOMO/LUMO energy gap is 2.2 eV.

In the absorption spectrum of **55** we can observe two characteristic intense bands: the first at 320 nm ( $\epsilon = 1.7 \times 10^4 \text{ M}^{-1} \text{ cm}^{-1}$ ) and the second less intense absorption extending from 360 to 450 nm.

The shape of signal is characteristic of cycloparaphenylene systems and the latter resembles very closely that of anthracene moiety - black line in Figure 82.

Optical transitions obtained through computational techniques are in excellent agree with those observed experimentally - Figure 82.

---

<sup>137</sup> Li, P.; Wong, B. M.; Zakharov, L. N.; Jasti, R. *Org. Lett.* **2016**, *18*, 1574–1577.

The absorption spectrum of **55** is mainly given by the superposition of the signals of [8]CPP and 9,10-DPA. This comparison suggest that the two molecular moieties maintain in the ground state their electronic structures.

The enlarged spectral absorption observed between 350–450 nm is similar to the absorptions predicted at 400, 410, and 380 nm for conformers **I**, **II**, and **III**, respectively - Table 7.

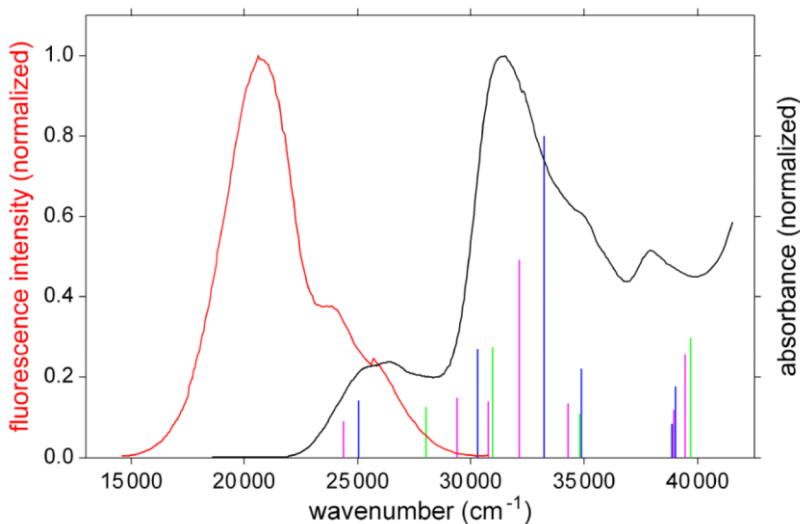


**Figure 82:** Normalized UV/vis absorption (black) and emission (red) spectra of **55** in  $\text{CH}_2\text{Cl}_2$  and computed vertical electronic transitions (vertical lines) of conformers **I** (blue), **II** (violet), and **III** (green).

The  $S_1 \leftarrow S_0$  transitions predicted about 400 nm (Table 7) was obtained from the excitation of one electron from the HOMO to the LUMO, which are both Kohn–Sham  $\pi$  orbitals localized over the 9,10-DPA moiety or on the other five CPP rings as shown in Figure 83.

The fluorescence spectrum of **55** - Figure 82 in red - is broad, ranging from 350 up to 650 nm, with a peak at 485 nm. The

poorly structured signal occurring at shorter wavelengths, is somewhat characteristic of the 9,10-DPA unit, whose fluorescence spectrum is characterized by vibronic peaks in the region between 400–450 nm.<sup>138</sup>

**Table 7:** Major electronic transitions (TD-DFT) of the most significant conformers of **55** (I-III) predicted at the (PCM)TDCAM-B3LYP/6-31+G\*\* level.

Transition	I			II			III		
	$\lambda/n$ m	f	Major Contributio ns <sup>a</sup>	$\lambda/n$ m	f	Major Contributio ns <sup>a</sup>	$\lambda/n$ m	f	Major Contributio ns <sup>a</sup>
S <sub>1</sub> ← So	399	0.2 7	H → L	410	0.2 5	H → L	380	0.0 5	H → L
S <sub>2</sub> ← So	330	0.5 0	H-1 → L+1 H → L+1 H-2 → L+2 H-1 → L	340	0.4 1	H-1 → L+1 H → L+1 H-1 → L H-2 → L+2	357	0.7 0	H-2 → L+2 H-1 → L H-1 → L+1 H → L+1
S <sub>3</sub> ← So	319	0.0 9	H-4 → L H → L+4	325	0.3 8	H-4 → L H → L+4 H → L+2	323	1.54	H-2 → L+1 H-1 → L+2 H → L+2
S <sub>4</sub> ← So	301	1.49	H-2 → L+1 H-1 → L+2 H → L+2 H-2 → L	311	1.36	H-2 → L H-2 → L+1 H-1 → L+2 H → L+2	317	10- 4	
S <sub>5</sub> ← So	287	0.41	H → L+3 H-1 → L+1 H → L+1	291	0.3 7	H → L+3 H-1 → L+1 H → L+1	295		H → L H-3 → L H-1 → L H-1 → L+1

[a] H: HOMO, L: LUMO

Differently by [8]CPP the maximum of emission spectrum is blue-shifted and the fluorescent quantum yield is increase to a value  $\Phi = 0.47$  (measured using quinine sulfate as a standard). Therefore, the localization of exciton on five phenylene rings, which characterizes the excited state geometries of [n]CPPs with  $n > 8$ ,<sup>91</sup> can also likely occur in **55**, making its

<sup>138</sup> Du, H.; Fuh, R.-C. A.; Li, J.; Corkan, L. A.; Lindsey, J. S. Photochem. Photobiol. 1998, 68, 141–142.

photophysical properties more similar to [9-12]CPP than [8]CPP.

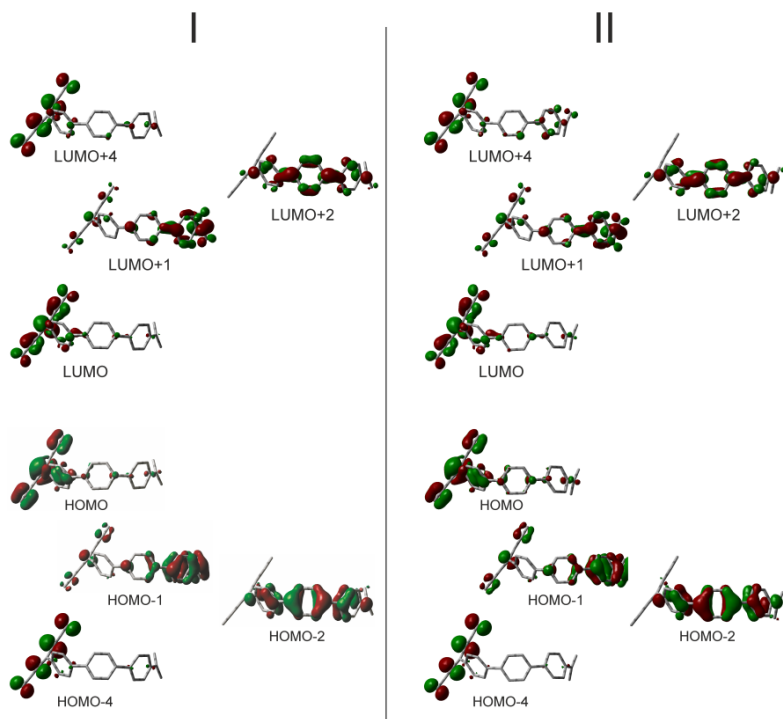


**Figure 83:** Isodensity surface plots of the frontier Kohn-Sham orbitals of the most populated conformers of **55** from CAM-B3LYP computations.

### 3.6.4 TTA- Upconversion Studies

Starting by the successfully use of 9,10-DPA in TTA Upconversion studies, we have investigated the optical response of **55** in solution with palladium(II) octaethylporphyrin (PdOEP) as sensitizer.

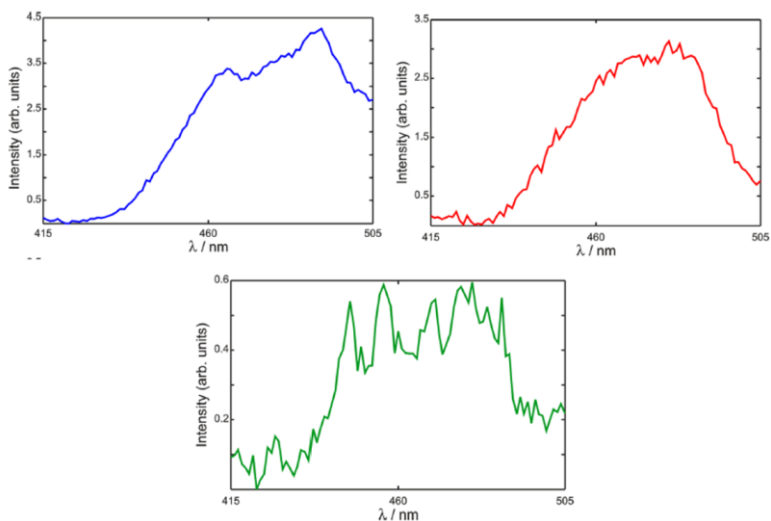


**Figure 84:** Upconverted emission spectra of **55** (1 mM) and PdOEP in  $\text{CH}_2\text{Cl}_2$ ,  $\lambda_{\text{exc}} = 540$  nm. Blue, [PdOEP] = 10  $\mu\text{M}$ ; red, [PdOEP] = 100  $\mu\text{M}$ ; green, [PdOEP] = 1.0 mM. The light source was passed through a 295 nm long pass cutoff emission filter prior to incidence on samples

Different emission spectra were recorded of a solution 1 mM in  $\text{CH}_2\text{Cl}_2$  of **55** and at different concentration of sensitizer (10–1000  $\mu\text{M}$ ), performed under nitrogen atmosphere. Excitation wavelength of the system is 540 nm, on the maximum of absorbance of PdOEP. The shape of the upconverted radiation is related at the concentration of the palladium complex, because of the partial overlap with its absorbance spectrum - Figure 84.

The upconverted spectrum is significantly red-shifted if confronted with that previously reported for 9,10-DPA,<sup>139</sup> demonstrating that emission involves the first excited state of the whole nanohoop. As reported by Parker and Hatchard and

<sup>139</sup> Balushev, S.; Miteva, T.; Yakutkin, V.; Nelles, G.; Yasuda, A.; Wegner, G. *Phys. Rev. Lett.* **2006**, *97*, 143901–143903.

few years later by Castellano,<sup>140</sup> light upconversion occurring via TTA is characterized by a quadratic dependence of the fluorescence intensity upon the incident light power.

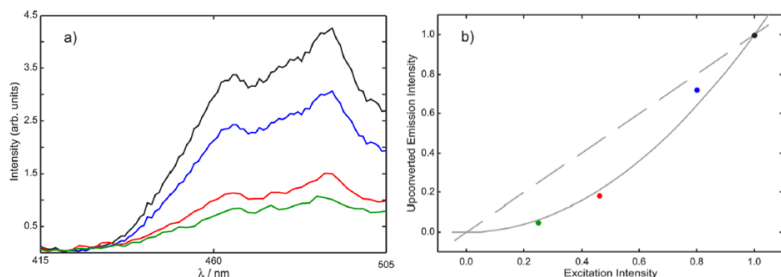


**Figure 85:** a) Upconverted emission intensity profiles of a solution of **55** (0.5 mM) and PdOEP (10 μM) in CH<sub>2</sub>Cl<sub>2</sub> at different incident power density; b) the corresponding normalized integrated emission as a function of the normalized incident power. Dashed line  $y = x$ , full line  $y = x^2$ ; maximum incident power 0.8 mW cm<sup>-2</sup>.

To have a clear idea about the observed anti-Stokes fluorescence of **55**/PdOEP system, we have studied the dependence of the emission signal as a function of the excitation light power - Figure 85a.

The integrated fluorescence intensities are reported as a function of the power density of the incident light, both normalized at their highest values. Clearly the results show that the emission intensity depends on the square of the power of the incident light - Figure 85b - and prove that the upconversion occurs via sensitized TTA.

To sum up, derivative **55** has been synthesized adapting the gram-scale synthesis recently reported by Jasti and fully characterized through 1D, 2D and VT NMR studies

<sup>140</sup> (a) Haeefe, A.; Blumhoff, J.; Khnayzer, R. S.; Castellano, F. N. *J. Phys. Chem. Lett.* **2012**, *3*, 299–303. (b) Deng, F.; Blumhoff, J.; Castellano, F. N. *J. Phys. Chem. A* **2013**, *117*, 4412–4419.

conformational studies have been performed by DFT calculations. The absorption spectrum is characterized by two low energy transitions, one attributable to the 9,10-DPA unit and another characteristic of [n]CPP systems. The emission spectrum resembling to that of larger size CPPs. In the presence of the octaethylporphyrin Pd(II) complex as a sensitizer, derivative **55** undergoes visible light upconversion. This is the first case reported in the literature in which a CPP derivative is involved as an emitter in low power light frequency conversion.

## 3.7 CPP-Based Luminescent Solar Concentrator <sup>141</sup>

### 3.7.1 Luminescent Solar Concentrator

Luminescent Solar Concentrators (LSC) utilize dyes or scattering effects in order to capture the light normal, incident to a surface and redirect it toward the edges to be harvested by photovoltaics devices. This kind of technology has been developed to deal with the outside global energy consumption using renewable sources. <sup>142</sup> The interest for this technology is related to exploiting solar radiation by use of large-area devices that needed a minimal amount of photovoltaic material, which makes the energy production cheaper. Furthermore, through this technology, it will make it possible to exploit the vertical surface of buildings.

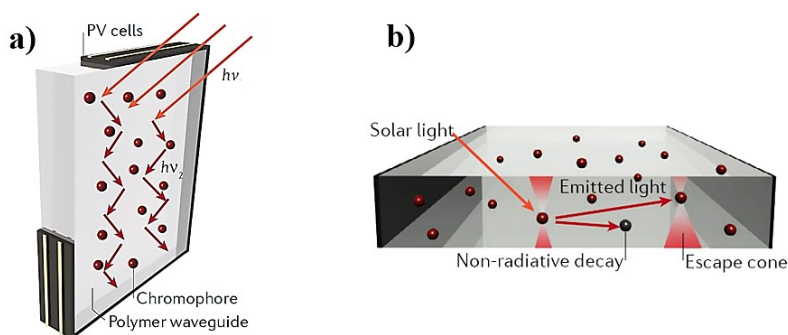


Figure 86: a) Schematization of LSC; b) Chromophore-related losses. <sup>143</sup>

<sup>141</sup> Manuscript in Preparation.

<sup>142</sup> Traverse, C. J.; Pandey, R.; Barr, M. C.; Lunt, R. R. *Nature Energy* **2017**, *2*, 849-860.

These materials are based on total internal reflection phenomenon that trap light radiation inside itself and guide in the edges, similarly that happens in the optical fibers - Figure 86a.

Different processes may limit the efficiency of LSC and can depend by chromophores or by optical quality of waveguides. As concerns the choice of the chromophore, surely a pivotal role is played by the molecules that show a high quantum yields and high Stoke-shifts. High Stoke-shifts ensure a low self-absorption phenomenon - Figure 86b. The light trapped inside the material is determinate by its refractive index. Moreover, waveguide more commonly used are made by polymers that can be affected bulk defect or roughness surface.<sup>143</sup>

In literature have been reported principally two classes of LSCs, coloured and colourless. The first-class features luminophores designed to harvest a high fraction of the impinging solar light, eventually re-emitting it with high efficiency and minimized re-absorption losses. Organic luminophores, such as the commercially available Lumogen, are particularly used for building coloured LSCs.

One of the issues connected with the use of the coloured LSC is their visual impact, in most cases limiting building aesthetic. The best result was obtained using quantum dots. Owing of their very broad absorption spectrum the colour distortion is limited.<sup>144</sup>

The second class is constituted by colourless luminophores in which the use of lanthanide chelates, highly conjugated

---

<sup>143</sup> Meinardi, F.; Bruni, F.; Brovelli, S. *Nature Reviews*, **2017**, 2, 1-9.

<sup>144</sup> Meinardi, F.; McDaniel, H.; Carulli, F.; Colombo, A.; Velizhanin, K. A.; Makarov, N. S.; Simonutti, R.; Klimov, V. I.; Brovelli, S. *Nature Nanotech* **2015**, 10, 878–885.

cyanines and high band gap quantum dots is very common.<sup>145</sup> The absorption of these compounds is essentially limited to the UV region, thus strongly limiting the photon harvesting capabilities. Their Stokes shift is very large, and reabsorption is almost zero. This feature becomes relevant when addressing large area devices, as those developed to replace standard windows. Re-absorption phenomenon strictly limits the maximum active area achievable with the use of standard luminophores, to the point that there is very little scope for devices having surfaces exceeding 100 cm<sup>2</sup>. As it is known,<sup>91</sup> the CPP macrocycles show interesting absorption and emission light properties: the absorption spectrum of CPP is independent by macrocycle dimension and remains completely localized within the UV region ( $\lambda_{\max}$  around 340 nm), instead, the emission maximum spans from 450 to 590 nm on going from the largest (13 phenyl ring) to the smallest (7 phenyl rings). Thus, in collaboration with prof. Luca Beverina and prof. Sergio Brovelli of University of Milano-Bicocca we have studied the performances of CPP derivatives as organic luminophores in luminescent solar concentrator.

### 3.7.2 Synthesis of [8] and [10] CPPs

The choice of [8] and [10]CPP - Figure 87 - is principally due to their high Stoke shift in solution, respectively of 190 nm and 130 nm, and their easy of synthesis on gram-scale.<sup>98</sup>

---

<sup>145</sup> Yang, C. and Lunt, R. R. *Advanced Optical Materials*, **2017**, 5, 1600851-1600856.

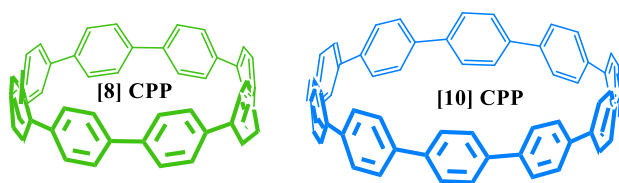


**Figure 87:** Derivatives synthesized for this application.

The synthesis of [8] and [10]CPPs were obtained following the synthetic procedure reported by Jasti.<sup>98</sup>

In order to study the photophysical properties of [8] and [10]CPP macrocycles in the solid state the absorption and emission spectra of both compounds in methyl methacrylate (MMA) solution were registered. [8]CPP shows an emission maximum at 550 nm and a moderate quantum yield, while the [10]CPP featuring an emission maximum at 480 nm and a quantum yield above 65 %, analogously to data obtained in solution.

### 3.7.3 Slabs Manufacturing and Characterization

The preparation of the LSC slabs was performed by the research group of the Prof. Beverina of the Università Milano Bicocca. As the embedding matrix for the preparation of LSC slabs, was selected PMMA because is the most common materials employed for this application and it is cheap.

Furthermore, use of PMMA matrix enables a direct comparison with other reported fluorophores. Firstly, was studied the cell cast method previously reported by Beverina and co-workers,

for the preparation of both Perylenediimides (PDIs) and lanthanide chelates LSCs.<sup>146</sup>

Thus, the solution of PMMA into unreacted MMA (the so-called syrup) was obtained by the reaction of distilled MMA with AIBS at 80 °C.

A solution of [8]CPP in MMA was added to the syrup, along with Lauroyl peroxide as radical initiators.

The viscous solution was degassed and subsequently poured in a cast constituted by two glass sheets and a 5 mm PVC separator. In the end, this have been immersed in a heated water bath at 56 °C for 48 h, followed by a final treatment at 110°C in an oven for 12 h.

The photoluminescence bands of the slab and CHCl<sub>3</sub> solution were compared, and in this way, we observe that the behavior of the chloroform solution of [8]CPP is accord with the literature data, while, significatively, the signal coming from the slab of [8]CPP was unexpected. In details, the emission band of the [8]CPP immobilized in slab is broadened in comparison with the behavior in CHCl<sub>3</sub> solution. This is indicative of a high energy shoulder connected with a reduction in the Stokes shift with respect to the solution signal.

The emissions decay profiles were also different as can observe in Figure 88.

---

<sup>146</sup> a) Sanguineti, A.; Monguzzi, A.; Vaccaro, G.; Meinardi, F.; Ronchi, E.; Moret, M.; Cosentino, U.; Moro, G.; Simonutti, R.; Mauri, V.; Tubino R.; Beverina, L. *Phys Chem Chem Phys*, **2012**, *14*, 6445–6448. b) Turrise, R.; Sanguineti, A.; Sassi, M.; Savoie, B.; Takai, A.; Patriarca, G.; Salamone, M.; Ruffo, R.; Vaccaro, G.; Meinardi, F.; Marks, T.; Facchetti A.; Beverina, L. *J. Mater. Chem. A*, **2015**, *3*, 8045–8054. c) Sanguineti, A.; Sassi, M.; Turrise, R.; Ruffo, R.; Vaccaro, G.; Meinardi, F.; Beverina, L. *Chem. Commun.* **2013**, *49*, 1618–1620.

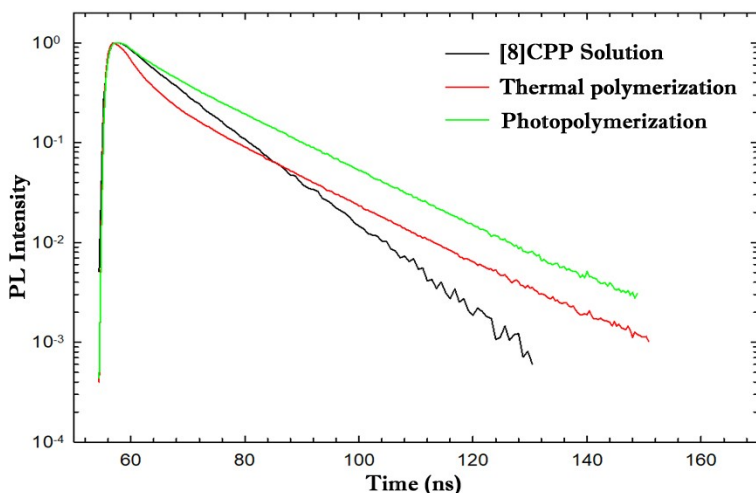


**Figure 88:** [8]CPP solution emission decay (black line), Emission decay of thermal and photopolymerized slabs (red and green respectively)

In fact, the decay profile of the solution of [8]Cycloparaphenylene can be fitted with a monoexponential decay with a lifetime of 10 ns - black line - whilst the slab signal shows a biexponential decay with a fast component and a slow component of 12.5 ns - red line.

Both the emission bands are coherent with the formation of a by-product during the thermal polymerization.

Thus, in order to overcome the problem, a photopolymerization approach was studied, and particularly the new slabs were prepared by irradiation of a solution of [8]CPP and Irgacure<sup>®</sup> 184 in a distilled MMA/lauroyl methacrylate 70/30 % wt - Figure 89.

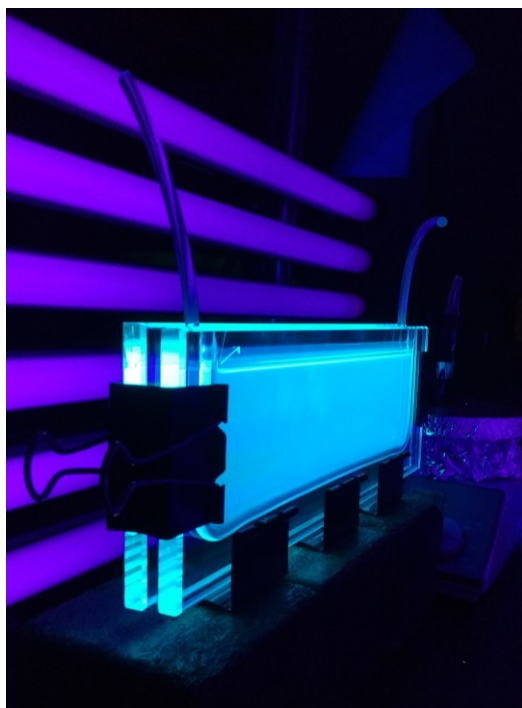


**Figure 89:** Photopolymerization process of MMA/PMMA syrup.

The photopolymerized slab of the [8]CPP shows an absorption emission profiles similar to that highlighted for the macrocycle in  $\text{CHCl}_3$  solution but differently by the thermal polymerized slab previously described - Figure 90, the emission band is unaffected by the broadening - green line in Figure 90.

Probably, the increase of the lifetime of the photoluminescence band of the [8]CPP in PMMA is due to the deactivation of roto-vibrational non-radiative decay pathways connected with the high viscosity of the medium.

Starting by the good results obtained with the slab doped with [8]CPP by photopolymerization approach, a slab of a [10]CPP was prepared in the same condition - Figure 91.

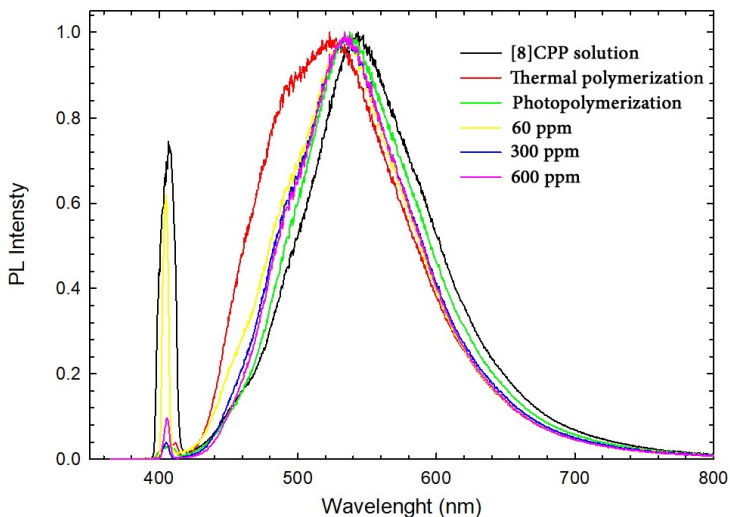


**Figure 90:** Emission of slabs containing [8]CPP at different concentration. Red line is the emission of slab obtained through thermal polymerization.

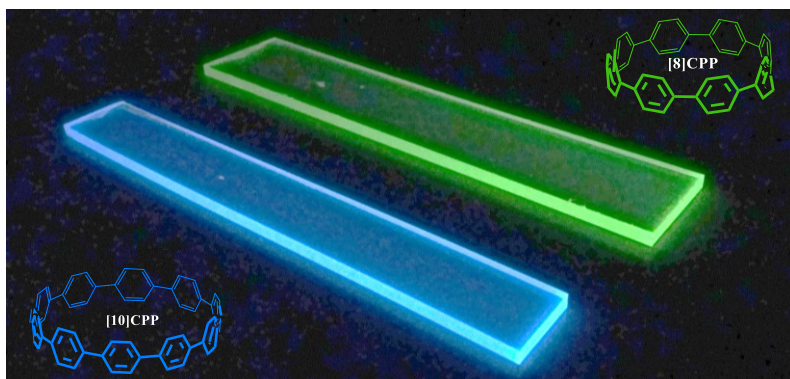


**Figure 91:** Photo of LSCs produced with [8]CPP and [10]CPP.

As for the time resolved luminescence, was observed in both cases a simple monoexponential decay with lifetimes of 14.6 and 17.7 ns for solution and slab, respectively Figure 92b.

To assess the magnitude of the reabsorption phenomena over the maximum useful dimension of an LSC, was measured the fluorescence of [8]CPP and [10]CPP slabs upon excitation at

405 nm, as a function of the distance between irradiation point and photodetector.

These results were compared with the experimental data reported for Lumogen Orang F205, a well-know fluorophore in coloured LSC devices and Europium chelate NB06 used for building colourless LSC.

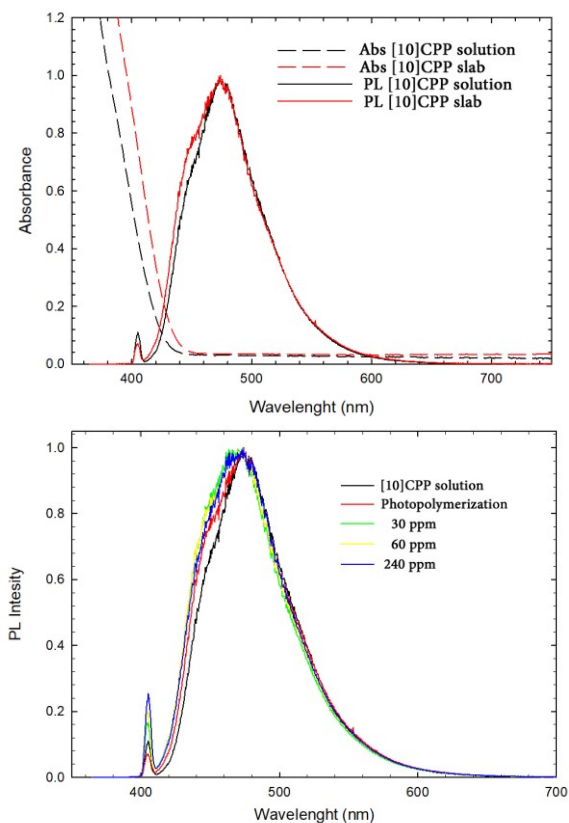


**Figure 92:** (Top) Absorption and emission of slab - red lines - and in solution - black line - of [10]CPP. (Bottom) Emission decay in slabs at different concentration of [10]CPP.

Comparison between Lumogen and [10]CPP shows a great difference in signal attenuation. In fact, Lumogen shows an attenuation of about 40 % at 10 cm from the excitation spot,

while [10]CPP only 10% at 10 cm and below 14 % at 20 cm - Figure 93b. [8]CPP shows an attenuation of 15% at 10 cm from excitation point that remain constant at 16 cm - Figure 93a. This behavior is very similar to that observed with Europium chelate NB06.

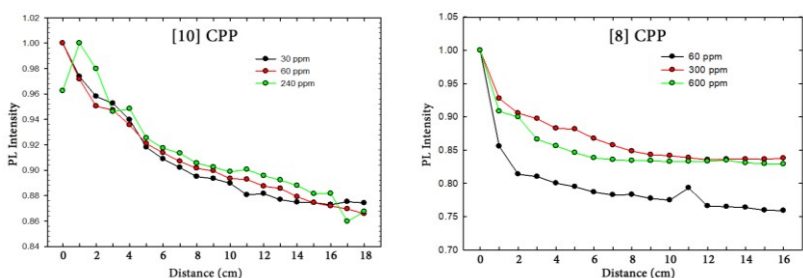


**Figure 93:** Evaluation of reabsorption phenomena in slab (left) [10]CPP and (right) [8]CPP as function of distance.

In summary, here have been prepared for the first time CPP-based LSCs.

The high Stokes shift of the CPP macrocycles, enables the preparation of slabs in which a low reabsorption was observed. The results here obtained show clearly the the photophysical performances of the CPP-based LSC closely matches with that of the lanthanide chelates based LSC, of interest for applications in colorless LSC.

# 4 Experimental Section

## 4.1 General Section

All chemicals reagents grade was used without further purification and were used as purchased from TCI and Sigma Aldrich. Tetrahydrofuran was dried by heating under reflux over sodium wire in the presence of benzophenone as indicator<sup>147</sup> while dimethylformamide were dried by activated 3 Å molecular sieves<sup>148</sup>. Other solvent was purchase by Sigma Aldrich. When necessary compounds were dried in vacuo over CaCl<sub>2</sub>. Reaction temperatures were measured externally. Reactions were monitored by Magery-Nagel TLC silica gel plates (0.25 mm) and visualized by UV light 254 nm, or by spraying with H<sub>2</sub>SO<sub>4</sub>-Ce(SO<sub>4</sub>)<sub>2</sub>. Flash chromatography was performed on Magery-Nagel silica gel (60, 40-63 μm).

NMR spectra were recorded on a 600 [600 (<sup>1</sup>H) and 150 MHz (<sup>13</sup>C)], 400 [400 (<sup>1</sup>H) and 100 MHz (<sup>13</sup>C)], 300 MHz [300 (<sup>1</sup>H) and 75 MHz (<sup>13</sup>C)] or 250 MHz [250 (<sup>1</sup>H) and 62.5 MHz (<sup>13</sup>C)] spectrometer. Chemical shifts are reported relative to the residual solvent peak<sup>149</sup>.

Melting points were determined with a Kofler apparatus.

HR MALDI mass spectra were recorded on a FT-ICR mass spectrometer equipped with a 7T magnet. The samples were

---

<sup>147</sup> Furniss, B. S.; Hannaford, A. J.; Smith, P. W. G.; Tatchell, A. R. Vogel's Textbook of Practical Organic Chemistry, 5<sup>th</sup> ed.; Pearson: Harlow, **1989** and references cited therein.

<sup>148</sup> Williams, D. B. G.; Lawton, M. *J. Org. Chem.* **2010**, *75*, 8351.

<sup>149</sup> Fulmer, G. R.; Miller, A. J. M.; Sherden, N. H.; Gottlieb, H. E.; Nudelman, A.; Stoltz, B.M.; Bercaw, J.E.; Goldberg, K.I. *Organometallics* **2010**, *29*, 2176–2179.

ionized in positive ion mode using MALDI ion source. The mass spectra were calibrated externally, and a linear calibration was applied.

## 4.2 Solid State Self-Assembly of Resorcin[6]arene

### 4.2.1 Procedure of preparation of **3**

Derivative **3** was obtained in accordance with the literature procedure reported in 2016 by our group.<sup>37</sup>

### 4.2.2 Crystal structure determination

Capsular self-assembled crystals were all of small dimensions and contained a large number of solvent molecules; consequently, to improve the intensity of the diffraction pattern, data collections were carried out using synchrotron radiation at the X-ray diffraction beam-line of the Elettra Synchrotron, Trieste, Italy, employing the rotating-crystal method with the cryo-cooling technique. Routinely, the crystal dipped in Paratone, as cryoprotectant, was mounted in a loop and flash frozen to 100 K with liquid nitrogen.

Diffraction data of capsular system containing toluene or ethyl acetate molecules (named **1A**) were indexed and integrated using the XDS package,<sup>150</sup> while MOSFLM<sup>151</sup> was used for crystal obtained from slow evaporation of DMF (named **1B**). Scaling was carried out with SCALA<sup>152,153</sup> for datasets

---

<sup>150</sup> Kabsch, W. *Acta Crystallogr.* **2010**, *D66*, 125–132.

<sup>151</sup> Battye, G. G.; Kontogiannis, L.; Johnson, O.; Powell, H. R.; Leslie, A. G. W. *Acta Crystallogr.* **2011**, *D67*, 271–281.

<sup>152</sup> Evans, P. R. *Acta Crystallogr.* **2006**, *D62*, 72–82.

<sup>153</sup> Winn, M. D.; Ballard, C. C.; Cowtan, K. D.; Dodson, E. J.; Emsley, P.; Evans, P. R.; Keegan, R. M.; Krissinel, E. B.; Leslie, A. G. W.; McCoy, A.; McNicholas, S. J.; Murshudov, G. N.; Pannu, N. S.; Potterton, E. A.;

collected from crystals of **1A**, whereas AIMLESSiii,<sup>139</sup> was used for that one collected from crystals of **1B**. The structures were solved by direct methods using SIR2011.<sup>154</sup> Non-hydrogen atoms at full occupancy, or with population equal to or higher than 0.5 were anisotropically refined (H atoms at the calculated positions) with bond length and angle restraints by full-matrix least-squares methods on F2 using SHELXL-14.<sup>139</sup>

The structure of **1A** shows disorder in the orientation of a phenyl ring: the two positions were refined at 0.4/0.6 of partial occupancy. Three orientations were identified for an ethyl acetate solvent molecules, refined at 0.4/0.3/0.3 of partial occupancy. A toluene solvent molecule and an ethyl acetate solvent molecule share the same binding site in the calixarene cavity. The two solvent molecules were refined at equal partial occupancy.

Restraints (DFIX, DANG) were applied on bond lengths and angles and thermal parameters (SIMU) for atoms involved in disordered fragments.

The cell contained also a severely disordered solvent molecule with partial occupancy, that was not modelled but taken into account using the SQUEEZE/PLATON<sup>155</sup> procedure. The residual electron density of 37 electrons/cell found in the inner space of the crystal (corresponding to about 6.1% of the cell volume) can be attributed or to 0.7 toluene solvent molecules or to 0.8 ethyl acetate solvent molecules.

---

Powell, H. R.; Read, R. J.; Vagin, A.; Wilson K. S. *Acta. Crystallogr.* **2011**, *D67*, 235–242.

<sup>154</sup> Burla, M. C.; Caliendo, R.; Camalli, M.; Carrozzini, B.; Cascarano, G. L.; De Caro, L.; Giacovazzo, C.; Polidori, G.; Siliqi, D.; Spagna, R. *J. Appl. Crystallogr.* **2007**, *40*, 609–613.

<sup>155</sup> Sheldrick, G. M. *Acta Crystallogr.* **2008**, *A64*, 112–122.

### 4.2.3 Calculation of the cavity volume for the capsular assembly 1A

The volume of the sub-cavities of the supramolecular capsule **1A** was estimated using the VOIDOO software,<sup>156</sup> starting from the crystallographic coordinates of **1A**. The following atomic radii were used for the calculations:

- carbon = 1.70 Å,
- oxygen = 1.60 Å,
- nitrogen = 1.65 Å,
- aliphatic hydrogen = 1.20 Å.

Four molecules of benzene were introduced in the model only at the aim of closing the openings in the capsule walls, so that the virtual probe with radius of 1.4 Å could define the void in the cavity.

The following parameters were changed from their default settings:

- Primary grid spacing: 0.1
- Maximum number of volume-refinement cycles: 30

The average volume of the void space inside the sub-cavity, shown in Figure S5, resulted 252 Å<sup>3</sup>.

Volumes of toluene and ethyl acetate guests (*VG*) were also calculated with the same program, and resulted 96 and 85 Å<sup>3</sup>, respectively.

---

<sup>156</sup> Kleywegt, G. J.; Jones, T. A. *Acta Crystallogr.* **1994**, *D50*, 178–185.

## 4.3 Synthesis of a Tetrasulfate-Resorcin[6]arene Cavitand

### 4.3.1 Synthesis of derivative 15

A solution of resorcin[6]arene **3** (0.16 g, 0.19 mmol) and  $K_2CO_3$  (0.55 g, 4.00 mmol) in dry DMA (24 mL) was stirred at 75 °C for 30 min, then was cooled at 25 °C and 1,1'-sulfonyldiimidazole was added. The reaction mixture was stirred at 75 °C, under atmosphere of  $N_2$  for 60 h. The solvent was evaporated and the solid was dissolved in ethyl acetate (50 mL) and washed with aqueous 1M HCl solution ( $2 \times 50$  mL) and  $H_2O$  ( $2 \times 50$  mL). The organic phase was dried with  $Na_2SO_4$  and evaporated to obtain a brown solid. The pure product **15** was purified by column chromatography (silica gel,  $CH_2Cl_2:MeOH$  99.5/0.5 v:v) as a yellow solid, 0.060 g, 30 % yield. **M.p.** > 125.3 °C dec.

**$^1H$  NMR** (600 MHz, TCDE, 403 K)  $\delta$  7.32 (s, *ArH*, 2H), 7.30 (s, *ArH*, 4H), 5.74 (br s, *OH*), 4.06 and 3.94 (br s, *ArCH<sub>2</sub>Ar*, 12H), 2.42 (s, *ArCH<sub>3</sub>*, 6H), 2.29 (s, *ArCH<sub>3</sub>*, 12H).

**$^{13}C$  NMR** (75 MHz, TCDE, 403 K)  $\delta$  9.34, 10.3, 29.3, 33.3, 119.71, 125.16, 126.36, 126.96, 127.93, 128.08, 133.79, 146.29, 146.42, 151.02.

**HRMS** (MALDI)  $m/z$   $[M + Na]^+$  calcd. for  $C_{48}H_{40}NaO_{20}S_4$ , 1087.0888; found 1087.0895.

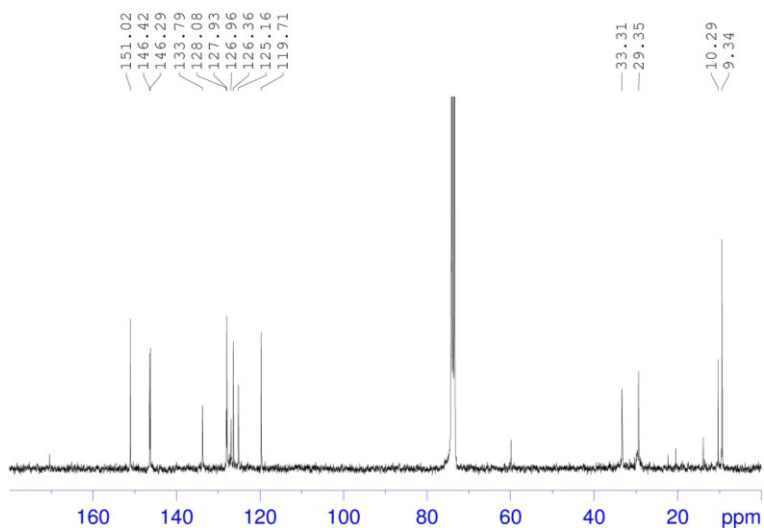


**Figure 94:**  $^{13}\text{C}$  NMR spectrum of **15** (TCDE, 75 MHz, 403 K).

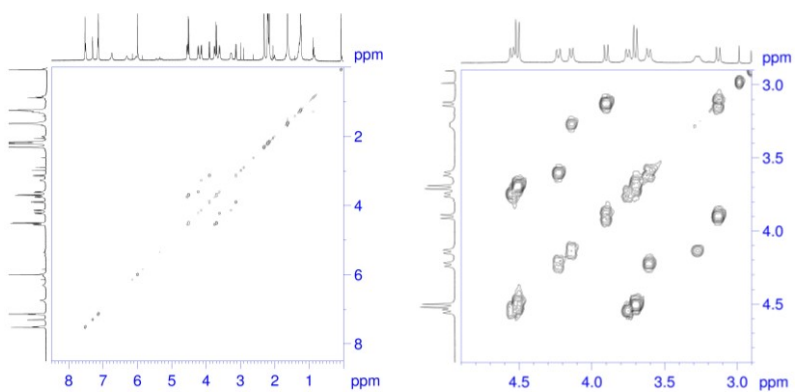


**Figure 95:** (left) 2D COSY spectrum (TCDE, 600 MHz, 298 K) of derivative **15**; (right) Expansion of 2D COSY spectrum (TCDE, 600 MHz, 298 K) of derivative **15**.

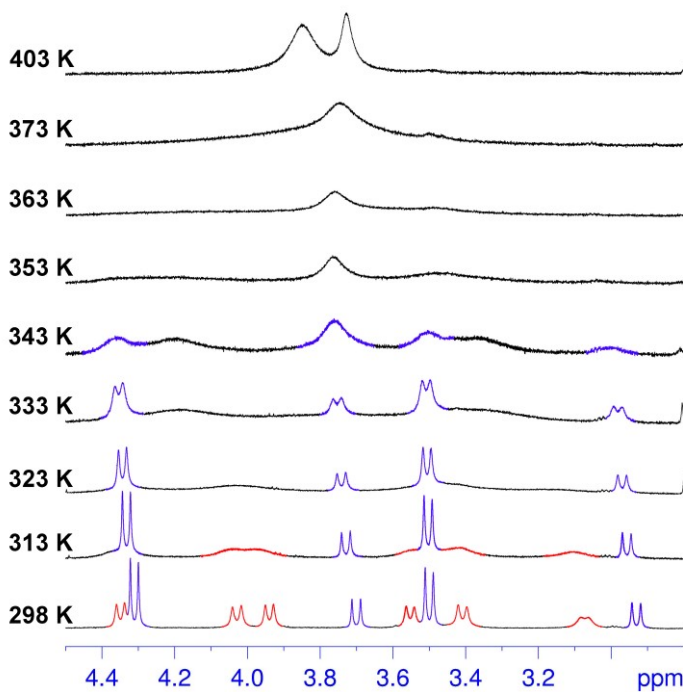


**Figure 96:** Expansion of methylene region of VT  $^1\text{H}$  NMR experiment of derivative **15** (TCDE, 600 MHz, 298 K).

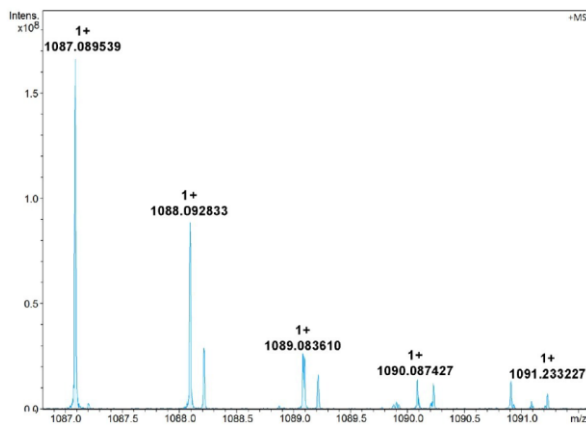


**Figure 97:** Significant portion of the MALDI FT-ICR mass spectrum of **15**  $[\text{M}+\text{Na}]^+$ , showing the isotopic envelope.

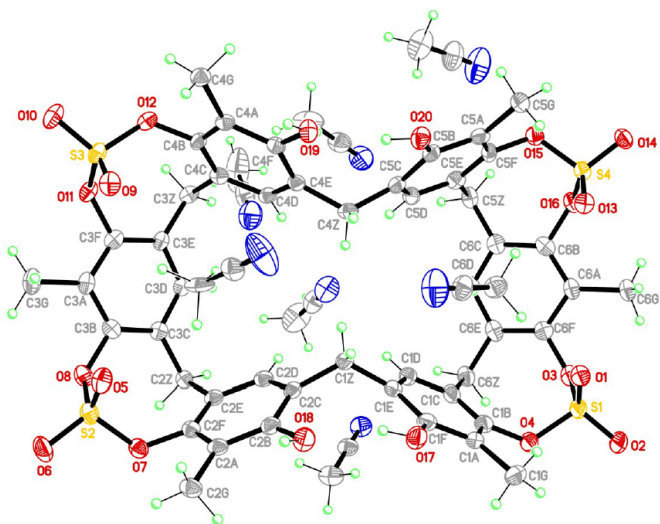


**Figure 98:** ORTEP representation of the derivative **15**. Ellipsoids displayed at 40% probability.

## 4.4 Biomolecular Recognition with Larger Resorcin[6]arene Derivatives

### 4.4.1 Synthesis of derivative 19

Derivative **19** was obtained in accordance with the literature procedure reported in 2016 by Liu and coworker.<sup>85</sup>

### 4.4.2 Synthesis of derivative 20

A solution of **12** (0.47 g, 0.58 mmol) and  $K_2CO_3$  (2.16 g, 15.66 mmol) in acetone (27 mL) was stirred a reflux for 1 h, then was cooled at 25 °C and propargyl bromide (0.70 mL, 9.74 mmol) was added. The reaction mixture was stirred at reflux for 24 h and after which a second addition of propargyl bromide (0.70 mL, 9.74 mmol) is carried out. After further 24 h, solvent was evaporated and the solid was dissolved in diethyl ether (50 mL) and washed with aqueous 0.1 M HCl solution ( $2 \times 100$  mL). The organic phase was dried with  $Na_2SO_4$  and evaporated to obtain pale yellow solid. Derivative **20** was obtained with 87 % of yield (0.65 g).

**$^1H$  NMR** (300 MHz,  $CDCl_3$ , 298 K)  $\delta$  6.39 (s, ArH, 6H), 4.34 (d,  $J=2.4$  Hz,  $-OCH_2-$ , 24H), 3.84 (s,  $-CH_2-$ , 12H), 2.48 (t,  $J=2.4$  Hz,  $-C\equiv CH$ , 12H), 2.26 (s,  $-CH_3$ , 18H).

**$^{13}C$  NMR** (100 MHz,  $CDCl_3$ , 298 K):  $\delta$  154.15, 129.95, 129.32, 125.34, 79.41, 75.34, 60.59, 29.85, 11.04.

**DEPT-135** (100 MHz,  $CDCl_3$ , 298 K):  $\delta$  129.95, 79.41, 75.34, 60.59, 29.85, 11.04.

HRMS (MALDI)  $m/z$   $[M]^+$  calcd. for  $C_{84}H_{73}O_{12}$ , 1273.5097; found 1273.5121.

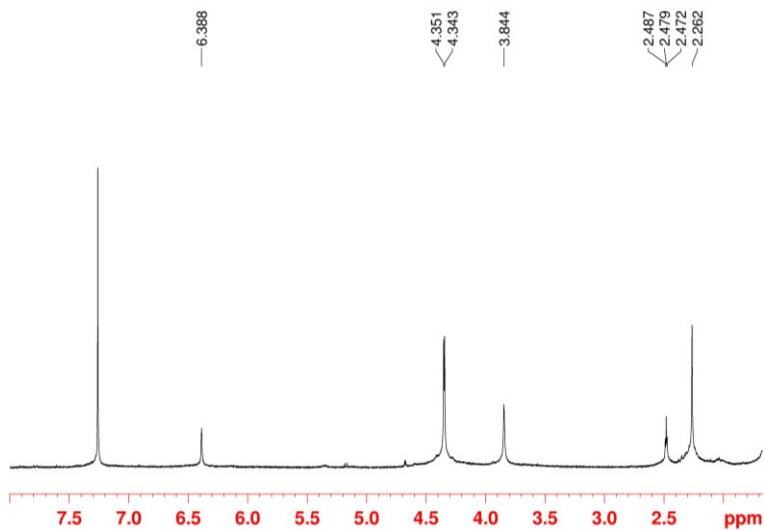


Figure 99:  $^1H$  NMR spectrum of **20** ( $CDCl_3$ , 300 MHz, 298 K).

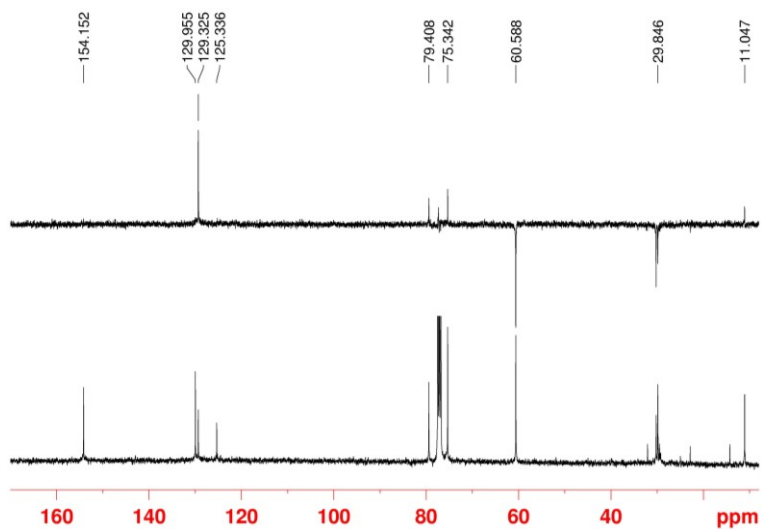


Figure 100:  $^{13}C$  NMR and DEPT-135 spectra of **21** ( $Acetone-d_6$ , 100 MHz, 298 K).

### 4.4.3 Synthesis of derivative 21

A solution of **10** (0.44 g, 0.82 mmol) and  $\text{K}_2\text{CO}_3$  (2.04 g, 14.72 mmol) in acetone (26 mL) was stirred a reflux for 1 h, then was cooled at 25 °C and propargyl bromide (0.74 mL, 9.84 mmol) was added. The reaction mixture was stirred at reflux for 24 h. Subsequently, solvent was evaporated and the solid was dissolved in ethyl acetate (50 mL) and washed with aqueous 1 M HCl solution ( $2 \times 50$  mL). The organic phase was dried with  $\text{Na}_2\text{SO}_4$  and evaporated to obtain pale yellow solid. Derivative **21** was delivered with 81 % of yield (0.70 g).

$^1\text{H}$  NMR (300 MHz, acetone- $d_6$ , 298 K)  $\delta$  6.22 (s, ArH, 4H), 4.48 (d,  $J= 2.4$  Hz,  $-\text{OCH}_2-$ , 16H), 3.98 (s,  $-\text{CH}_2-$ , 8H), 3.04 (t,  $J= 2.4$  Hz,  $-\text{C}\equiv\text{CH}$ , 8H), 2.31 (s,  $-\text{CH}_3$ , 12H).

$^{13}\text{C}$  NMR (75.48 MHz, acetone- $d_6$ , 298 K)  $\delta$  155.28, 130.72, 129.58, 125.37, 80.37, 76.79, 61.21, 30.85, 11.11.

DEPT-135 (75.48 MHz, acetone- $d_6$ , 298 K)  $\delta$  129.58, 80.37, 76.79, 61.21, 30.85, 11.11.

HRMS (MALDI)  $m/z$   $[\text{M}]^+$  calcd. for  $\text{C}_{56}\text{H}_{49}\text{O}_8$ , 849.3422; found 849.3492.

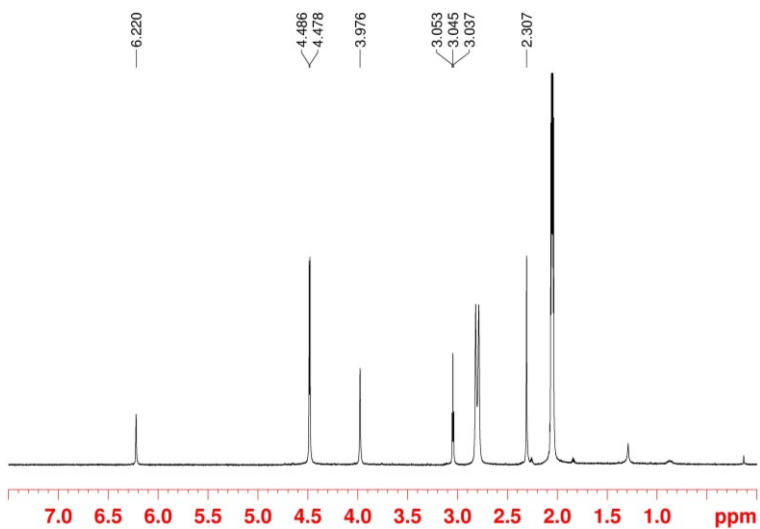


**Figure 101:**  $^1\text{H}$  NMR spectrum of **21** (Acetone- $d_6$ , 300 MHz, 298 K).

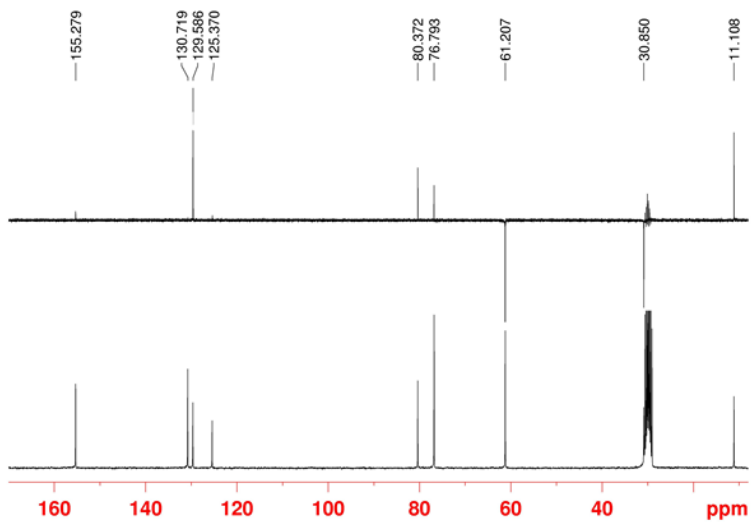


**Figure 102:**  $^{13}\text{C}$  NMR and DEPT-135 spectra of **21** (Acetone- $d_6$ , 75 MHz, 298 K).

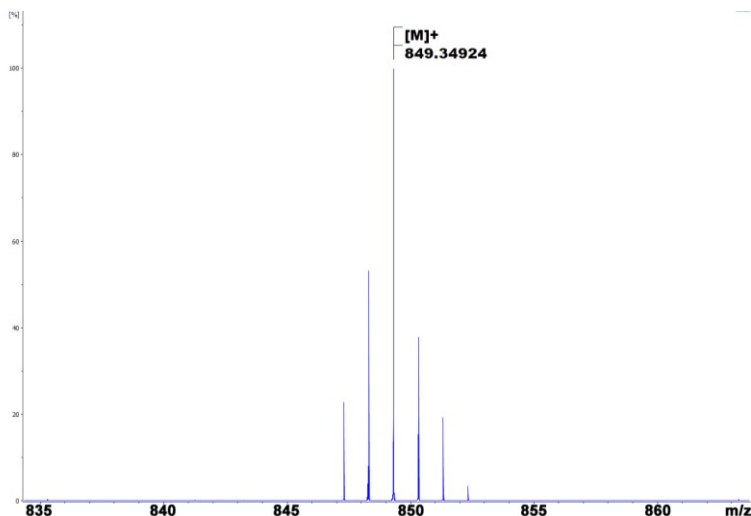


**Figure 103:** Significant portion of the MALDI FT-ICR mass spectrum of **21**  $[M+Na]^+$ , showing the isotopic envelop.

#### 4.4.4 Synthesis of derivative **22**

Derivative **19** (3.99 mg, 4.70  $\mu\text{mol}$ ) and derivative **61** (10.69 mg, 41.40  $\mu\text{mol}$ ) were dissolved in THF/ $\text{H}_2\text{O}$  (v:v) 2:1 (1.00 mL) in an ACE pressure tube and  $\text{Cu}_2\text{SO}_4 \cdot 5\text{H}_2\text{O}$  (0.35 mg, 1.40  $\mu\text{mol}$ ) and sodium ascorbate (0.56 mg, 2.80  $\mu\text{mol}$ ) was added. The reaction mixture was heated under microwave irradiation for 45 min at 80° C. The reaction mixture was filtered off through a pad of celite<sup>®</sup> and the filtrate was concentrated under reduced pressure to deliver a yellow solid.

The mixture was purified through chromatographic column (silica gel, gradient: From MeOH to  $\text{NH}_3$  4% in MeOH) to give derivative **22** with 27 % of yield (3.7 mg).

**$^1\text{H}$  NMR** (600 MHz,  $\text{CD}_3\text{OD}$ , 298 K)  $\delta$  8.09 (s, *H*-Triazole, 4H), 7.36 (s, *H*-Triazole, 4H), 7.22 (s, ArH, 2H), 6.99 (s, ArH, 2H), 6.72 (s, ArH, 2H), 5.98 (s, ArH, 2H), 5.21 and 5.14 (AB,

$J = 12.0$  Hz,  $-OCH_2$ -Triazole, 8H), 4.89 (overlapped to signal of  $H_2O$ ,  $-OCH_2$ -Triazole), 4.55 (q,  $J = 7.2$  Hz, Ar- $CH(CH_3)$ -Ar, 4H), 4.45 (*broad*, 12 H) 4.28 (*broad*, 8 H), 3.94-3.87 (overlapped, 16H), 3.68-3.63 (overlapped, 16H), 3.32 - 3.25 (AB, overlapped to signal of  $CH_3OH$ ), 3.04-2.98 (m, 8H), 2.86-2.78 (m, 8H), 2.66-2.64 (m, 16H) 2.45-2.32 (overlapped, 16H) 1.94 (*broad*,  $-CH_2-$ , 8H), 1.83 (*broad*,  $-CH_2-$ , 8H), 1.60-1.33 (overlapped, 44H).

$^{13}C$  NMR (150 MHz,  $CD_3OD$ , 298 K)  $\delta$  155.22, 154.05, 144.19, 143.89, 130.75, 129.47, 126.44, 123.83, 123.67, 79.35, 75.90, 73.20, 62.75, 61.09, 61.06, 59.12, 55.19, 55.08, 51.01, 50.01, 31.64, 31.09, 30.60, 29.96, 29.86, 29.41, 29.33, 29.16, 29.02, 28.90, 28.80, 28.44, 27.44, 27.41, 26.70, 26.60, 26.45, 26.27, 26.00, 25.48, 22.29, 18.85, 12.99.

**HRMS** (MALDI)  $m/z$   $[M+H]^+$  calcd. for  $C_{144}H_{224}N_{32}O_{32}$ , 2915.6991; found 2915.7250.

$[\alpha]_D$  (c: 3.7 mg/mL) =  $-20.99^\circ$ .

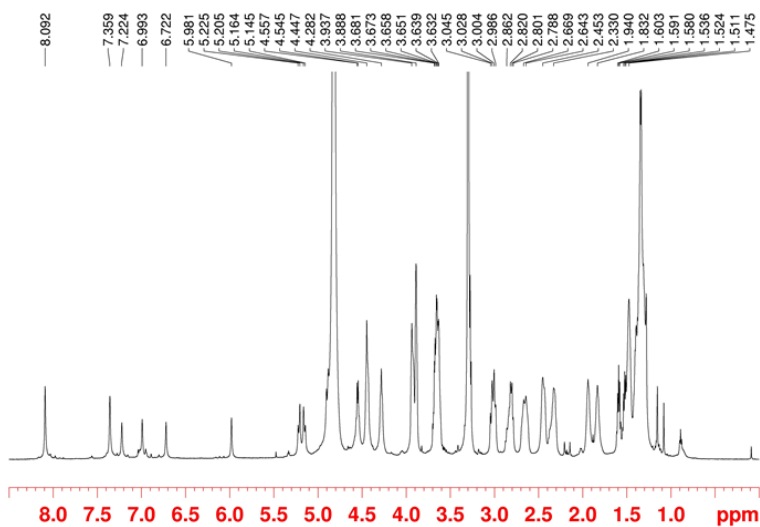


Figure 104:  $^1\text{H}$  NMR of derivative **22** ( $\text{CD}_3\text{OD}$ , 600 MHz, 298K).

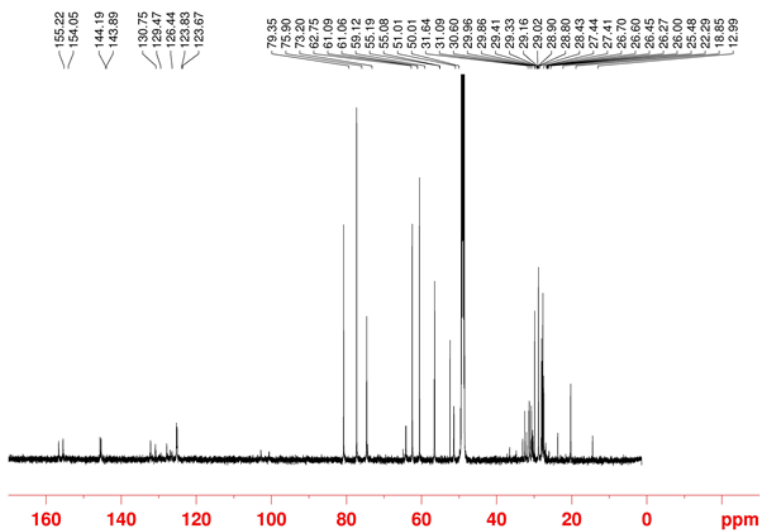
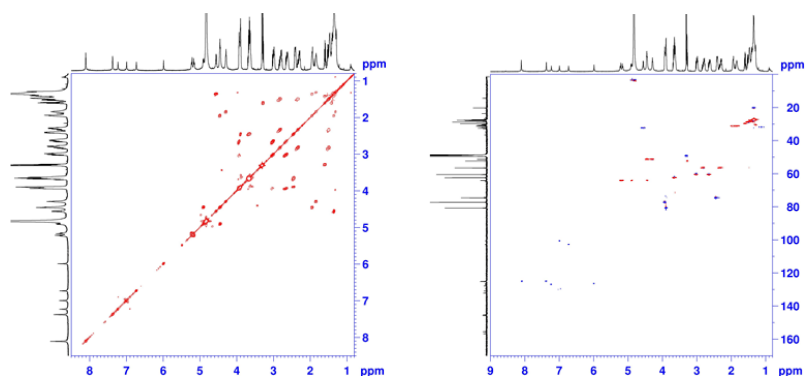
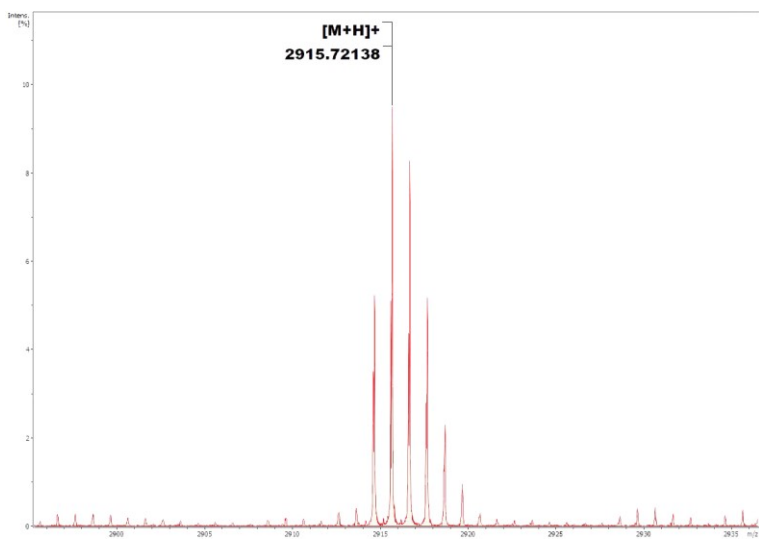


Figure 105:  $^{13}\text{C}$  NMR spectrum of **22** ( $\text{CD}_3\text{OD}$ , 150 MHz, 298 K).



**Figure 106:** (left) 2D COSY spectrum ( $\text{CD}_3\text{OD}$ , 150 MHz, 298 K) of derivative **22**; (right) 2D HSQC spectrum ( $\text{CD}_3\text{OD}$ , 150 MHz, 298 K) of derivative **22**.



**Figure 107:** Significant portion of the MALDI FT-ICR mass spectrum of **22**  $[\text{M}+\text{H}]^+$ .

#### 4.4.5 Synthesis of derivative **24**

Derivative **21** (4.06 mg, 4.83  $\mu\text{mol}$ ) and derivative **61** (9.98 mg, 38.6  $\mu\text{mol}$ ) were dissolved in THF/ $\text{H}_2\text{O}$  (v:v) 2:1 (1.00 mL) in an ACE pressure tube and  $\text{Cu}_2\text{SO}_4 \cdot 5\text{H}_2\text{O}$  (0.36 mg, 1.40  $\mu\text{mol}$ ) and sodium ascorbate (0.57 mg, 2.90  $\mu\text{mol}$ ) was added. The

reaction mixture was heated under microwave irradiation for 45 min at 80° C. The reaction mixture was filtered off through a pad of celite® and the filtrate was concentrated under reduced pressure to deliver a yellow solid.

The mixture was purified through chromatographic column (silica gel, gradient: From MeOH to NH<sub>3</sub> 4% in MeOH) to give derivative **24** with 44 % of yield (6.2 mg).

**<sup>1</sup>H NMR** (600 MHz, CD<sub>3</sub>OD, 298 K)  $\delta$  7.78 (s, *H*-Triazole, 8H), 6.26 (s, *ArH*, 4H), 4.82 (overlapped, -OCH<sub>2</sub>-Triazole, 16H), 4.34 (t, *J*= 7.4 Hz, triazole-CH<sub>2</sub>, 16H), 3.94 (m, -CHOH, 8H), 3.90 (m, -CHOH, 8H), 3.80 (s, *Ar-CH<sub>2</sub>-Ar*, 8H), 3.66 (m, *N-CH<sub>2</sub>-CHOH*, 16H), 3.02 (d, *J*= 11.4 Hz, -CH<sub>2</sub>OH-, 8H), 2.82 (m, CH<sub>2</sub>-N, 8H), 2.67 (m, -CH<sub>2</sub>OH, 8H), 2.46 (m, -CHOH, 8H), 2.31 (m, CH<sub>2</sub>-N, 8H), 2.30 (s, *Ar-CH<sub>3</sub>*, 12H), 1.86 (m, CH<sub>2</sub>, 16H), 1.48 (m, CH<sub>2</sub>, 16H), 1.29 (overlapped, CH<sub>2</sub>, 32H).

**<sup>13</sup>C NMR** (100 MHz, CD<sub>3</sub>OD, 298 K)  $\delta$  155.73, 145.10, 131.08, 130.24, 125.76, 125.41, 80.64, 77.25, 74.71, 66.67, 62.46, 60.54, 56.59, 51.34, 31.23, 28.71, 27.81, 27.35, 11.40.

**HRMS** (MALDI) *m/z* [M + H]<sup>+</sup> calcd. for C<sub>144</sub>H<sub>224</sub>N<sub>32</sub>O<sub>32</sub>, 2915.6991; found 2915.6992.

**[ $\alpha$ ]<sub>D</sub>** (c: 4.1 mg/mL) = -21.01°.

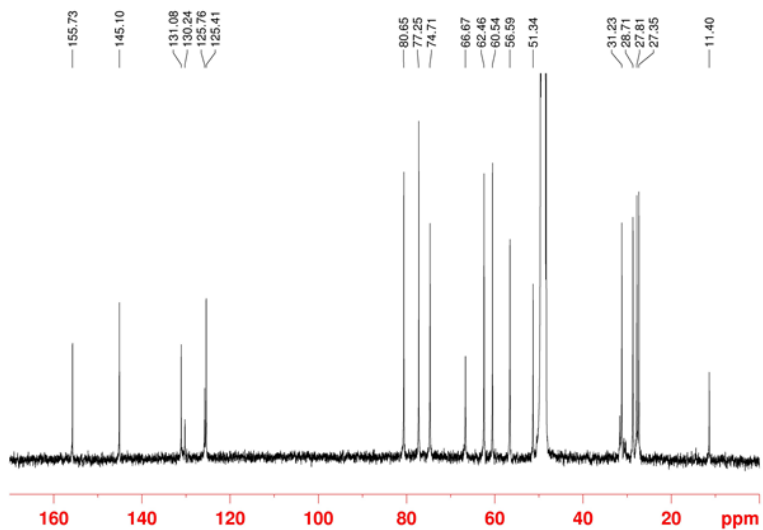


**Figure 108:**  $^{13}\text{C}$  NMR spectrum of **24** ( $\text{CD}_3\text{OD}$ , 150 MHz, 298 K).

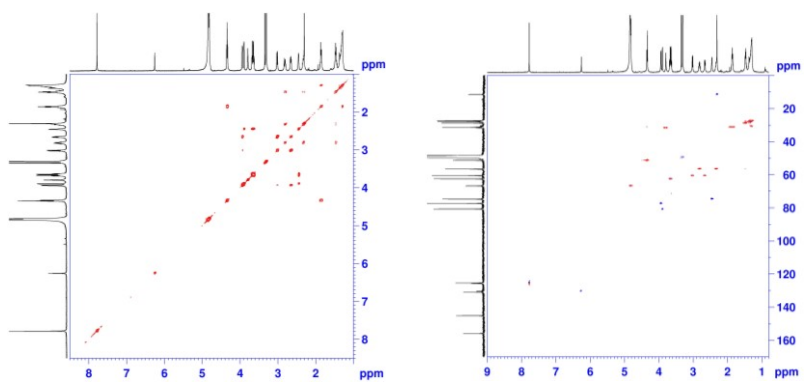


**Figure 109:** (left) 2D COSY spectrum ( $\text{CD}_3\text{OD}$ , 150 MHz, 298 K) of derivative **24**; (right) 2D HSQC spectrum ( $\text{CD}_3\text{OD}$ , 150 MHz, 298 K) of derivative **24**.

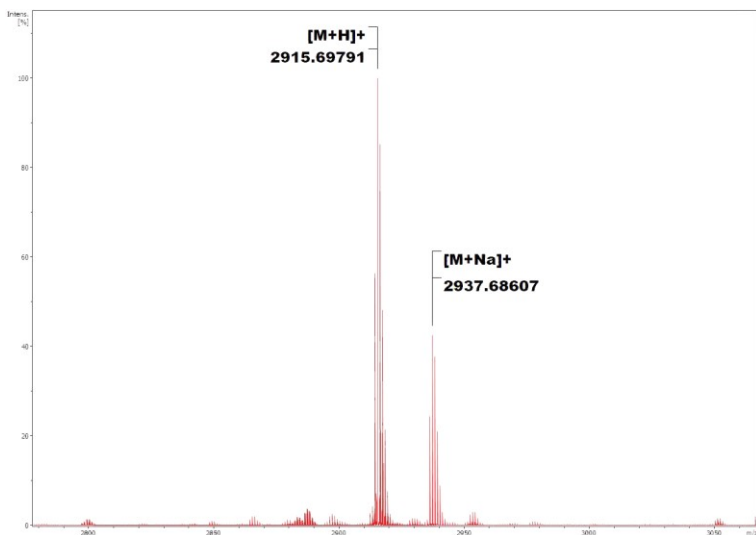


**Figure 110:** Significant portion of the MALDI FT-ICR mass spectrum of **24**  $[M+H]^+$  and **24**  $[M+Na]^+$ .

#### 4.4.6 Synthesis of derivative **23**

Derivative **21** (4.00 mg, 3.14  $\mu\text{mol}$ ) and derivative **61** (9.73 mg, 37.7  $\mu\text{mol}$ ) were dissolved in THF/ $\text{H}_2\text{O}$  (v:v) 2:1 (1.00 mL) in an ACE pressure tube and  $\text{Cu}_2\text{SO}_4 \cdot 5\text{H}_2\text{O}$  (0.23 mg, 0.94  $\mu\text{mol}$ ) and sodium ascorbate (0.37 mg, 1.9  $\mu\text{mol}$ ) was added. The reaction mixture was heated under microwave irradiation for 45 min at 80° C. The reaction mixture was filtered off through a pad of celite<sup>®</sup> and the filtrate was concentrated under reduced pressure to deliver a yellow solid.

The mixture was purified through chromatographic column (silica gel, gradient: From MeOH to  $\text{NH}_3$  4% in MeOH) to give derivative **23** with 14% of yield (1.9 mg).

**$^1\text{H}$  NMR** (400 MHz,  $\text{CD}_3\text{OD}$ , 298 K)  $\delta$  7.89 (s, *H*-Triazole, 12H), 6.42 (s, *ArH*, 6H), 4.71 (s,  $-\text{OCH}_2$ -Triazole, 24H), 4.32 (t,  $J=6.5$  Hz, triazolo- $\text{CH}_2$ -, 24H), 3.95 (m,  $-\text{CHOH}$ , 12H), 3.90

(m, -CHOH, 12H), 3.83 (broad, Ar-CH<sub>2</sub>-Ar, 12H), 3.66 (m, N-CH<sub>2</sub>-CHOH, 24H), 3.03 (d, *J*= 9.8 Hz, -CH<sub>2</sub>OH-, 12H), 2.83 (m, CH<sub>2</sub>-N, 12 H), 2.67 (m, -CH<sub>2</sub>OH, 12H), 2.50 (broad, -CHOH, 12H), 2.34 (m, CH<sub>2</sub>-N, 12 H) 2.21 (s, Ar-CH<sub>3</sub>, 18H), 1.83 (m, CH<sub>2</sub>, 24H), 1.47 (m, CH<sub>2</sub>, 24H), 1.29 (overlapped, CH<sub>2</sub>, 48H).

<sup>13</sup>C NMR (100 MHz, CD<sub>3</sub>OD, 298 K) δ 155.53, 145.01, 130.89, 126.35, 125.46, 80.90, 77.38, 74.39, 62.56, 60.54, 56.39, 31.27, 28.95, 27.90, 27.40, 11.19.

HRMS (MALDI) *m/z* [M]<sup>+</sup> calcd. for C<sub>216</sub>H<sub>336</sub>N<sub>48</sub>O<sub>48</sub>, 4395.5286; found 4395.5910.

[α]<sub>D</sub> (c: 1.9 mg/mL) = - 33.50°.

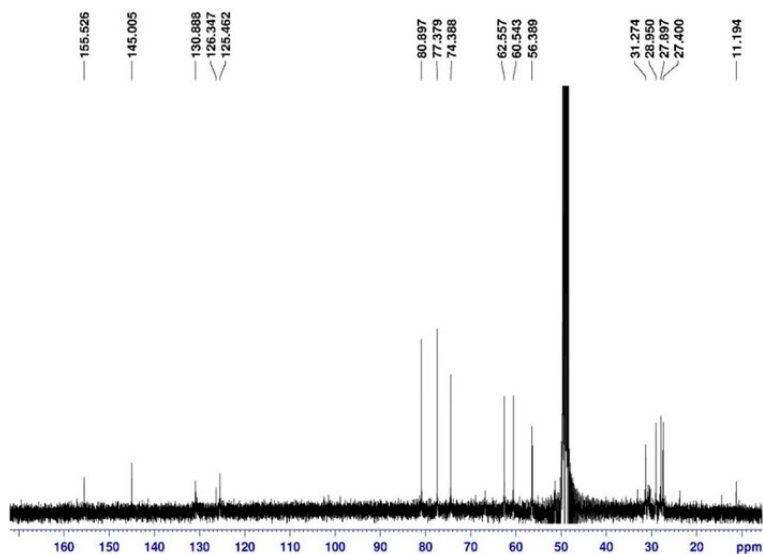
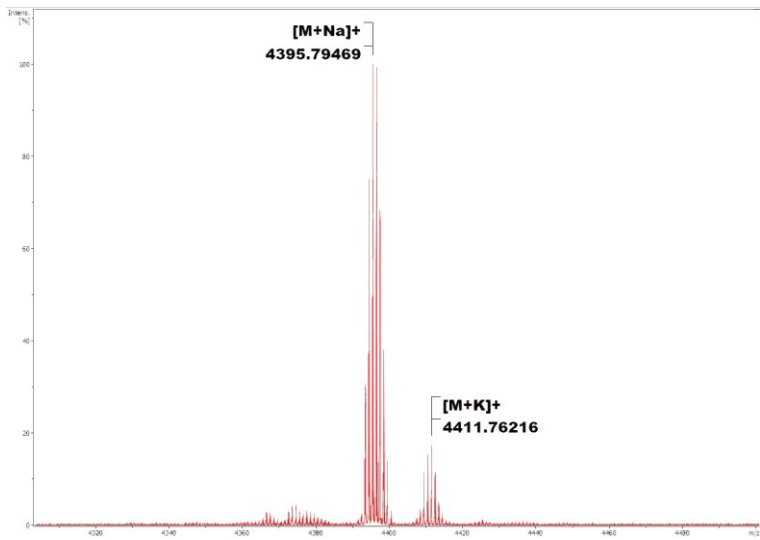


Figure 111: <sup>13</sup>C NMR spectrum of **23** (CD<sub>3</sub>OD, 150 MHz, 298 K).



**Figure 112:** Significant portion of the MALDI FT-ICR mass spectrum of **23** [M+Na]<sup>+</sup> and **23** [M+K]<sup>+</sup>.

## 4.5 Tuning Cycloparaphenylene Host Properties by Chemical Modification

### 4.5.1 Synthesis of derivative 48

A solution of 1,4-dibromobenzene (8.63 g, 36.6 mmol) in anhydrous THF (400 mL) was cooled at  $-78\text{ }^{\circ}\text{C}$ , and a 2.5 M solution of *n*-butyllithium in hexane (17.1 mL, 42.8 mmol) was added over 15 min. Compound 5 (3.00 g, 17.8 mmol) was then added to the reaction mixture as a solid in three equal portions over 15 min. The solution was stirred for 5 h at  $-78\text{ }^{\circ}\text{C}$  and then added to 100 mL of water. The mixture was further diluted by addition of 100 mL of diethyl ether, and the organic layer was separated. The aqueous layer was extracted with diethyl ether ( $2 \times 50\text{ mL}$ ), and the combined organic layers were washed with a saturated brine solution (150 mL). The organic phase was then dried over  $\text{Na}_2\text{SO}_4$ , filtered, and evaporated under reduced pressure. The crude product was purified by column chromatography on silica gel using petroleum ether/ethyl acetate (4:6). The product **48** was isolated as a white solid in 65% yield (5.60 g). **Mp**: 75.3-76.1  $^{\circ}\text{C}$ .

**$^1\text{H}$  NMR** (400 MHz,  $\text{CD}_2\text{Cl}_2$ , 298 K):  $\delta$  7.45 (d,  $J = 8.4\text{ Hz}$ , ArH, 4H), 7.26 (d,  $J = 8.4\text{ Hz}$ , ArH, 4H), 4.99 (s, CH=COMe, 2H), 3.54 (s, OCH<sub>3</sub>, 6H), 2.96 (s, OH, 2H).

**$^{13}\text{C}$  NMR** (62.5 MHz,  $\text{CDCl}_3$ , 298 K):  $\delta$  155.4, 144.7, 131.7, 127.7, 121.4, 103.1, 73.9, 55.5.

**HRMS (ESI<sup>-</sup>)**  $m/z$   $[\text{M}-\text{H}]^-$  calcd for  $\text{C}_{20}\text{H}_{17}\text{Br}_2\text{O}_4$ , 478.9499; found, 478.9479.

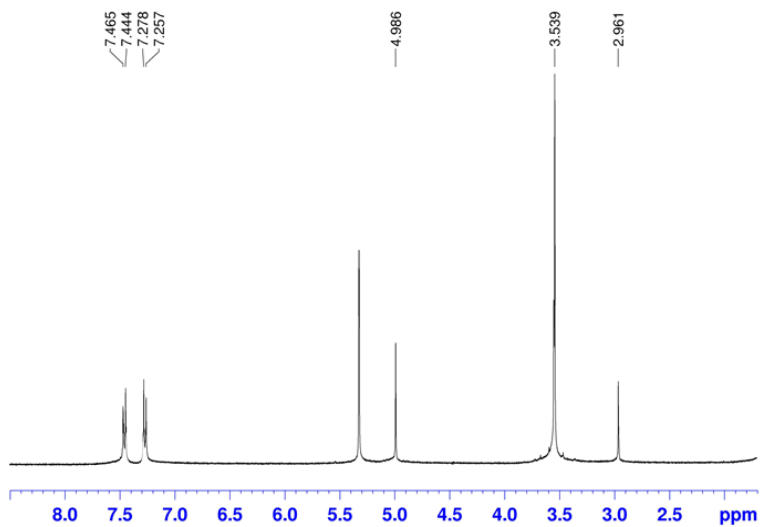


**Figure 113:**  $^1\text{H}$  NMR spectrum of **48** ( $\text{CD}_2\text{Cl}_2$ , 400 MHz, 298 K).

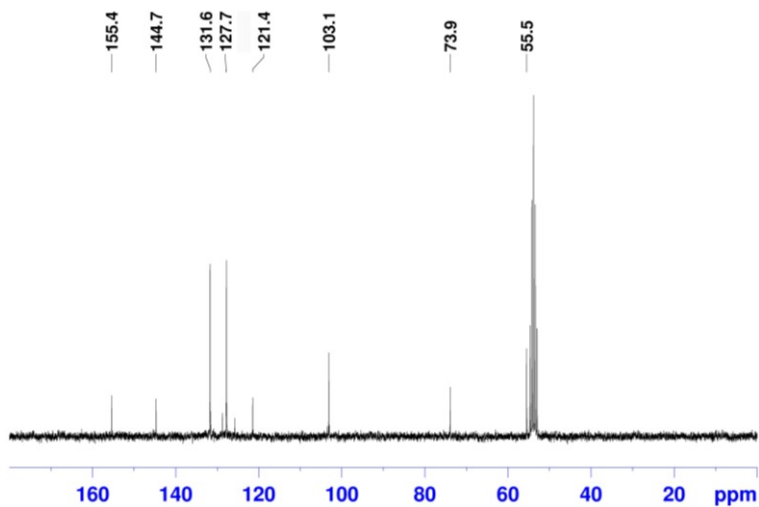


**Figure 114:**  $^{13}\text{C}$  NMR spectrum of **48** ( $\text{CD}_2\text{Cl}_2$ , 100 MHz, 298 K).

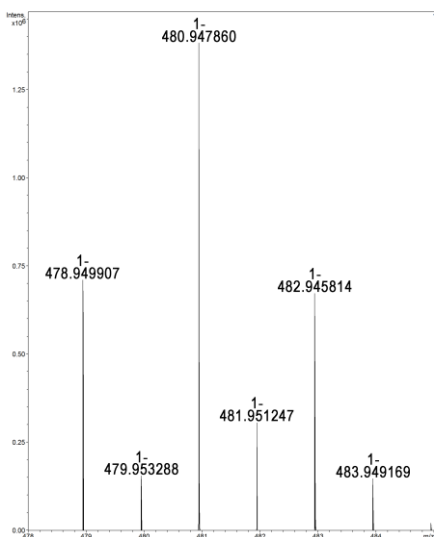


**Figure 115:** Significant portion of the HR MALDI FT-ICR mass spectrum of **48** [M-H]<sup>-</sup> showing the isotopic envelop.

## 4.5.2 Synthesis of derivative **49**

Compound **48** (5.60 g, 11.6 mmol) in anhydrous THF (110 mL) was cooled at 0 °C, followed by addition of NaH (1.86 g, 46.4 mmol, 60% in mineral oil). The mixture was stirred for 30 min, and subsequently iodomethane (4.3 mL, 69.6 mmol) was added. The reaction mixture was then stirred at room temperature overnight. The excess of sodium hydride was then quenched by addition of 50 mL of water followed by addition of 70 mL of ethyl ether. The organic layer was separated, and the aqueous phase was extracted with ethyl ether. The combined organic layers were dried over sodium sulfate, filtered, and evaporated under reduced pressure. The crude product was purified by column chromatography on silica gel using petroleum ether/ethyl ether (6:4). The product **49** was

isolated as a white solid in 81% yield (4.79 g). **Mp**: 119.5-120.7 °C.

**<sup>1</sup>H NMR** (300 MHz, CD<sub>2</sub>Cl<sub>2</sub>, 298 K): δ 7.43 (d, *J* = 8.8 Hz, ArH, 4H), 7.28 (d, *J* = 8.8 Hz, ArH, 4H), 4.85 (s, CH=COMe, 2H), 3.55 (s, OCH<sub>3</sub>, 6H), 3.33 (s, OCH<sub>3</sub>, 6H).

**<sup>13</sup>C NMR** (75 MHz, CD<sub>2</sub>Cl<sub>2</sub>, 298 K): δ 155.6, 143.7, 131.4, 128.4, 121.4, 104.2, 79.0, 55.4, 51.6.

**HRMS (ESI+)** *m/z* [M + Na]<sup>+</sup> calcd for C<sub>22</sub>H<sub>22</sub>Br<sub>2</sub>NaO<sub>4</sub>, 530.9777; found, 530.9798.

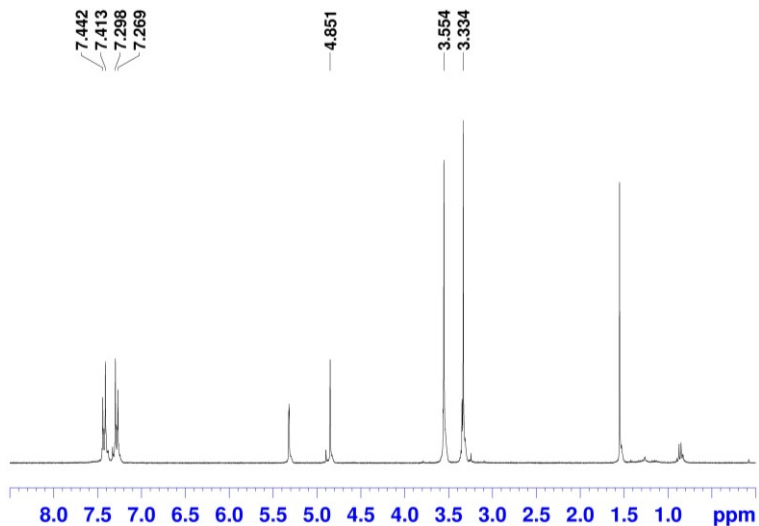


**Figure 116:** <sup>1</sup>H NMR spectrum of **49** (CD<sub>2</sub>Cl<sub>2</sub>, 300 MHz, 298 K).

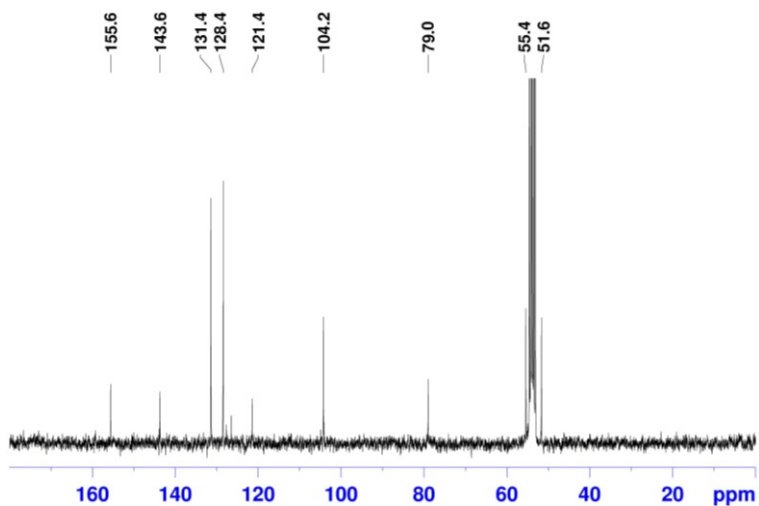


**Figure 117:**  $^{13}\text{C}$  NMR spectrum of **49** ( $\text{CD}_2\text{Cl}_2$ , 75 MHz, 298 K).

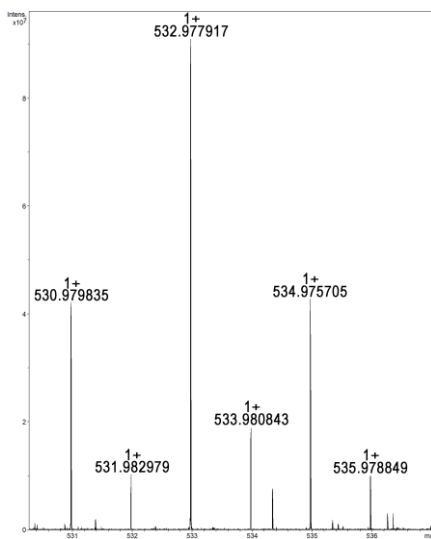


**Figure 118:** Significant portion of the HR MALDI FT-ICR mass spectrum of **49**  $[\text{M}+\text{Na}]^+$  showing the isotopic envelop.

### 4.5.3 Synthesis of derivative 50

Compound **49** (1.30 g, 2.55 mmol) was dissolved in 30 mL of dry THF and cooled to  $-78\text{ }^{\circ}\text{C}$ , and a 2.5 M solution of *n*-butyllithium in hexanes (2.3 mL, 5.6 mmol) was added over 15 min. Finally, isopropyl pinacol borate (2.3 mL, 11.5 mmol) was rapidly added, and the mixture was stirred for 5 h under argon. Then, 25 mL of water and 30 mL of ethyl ether were added to the solution, and the biphasic mixture was stirred for 30 min and heated at room temperature. The organic phase was separated, and the aqueous layer was extracted with ethyl ether ( $3 \times 25\text{ mL}$ ). The combined organic phases were dried over sodium sulfate and concentrated under reduced pressure. The crude was purified by column chromatography on silica gel using petroleum ether/ethyl ether (7:3) to deliver compound **50** as a white solid in 53% yield (0.82 g). **Mp**: 129.0–130.0  $^{\circ}\text{C}$ .

**$^1\text{H}$  NMR** (400 MHz,  $\text{CDCl}_3$ , 298 K):  $\delta$  7.75 (d,  $J = 7.8\text{ Hz}$ , ArH, 4H), 7.45 (d,  $J = 7.8\text{ Hz}$ , ArH, 4H), 4.90 (s, CH=COMe, 2H), 3.55 (s, O CH<sub>3</sub>, 6H), 3.41 (s, O CH<sub>3</sub>, 6H), 1.34 (s, CH<sub>3</sub>, 24H).

**$^{13}\text{C}$  NMR** (100 MHz,  $\text{CDCl}_3$ , 298 K):  $\delta$  155.3, 147.0, 134.8, 125.4, 104.4, 83.9, 79.4, 55.2, 51.5, 25.0.

**DEPT 135** (62.5 MHz,  $\text{CDCl}_3$ , 298 K): 134.8, 125.4, 104.4, 55.2, 51.5, 25.0.

**HRMS (MALDI)**  $m/z$   $[\text{M}+\text{Ag}]^+$  calcd for  $\text{C}_{34}\text{H}_{46}\text{AgB}_2\text{O}_8$ , 711.2430; found, 711.2418.

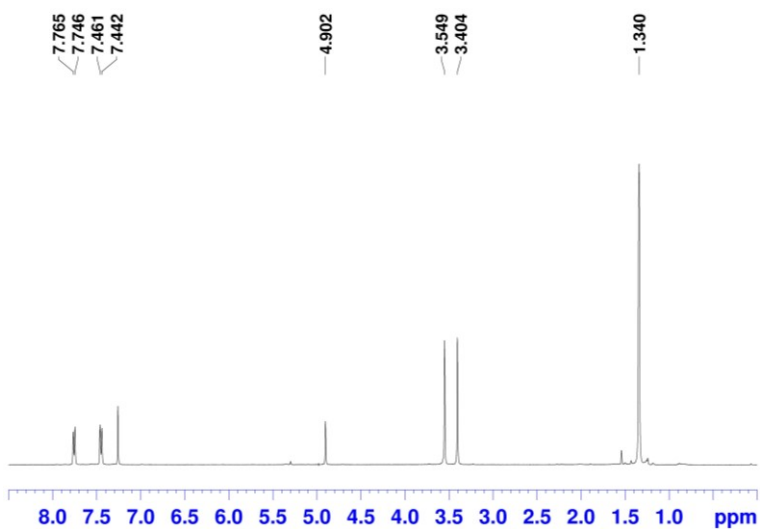


**Figure 119:**  $^1\text{H}$  NMR spectrum of **50** ( $\text{CDCl}_3$ , 400 MHz, 298 K).

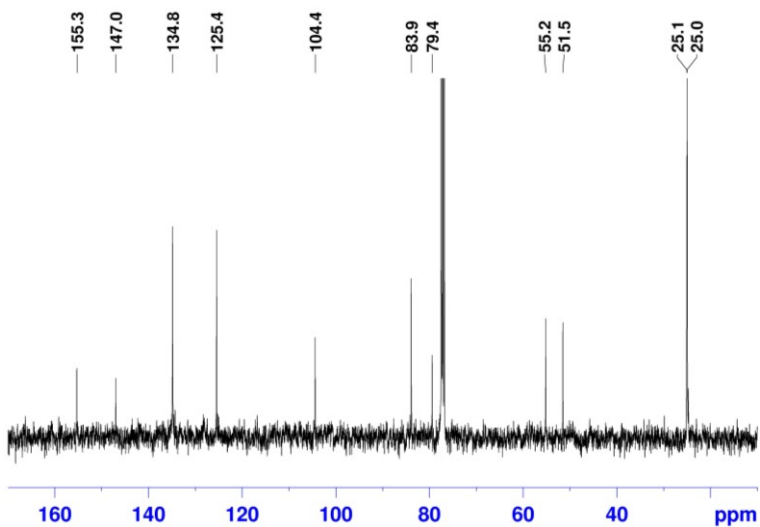


**Figure 120:**  $^{13}\text{C}$  NMR spectrum of **50** ( $\text{CDCl}_3$ , 100 MHz, 298 K).

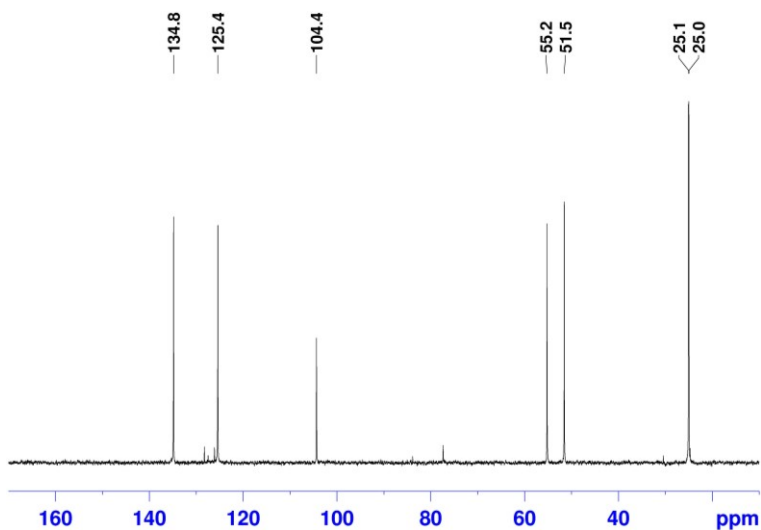


**Figure 121:** DEPT-135 spectrum of **50** (CDCl<sub>3</sub>, 62.5 MHz, 298 K).

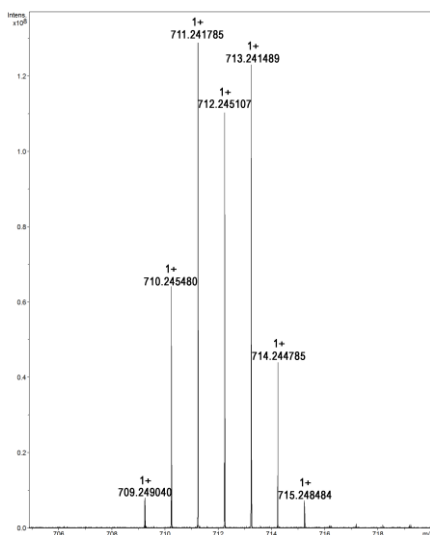


**Figure 122:** Significant portion of the HR MALDI FT-ICR mass spectrum of **50** [M+Ag]<sup>+</sup> showing the isotopic envelope.

#### 4.5.4 Synthesis of derivative 51

Diboronate **50** (1.81 g, 3.00 mmol), dibromide **36** (1.99 g, 3.00 mmol), S-Phos (1.48 mg, 3.6 mmol), and  $K_3PO_4$  (2.55 g, 12.0 mmol) in DMF (600 mL) and  $H_2O$  (60 mL) were stirred and degassed twice through the freeze/pump/thaw technique. Finally,  $Pd(OAc)_2$  (404 mg, 2.1 mmol) was added, and the mixture was stirred at 100 °C for 48 h under argon. After cooling at room temperature, the mixture was filtered through Celite<sup>®</sup>, and 100 mL of water and 100 mL of  $CH_2Cl_2$  were added. The biphasic mixture was stirred for 10 min, and then the organic layer was extracted while the aqueous phase was washed with  $CH_2Cl_2$  ( $5 \times 50$  mL). The combined organic phases were washed with 150 mL of NaCl aqueous solution and dried over sodium sulfate. The solvent was removed under reduced pressure, and the crude product was purified by chromatography column on silica gel (gradient of petroleum ether/  $CH_2Cl_2$ /Et<sub>2</sub>O = 30:65:5) to give derivative **51** as a white solid in 31% yield (0.79 g). **Mp**: >293 °C dec.

<sup>1</sup>H NMR (600 MHz,  $CDCl_3$ , 298 K):  $\delta$  7.53–7.49 (overlapped, *ArH*, 12H), 7.36 (d,  $J = 7.6$  Hz, *ArH*, 4H), 7.13 (d,  $J = 8.2$  Hz, *ArH*, 4H), 6.14 (overlapped, *CH=CH*, 4H), 6.05 (d,  $J = 10.1$  Hz *CH=CH*, 4H), 5.05 (s, *CH=COMe*, 2H), 3.66 (s, *OCH<sub>3</sub>*, 6H), 3.47 (s, *OCH<sub>3</sub>*, 6H), 3.41 (s, *OCH<sub>3</sub>*, 6H), 3.40 (s, *OCH<sub>3</sub>*, 6H).

<sup>13</sup>C NMR (150 MHz,  $CDCl_3$ , 298 K):  $\delta$  155.5, 143.6, 142.9, 141.6, 139.9, 139.8, 133.9, 133.6, 133.0, 132.7, 127.0, 127.0, 126.5, 126.4, 126.4, 105.0, 79.8, 74.8, 74.2, 55.3, 52.3, 51.9, 51.8.

**DEPT 135** (150 MHz,  $\text{CDCl}_3$ , 298 K):  $\delta$  133.9, 133.6, 133.0, 132.7, 127.0, 127.0, 126.5, 126.4, 126.4, 105.0, 55.3, 52.3, 52.0, 51.8.

**HRMS (MALDI)**  $m/z$   $[\text{M}+\text{Ag}]^+$  calcd for  $\text{C}_{56}\text{H}_{54}\text{AgO}_8$ , 961.2870; found, 961.2859.

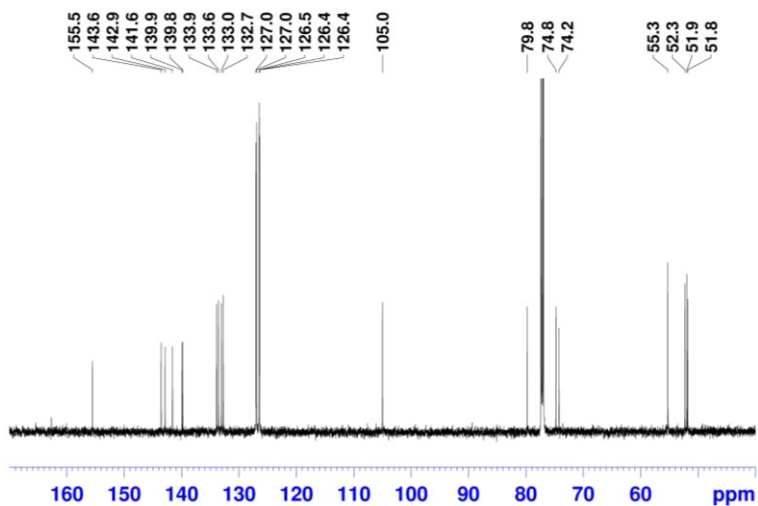


**Figure 123:**  $^{13}\text{C}$  NMR spectrum of **51** ( $\text{CDCl}_3$ , 150 MHz, 298 K).

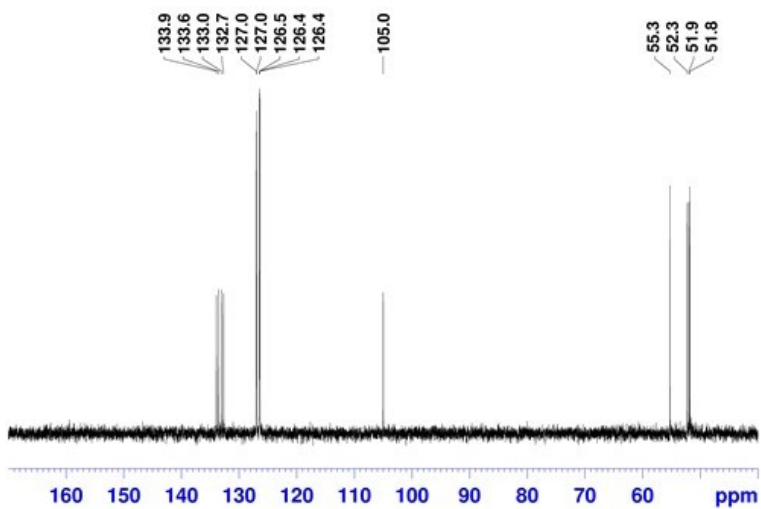


**Figure 124:** DEPT-135 spectrum of **51** ( $\text{CDCl}_3$ , 150 MHz, 298 K).

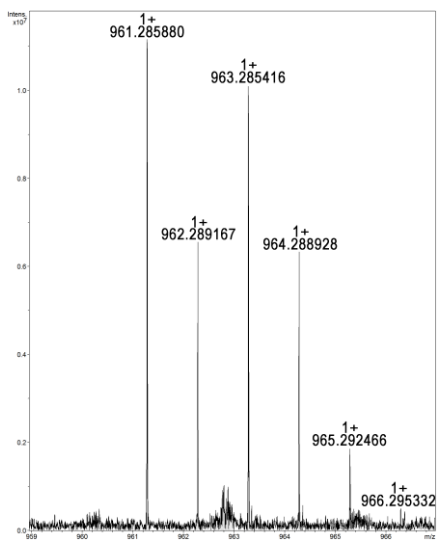


**Figure 125:** Significant portion of the HR MALDI FT-ICR mass spectrum of **51**  $[\text{M}+\text{Ag}]^+$  showing the isotopic envelop.

### 4.5.5 Synthesis of derivative 46

A suspension of SnCl<sub>2</sub> (954 mg, 5.03 mmol) in 110 mL of THF under argon was added of HCl (13 mL, 37%) and degassed. Then, derivative **51** was added (430 mg, 0.50 mmol), and the reaction mixture was stirred for 8 h at room temperature. Subsequently an aqueous solution of NaHCO<sub>3</sub> (45 mL) and CHCl<sub>3</sub> (50 mL) were added, and the mixture was stirred for 5 min. The organic layer was separated, and the aqueous phase was extracted with CHCl<sub>3</sub> (2 × 30 mL). The combined organic layers were dried on Na<sub>2</sub>SO<sub>4</sub> and filtered, and the solvent was removed in vacuum. The crude product was purified by column chromatography on silica gel using petroleum ether/CH<sub>2</sub>Cl<sub>2</sub> (7:3). The product **46** was obtained as a yellow solid in 56% yield (0.19 g). **Mp**: >325 °C dec.

**<sup>1</sup>H NMR** (600 MHz, CDCl<sub>3</sub>, 298 K): δ 7.59 (d, *J* = 8.4 Hz, ArH, 4H), 7.52– 7.50 (overlapped, ArH, 8H), 7.48–7.46 (overlapped, ArH, 12H), 7.41 (d, *J* = 8.4 Hz, ArH, 4H), 6.83 (s, CH=COMe, 2H), 3.73 (s, OMe, 6H).

**<sup>13</sup>C NMR** (150 MHz, CDCl<sub>3</sub>, 298 K): δ 152.7, 138.7, 138.5, 138.0, 137.9, 137.8, 137.7, 136.3, 129.3, 129.0, 127.9, 127.7, 127.6, 127.5, 127.1, 115.5, 57.1.

**DEPT 135** (150 MHz, CDCl<sub>3</sub>, 298 K): δ 129.2, 127.8, 127.7, 127.5, 127.5, 127.0, 115.4, 57.0.

**HRMS (MALDI)** *m/z* [M]<sup>+</sup> calcd for C<sub>50</sub>H<sub>36</sub>O<sub>2</sub>, 668.2710; found, 668.2708.

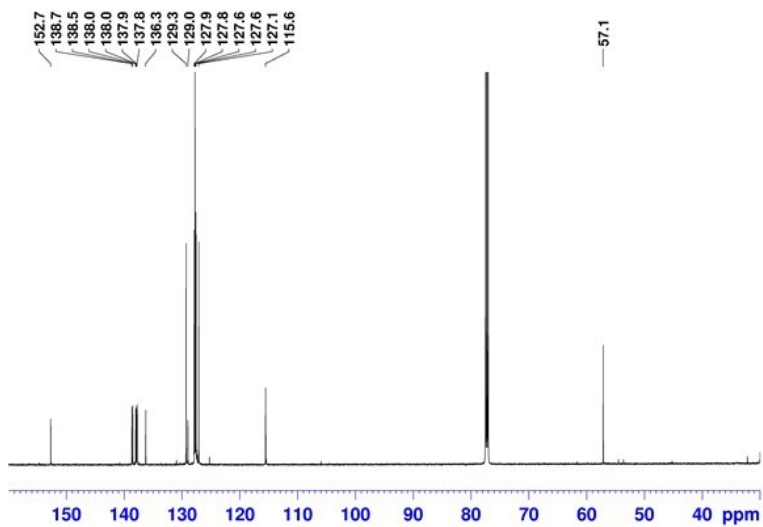


**Figure 126:**  $^{13}\text{C}$  NMR spectrum of **46** ( $\text{CDCl}_3$ , 150 MHz, 298 K).

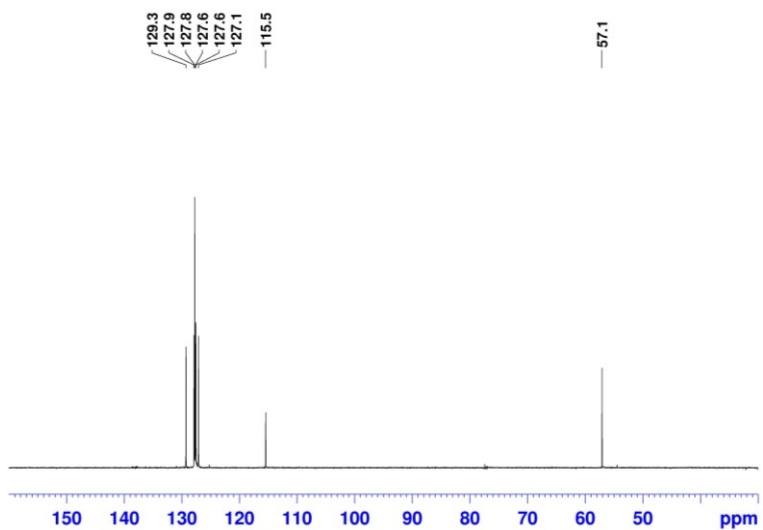


**Figure 127:** DEPT-135 spectrum of **46** ( $\text{CDCl}_3$ , 150 MHz, 298 K).

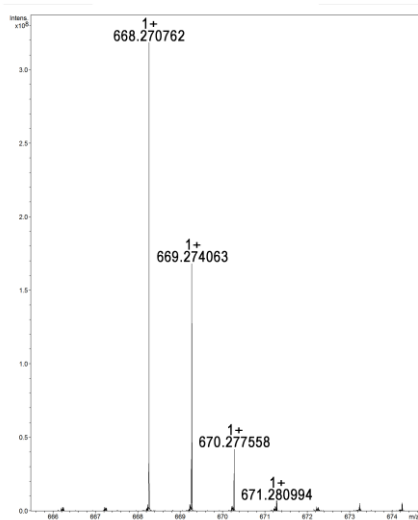


**Figure 128:** Significant portion of the HR MALDI FT-ICR mass spectrum of **46**  $[M+Ag]^+$  showing the isotopic envelop.

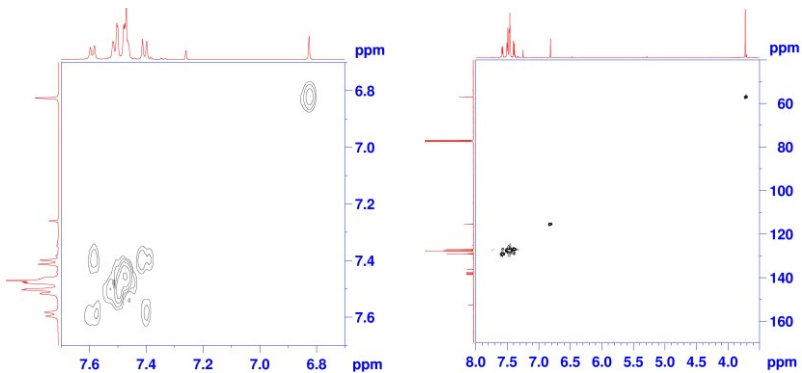


**Figure 129:** (left) Significant portion of the 2D COSY spectrum ( $CDCl_3$ , 150 MHz, 298 K) of derivative **46**; (right) 2D HSQC spectrum ( $CDCl_3$ , 150 MHz, 298 K) of derivative **46**.

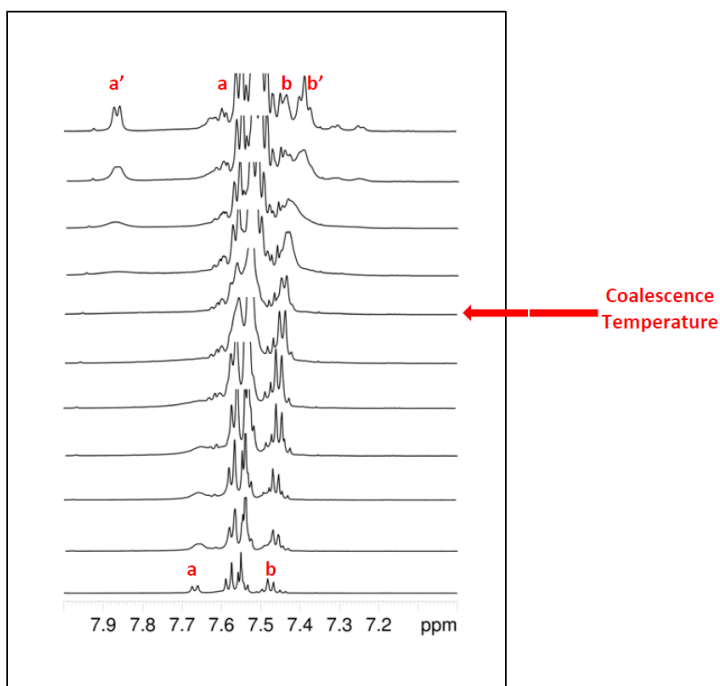


**Figure 130:** Relevant aromatic region of the  $^1\text{H}$  NMR spectrum of **46** (600 MHz,  $\text{CD}_2\text{Cl}_2$ ) at (from bottom to top): 298, 273, 263, 253, 243, 233, 223, 213, 203, 193, and 183 K.

### 4.5.6 Titration experiments

$^1\text{H}$  NMR titration were performed at 298 K in  $\text{CDCl}_3$ . The guest concentration was kept constant (1.0 mM) while the host concentration was varied. In all cases, the signals of the guest were followed, and the data were analyzed by a nonlinear curve fitting method for the determination of  $K$ . Thus, the observed chemical shifts were fitted with the calculated one using following equation:

$$\delta_{obs} = \delta_R + \frac{\Delta_0}{2[R^0]} \left\{ [R^0] + [S^0] + \frac{1}{K} - \sqrt{\left[ \left( [R^0] + [S^0] + \frac{1}{K} \right)^2 - 4[R^0][S^0] \right]} \right\}$$

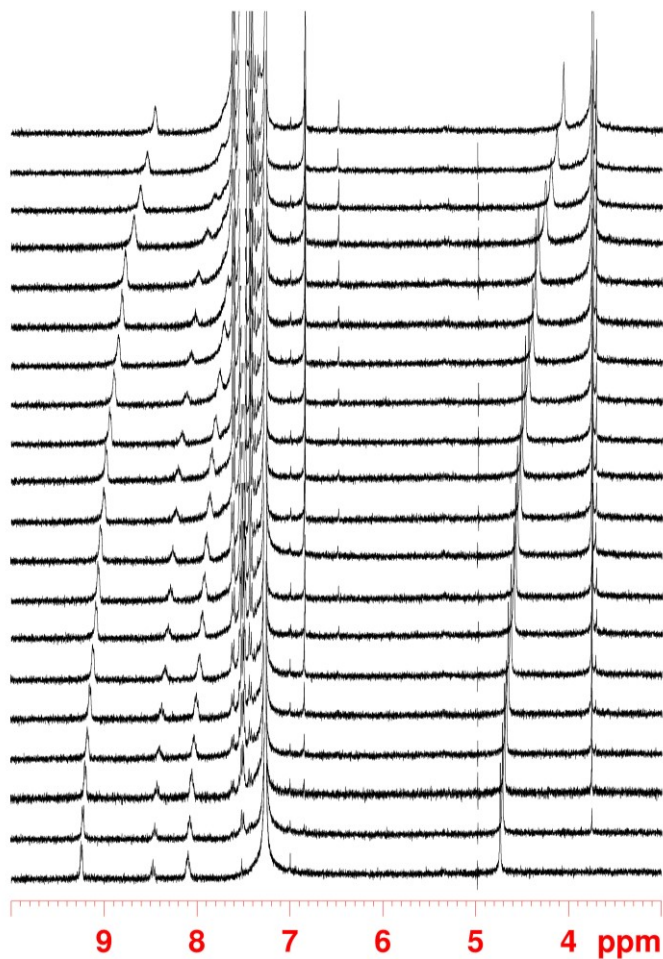


**Figure 131:** Titration of  $\text{NMP}^+$  with **46**. Region of the  $^1\text{H}$  NMR spectra ( $\text{CDCl}_3$ , 400 MHz, 298 K) of  $\text{NMP}^+$  after addition of (from bottom to top) 0.0, 0.1, 0.2, 0.3, 0.4, 0.5, 0.6, 0.7, 0.8, 0.9, 1.0, 1.2, 1.4, 1.6, 1.8, 2.0, 2.5, 3.0, 3.5 and 4.0 equiv of Host **46**.

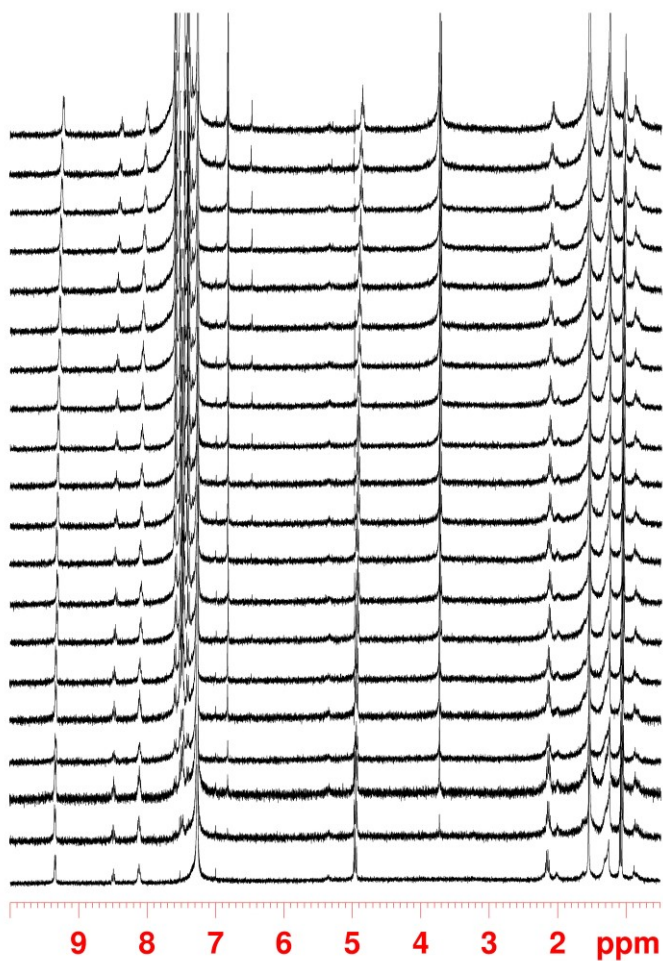


**Figure 132:** Titration of  $\text{NPP}^+$  with **46**. Region of the  $^1\text{H}$  NMR spectra ( $\text{CDCl}_3$ , 400 MHz, 298 K) of  $\text{NMP}^+$  after addition of (from bottom to top) 0.0, 0.1, 0.2, 0.3, 0.4, 0.5, 0.6, 0.7, 0.8, 0.9, 1.0, 1.2, 1.4, 1.6, 1.8, 2.0, 2.5, 3.0, 3.5 and 4.0 equiv of Host **46**.

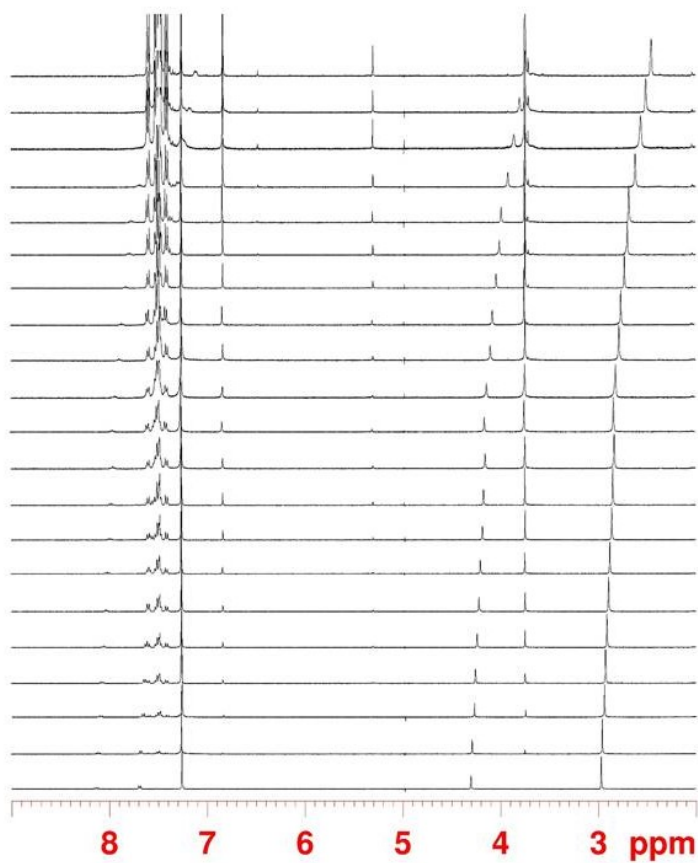


**Figure 133:** Titration of  $\text{NML}^+$  with **46**. Region of the  $^1\text{H}$  NMR spectra ( $\text{CDCl}_3$ , 400 MHz, 298 K) of  $\text{NMP}^+$  after addition of (from bottom to top) 0.0, 0.1, 0.2, 0.3, 0.4, 0.5, 0.6, 0.7, 0.8, 0.9, 1.0, 1.2, 1.4, 1.6, 1.8, 2.0, 2.5, 3.0, 3.5 and 4.0 equiv of Host **46**.

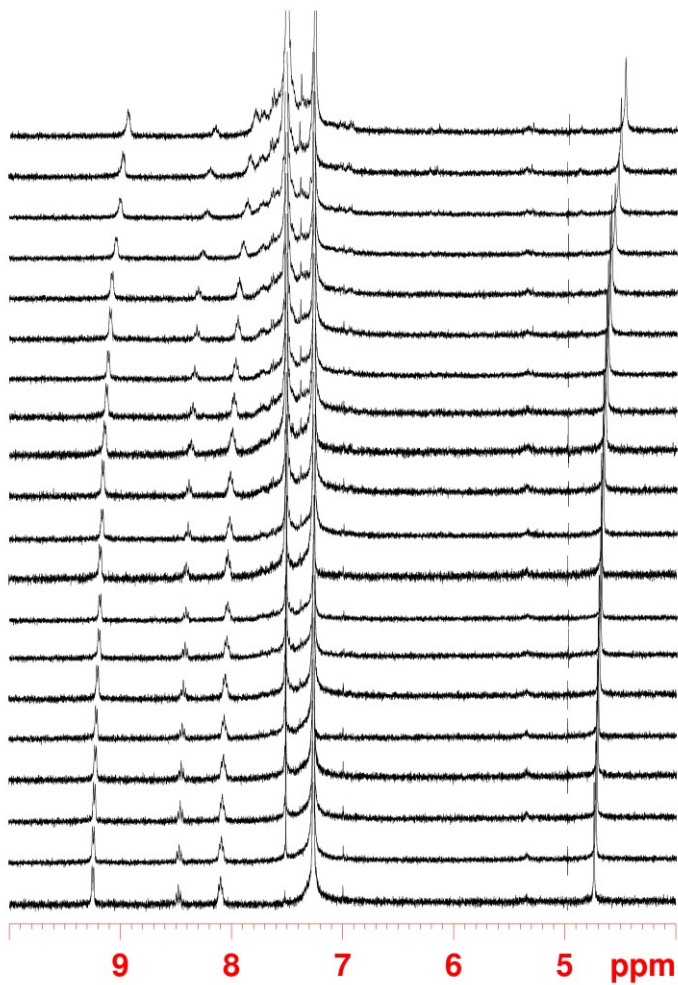


**Figure 134:** Titration of  $\text{NMP}^+$  with  $[\mathbf{8}]\text{CPP}$ . Region of the  $^1\text{H}$  NMR spectra ( $\text{CDCl}_3$ , 400 MHz, 298 K) of  $\text{NMP}^+$  after addition of (from bottom to top) 0.0, 0.1, 0.2, 0.3, 0.4, 0.5, 0.6, 0.7, 0.8, 0.9, 1.0, 1.2, 1.4, 1.6, 1.8, 2.0, 2.5, 3.0, 3.5 and 4.0 equiv of Host  $[\mathbf{8}]\text{CPP}$ .

## 4.5.7 DFT calculation

Preliminary conformational searches have been performed by molecular mechanics calculations (Spartan 02). The minimized structures were optimized by DFT calculations (Gaussian 09) at B3LYP/6-31G(d,p) level of theory using Grimme's dispersion corrections (IOp(3/124 = 3)).<sup>157,158</sup>

### Atomic coordinates of 46

1 C1	-2.2925	-5.2360	-0.1306 C	20 C20	-6.3133	1.1171	-1.1117 C
2 C2	-1.5724	-5.6851	-1.2548 C	21 C21	-6.4079	-0.2715	-1.1467 C
3 C3	-0.1827	-5.7640	-1.2346 C	22 C22	-5.9985	-1.0565	-0.0514 C
4 C4	0.5501	-5.4013	-0.0881 C	23 C23	-5.7221	-0.3746	1.1472 C
5 C5	-0.1846	-5.1866	1.0916 C	24 C24	-5.6272	1.0117	1.1819 C
6 C6	-1.5722	-5.1039	1.0702 C	25 C25	-2.9900	4.9788	-0.0106 C
7 C7	-5.5171	-2.4552	-0.1979 C	26 C26	-3.3835	4.3498	-1.2053 C
8 C8	-4.8440	-2.8101	-1.3807 C	27 C27	-4.4331	3.4391	-1.2287 C
9 C9	-3.9203	-3.8482	-1.4003 C	28 C28	-5.1415	3.1119	-0.0587 C
10 C10	-3.6244	-4.5842	-0.2389 C	29 C29	-4.8978	3.9131	1.0738 C
11 C11	-4.4685	-4.3811	0.8703 C	30 C30	-3.8468	4.8260	1.0969 C
12 C12	-5.3928	-3.3399	0.8908 C	31 C31	4.9950	1.1223	0.1097 C
13 C13	4.0940	-3.0324	0.0133 C	32 C32	4.6101	-0.9605	1.3604 C
14 C14	3.8569	-3.9610	1.0470 C	33 C33	4.7898	-1.7273	0.1847 C
15 C15	2.8066	-4.8740	0.9651 C	34 C34	5.4639	0.3384	-0.9712 C
16 C16	1.9506	-4.9079	-0.1504 C	35 C35	2.5940	4.6306	0.0126 C
17 C17	2.3339	-4.1416	-1.2655 C	36 C36	3.4242	4.3904	1.1234 C
18 C18	3.3752	-3.2271	-1.1835 C	37 C37	4.3639	3.3624	1.1083 C
19 C19	-5.8050	1.7839	0.0200 C	38 C38	3.8596	2.9282	-1.1938 C

<sup>157</sup> Gaussian 09, Revision A.1, Frisch, M. J.; Trucks, G. W.; Schlegel, H. B.; Scuseria, G. E.; Robb, M. A.; Cheeseman, J. R.; Scalmani, G.; Barone, V.; Mennucci, B.; Petersson, G. A.; Nakatsuji, H.; Caricato, M.; Li, X.; Hratchian, H. P.; Izmaylov, A. F.; Bloino, J.; Zheng, G.; Sonnenberg, J. L.; Hada, M.; Ehara, M.; Toyota, K.; Fukuda, R.; Hasegawa, J.; Ishida, M.; Nakajima, T.; Honda, Y.; Kitao, O.; Nakai, H.; Vreven, T.; Montgomery, Jr., J. A.; Peralta, J. E.; Ogliaro, F.; Bearpark, M.; Heyd, J. J.; Brothers, E.; Kudin, K. N.; Staroverov, V. N.; Kobayashi, R.; Normand, J.; Raghavachari, K.; Rendell, A.; Burant, J. C.; Iyengar, S. S.; Tomasi, J.; Cossi, M.; Rega, N.; Millam, J. M.; Klene, M.; Knox, J. E.; Cross, J. B.; Bakken, V.; Adamo, C.; Jaramillo, J.; Gomperts, R.; Stratmann, R. E.; Yazyev, O.; Austin, A. J.; Cammi, R.; Pomelli, C.; Ochterski, J. W.; Martin, R. L.; Morokuma, K.; Zakrzewski, V. G.; Voth, G. A.; Salvador, P.; Dannenberg, J. J.; Dapprich, S.; Daniels, A. D.; Farkas, Ö.; Foresman, J. B.; Ortiz, J. V.; Cioslowski, J.; Fox, D. J. Gaussian, Inc., Wallingford CT, 2009.

<sup>158</sup> Grimme, S. *J. Comput. Chem.*, **2006**, *27*, 1787–1799.

39 C39	2.9177	3.9494	-1.1750 C	13 7 8 Ar
40 C40	1.2575	5.2701	0.1259 C	14 7 12 Ar
41 C41	0.5088	5.0626	1.2983 C	15 7 22 1
42 C42	-0.8783	5.1499	1.2931 C	16 8 9 Ar
43 C43	-1.5860	5.4505	0.1154 C	17 8 55 1
44 C44	-0.8246	5.8828	-0.9877 C	18 9 10 Ar
45 C45	0.5649	5.7945	-0.9826 C	19 9 56 1
46 O46	4.2360	-1.6231	2.4972 O	20 10 11 Ar
47 O47	5.9573	1.0173	-2.0557 O	21 11 12 Ar
48 C48	6.4233	0.2704	-3.1672 C	22 11 57 1
49 C49	3.8424	-0.8725	3.6343 C	23 12 58 1
50 C50	4.5147	2.5255	-0.0148 C	24 13 14 Ar
51 H51	-2.0981	-5.8967	-2.1817 H	25 13 18 Ar
52 H52	0.3441	-6.0318	-2.1463 H	26 13 33 1
53 H53	0.3390	-4.9229	2.0051 H	27 14 15 Ar
54 H54	-2.0851	-4.7770	1.9690 H	28 14 76 1
55 H55	-4.9216	-2.1695	-2.2532 H	29 15 16 Ar
56 H56	-3.3105	-3.9806	-2.2880 H	30 15 77 1
57 H57	-4.3455	-4.9926	1.7597 H	31 16 17 Ar
58 H58	-5.9674	-3.1634	1.7958 H	32 17 18 Ar
59 H59	-6.5602	1.6843	-2.0048 H	33 17 78 1
60 H60	-6.7255	-0.7547	-2.0664 H	34 18 75 1
61 H61	-5.4202	-0.9368	2.0251 H	35 19 20 Ar
62 H62	-5.2546	1.4829	2.0856 H	36 19 24 Ar
63 H63	-2.7658	4.4506	-2.0918 H	37 19 28 1
64 H64	-4.5974	2.8618	-2.1328 H	38 20 21 Ar
65 H65	-5.4858	3.7645	1.9752 H	39 20 59 1
66 H66	-3.6404	5.3681	2.0155 H	40 21 22 Ar
67 H67	3.2832	4.9621	2.0365 H	41 21 60 1
68 H68	4.9319	3.1562	2.0113 H	42 22 23 Ar
69 H69	3.9945	2.3521	-2.1006 H	43 23 24 Ar
70 H70	2.3232	4.1194	-2.0671 H	44 23 61 1
71 H71	1.0008	4.6764	2.1852 H	45 24 62 1
72 H72	-1.4210	4.8279	2.1761 H	46 25 26 Ar
73 H73	-1.3273	6.2178	-1.8906 H	47 25 30 Ar
74 H74	1.1130	6.0625	-1.8815 H	48 25 43 1
75 H75	3.5291	-2.5482	-2.0155 H	49 26 27 Ar
76 H76	4.4421	-3.9121	1.9558 H	50 26 63 1
77 H77	2.6022	-5.5152	1.8183 H	51 27 28 Ar
78 H78	1.7134	-4.1442	-2.1560 H	52 27 64 1
79 H79	6.8199	1.0007	-3.8741 H	53 28 29 Ar
80 H80	7.2214	-0.4254	-2.8792 H	54 29 30 Ar
81 H81	5.6149	-0.2946	-3.6500 H	55 29 65 1
82 H82	4.6563	-0.2342	4.0012 H	56 30 66 1
83 H83	2.9627	-0.2500	3.4274 H	57 31 34 Ar
84 H84	3.5898	-1.6055	4.4020 H	58 31 50 1
85 C85	4.6726	0.4323	1.2884 C	59 31 85 Ar
86 C86	5.3277	-1.0499	-0.9277 C	60 32 33 Ar
87 H87	4.3157	1.0132	2.1280 H	61 32 46 1
88 H88	5.5589	-1.6347	-1.8095 H	62 32 85 Ar
@<TRIPOS>BOND				63 33 86 Ar
1 1 2 Ar				64 34 47 1
2 1 6 Ar				65 34 86 Ar
3 1 10 1				66 35 36 Ar
4 2 3 Ar				67 35 39 Ar
5 2 51 1				68 35 40 1
6 3 4 Ar				69 36 37 Ar
7 3 52 1				70 36 67 1
8 4 5 Ar				71 37 50 Ar
9 4 16 1				72 37 68 1
10 5 6 Ar				73 38 39 Ar
11 5 53 1				74 38 50 Ar
12 6 54 1				75 38 69 1

76 39 70 1  
 77 40 41 Ar  
 78 40 45 Ar  
 79 41 42 Ar  
 80 41 71 1  
 81 42 43 Ar  
 82 42 72 1  
 83 43 44 Ar  
 84 44 45 Ar  
 85 44 73 1  
 86 45 74 1  
 87 46 49 1  
 88 47 48 1  
 89 48 79 1  
 90 48 80 1  
 91 48 81 1  
 92 49 82 1  
 93 49 83 1  
 94 49 84 1  
 95 85 87 1  
 96 86 88 1

37 C37 -4.2572 -3.6203 0.8717 C  
 38 C38 -4.3905 -2.7771 -0.2524 C  
 39 C39 -3.5759 -3.0891 -1.3623 C  
 40 C40 -2.5386 -4.0100 -1.2594 C  
 41 C41 -0.8995 -5.2200 0.1651 C  
 42 C42 -0.2445 -4.9261 1.3747 C  
 43 C43 1.1429 -4.9343 1.4626 C  
 44 C44 1.9504 -5.2424 0.3492 C  
 45 C45 1.2831 -5.7618 -0.7797 C  
 46 C46 -0.1056 -5.7435 -0.8733 C  
 47 O47 -5.4709 1.1179 2.4952 O  
 48 O48 -5.3963 -1.1863 -2.5130 O  
 49 C49 -5.7477 -0.3745 -3.6286 C  
 50 C50 -5.7841 0.2902 3.6109 C  
 51 H51 1.6288 4.6324 -2.1947 H  
 52 H52 -0.8046 4.5851 -2.1177 H  
 53 H53 -0.7076 6.0061 1.9392 H  
 54 H54 1.7348 6.0702 1.8573 H  
 55 H55 5.6511 3.4304 -2.1414 H  
 56 H56 3.8589 5.0884 -2.1313 H  
 57 H57 3.1844 4.3236 2.0465 H  
 58 H58 4.9635 2.6720 2.0361 H  
 59 H59 5.3997 -1.2063 -2.2017 H  
 60 H60 5.3927 1.2046 -2.2423 H  
 61 H61 6.7582 1.2923 1.8347 H  
 62 H62 6.7734 -1.1409 1.8780 H  
 63 H63 3.5686 -4.9051 -1.8636 H  
 64 H64 5.3570 -3.2966 -2.0686 H  
 65 H65 5.3407 -2.7376 2.1971 H  
 66 H66 3.6491 -4.4468 2.4154 H  
 67 H67 -3.1131 -5.1183 1.8877 H  
 68 H68 -4.9353 -3.5156 1.7127 H  
 69 H69 -3.7001 -2.5398 -2.2858 H  
 70 H70 -1.8646 -4.1303 -2.1027 H  
 71 H71 -0.8195 -4.5614 2.2206 H  
 72 H72 1.5945 -4.5765 2.3810 H  
 73 H73 1.8521 -6.1208 -1.6311 H  
 74 H74 -0.5761 -6.0819 -1.7918 H  
 75 H75 -4.9121 3.4401 -1.7476 H  
 76 H76 -3.8463 2.5310 2.3158 H  
 77 H77 -2.0160 4.1210 2.1885 H  
 78 H78 -3.0949 5.0498 -1.8658 H  
 79 H79 -5.9536 -1.0661 -4.4458 H  
 80 H80 -6.6428 0.2216 -3.4186 H  
 81 H81 -4.9282 0.2937 -3.9235 H  
 82 H82 -6.6514 -0.3457 3.4012 H  
 83 H83 -4.9342 -0.3392 3.9041 H  
 84 H84 -6.0212 0.9719 4.4280 H  
 85 C85 -5.2123 -0.8418 1.0927 C  
 86 C86 -5.2218 0.7824 -1.1074 C  
 87 H87 -5.1232 -1.4606 1.9753 H  
 88 H88 -5.1496 1.4040 -1.9898 H  
 89 C89 0.1949 -1.1292 -0.1121 C  
 90 N90 -0.3226 0.1136 -0.2648 N  
 91 C91 0.4606 1.2151 -0.1523 C  
 92 C92 1.8117 1.0927 0.1174 C  
 93 C93 2.3653 -0.1807 0.2742 C  
 94 C94 1.5423 -1.3023 0.1594 C  
 95 C95 -1.7712 0.2866 -0.5325 C  
 96 H96 -0.4960 -1.9584 -0.2153 H  
 97 H97 -0.0279 2.1742 -0.2873 H  
 98 H98 2.4175 1.9875 0.2048 H  
 99 H99 3.4242 -0.2962 0.4789 H

### Atomic coordinates of NMP<sup>+</sup> ⊂ 46 complex

1 C1 1.8921 5.2605 -0.1432 C  
 2 C2 1.1302 4.9645 -1.2897 C  
 3 C3 -0.2604 4.9328 -1.2444 C  
 4 C4 -0.9568 5.1910 -0.0485 C  
 5 C5 -0.2028 5.6957 1.0292 C  
 6 C6 1.1881 5.7318 0.9821 C  
 7 C7 5.3802 2.8242 -0.0804 C  
 8 C8 5.1098 3.6120 -1.2178 C  
 9 C9 4.0880 4.5569 -1.2124 C  
 10 C10 3.2909 4.7614 -0.0684 C  
 11 C11 3.7344 4.1605 1.1251 C  
 12 C12 4.7551 3.2140 1.1191 C  
 13 C13 -4.4534 2.7335 0.2532 C  
 14 C14 -3.6912 3.0702 1.3919 C  
 15 C15 -2.6542 3.9930 1.3194 C  
 16 C16 -2.3282 4.6451 0.1174 C  
 17 C17 -3.2338 4.4840 -0.9491 C  
 18 C18 -4.2725 3.5591 -0.8787 C  
 19 C19 5.9735 -1.3950 -0.1217 C  
 20 C20 5.7294 -0.6818 -1.3120 C  
 21 C21 5.7269 0.7072 -1.3379 C  
 22 C22 5.9665 1.4610 -0.1741 C  
 23 C23 6.4497 0.7524 0.9443 C  
 24 C24 6.4561 -0.6403 0.9685 C  
 25 C25 3.3468 -4.7270 0.2854 C  
 26 C26 3.9582 -4.4572 -0.9559 C  
 27 C27 4.9730 -3.5146 -1.0775 C  
 28 C28 5.4098 -2.7637 0.0315 C  
 29 C29 4.9803 -3.2192 1.2941 C  
 30 C30 3.9883 -4.1863 1.4184 C  
 31 C31 -5.0659 -1.4520 -0.1669 C  
 32 C32 -5.3113 0.5402 1.2685 C  
 33 C33 -5.1070 1.3971 0.1553 C  
 34 C34 -5.2758 -0.6018 -1.2838 C  
 35 C35 -2.2655 -4.6809 -0.0534 C  
 36 C36 -3.2179 -4.5409 0.9736 C

100 H100	1.9324	-2.3069	0.2744 H
101 H101	-1.9004	1.0157	-1.3318 H
102 H102	-2.1969	-0.6705	-0.8275 H
103 H103	-2.2675	0.6506	0.3681 H

@<TRIPOS>BOND

1 1 2 Ar  
2 1 6 Ar  
3 1 10 1  
4 2 3 Ar  
5 2 51 1  
6 3 4 Ar  
7 3 52 1  
8 4 5 Ar  
9 4 16 1  
10 5 6 Ar  
11 5 53 1  
12 6 54 1  
13 7 8 Ar  
14 7 12 Ar  
15 7 22 1  
16 8 9 Ar  
17 8 55 1  
18 9 10 Ar  
19 9 56 1  
20 10 11 Ar  
21 11 12 Ar  
22 11 57 1  
23 12 58 1  
24 13 14 Ar  
25 13 18 Ar  
26 13 33 1  
27 14 15 Ar  
28 14 76 1  
29 15 16 Ar  
30 15 77 1  
31 16 17 Ar  
32 17 18 Ar  
33 17 78 1  
34 18 75 1  
35 19 20 Ar  
36 19 24 Ar  
37 19 28 1  
38 20 21 Ar  
39 20 59 1  
40 21 22 Ar  
41 21 60 1  
42 22 23 Ar  
43 23 24 Ar  
44 23 61 1  
45 24 62 1  
46 25 26 Ar  
47 25 30 Ar  
48 25 44 1  
49 26 27 Ar  
50 26 63 1  
51 27 28 Ar  
52 27 64 1  
53 28 29 Ar  
54 29 30 Ar  
55 29 65 1  
56 30 66 1  
57 31 34 Ar  
58 31 38 1

59 31 85 Ar  
60 32 33 Ar  
61 32 47 1  
62 32 85 Ar  
63 33 86 Ar  
64 34 48 1  
65 34 86 Ar  
66 35 36 Ar  
67 35 40 Ar  
68 35 41 1  
69 36 37 Ar  
70 36 67 1  
71 37 38 Ar  
72 37 68 1  
73 38 39 Ar  
74 39 40 Ar  
75 39 69 1  
76 40 70 1  
77 41 42 Ar  
78 41 46 Ar  
79 42 43 Ar  
80 42 71 1  
81 43 44 Ar  
82 43 72 1  
83 44 45 Ar  
84 45 46 Ar  
85 45 73 1  
86 46 74 1  
87 47 50 1  
88 48 49 1  
89 49 79 1  
90 49 80 1  
91 49 81 1  
92 50 82 1  
93 50 83 1  
94 50 84 1  
95 85 87 1  
96 86 88 1  
97 89 90 Ar  
98 89 94 2  
99 89 96 1  
100 90 91 Ar  
101 90 95 1  
102 91 92 2  
103 91 97 1  
104 92 93 Ar  
105 92 98 1  
106 93 94 Ar  
107 93 99 1  
108 94 100 1  
109 95 101 1  
110 95 102 1  
111 95 103 1

### Atomic coordinates of NPP<sup>+</sup>C 46 complex

1 C1	1.4762	5.3124	-0.1926 C
2 C2	0.6695	4.9423	-1.2880 C

3 C3	-0.7138	4.8433	-1.1715 C	66 H66	4.5379	-4.8447	2.0798 H
4 C4	-1.3638	5.1004	0.0506 C	67 H67	-2.4083	-5.4211	1.9982 H
5 C5	-0.5854	5.6918	1.0637 C	68 H68	-4.3540	-3.9556	2.0071 H
6 C6	0.7968	5.8012	0.9419 C	69 H69	-3.4729	-2.7493	-2.0209 H
7 C7	5.1675	3.1607	0.0528 C	70 H70	-1.5116	-4.1980	-2.0219 H
8 C8	4.6708	3.5797	-1.1977 C	71 H71	-0.1570	-4.7835	2.2211 H
9 C9	3.5827	4.4401	-1.2986 C	72 H72	2.2724	-4.6394	2.2361 H
10 C10	2.9074	4.9051	-0.1528 C	73 H73	2.3761	-5.8638	-1.8857 H
11 C11	3.5525	4.6759	1.0797 C	74 H74	-0.0651	-6.0028	-1.9005 H
12 C12	4.6613	3.8418	1.1780 C	75 H75	-5.2626	2.9953	-1.3489 H
13 C13	-4.5993	2.3631	0.6217 C	76 H76	-3.8344	2.2573	2.6374 H
14 C14	-3.8009	2.7950	1.7011 C	77 H77	-2.1812	4.0089	2.3663 H
15 C15	-2.8641	3.8094	1.5463 C	78 H78	-3.6131	4.7604	-1.6144 H
16 C16	-2.6775	4.4616	0.3156 C	79 H79	-6.4560	-1.7237	-3.7939 H
17 C17	-3.6359	4.2004	-0.6836 C	80 H80	-7.1823	-0.6915	-2.5276 H
18 C18	-4.5781	3.1860	-0.5284 C	81 H81	-5.8013	-0.0975	-3.4941 H
19 C19	6.2193	-0.9656	0.1828 C	82 H82	-6.0712	-0.9662	3.9465 H
20 C20	6.5993	-0.1900	-0.9300 C	83 H83	-4.3225	-0.7477	4.2568 H
21 C21	6.4443	1.1935	-0.9304 C	84 H84	-5.4975	0.4173	4.9185 H
22 C22	5.8960	1.8692	0.1789 C	85 C85	-4.8573	-1.2748	1.4878 C
23 C23	5.7733	1.1193	1.3651 C	86 C86	-5.3029	0.3408	-0.6697 C
24 C24	5.9341	-0.2617	1.3685 C	87 H87	-4.6028	-1.8836	2.3452 H
25 C25	3.8650	-4.4987	0.0510 C	88 H88	-5.4078	0.9614	-1.5500 H
26 C26	4.1993	-3.8109	-1.1301 C	89 C89	0.1312	-1.0188	-0.2583 C
27 C27	5.1258	-2.7746	-1.1224 C	90 N90	-0.2378	0.2602	-0.5109 N
28 C28	5.7626	-2.3756	0.0671 C	91 C91	0.5951	1.2940	-0.2405 C
29 C29	5.6088	-3.2228	1.1832 C	92 C92	1.8547	1.0644	0.2865 C
30 C30	4.6804	-4.2603	1.1755 C	93 C93	2.2592	-0.2486	0.5375 C
31 C31	-4.7846	-1.8618	0.2106 C	94 C94	1.3803	-1.3001	0.2687 C
32 C32	-5.0947	0.0851	1.6938 C	95 C95	-1.5396	0.5296	-1.1886 C
33 C33	-5.1158	0.9649	0.5779 C	96 H96	-0.5969	-1.7882	-0.4935 H
34 C34	-5.2040	-1.0379	-0.8625 C	97 H97	0.2249	2.2883	-0.4678 H
35 C35	-1.7305	-4.8518	0.0252 C	98 H98	2.5048	1.9083	0.4883 H
36 C36	-2.6177	-4.8217	1.1169 C	99 H99	3.2514	-0.4445	0.9307 H
37 C37	-3.7280	-3.9810	1.1205 C	100 H100	1.6508	-2.3327	0.4586 H
38 C38	-4.0027	-3.1167	0.0404 C	101 H101	-2.2248	-0.2719	-0.9067 H
39 C39	-3.2417	-3.3189	-1.1302 C	102 H102	-1.9336	1.4641	-0.7837 H
40 C40	-2.1334	-4.1593	-1.1321 C	103 C103	-1.3524	0.6023	-2.7090 C
41 C41	-0.3196	-5.3037	0.1307 C	104 H104	-0.6472	1.4086	-2.9444 H
42 C42	0.3872	-5.0508	1.3205 C	105 H105	-0.8934	-0.3305	-3.0580 H
43 C43	1.7764	-4.9683	1.3282 C	106 C106	-2.6804	0.8355	-3.4343 C
44 C44	2.5246	-5.1359	0.1470 C	107 H107	-2.5155	0.9070	-4.5124 H
45 C45	1.8294	-5.6156	-0.9808 C	108 H108	-3.3769	0.0119	-3.2523 H
46 C46	0.4398	-5.6947	-0.9896 C	109 H109	-3.1537	1.7647	-3.1022 H
47 O47	-5.1880	0.6342	2.9396 O	@<TRIPOS>BOND			
48 O48	-5.3571	-1.6093	-2.1018 O	1 1 2 Ar			
49 C49	-6.2493	-0.9807	-3.0225 C	2 1 6 Ar			
50 C50	-5.2707	-0.2280	4.0695 C	3 1 10 1			
51 H51	1.1283	4.6156	-2.2150 H	4 2 3 Ar			
52 H52	-1.2827	4.4467	-2.0076 H	5 2 51 1			
53 H53	-1.0584	6.0088	1.9884 H	6 3 4 Ar			
54 H54	1.3571	6.2091	1.7769 H	7 3 52 1			
55 H55	5.0655	3.1461	-2.1104 H	8 4 5 Ar			
56 H56	3.2049	4.6751	-2.2883 H	9 4 16 1			
57 H57	3.1287	5.0697	1.9972 H	10 5 6 Ar			
58 H58	5.0775	3.6535	2.1623 H	11 5 53 1			
59 H59	6.9436	-0.6788	-1.8365 H	12 6 54 1			
60 H60	6.6793	1.7405	-1.8381 H	13 7 8 Ar			
61 H61	5.4173	1.5922	2.2739 H	14 7 12 Ar			
62 H62	5.6967	-0.8089	2.2757 H	15 7 22 1			
63 H63	3.6267	-3.9861	-2.0351 H	16 8 9 Ar			
64 H64	5.2404	-2.1761	-2.0202 H	17 8 55 1			
65 H65	6.1662	-3.0234	2.0938 H	18 9 10 Ar			

19 9 56 1  
20 10 11 Ar  
21 11 12 Ar  
22 11 57 1  
23 12 58 1  
24 13 14 Ar  
25 13 18 Ar  
26 13 33 1  
27 14 15 Ar  
28 14 76 1  
29 15 16 Ar  
30 15 77 1  
31 16 17 Ar  
32 17 18 Ar  
33 17 78 1  
34 18 75 1  
35 19 20 Ar  
36 19 24 Ar  
37 19 28 1  
38 20 21 Ar  
39 20 59 1  
40 21 22 Ar  
41 21 60 1  
42 22 23 Ar  
43 23 24 Ar  
44 23 61 1  
45 24 62 1  
46 25 26 Ar  
47 25 30 Ar  
48 25 44 1  
49 26 27 Ar  
50 26 63 1  
51 27 28 Ar  
52 27 64 1  
53 28 29 Ar  
54 29 30 Ar  
55 29 65 1  
56 30 66 1  
57 31 34 Ar  
58 31 38 1  
59 31 85 Ar  
60 32 33 Ar  
61 32 47 1  
62 32 85 Ar  
63 33 86 Ar  
64 34 48 1  
65 34 86 Ar  
66 35 36 Ar  
67 35 40 Ar  
68 35 41 1  
69 36 37 Ar  
70 36 67 1  
71 37 38 Ar  
72 37 68 1  
73 38 39 Ar  
74 39 40 Ar  
75 39 69 1  
76 40 70 1  
77 41 42 Ar  
78 41 46 Ar  
79 42 43 Ar  
80 42 71 1  
81 43 44 Ar

82 43 72 1  
83 44 45 Ar  
84 45 46 Ar  
85 45 73 1  
86 46 74 1  
87 47 50 1  
88 48 49 1  
89 49 79 1  
90 49 80 1  
91 49 81 1  
92 50 82 1  
93 50 83 1  
94 50 84 1  
95 85 87 1  
96 86 88 1  
97 89 90 Ar  
98 89 94 2  
99 89 96 1  
100 90 91 Ar  
101 90 95 1  
102 91 92 2  
103 91 97 1  
104 92 93 Ar  
105 92 98 1  
106 93 94 Ar  
107 93 99 1  
108 94 100 1  
109 95 101 1  
110 95 102 1  
111 95 103 1  
112 103 104 1  
113 103 105 1  
114 103 106 1  
115 106 107 1  
116 106 108 1  
117 106 109 1

### Atomic coordinates of NML<sup>+</sup>⊂ 46 complex

1 C1	-2.5085	5.0909	0.1640	C
2 C2	-1.6844	5.2046	1.3028	C
3 C3	-0.2994	5.2926	1.1905	C
4 C4	0.3385	5.2973	-0.0660	C
5 C5	-0.5020	5.4545	-1.1843	C
6 C6	-1.8830	5.3419	-1.0735	C
7 C7	-5.7269	2.2891	0.0422	C
8 C8	-5.1487	2.6565	1.2730	C
9 C9	-4.2342	3.7017	1.3582	C
10 C10	-3.8449	4.4343	0.2190	C
11 C11	-4.6342	4.2399	-0.9341	C
12 C12	-5.5478	3.1943	-1.0224	C
13 C13	4.0532	3.1485	-0.2392	C
14 C14	3.2461	3.3122	-1.3827	C
15 C15	2.1221	4.1273	-1.3583	C
16 C16	1.7493	4.8478	-0.2063	C
17 C17	2.6799	4.8545	0.8519	C
18 C18	3.7999	4.0220	0.8375	C
19 C19	-5.7257	-1.9525	-0.3336	C
20 C20	-6.3133	-1.3594	0.8042	C

21 C21	-6.5108	0.0165	0.8874 C	84 H84	6.4399	1.9666	-4.1709 H
22 C22	-6.1359	0.8738	-0.1670 C	85 C85	5.5330	-0.2179	-1.0775 C
23 C23	-5.8001	0.2514	-1.3850 C	86 C86	4.7948	1.2222	1.1370 C
24 C24	-5.6028	-1.1225	-1.4658 C	87 H87	5.8222	-0.7817	-1.9553 H
25 C25	-2.7103	-4.9782	-0.0380 C	88 H88	4.4290	1.7676	1.9976 H
26 C26	-3.4908	-4.6340	1.0826 C	89 C89	-0.6611	-0.9946	-0.5760 C
27 C27	-4.5800	-3.7771	0.9716 C	90 N90	0.2252	-0.2107	0.1177 N
28 C28	-4.9745	-3.2380	-0.2691 C	91 C91	-0.1884	0.8497	0.8851 C
29 C29	-4.3594	-3.8007	-1.4069 C	92 C92	-1.5436	1.1389	0.9620 C
30 C30	-3.2497	-4.6344	-1.2938 C	93 C93	-2.4692	0.3529	0.2855 C
31 C31	5.2289	-0.9359	0.0995 C	94 C94	-2.0189	-0.7157	-0.4796 C
32 C32	5.3817	1.1654	-1.1843 C	95 C95	1.6796	-0.4891	0.0558 C
33 C33	4.8450	1.8955	-0.0926 C	96 H96	-1.8628	1.9924	1.5464 H
34 C34	5.0227	-0.1518	1.2634 C	97 H97	-3.5277	0.5750	0.3474 H
35 C35	2.9077	-4.5224	0.0029 C	98 H98	-2.7183	-1.3486	-1.0110 H
36 C36	3.2451	-3.8425	-1.1830 C	99 H99	2.1981	0.3703	-0.3709 H
37 C37	4.1481	-2.7851	-1.1716 C	100 H100	2.0604	-0.6749	1.0600 H
38 C38	4.7719	-2.3537	0.0210 C	101 H101	1.8748	-1.3655	-0.5492 H
39 C39	4.6370	-3.2147	1.1319 C	102 C102	0.8284	1.6669	1.6206 C
40 C40	3.7197	-4.2643	1.1223 C	103 H103	1.3742	1.0628	2.3536 H
41 C41	1.5700	-5.1646	0.1091 C	104 H104	1.5640	2.1146	0.9461 H
42 C42	0.8845	-5.7309	-0.9844 C	105 H105	0.3242	2.4768	2.1461 H
43 C43	-0.5057	-5.8407	-0.9882 C	106 C106	-0.1727	-2.1304	-1.4243 C
44 C44	-1.2824	-5.3777	0.0943 C	107 H107	0.3558	-2.8842	-0.8346 H
45 C45	-0.5766	-5.0152	1.2579 C	108 H108	-1.0298	-2.6182	-1.8872 H
46 C46	0.8090	-4.9155	1.2670 C	109 H109	0.4969	-1.7848	-2.2185 H
47 O47	5.6355	1.8681	-2.3263 O	@<TRIPOS>BOND			
48 O48	4.8816	-0.8010	2.4597 O	1 1 2 Ar			
49 C49	4.8080	-0.0355	3.6558 C	2 1 6 Ar			
50 C50	6.2440	1.1971	-3.4240 C	3 1 10 1			
51 H51	-2.1133	5.1403	2.2975 H	4 2 3 Ar			
52 H52	0.2952	5.2590	2.0985 H	5 2 51 1			
53 H53	-0.0714	5.5827	-2.1722 H	6 3 4 Ar			
54 H54	-2.4665	5.3502	-1.9874 H	7 3 52 1			
55 H55	-5.3065	2.0356	2.1495 H	8 4 5 Ar			
56 H56	-3.7338	3.8599	2.3077 H	9 4 16 1			
57 H57	-4.4789	4.8578	-1.8121 H	10 5 6 Ar			
58 H58	-6.0663	3.0326	-1.9627 H	11 5 53 1			
59 H59	-6.5501	-1.9654	1.6727 H	12 6 54 1			
60 H60	-6.8889	0.4344	1.8159 H	13 7 8 Ar			
61 H61	-5.5498	0.8591	-2.2482 H	14 7 12 Ar			
62 H62	-5.2223	-1.5241	-2.3985 H	15 7 22 1			
63 H63	-3.1967	-4.9669	2.0726 H	16 8 9 Ar			
64 H64	-5.0616	-3.4471	1.8857 H	17 8 55 1			
65 H65	-4.6926	-3.5240	-2.4018 H	18 9 10 Ar			
66 H66	-2.7433	-4.9416	-2.2036 H	19 9 56 1			
67 H67	2.6966	-4.0496	-2.0972 H	20 10 11 Ar			
68 H68	4.2601	-2.2037	-2.0804 H	21 11 12 Ar			
69 H69	5.1870	-3.0103	2.0393 H	22 11 57 1			
70 H70	3.5826	-4.8437	2.0308 H	23 12 58 1			
71 H71	1.4376	-6.0335	-1.8690 H	24 13 14 Ar			
72 H72	-0.9925	-6.2331	-1.8759 H	25 13 18 Ar			
73 H73	-1.1167	-4.6807	2.1366 H	26 13 33 1			
74 H74	1.2948	-4.5088	2.1481 H	27 14 15 Ar			
75 H75	4.4563	4.0132	1.7030 H	28 14 76 1			
76 H76	3.4484	2.7194	-2.2662 H	29 15 16 Ar			
77 H77	1.4643	4.1126	-2.2204 H	30 15 77 1			
78 H78	2.5032	5.4738	1.7263 H	31 16 17 Ar			
79 H79	4.8734	-0.7534	4.4740 H	32 17 18 Ar			
80 H80	5.6380	0.6764	3.7266 H	33 17 78 1			
81 H81	3.8588	0.5110	3.7385 H	34 18 75 1			
82 H82	7.1889	0.7266	-3.1289 H	35 19 20 Ar			
83 H83	5.5801	0.4370	-3.8556 H	36 19 24 Ar			

37 19 28 1  
38 20 21 Ar  
39 20 59 1  
40 21 22 Ar  
41 21 60 1  
42 22 23 Ar  
43 23 24 Ar  
50 26 63 1  
51 27 28 Ar  
52 27 64 1  
53 28 29 Ar  
54 29 30 Ar  
55 29 65 1  
56 30 66 1  
57 31 34 Ar  
58 31 38 1  
59 31 85 Ar  
60 32 33 Ar  
61 32 47 1  
62 32 85 Ar  
63 33 86 Ar  
64 34 48 1  
65 34 86 Ar  
66 35 36 Ar  
67 35 40 Ar  
68 35 41 1  
69 36 37 Ar  
70 36 67 1  
71 37 38 Ar  
72 37 68 1  
73 38 39 Ar  
74 39 40 Ar  
75 39 69 1  
76 40 70 1  
77 41 42 Ar  
78 41 46 Ar  
79 42 43 Ar  
80 42 71 1  
81 43 44 Ar  
82 43 72 1  
83 44 45 Ar  
84 45 46 Ar  
85 45 73 1  
86 46 74 1  
87 47 50 1  
88 48 49 1  
89 49 79 1  
90 49 80 1  
91 49 81 1  
92 50 82 1  
93 50 83 1  
94 50 84 1  
95 85 87 1  
96 86 88 1  
97 89 90 Ar  
98 89 94 Ar  
99 89 106 1  
100 90 91 Ar  
101 90 95 1  
102 91 92 Ar  
103 91 102 1  
104 92 93 Ar  
105 92 96 1

44 23 61 1  
45 24 62 1  
46 25 26 Ar  
47 25 30 Ar  
48 25 44 1  
49 26 27 Ar  
  
106 93 94 Ar  
107 93 97 1  
108 94 98 1  
109 95 99 1  
110 95 100 1  
111 95 101 1  
112 102 103 1  
113 102 104 1  
114 102 105 1  
115 106 107 1  
116 106 108 1  
117 106 109 1

## **$\Delta E$ for the Formation of Pyridinium Complexes of 1 Obtained by Single Point DFT Calculations at B3LYP/6- 31G(d,p) level of theory using Grimme's dispersion corrections (IOp(3/124 = 3)))**

Energies were obtained by single point calculations on DFT-  
optimized structures. All calculations were performed at  
B3LYP/6-31G(d,p) level of theory using Grimme's dispersion  
corrections (IOp(3/124 = 3)))

$$\Delta E \text{ NMP}^+\text{C1 complex} = E_{\text{NMP}^+\text{C1}} - (E_1 + E_{\text{NMP}^+}) = (-65.45244980) - [(-2077.43558538) + (-287.986596007)] = \mathbf{-0.039 \text{ A. U. (-24,47 KCAL/MOL)}}$$

$$\Delta E \text{ NPP}^+\text{C1 complex} = E_{\text{NPP}^+\text{C1}} - (E_1 + E_{\text{NPP}^+}) = (-2444.08960840) - [(-2077.43558538) + (-366,627387657)] = \mathbf{-0.027 \text{ A. U. (-16,94 KCAL/MOL)}}$$

$$\Delta E \text{ NML}^+\text{C1 complex} = E_{\text{NML}^+\text{C1}} - (E_1 + E_{\text{NML}^+}) = (-2444.09471826) - [(-2077.43558538) + (-366.637846625)] = \mathbf{-0.021 \text{ A. U. (-13,17 KCAL/MOL)}}$$

## 4.6 Synthesis, Optoelectronic and Supramolecular Properties of a CPP-Calix[4]arene Hybrid Host

### 4.6.1 Synthesis of derivative 52

A suspension of *p*-tert-butylcalix[4]arene (11.2 g, 17.2 mmol) in 400 mL of acetonitrile and K<sub>2</sub>CO<sub>3</sub> (2.85 g, 20.6 mmol) was refluxed for 1 h. After that the solution was cooled to room temperature and 4-Bromobenzyl bromide (9.5 g, 38.0 mmol) was added. The solution was stirred overnight at reflux and subsequently cooled at room temperature. Reaction mixture was spilled in 300 mL of a solution 1 M of HCl and ice. The mixture was washed with CH<sub>2</sub>Cl<sub>2</sub> (70 mL), extracted twice and finally the organic phase were dried over sodium sulfate. Subsequently, the extract was concentrated to give a solid light brown product that could be recrystallized from MeOH and CHCl<sub>3</sub> producing white, crystalline diol (12.8 g, 77%).

Subsequently diol (12.8 g, 13.0 mmol) in 400 mL of dry DMF was cooled to 0°C and NaH (2.3 g 60% dispersion in mineral oil, 58 mmol) was added and stirred for 15 min. Finally, the reaction mixture was added methyl iodide (11 mL, 0.13 mol) and stirred overnight at room temperature. At reaction mixture was added of 200 mL of a solution 1 M of HCl. The mixture was washed with CH<sub>2</sub>Cl<sub>2</sub> (50 mL), extracted twice and finally the organic phase were dried over sodium sulfate. The extract was concentrated under reduced pressure to give a solid off-white product. Methanol was added and purification by precipitation was performed to give derivative **52** (11.9 g, 90 %).

**$^1\text{H}$  NMR** (250 MHz, TCDE, 373 K):  $\delta$  7.36 (d,  $J = 8.0$  Hz, ArH, 4 H),  $\delta$  7.17 (d,  $J = 8.2$  Hz, ArH, 4 H), 6.91 (s, ArH, 2 H), 6.52 (s, ArH, 4 H), 4.58 (s,  $\text{CH}_2\text{-Ar}$ , 4 H), 3.90 (d,  $J = 12.7$  Hz,  $\text{ArCH}_2\text{Ar}$ , 4 H), 3.31 (s,  $\text{OCH}_3$ , 6 H), 3.12 (d,  $J = 13.3$  Hz  $\text{ArCH}_2\text{Ar}$ , 4 H), 1.15 (s,  $t\text{Bu}$ , 18H), 0.88 (s,  $t\text{Bu}$ , 18 H).

**$^{13}\text{C}$  NMR** (75 MHz, TCDE, 373 K):  $\delta$  155.5, 153.3, 144.5, 144.3, 137.4, 134.5, 131.8, 131.3, 130.0, 126.0, 125.1, 121.5, 75.6, 59.1, 33.7, 33.4, 31.4, 31.1.

**HRMS** (MALDI)  $m/z$   $[\text{M} + \text{Na}]^+$  calcd for  $\text{C}_{60}\text{H}_{70}\text{Br}_2\text{NaO}_4$ , 1037.3512; found 1037.3563.

**Mp:** 225.2-226.3  $^\circ\text{C}$ .

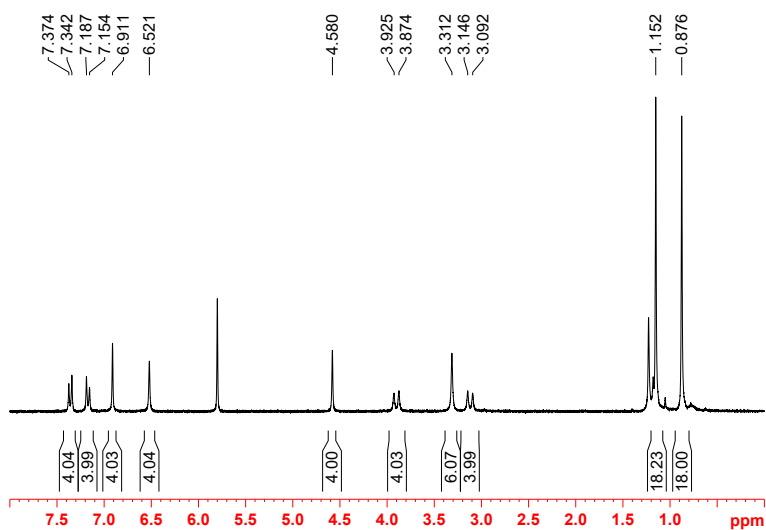


**Figure 135:**  $^1\text{H}$  NMR spectrum of **52** (TCDE- $d_2$ , 250 MHz, 373 K).

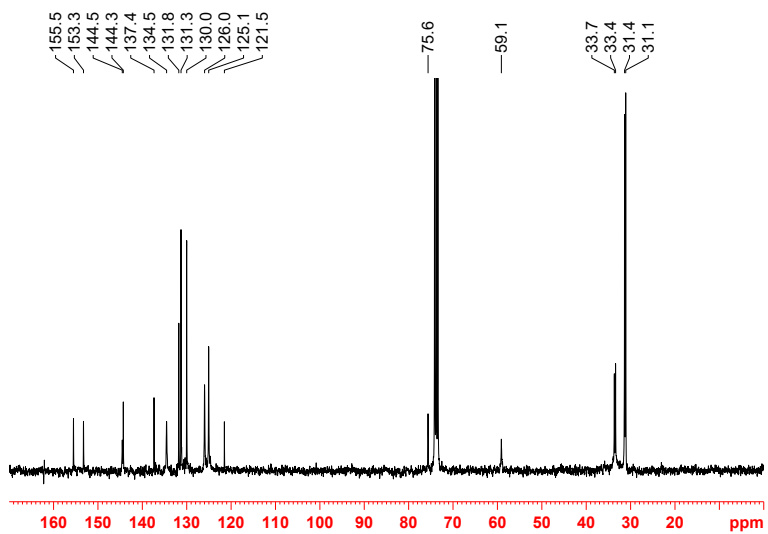


**Figure 136:**  $^{13}\text{C}$  NMR spectrum of **52** (TCDE-*d*2, 75 MHz, 298 K).

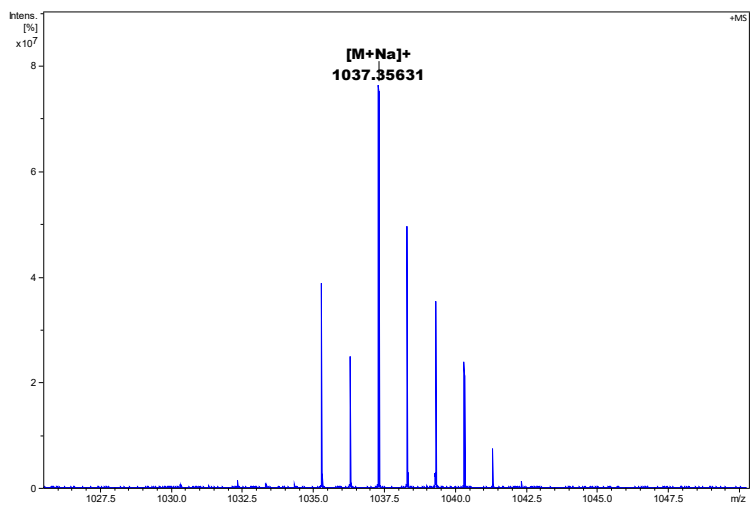


**Figure 137:** Significant portion of the HR MALDI FT-ICR mass spectrum of **52**  $[\text{M}+\text{Na}]^+$ .

## 4.6.2 Synthesis of derivative 53

A mixture of dibromide **52** (2.50 g, 2.46 mmol), diboronate<sup>159</sup> **29** (1.34 g, 2.46 mmol), S-Phos (205 mg, 0.50 mmol), and K<sub>3</sub>PO<sub>4</sub> (2.08 g, 9.85 mmol) in DMF/H<sub>2</sub>O (500 mL/50 mL) were mixed and degassed twice through the freeze/pump/thaw technique. Finally, Pd(OAc)<sub>2</sub> (110 mg, 0.72 mmol) was added and the mixture was stirred for 3 days at 100 °C under argon. After cooling to room temperature, the mixture was filtered through a short plug of Celite® and added to 200 mL of water and 200 mL of CH<sub>2</sub>Cl<sub>2</sub>. The aqueous layer was washed with CH<sub>2</sub>Cl<sub>2</sub> (4 × 50 mL). Organic phases were washed with 200 mL of a saturated brine solution and dried over sodium sulfate. After filtration, the solvent was evaporated under vacuum and the crude was purified through chromatographic column on silica gel (hexane/ethyl acetate = 9/1) to give the macrocycle **53** as white solids, (164 mg, 5.8 %).

<sup>1</sup>H NMR (600 MHz, CDCl<sub>3</sub>, 298 K): δ 7.45-7.55 (overlapped, ArH, 16 H), δ 6.92-7.08 (overlapped, ArH, 6 H), 6.43-6.52 (overlapped, ArH, 2 H), 6.12-6.18 (overlapped, CH=CH, 4 H), 4.67-4.74 (overlapped, CH<sub>2</sub>-Ar, 4 H), 4.28-4.34 (overlapped, ArCH<sub>2</sub>Ar, 1 H), 3.65-3.78 (overlapped, ArCH<sub>2</sub>Ar, 3 H), 3.41-3.49 (overlapped, OCH<sub>3</sub>, 12 H), 3.08-3.14 (overlapped, ArCH<sub>2</sub>Ar, 4 H), 1.31 (broad, *t*Bu, 9 H), 1.06-0.98 (overlapped, *t*Bu, 27 H).

<sup>13</sup>C NMR (150 MHz, CDCl<sub>3</sub>, 298 K): δ 155.9, 154.1, 145.4, 144.2, 143.5, 142.7, 140.3, 137.5, 135.9, 133.6, 132.5, 129.2, 128.6, 128.2, 127.3, 126.6, 126.2, 125.6, 125.1, 124.4, 74.9, 57.9, 52.2, 38.0, 34.3, 33.8, 31.8, 31.5, 31.3, 29.9.

---

<sup>159</sup> Darzi, E. R.; Sisto, T. J.; Jasti, R. *J. Org. Chem.* **2012**, *77*, 6624.

HRMS (MALDI)  $m/z$   $[M + Na]^+$  calcd for  $C_{80}H_{88}NaO_6$ , 1167.6473; found 1167.6645.

Mp: 268.2-269.5 °C.

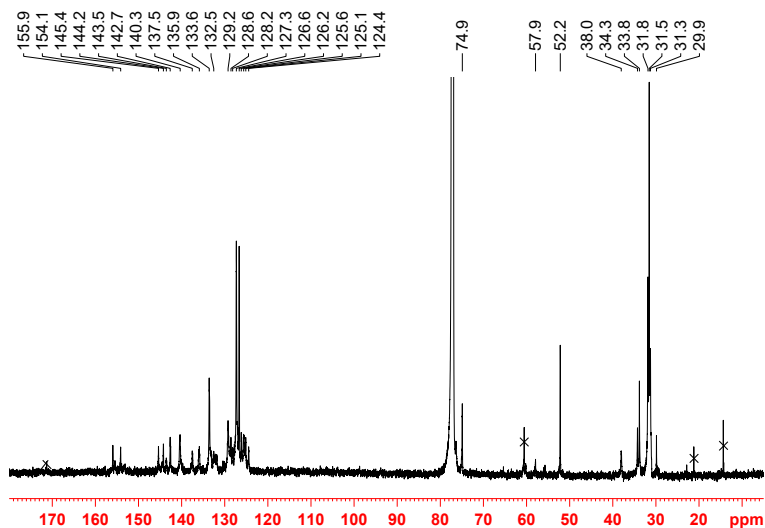


Figure 138:  $^{13}C$  NMR spectrum of **53** ( $CDCl_3$ , 150 MHz, 298 K).

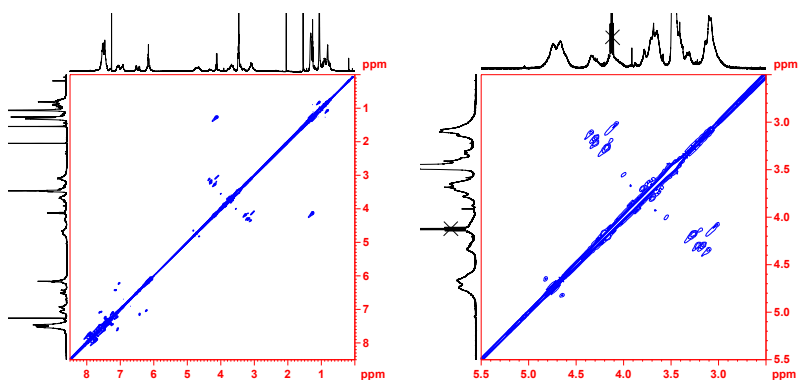
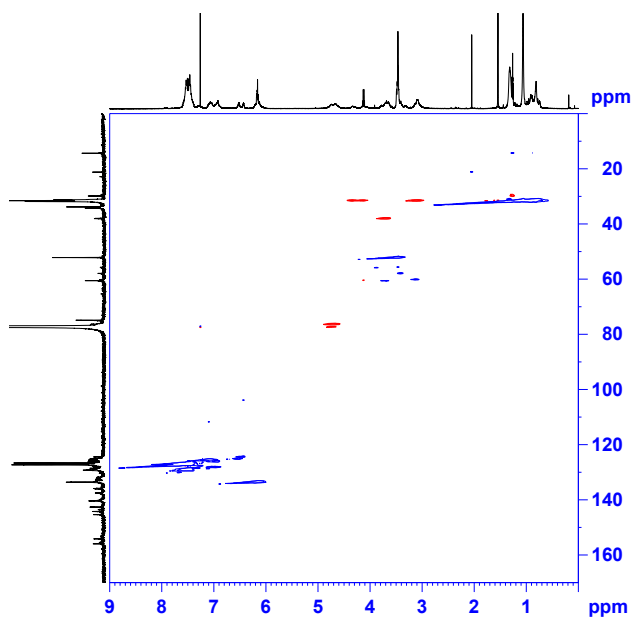
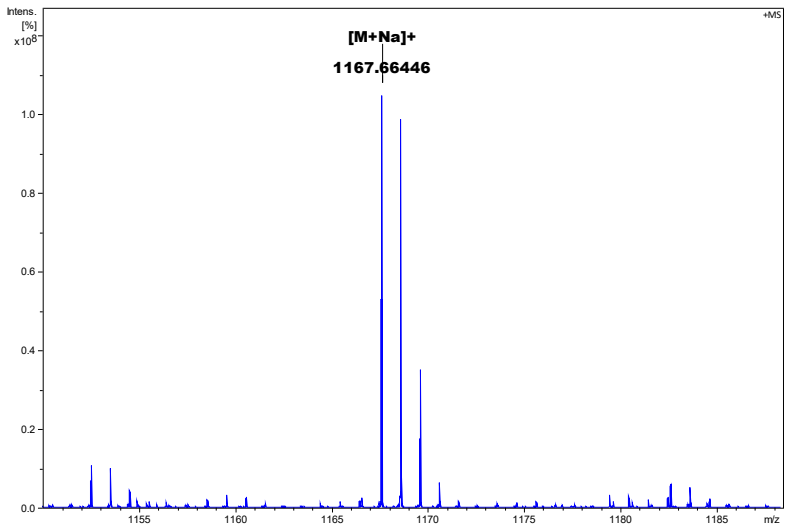


Figure 139: (Left) Full COSY spectrum of **53** and (Right) significant portion of the COSY spectrum between 2.5 and 5.5 ppm ( $CDCl_3$ , 600 MHz, 298 K).



**Figure 140:** HSQC spectrum of **53** (CDCl<sub>3</sub>, 600 MHz, 298 K).



**Figure 141:** Significant portion of the HR MALDI FT-ICR mass spectrum of **53** [M+Na]<sup>+</sup>.

### 4.6.3 Synthesis of derivative 54

A suspension of SnCl<sub>2</sub> (250 mg, 1.32 mmol) in 27 mL of THF under nitrogen was added of HCl (3 mL, 37%) and degassed. Then, derivative **53** was added (267 mg, 0.23 mmol), and the reaction mixture was stirred for 7 h at room temperature. Subsequently an aqueous saturated solution of NaHCO<sub>3</sub> (50 mL) and CH<sub>2</sub>Cl<sub>2</sub> (30 mL) were added. The organic layer was separated, and the aqueous phase was extracted with CH<sub>2</sub>Cl<sub>2</sub> (1 × 30 mL). The combined organic layers were dried on Na<sub>2</sub>SO<sub>4</sub> and filtered, and the solvent was removed in vacuum. The crude product was purified by column chromatography on silica gel using Hexane/Toluene/CHCl<sub>3</sub> (35:35:30). The product **54** was obtained as an off-white solid (38 mg, 14%).

**<sup>1</sup>H NMR** (300 MHz, TCDE, 393 K): δ 7.51 (broad, ArH, 20 H), δ 6.96 (s, ArH, 4 H), 6.58 (s, ArH, 4 H), 4.66 (s, CH<sub>2</sub>-Ar, 4 H), 4.05 (d, *J* = 11.7 Hz, ArCH<sub>2</sub>Ar, 4 H), 3.34 (s, OMe, 6 H), 3.21 (d, *J* = 12.5 Hz, ArCH<sub>2</sub>Ar, 4 H), 1.15 (s, *t*Bu, 18 H), 0.90 (s, *t*Bu, 18 H).

**<sup>13</sup>C NMR** (150 MHz, CD<sub>2</sub>Cl<sub>2</sub>, 298 K): δ 156.3, 154.5, 145.7, 144.6, 140.4, 140.0, 139.9, 138.1, 136.2, 134.8, 133.6, 132.8, 130.5, 130.0, 129.8, 129.5, 129.4, 129.3, 129.0, 128.7, 128.6, 127.9, 127.8, 127.7, 127.3, 127.1, 126.0, 125.7, 112.2, 79.6, 78.0, 77.8, 77.6, 76.6, 60.7, 56.0, 38.2, 36.6, 34.4, 34.0, 32.4, 32.0, 31.8, 31.6, 30.1, 29.8, 23.1, 23.1, 14.3.

**HRMS** (MALDI) *m/z* [M + Na]<sup>+</sup> calcd for C<sub>78</sub>H<sub>82</sub>NaO<sub>4</sub>, 1105.6105; found 1105.6147.

**Mp**: 256.6-257.8 °C.

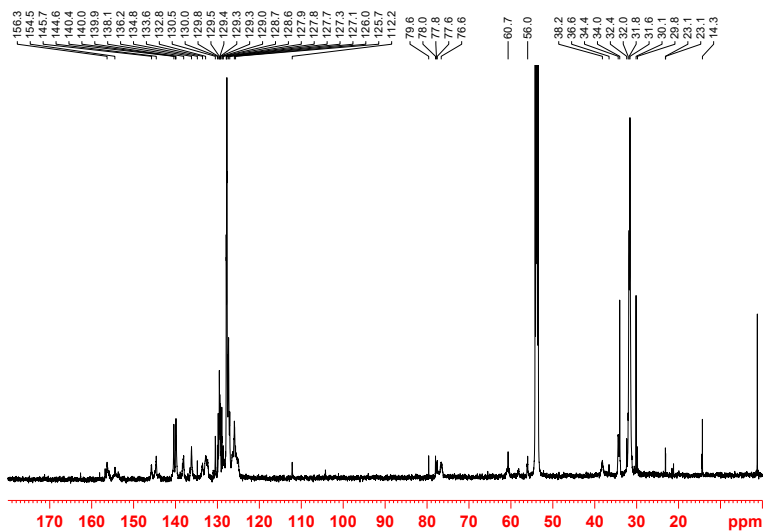


**Figure 142:**  $^{13}\text{C}$  NMR spectrum of **54** ( $\text{CD}_2\text{Cl}_2$ , 150 MHz, 298 K).

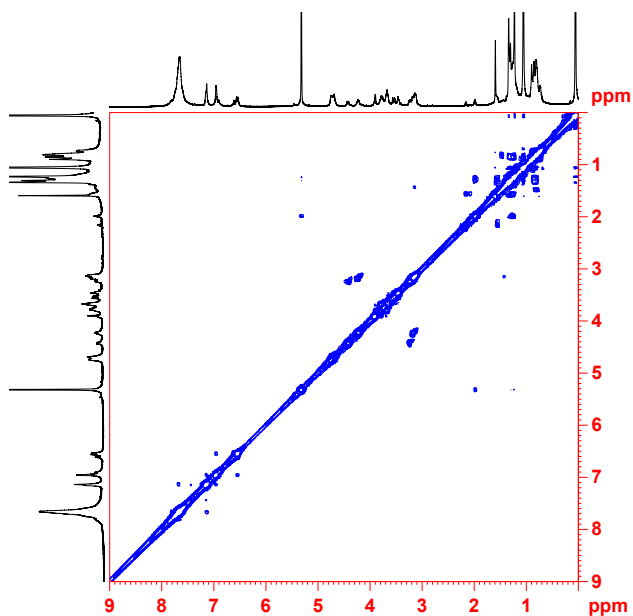


**Figure 143:** COSY spectrum of **54** ( $\text{CD}_2\text{Cl}_2$ , 600 MHz, 263 K).

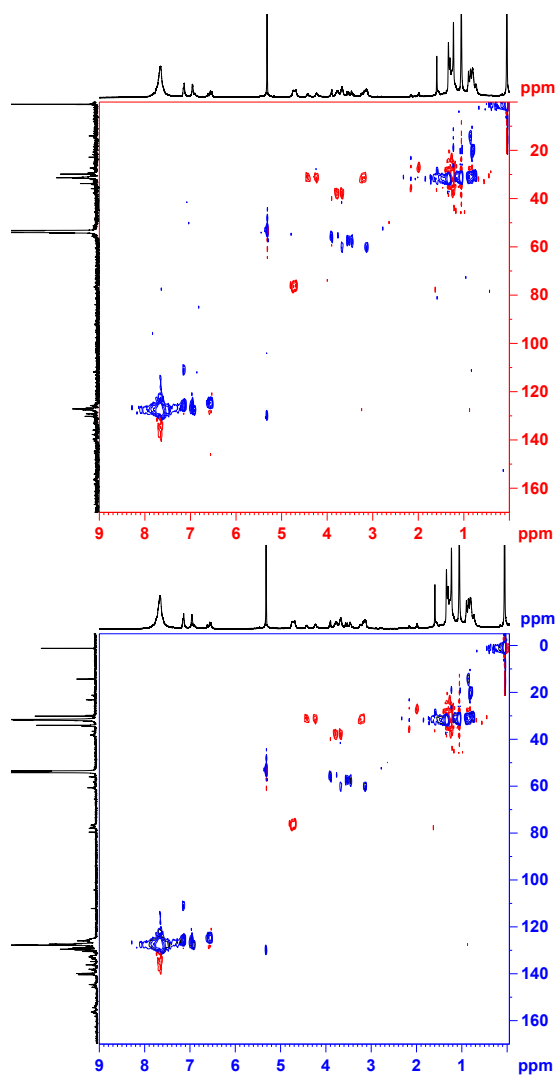


**Figure 144:** (Top) HSQC spectrum of **54** (CD<sub>2</sub>Cl<sub>2</sub>, 600 MHz, 263 K); (Bottom) HSQC spectrum of **54** (CD<sub>2</sub>Cl<sub>2</sub>, 600 MHz, 298 K).

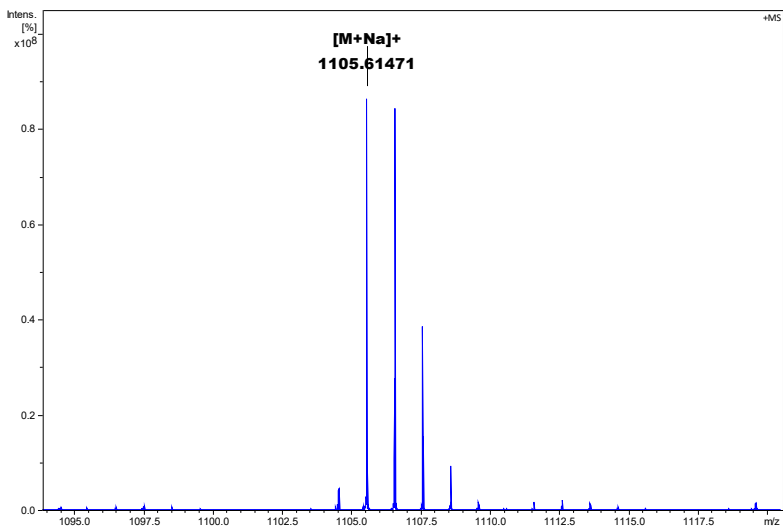


**Figure 145:** Significant portion of the HR MALDI FT-ICR mass spectrum of **54** [M+Na]<sup>+</sup>.

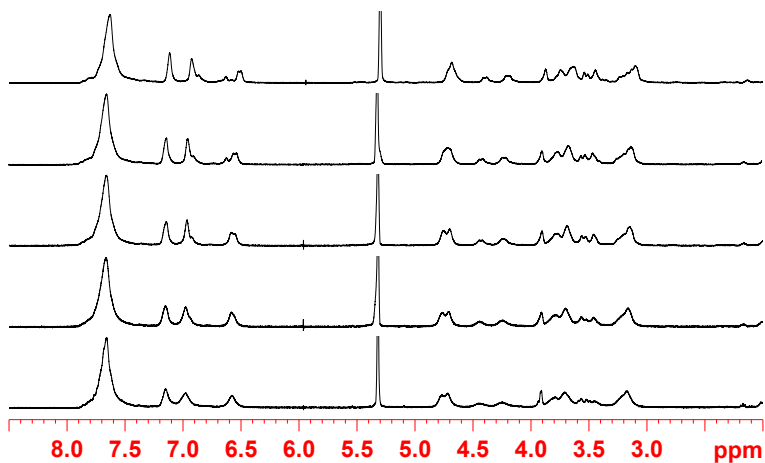


**Figure 146:** Relevant aromatic region of the <sup>1</sup>H NMR spectrum of **54** (400 MHz, CH<sub>2</sub>Cl<sub>2</sub>) at (from bottom to top): 298, 283, 273, 263 and 253 K.

## 4.6.4 UV-Vis and Fluorescence Characterization

Absorbance measurements was performed in a 1 cm Quartz cuvette with dichloromethane (Spectrophotometric Grade) using a Cary 50 UV-vis spectrophotometer from Varian. The extinction coefficients were calculated by measuring the slope of Beer-Lambert plots (absorbance at 300 nm).

Fluorescence spectra was obtaining in a 1 cm Quartz cuvette with dichloromethane (Spectrophotometric Grade) using a Cary Eclipse Spectrophotometer from Varian and was measured by excitation at 300 nm.

The quantum efficiency of **54** was determined like described by Williams<sup>160</sup> using anthracene in ethanol (Spectrophotometric Grade) as external standards at room temperature. The fluorescence of **54** was integrated from 330 - 500 nm while the fluorescence of anthracene was integrated from 360 - 480 nm.

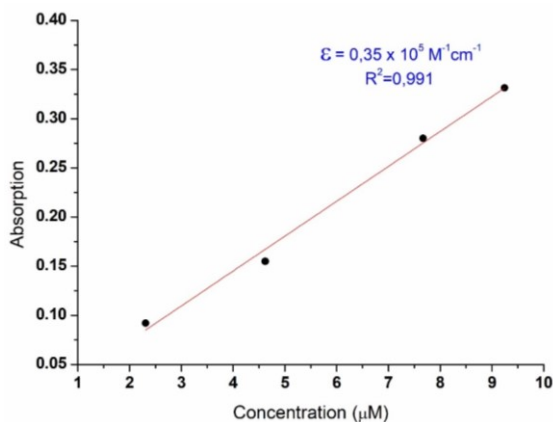


**Figure 147:** Beer-Lambert plots for the determination of the extinction coefficient of **54** ( $\epsilon = 0.35 \times 10^5 \text{ M}^{-1} \text{ cm}^{-1}$ ).

<sup>160</sup> Williams, A. T. R.; Winfield, S. A.; Miller, J. N. *Analyst*, **1983**, *108*, 1067-1071.

## 4.6.5 Binding Studies

Determination of Association Constants by fluorescence titration. Fluorescence titrations were performed at 298 K in a 1 cm Quartz cuvette using a mixture of dichloromethane : acetonitrile 9:1 as solvent. The changes in the fluorescent intensity of **54** at 393 nm were recorded.

The host concentration was kept constant (5.4  $\mu\text{M}$ ) while the guest concentration was varied (0.54 - 16.2  $\mu\text{M}$  of  $\text{LiPF}_6$  or  $\text{NaPF}_6$  - 0.1-3.0 equivalents).

After guest addition, the samples were left to equilibrated for 24 hours at room temperature before the fluorescence readings were recorded.

The Stern - Volmer Constants ( $K_{SV}$  - eq. 1) and Binding Constant ( $K_{ass}$  - eq. 2) were determined by using the following equations:

$$\frac{F_0}{F} = 1 + K_{SV} [Guest] \quad (eq. 1)$$

$$\frac{F}{F_0} = \frac{\left\{ 1 + \left( \frac{K_f}{K_s} \right) K_{ass} [Guest] \right\}}{(1 + K_{ass} [Guest])} \quad (eq. 2)$$

## 4.6.6 Computational details

Geometry optimizations of the lowest energy conformers were performed at the density functional level of theory (DFT); the B3LYP functional was employed, in conjunction with the 6-31G(d) basis set. Excitation energies and oscillator strengths were computed for each conformer by using the time dependent (TD) DFT approach. The CAM-B3LYP functional with the 6-31+G(d) basis set including diffuse functions was adopted for TDDFT computations.<sup>161</sup> Solvent (dichloromethane) effects were

---

<sup>161</sup> Yanai, T.; Tew, D. P.; Handy, N. C. *Chem. Phys. Lett.* **2004**, *393*, 117-129.

evaluated by the polarizable continuum model (PCM) and were included in all computations.<sup>162</sup> DFT and TDDFT computations were carried out by using the Gaussian package.<sup>163</sup>

**Table 8:** Low energy electronic transitions of the most significant conformers of **54** predicted at the (PCM)TDCAM-B3LYP/6-31+G(d) level.

Transition	Paco			Cone		
	$\lambda/\text{nm}$	Osc. Strength	Major Contributions	$\lambda/\text{nm}$	Osc. Strength	Major Contributions
$S_1 \leftarrow S_0$	346	0.35	H $\rightarrow$ L	346	0.36	H $\rightarrow$ L
$S_2 \leftarrow S_0$	285	1.04	H-4 $\rightarrow$ L	285	1.14	H-3 $\rightarrow$ L
			H $\rightarrow$ L+1			H $\rightarrow$ L+1
$S_3 \leftarrow S_0$	275	0.58	H-11 $\rightarrow$ L	275	0.60	H-11 $\rightarrow$ L
			H $\rightarrow$ L+2			H $\rightarrow$ L+2

<sup>162</sup> Miertuš, S.; Scrocco, E.; Tomasi, J. *Chem. Phys.* **1981**, *55*, 117-129.

<sup>163</sup> Gaussian 09, Revision D.1, M. J. Frisch, G. W. Trucks, H. B. Schlegel, G. E. Scuseria, M. A. Robb, J. R. Cheeseman, G. Scalmani, V. Barone, G. A. Petersson, H. Nakatsuji, X. Li, M. Caricato, A. Marenich, J. Bloino, B. G. Janesko, R. Gomperts, B. Mennucci, H. P. Hratchian, J. V. Ortiz, A. F. Izmaylov, J. L. Sonnenberg, D. Williams-Young, F. Ding, F. Lipparini, F. Egidi, J. Goings, B. Peng, A. Petrone, T. Henderson, D. Ranasinghe, V. G. Zakrzewski, J. Gao, N. Rega, G. Zheng, W. Liang, M. Hada, M. Ehara, K. Toyota, R. Fukuda, J. Hasegawa, M. Ishida, T. Nakajima, Y. Honda, O. Kitao, H. Nakai, T. Vreven, K. Throssell, J. A. Montgomery, Jr., J. E. Peralta, F. Ogliaro, M. Bearpark, J. J. Heyd, E. Brothers, K. N. Kudin, V. N. Staroverov, T. Keith, R. Kobayashi, J. Normand, K. Raghavachari, A. Rendell, J. C. Burant, S. S. Iyengar, J. Tomasi, M. Cossi, J. M. Millam, M. Klene, C. Adamo, R. Cammi, J. W. Ochterski, R. L. Martin, K. Morokuma, O. Farkas, J. B. Foresman, and D. J. Fox, Gaussian, Inc., Wallingford CT, **2016**.

**Cartesian coordinates (PCM/B3LYP/6-31G\*) of paco conformer**

C	2.984351	2.730984	0.505809
C	4.350474	2.714015	0.190153
C	4.813891	2.782834	-1.127893
C	3.846154	2.752483	-2.144732
C	2.476172	2.755065	-1.879167
C	2.059275	2.846466	-0.539535
O	0.707800	3.038839	-0.265343
C	1.466187	2.576668	-3.004770
C	2.526151	2.561095	1.948333
C	2.498496	-2.552949	2.007721
C	1.552820	-2.540126	-2.967443
C	6.374721	-2.850900	-1.260727
C	7.145053	-1.803412	-0.424097
C	6.838568	-4.266924	-0.839001
C	6.307424	2.911289	-1.483122
C	6.704583	1.890438	-2.574042
C	7.220266	2.685105	-0.262259
C	6.561897	4.341054	-2.020953
C	0.422182	-4.452789	-0.131046
C	0.388072	4.445533	-0.109819
C	-3.059756	4.197252	1.477253
C	-3.071721	-4.310615	1.363531
C	-1.685018	-4.315444	1.247187
H	5.054313	2.641479	1.012862
H	4.158212	2.720237	-3.184265
H	0.705774	3.364436	-2.969617
H	1.991999	2.691381	-3.959373
H	1.437752	2.657285	1.979513
H	2.933914	3.367861	2.569916
H	1.409028	-2.640645	2.017432
H	2.888766	-3.352406	2.649424
H	0.818519	-3.353128	-2.962193
H	2.106487	-2.625938	-3.908867
H	8.220955	-1.879741	-0.623109
H	6.823470	-0.786443	-0.672553
H	6.999987	-1.945015	0.651607
H	7.918476	-4.381663	-0.996694
H	6.629865	-4.455914	0.219895
H	6.325448	-5.038167	-1.425447
H	7.776710	1.969390	-2.791577
H	6.496127	0.865468	-2.249697
H	6.167396	2.059165	-3.512896
H	8.270088	2.760550	-0.568006
H	7.052441	3.434459	0.519335
H	7.070023	1.693075	0.178687
H	7.618140	4.469185	-2.289812
H	5.958848	4.545083	-2.912798
H	6.309599	5.094616	-1.265626
H	0.956138	-4.858583	0.738685
H	0.779652	-4.983072	-1.022730
H	0.706678	4.992580	-1.006229

H	0.951856	4.843863	0.744667
H	-3.484316	3.807636	2.397328
H	-3.522068	-3.997476	2.300452
H	-1.075758	-4.040231	2.104682
C	2.953109	1.231945	2.563454
C	3.852159	1.213482	3.639766
C	4.301916	0.023596	4.223338
C	3.826923	-1.177964	3.673600
C	2.931889	-1.215450	2.600710
C	2.484025	0.006830	2.062402
O	1.630668	-0.000909	0.976024
C	5.287716	-0.008798	5.406906
C	5.690058	1.402826	5.874846
C	6.573749	-0.760064	4.986487
C	4.636960	-0.743227	6.603222
H	4.201129	2.168733	4.018378
H	4.164417	-2.126297	4.085081
H	6.387281	1.325742	6.716872
H	6.191102	1.969199	5.081527
H	4.823594	1.982011	6.213858
H	7.285158	-0.794933	5.820899
H	6.362189	-1.791359	4.685014
H	7.062110	-0.257423	4.143608
H	5.333357	-0.783539	7.449822
H	3.729702	-0.224395	6.934191
H	4.361316	-1.772158	6.348987
C	4.358152	-2.716699	0.295645
C	4.857785	-2.740990	-1.013684
C	3.919353	-2.680146	-2.052411
C	2.538988	-2.707746	-1.818191
C	2.090040	-2.832994	-0.495066
C	2.989694	-2.734710	0.577718
O	0.734344	-3.040476	-0.255385
C	6.743098	-2.643694	-2.742627
H	5.046386	-2.673161	1.135410
H	4.251634	-2.607127	-3.081898
H	7.830354	-2.708150	-2.865006
H	6.294679	-3.408451	-3.386658
H	6.423283	-1.660643	-3.106841
C	-0.581640	-1.209083	-2.645868
C	-1.326641	-0.023242	-2.552318
C	-0.626195	1.181878	-2.677375
C	0.748427	1.228945	-2.946686
C	1.434195	0.015860	-3.118086
C	0.788139	-1.218333	-2.920458
O	2.779978	0.030003	-3.454308
C	-2.844992	-0.085146	-2.295874
C	-3.506914	1.303494	-2.368305
C	-3.515177	-0.985611	-3.361071
C	-3.111845	-0.672879	-0.890344
H	-1.071598	-2.165669	-2.491269
H	-1.144661	2.126150	-2.556179
H	-4.585824	1.204830	-2.203612
H	-3.121066	1.982292	-1.600766
H	-3.359246	1.773798	-3.347929

H	-4.598505	-1.027048	-3.193249
H	-3.343311	-0.594125	-4.370883
H	-3.135638	-2.012044	-3.329729
H	-4.189659	-0.780401	-0.717785
H	-2.651797	-1.658302	-0.766556
H	-2.710516	-0.013502	-0.112243
C	-1.677961	4.195963	1.316152
C	-1.095547	4.591613	0.105469
C	-1.936467	5.073313	-0.905472
C	-3.322340	5.087394	-0.743637
C	-3.916431	4.601012	0.433993
H	-1.046038	3.840085	2.126095
H	-1.505339	5.421500	-1.841280
H	-3.947586	5.447642	-1.555828
C	-1.067227	-4.611187	0.025886
C	-1.879715	-4.992287	-1.049948
C	-3.269962	-4.999420	-0.934486
C	-3.897124	-4.606916	0.261292
H	-1.421872	-5.265568	-1.997923
H	-3.872487	-5.279541	-1.794134
C	-9.021372	0.713768	-0.090609
C	-8.429292	1.407670	0.985274
C	-8.145551	0.650375	2.137516
C	-8.141429	-0.738753	2.097314
C	-8.419624	-1.428724	0.902536
C	-9.015025	-0.677975	-0.132037
H	-9.379280	1.259361	-0.959586
H	-7.737302	1.135561	3.018121
H	-7.730220	-1.273182	2.947791
H	-9.366079	-1.175452	-1.032290
C	-5.342311	-4.270282	0.332043
C	-5.958967	-3.655486	-0.771386
C	-7.108753	-2.889163	-0.614540
C	-7.693730	-2.702633	0.652724
C	-7.221316	-3.523900	1.695920
C	-6.065711	-4.284934	1.540267
H	-5.456793	-3.645040	-1.733979
H	-7.453892	-2.300607	-1.458586
H	-7.700829	-3.493559	2.670550
H	-5.678814	-4.834137	2.394450
C	-7.198999	3.434768	1.893256
C	-7.713258	2.699635	0.805952
C	-7.176345	2.990965	-0.462922
C	-6.028649	3.764264	-0.599682
C	-5.363599	4.278148	0.527051
C	-6.043092	4.198770	1.758005
H	-7.642538	3.329469	2.879505
H	-7.555944	2.477302	-1.340288
H	-5.565812	3.835436	-1.579145
H	-5.620024	4.672517	2.639808
C	0.237238	0.003131	1.299140
H	-0.293085	0.004045	0.347156
H	-0.043501	-0.889277	1.871261
H	-0.038142	0.897889	1.870352
C	3.024411	0.035986	-4.861149

H	2.592881	0.922988	-5.342985
H	4.109618	0.048888	-4.988348
H	2.613552	-0.859073	-5.346401

### Cartesian coordinates (PCM/B3LYP/6-31G\*) of cone conformer

C	-2.296861	-1.880104	2.318554
C	-3.697956	-1.881047	2.296696
C	-4.430901	-2.466806	1.258229
C	-3.701616	-2.962326	0.167630
C	-2.305220	-2.972901	0.136158
C	-1.610391	-2.510064	1.268485
O	-0.231405	-2.677903	1.349947
C	-1.572741	-3.399454	-1.136468
C	-1.553967	-1.147266	3.432983
C	-1.399441	3.362639	1.090320
C	-1.744665	1.109301	-3.467776
C	-5.960683	2.692928	-1.039380
C	-6.285524	4.201383	-1.170266
C	-6.690651	1.942211	-2.169714
C	-5.965242	-2.603211	1.289149
C	-6.600838	-1.806715	2.445227
C	-6.319717	-4.098790	1.477378
C	-6.588257	-2.105401	-0.035269
C	0.103438	3.846568	-2.120694
C	0.117152	-3.964586	1.922870
C	3.750988	-4.317735	0.854768
C	3.694479	4.865105	-1.326904
C	2.300180	4.843461	-1.345581
H	-4.213319	-1.401961	3.122490
H	-4.228656	-3.347438	-0.700470
H	-0.498408	-3.311611	-0.964808
H	-1.784415	-4.452314	-1.361319
H	-0.483645	-1.329918	3.316837
H	-1.848347	-1.554241	4.408253
H	-0.340568	3.258678	0.845748
H	-1.576441	4.418983	1.328398
H	-0.663138	1.249350	-3.418200
H	-2.084417	1.529829	-4.422231
H	-7.368995	4.367024	-1.117648
H	-5.815680	4.781915	-0.368510
H	-5.927255	4.598146	-2.127534
H	-7.772458	2.086883	-2.069938
H	-6.400313	2.312080	-3.159485
H	-6.492341	0.864729	-2.136738
H	-7.690724	-1.918970	2.414751
H	-6.262134	-2.164756	3.423927
H	-6.371946	-0.737053	2.375887
H	-7.408183	-4.237089	1.494929
H	-5.913962	-4.709415	0.663206

H	-5.912820	-4.482578	2.420334
H	-7.681304	-2.183095	0.010167
H	-6.328781	-1.058244	-0.223820
H	-6.253491	-2.691477	-0.897110
H	-0.329301	4.684269	-1.559343
H	-0.338622	3.851390	-3.126582
H	-0.313462	-4.758808	1.298347
H	-0.324416	-4.046792	2.924376
H	4.298040	-4.441589	-0.074884
H	4.204670	5.543800	-0.649047
H	1.747786	5.502250	-0.679566
C	-1.851206	0.349103	3.430585
C	-2.668808	0.918528	4.417444
C	-3.030978	2.271410	4.402274
C	-2.576495	3.046573	3.322255
C	-1.765064	2.524901	2.310604
C	-1.371550	1.178101	2.405830
O	-0.547172	0.644440	1.435222
C	-3.902358	2.915659	5.497663
C	-4.324949	1.904856	6.580835
C	-5.186122	3.504782	4.865697
C	-3.106381	4.051598	6.184152
H	-3.022607	0.270953	5.213057
H	-2.861491	4.093776	3.254904
H	-4.936546	2.410167	7.336893
H	-4.923627	1.087063	6.163706
H	-3.459283	1.468831	7.092303
H	-5.812205	3.968359	5.638093
H	-4.957102	4.271750	4.118530
H	-5.775434	2.721517	4.374955
H	-3.716465	4.530128	6.960205
H	-2.198218	3.661798	6.658757
H	-2.806203	4.825848	5.470126
C	-3.618952	2.985032	-0.069525
C	-4.432289	2.513997	-1.110516
C	-3.786102	1.909369	-2.194661
C	-2.389802	1.864558	-2.307247
C	-1.618197	2.470525	-1.303674
C	-2.224101	2.953072	-0.129244
O	-0.242084	2.598682	-1.466257
C	-6.510112	2.179649	0.311570
H	-4.075857	3.384850	0.831240
H	-4.368323	1.448922	-2.985947
H	-7.600611	2.293109	0.342751
H	-6.273344	1.120183	0.455675
H	-6.098399	2.731622	1.162509
C	-3.030388	-0.904767	-4.338748
C	-3.453735	-2.243463	-4.284886
C	-2.937138	-3.037578	-3.253692
C	-2.003423	-2.550498	-2.327023
C	-1.552393	-1.230277	-2.469547
C	-2.097066	-0.374242	-3.443828
O	-0.598707	-0.739999	-1.598104
C	-4.466297	-2.770536	-5.319651
C	-3.888125	-2.593884	-6.744027

C	-4.789153	-4.263418	-5.117844
C	-5.787319	-1.973077	-5.203017
H	-3.438616	-0.243536	-5.099370
H	-3.260690	-4.068033	-3.148095
H	-4.601452	-2.958841	-7.493153
H	-3.675491	-1.543747	-6.970163
H	-2.955499	-3.158268	-6.860104
H	-5.500980	-4.592270	-5.883448
H	-3.893798	-4.889368	-5.206588
H	-5.245118	-4.454727	-4.139817
H	-6.517052	-2.333368	-5.938731
H	-6.226104	-2.086977	-4.204864
H	-5.634657	-0.903316	-5.381026
C	2.360088	-4.339626	0.829942
C	1.616568	-4.082916	1.988740
C	2.310235	-3.887869	3.189390
C	3.704253	-3.877424	3.221067
C	4.454838	-4.044017	2.043864
H	1.844829	-4.516430	-0.111118
H	1.754120	-3.720285	4.108847
H	4.211738	-3.705495	4.166142
C	1.602620	3.968138	-2.186654
C	2.342067	3.163388	-3.062530
C	3.733099	3.172042	-3.037391
C	4.441459	3.993250	-2.138218
H	1.824058	2.489904	-3.740907
H	4.277207	2.479495	-3.672425
C	8.909609	-1.240648	-0.885856
C	9.062192	-1.325352	0.510867
C	9.547240	-0.171822	1.161192
C	9.545261	1.062193	0.516796
C	9.057605	1.186659	-0.800755
C	8.907298	-0.008364	-1.529252
H	8.591798	-2.112261	-1.449262
H	9.806504	-0.210568	2.215875
H	9.802726	1.950455	1.087677
H	8.587396	0.026187	-2.565884
C	5.890241	3.748586	-1.920376
C	6.731415	3.231159	-2.924440
C	7.911950	2.566509	-2.602167
C	8.292527	2.377524	-1.258491
C	7.578210	3.107789	-0.289095
C	6.403575	3.777169	-0.612389
H	6.422471	3.279247	-3.965167
H	8.487497	2.104851	-3.399970
H	7.846350	3.016756	0.758531
H	5.806782	4.194539	0.192880
C	7.580691	-2.005488	2.377132
C	8.300133	-2.383429	1.226972
C	7.926834	-3.597079	0.615689
C	6.748687	-4.246480	0.975476
C	5.902383	-3.719774	1.970413
C	6.408432	-2.658318	2.740150
H	7.842748	-1.090723	2.898898
H	8.506367	-3.986545	-0.216982

H	6.445370	-5.130792	0.421570
H	5.807334	-2.237035	3.540193
C	0.844871	0.738741	1.739482
H	1.376915	0.267306	0.912254
H	1.164979	1.784833	1.829776
H	1.089032	0.213321	2.671376
C	0.742496	-0.888422	-2.064696
H	0.888589	-0.394016	-3.033628
H	1.386040	-0.415706	-1.320932
H	1.016683	-1.946897	-2.165251

## 4.7 A [8]CPP Derivative as Emitter in Triplet-Triplet Annihilation Upconversion

### 4.7.1 Synthesis of derivative 56

1,4-Dibromobenzene (10.0 g, 42.4 mmol) was dissolved in 450 mL of dry THF and cooled to  $-78\text{ }^{\circ}\text{C}$ . To this solution was added a 2.5 M solution of *n*-butyllithium in *n*-hexane (18.2 mL, 45.5 mmol) over 15 min and the reaction mixture was stirred for 30 min. Anthraquinone (4.31 g, 20.7 mmol) was added to the reaction mixture in three equal portions over 30 min. The solution was stirred for 2 h at  $-78\text{ }^{\circ}\text{C}$  and then added to 180 mL of water. The mixture was further diluted by the addition of 180 mL of diethyl ether and the organic layer was separated. The aqueous layer was extracted with diethyl ether (3 x 70 mL) and the combined organic layers were washed with a saturated brine solution (100 mL). The organic phase was then dried over sodium sulfate, filtered and evaporated under reduced pressure to give the diol product which was used without further purification. The diol was dissolved in 70 mL of dry THF and sodium hydride (2.07 g, 51.7 mmol, 60% in mineral oil) was added at  $0\text{ }^{\circ}\text{C}$ . The mixture was stirred for 30 min and methyl iodide (5.2 mL, 83 mmol) was added. The mixture was allowed to warm to room temperature and stirred for an additional 18 h. The excess of sodium hydride was then quenched by addition of 100 mL of water and filtered. The white solid was washed with 120 mL of ethyl ether and dried in vacuum for 12 h, to give **56** in 53% of yield (6.04 g). **M. p.**  $> 310\text{ }^{\circ}\text{C}$  dec.

$^1\text{H}$  NMR (400 MHz, 298 K,  $\text{CDCl}_3$ ):  $\delta$  (ppm) 7.49 (m, 4H, Ar-H), 7.30 - 7.33 (overlapped, 8H, Ar-H), 7.19 (d,  $J = 8.5$  Hz, 4H, Ar-H), 2.93 (s, 6H, OMe);

$^{13}\text{C}$  NMR (100 MHz,  $\text{CDCl}_3$ ):  $\delta$  (ppm) 147.9, 138.2, 131.0, 128.7, 128.2, 121.1, 78.7, 51.3.

HRMS (ESI+):  $m/z$   $[\text{M}+\text{Na}]^+$  calculated for  $\text{C}_{28}\text{H}_{22}\text{Br}_2\text{NaO}_2$ : 572.9864, found 572.9859.

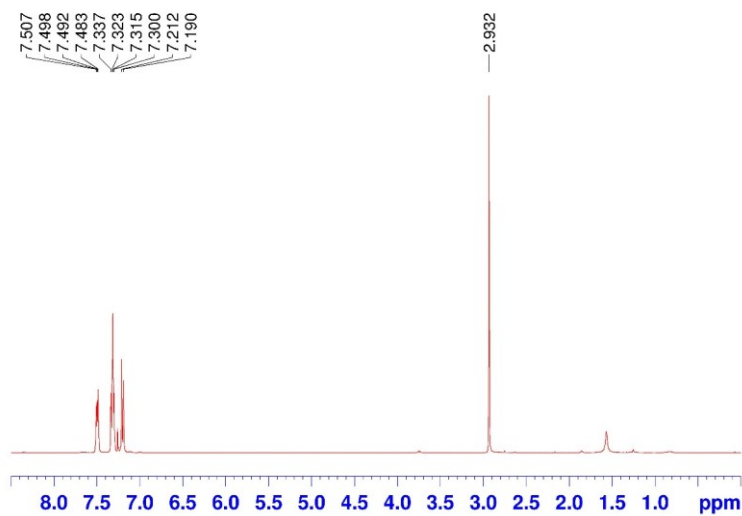
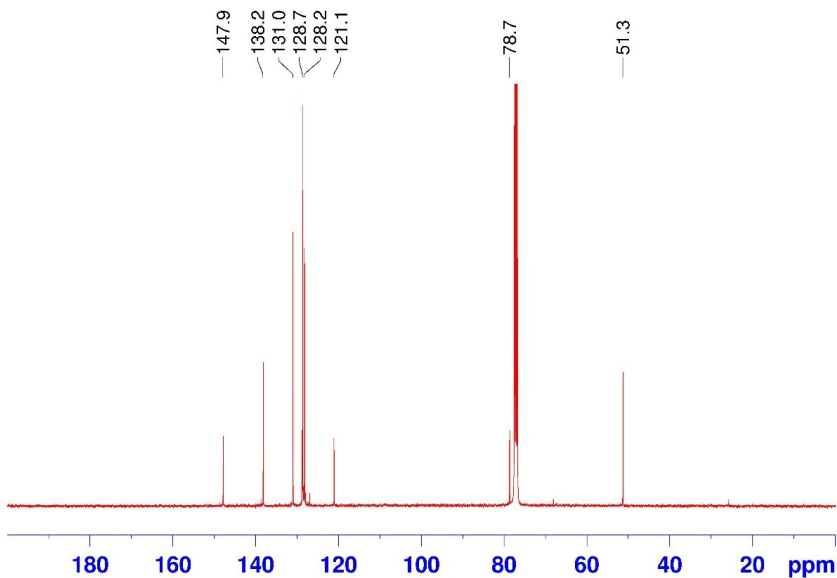
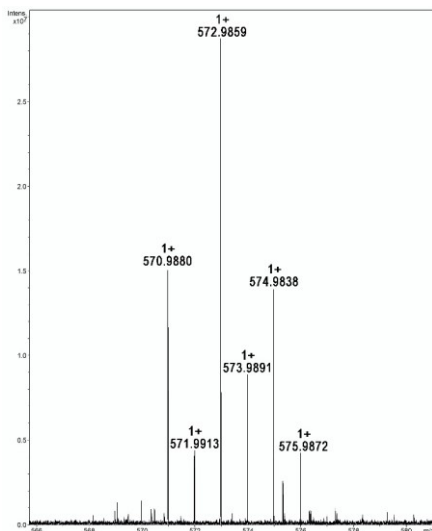


Figure 148:  $^1\text{H}$  NMR spectrum of **56** ( $\text{CDCl}_3$ , 400 MHz, 298 K).



**Figure 149:**  $^{13}\text{C}$  NMR spectrum of **56** ( $\text{CDCl}_3$ , 100 MHz, 298 K).



**Figure 150:** Significant portion of the HR ESI FT-ICR mass spectrum of **56**  $[\text{M}+\text{Na}]^+$ .

## 4.7.2 Synthesis of derivative 57

Dibromide **56** (2.53 g, 4.77 mmol) was dissolved in 280 mL of dry THF and cooled to  $-78$  °C. Then a 2.5 M solution of *n*-butyllithium in hexane (9 mL, 22.5 mmol) was added over 10 min. Then isopropyl pinacol borate (8.50 mL, 42.0 mmol) was added rapidly and the solution was stirred for 5 h under argon. 200 mL of water and 100 mL of ethyl acetate were added to the solution and the biphasic mixture was stirred for 30 min at room temperature. The organic phase was extracted, and the aqueous layer was washed with ethyl acetate (3 x 70 mL). The combined organic layers were dried over sodium sulfate, filtered and concentrated in vacuum to give a colorless oil that was purified by chromatography on silica gel (hexane/ethyl acetate, 7:3). The product **57** was obtained as a white solid in 41% of yield (1.30 g). **M.p.**: 252.2-253.3°C.

**<sup>1</sup>H NMR** (400 MHz, 298 K, CDCl<sub>3</sub>):  $\delta$  (ppm) 7.68 (d,  $J = 8.1$  Hz, 4H, Ar-H), 7.48 (m, 4H, Ar-H), 7.43 (d,  $J = 8.1$  Hz, 4H, Ar-H), 7.24 (m, 4H, Ar-H), 2.94 (s, 6H, OMe), 1.30 (s, 24H, CH<sub>3</sub>).

**<sup>13</sup>C NMR** (62.5 MHz, CDCl<sub>3</sub>):  $\delta$  (ppm) 152.1, 138.5, 134.5, 128.5, 128.4, 126.2, 83.8, 79.0, 51.2, 25.0.

**HRMS (ESI+)**:  $m/z$  [M+Na]<sup>+</sup> calculated for C<sub>40</sub>H<sub>46</sub>B<sub>2</sub>NaO<sub>6</sub>: 667.3378, found 667.3380.

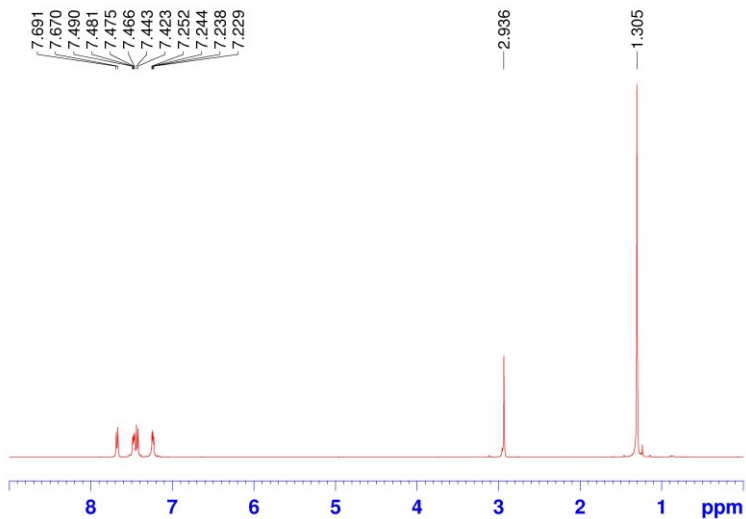


**Figure 151:**  $^1\text{H}$  NMR spectrum of **57** ( $\text{CDCl}_3$ , 400 MHz, 298 K).

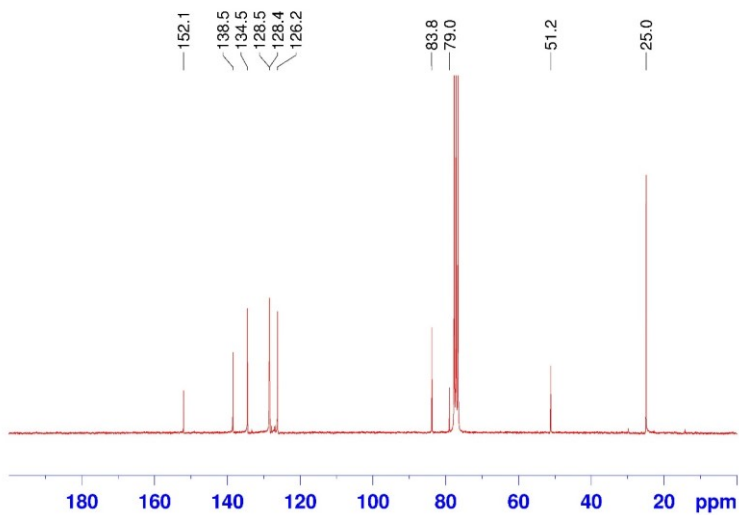


**Figure 152:**  $^{13}\text{C}$  NMR spectrum of **57** ( $\text{CDCl}_3$ , 62.5 MHz, 298 K).

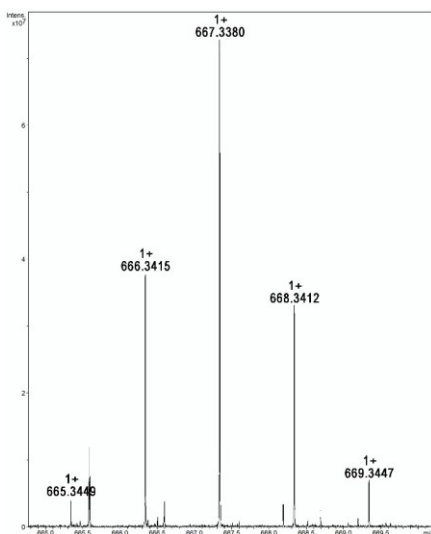


**Figure 153:** Significant portion of the HR ESI FT-ICR mass spectrum of **57**  $[M+Na]^+$ .

### 4.7.3 Synthesis of derivative **58**

Dibromide **36** (1.99 g, 3.00 mmol), diboronate **57** (1.93 g, 3.00 mmol), S-Phos (246 mg, 0.61 mmol) and  $K_3PO_4$  (2.55 g, 12.0 mmol) in a mixture of DMF/ $H_2O$  (600 mL/60mL) was mixed and degassed twice through freeze/pump/thaw technique. Then  $Pd(OAc)_2$  (471 mg, 2.11 mmol) was added and the mixture was stirred at 100 °C for 19 h under argon. After cooling to room temperature, the mixture was filtered through a short plug of Celite® and added to 150 mL of water and 100 mL of  $CHCl_3$ . The biphasic mixture was stirred for 30 min and separated. The aqueous layer was washed with  $CHCl_3$  (3 x 80 mL). The combined organic layers were washed with 200 mL of a saturated brine solution and dried over sodium sulfate. After filtration the solvent was evaporated under vacuum, the crude mixture was purified by column chromatography on silica gel

(Hexane/CH<sub>2</sub>Cl<sub>2</sub>/Et<sub>2</sub>O = 29:70:1) to give the macrocycle **58** as a white solid in 10 % of yield (0.27 g). **M. p.** > 305 °C dec.

**<sup>1</sup>H NMR** (600 MHz, 298 K, CDCl<sub>3</sub>):  $\delta$  (ppm) 7.85 (m, 4H, Ar-H), 7.50 (s, 4H, Ar), 7.47 (m, 4H, Ar-H), 7.44 (d,  $J$  = 8.5 Hz, 4H, CH=CH), 7.38 (d,  $J$  = 8.5 Hz, 4H, CH=CH), 7.17 (d,  $J$  = 8.5 Hz, 4H, CH=CH), 6.92 (d,  $J$  = 8.5 Hz, 4H, CH=CH), 6.11 (d,  $J$  = 10.3 Hz, 4H, CH=CH), 6.03 (d,  $J$  = 10.3 Hz, 4H, CH=CH), 3.46 (s, 6H, OMe), 3.41 (s, 6H, OMe), 3.15 (s, 6H, OMe).

**<sup>13</sup>C NMR** (150 MHz, 298 K, CDCl<sub>3</sub>):  $\delta$  (ppm) 145.0, 143.4, 142.8, 139.8, 139.5, 138.6, 133.5, 133.0, 128.3, 127.5, 126.9, 126.3, 126.1, 80.3, 74.6, 74.3, 52.2, 52.0.

**DEPT-135** (150 MHz, CDCl<sub>3</sub>):  $\delta$  (ppm) 133.5, 133.0, 128.3, 127.5, 126.9, 126.3, 126.1, 52.2, 52.0.

**HRMS (MALDI):**  $m/z$  [M]<sup>+</sup> calculated for C<sub>62</sub>H<sub>54</sub>O<sub>6</sub>: 894.3921, found 894.3895.

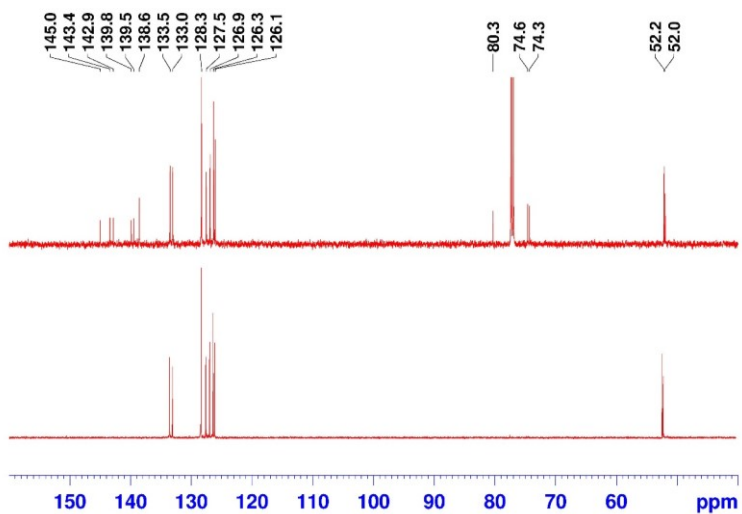


**Figure 154:**  $^{13}\text{C}$  NMR e DEPT-135 spectra of **58** ( $\text{CDCl}_3$ , 150 MHz, 298 K).

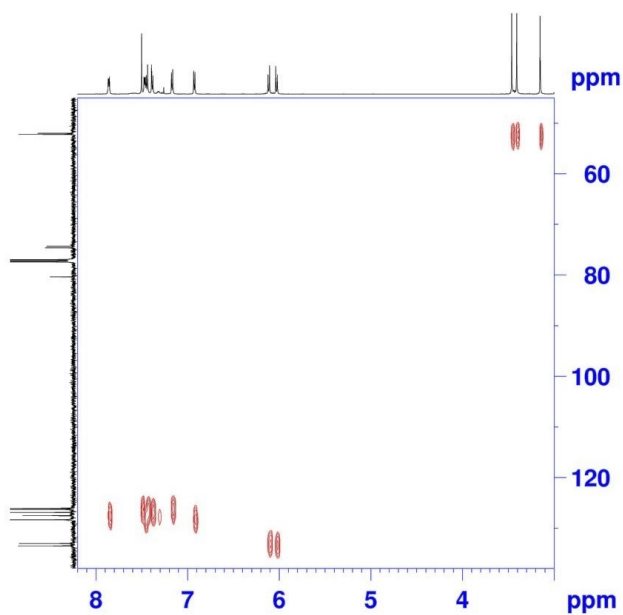


**Figure 155:** 2D HSQC spectrum of **58** ( $\text{CDCl}_3$ , 150 MHz, 298 K).

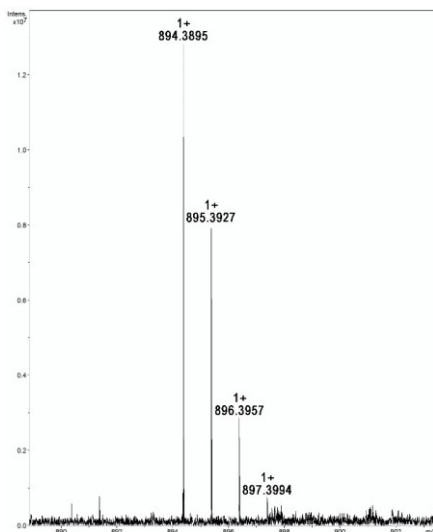


**Figure 156:** Significant portion of the HR MALDI FT-ICR mass spectrum of **58** [M]<sup>+</sup>.

#### 4.7.4 Synthesis of derivative **55**

Derivative **58** (225 mg, 0.25 mmol) was dissolved in 18 mL of dry THF, under argon, and the solution was degassed through freeze/pump/thaw technique and cooled to  $-78\text{ }^{\circ}\text{C}$ . Then, a solution of sodium naphthalenide in dry THF, freshly prepared (2.7 mL, 2.7 mmol) was added and the reaction mixture was stirred for 3 h at  $-78\text{ }^{\circ}\text{C}$ . Then  $\text{I}_2$  was added (3 mL of a 1.0 M solution in THF) and the reaction mixture was warmed at room temperature. Subsequently a saturated solution of sodium thiosulfate (50 mL) and  $\text{CHCl}_3$  (50 mL) were added, and the reaction mixture was stirred for 10 min. The organic layer was extracted and the aqueous phase was washed with  $\text{CHCl}_3$  (3 x 50 mL) and finally the combined organic layers was washed with a saturated brine solution (60 mL) and dried over sodium sulfate and filtered. The solvent was removed under reduced pressure, and the crude product was purified by

chromatography column on silica gel under nitrogen flow (*n*-hexane/CH<sub>2</sub>Cl<sub>2</sub> = 3:7), to give the product **55** as a yellow solid in 11 % of yield (19 mg). **M. p.** > 285 °C dec.

**<sup>1</sup>H NMR** (600 MHz, 298 K, CDCl<sub>3</sub>): δ (ppm) 7.89 (m, 2H, Ar-H), 7.72 (m, 2H, Ar-H), 7.49 (s, 4H, Ar-H), 7.47 (s, 8H, Ar-H), 7.42-7.40 (overlapped, 8H, Ar-H), 7.22 (d, *J* = 8.3 Hz, 4H, Ar-H), 7.11-7.08 (overlapped, 4H, Ar-H), 7.02-7.00 (overlapped, 4H, Ar-H).

**<sup>13</sup>C NMR** (150 MHz, CDCl<sub>3</sub>): δ (ppm) 146.6, 146.5, 142.7, 140.3, 139.7, 138.8, 138.4, 137.2, 137.0, 136.9, 128.6, 128.3, 128.0, 127.9, 127.8, 127.7, 127.6, 127.5, 127.5, 127.4, 127.2, 127.1, 127.1.

**DEPT-135** (150 MHz, CDCl<sub>3</sub>): δ (ppm) 128.6, 128.3, 128.0, 127.9, 127.8, 127.7, 127.6, 127.5, 127.5, 127.4, 127.2, 127.10, 127.12.

**HRMS (MALDI):** *m/z* [M]<sup>+</sup> calculated for C<sub>56</sub>H<sub>36</sub>: 708.2811, found 708.2812.

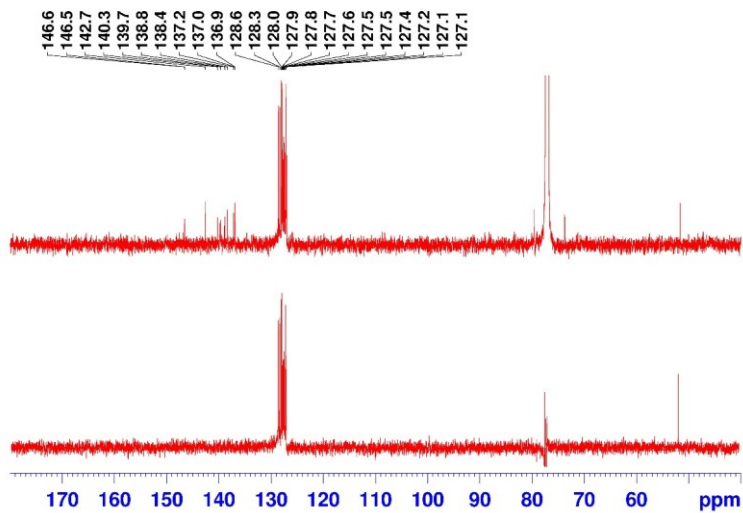


**Figure 157:**  $^{13}\text{C}$  NMR and DEPT-135 spectra of **55** ( $\text{CDCl}_3$ , 150 MHz, 298 K).

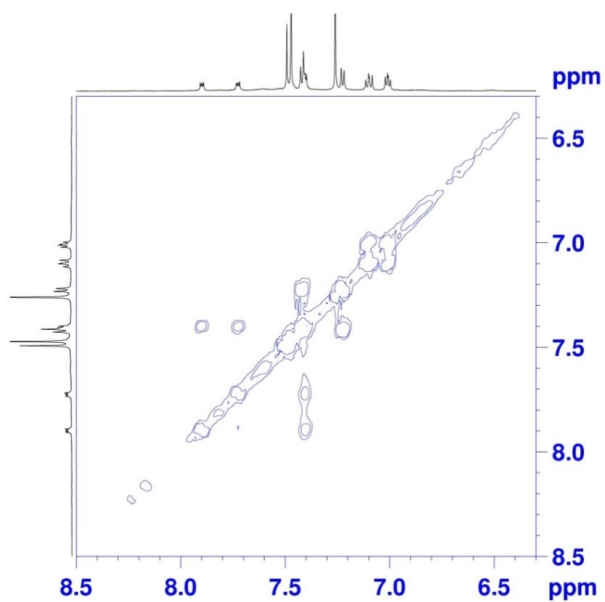


**Figure 158:** 2D COSY spectrum of **55** ( $\text{CDCl}_3$ , 150 MHz, 298 K).

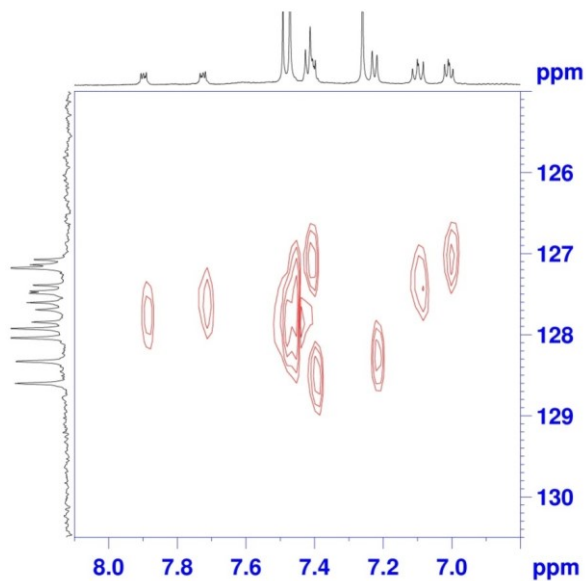


**Figure 159:** Expansion of 2D HSQC spectrum of **55** ( $\text{CDCl}_3$ , 150 MHz, 298 K).

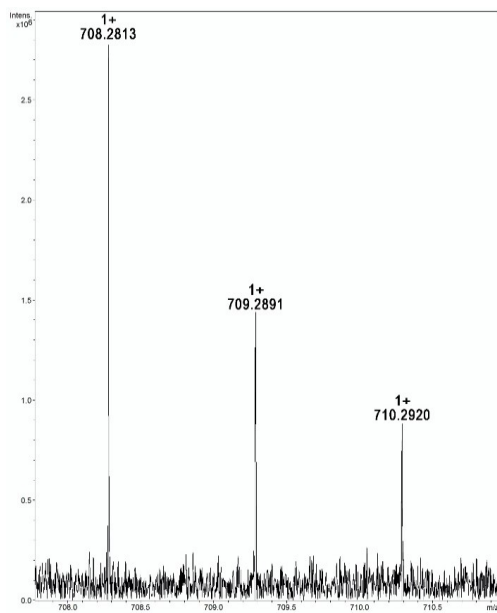


**Figure 160:** Significant portion of the HR MALDI FT-ICR mass spectrum of **55**  $[\text{M}]^+$ .

### 4.7.5 Optoelectronic Characterization

Optical absorption spectra were measured on a Cary 50 UV-vis spectrophotometer from Varian. Steady-state luminescence spectra were recorded on a modular fluorescence spectrometer from Acton Research, equipped with a xenon lamp. Light source was passed through a 295 nm long pass cut-off emission filter prior to incidence on the sample. All solution samples were deaerated with nitrogen. Relative quantum yields of **55** in dichloromethane were determined as described by Williams using quinine sulfate (0.1 M H<sub>2</sub>SO<sub>4</sub>) as standard. Excitation occurred at 319 nm and the fluorescence of **55** was integrated from 350 – 650 nm, both for **55** and for quinine sulphate. In up-conversion measurements an additional longpass filter cutting at ca. 300 nm has been employed to completely cut down possible emission produced by excitation of second order diffraction. The quantum yield measurements were performed in accord with the method reported by Miller and co-workers.<sup>115,164</sup> The CPP **55** solutions were diluted to give absorbance values in the range 0.02-0.35, within the expected linear calibration range of fluorescence emission versus concentration. The quantum yields were calculated according to equation reported by Miller.

$$\Phi_X = \Phi_R \frac{I_X}{I_R} \frac{A_R}{A_X} \frac{\eta_X^2}{\eta_R^2}$$

$\Phi_R$  is the quantum yield of the standard,  $A$  is the absorbance of the solution,  $I$  is the integrated intensity of the exciting light

---

<sup>164</sup> Parker, C. A.; Hatchard, C. G. *Proc. Chem Soc.*, London **1962**, 386-387.

and  $\eta$  is the average refractive index of the solution. Subscripts R and X refer to the reference and unknown compound, respectively. Cyclic voltammetry measurements were performed in  $\text{CH}_2\text{Cl}_2$  with TBAP as electrolyte. All potentials were referenced to the platinum quasi-reference electrode. The potential has been calibrated with ferrocene/ferrocenium ( $\text{Fc}/\text{Fc}^+$ ) redox couple.

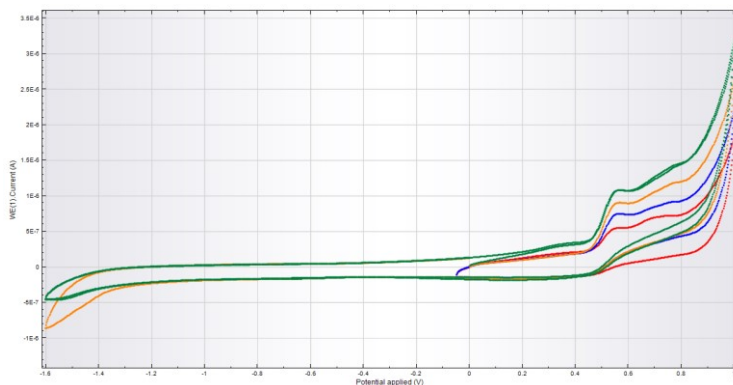


**Figure 161:** Cyclic voltammetry of **55**, 2.1 mM in  $\text{CH}_2\text{Cl}_2$  with TBAP as electrolyte 100 mM. Scan rate 100 mV/s. Working electrode, GCE. Counter electrode, Pt bar. The potential of the GCE was controlled with respect to a Pt wire as quasireference electrode.

## 4.7.6 Computational Details

Constrained and unconstrained geometry optimizations were carried at the density functional level of theory (DFT), by using the B97D functional including the empirical correction for dispersion energy proposed by Grimme,<sup>165</sup> in conjunction with the density fitting approximation and the TZVP basis set. The nature of the stationary points was verified by computing the eigenvalues of the Hessian matrix. B97D was chosen because

<sup>165</sup> Schwabe, T.; Grimme, S. *Phys. Chem. Chem. Phys.* **2006**, *8*, 4398–4401

it has been proven to be the most accurate method in predicting torsional barriers of substituted biphenyls.<sup>166</sup> Time dependent (TD) DFT computations were carried out by using the CAM-B3LYP range-separated hybrid functional.<sup>167</sup> Indeed, it is well known that electronic excitations in conjugated oligomers have a charge transfer nature, with structural distortions that can be modelled only with the use of range-corrected hybrid DFT models including long range electronic exchange interactions.<sup>88,168</sup> The same functional was adopted for the computation of the first oxidation potential. The restricted open shell (RO) formalism was used because it yields more accurate oxidation potentials when used with the CAM-B3LYP functional. The absolute potential of Fc<sup>+</sup>/Fc in dichloromethane has been set to 4.98 V.<sup>169</sup> The 6-31+G(d,p) basis set was adopted for all the computations employing the CAM-B3LYP functional. Effects due to solvent (dichloromethane) polarization were included in all computations by the polarizable continuum model (PCM).<sup>170</sup> DFT and TDDFT computations were carried out by using the Gaussian program.<sup>144</sup>

---

<sup>166</sup> Masson, E. *Org. Biomol. Chem.* **2013**, *11*, 2859-2871.

<sup>167</sup> Yanai, T.; Tew, D. P.; Handy, N. C. *Chem. Phys. Lett.* **2004**, *393*, 51-57.

<sup>168</sup> Capobianco, A.; Borrelli, R.; Landi, A.; Velardo, A.; Peluso, A. *J Phys. Chem A*, **2016**, *120*, 5581-5589.

<sup>169</sup> a) Capobianco, A.; Velardo, A.; Peluso, A. *Comp. Theor. Chem.* **2015**, *1070*, 68-75; b) Capobianco, A.; Caruso, T.; Peluso, A. *Phys. Chem. Chem. Phys.* **2015**, *17*, 4750-4756.

<sup>170</sup> Miertuš, S.; Scrocco, E.; Tomasi, J. *Chem. Phys.* **1981**, *55*, 117-129.

Atomic coordinates:  
**Conformer I of derivative**  
**55**

C	-0.204783	-2.167246	5.422375
C	-0.204783	-2.167246	-5.422375
C	0.001765	-6.084557	-1.425602
C	0.001765	-6.084557	1.425602
C	-0.243686	-3.528244	-4.830516
C	-0.243686	-3.528244	4.830516
C	-0.246445	0.680894	-5.442208
C	-0.246445	0.680894	5.442208
C	-0.132141	-5.526497	2.792095
C	-0.132141	-5.526497	-2.792095
C	-0.300643	2.030100	4.828988
C	-0.300643	2.030100	-4.828988
C	0.056838	3.982473	2.793269
C	0.056838	3.982473	-2.793269
C	0.395044	4.512544	1.438573
C	0.395044	4.512544	-1.438573
C	0.971509	-0.026080	5.379282
C	-1.407015	-0.063146	5.741217
C	0.971509	-0.026080	-5.379282
C	-1.407015	-0.063146	-5.741217
H	1.892718	0.515764	5.176204
H	-2.355415	0.452897	5.877983
H	1.892718	0.515764	-5.176204
H	-2.355415	0.452897	-5.877983
C	0.978572	-5.271851	-3.626481
C	-1.353790	-4.925074	-3.160987
C	-1.353790	-4.925074	3.160987
C	0.978572	-5.271851	3.626481
H	1.824889	-4.078626	5.189571
H	-2.340490	-3.409945	4.288448
H	-2.340490	-3.409945	-4.288448
H	1.824889	-4.078626	-5.189571
C	-1.298728	2.255844	3.857686
C	0.753946	2.961748	4.897917
C	-1.298728	2.255844	-3.857686
C	0.753946	2.961748	-4.897917
C	0.921003	3.931830	3.903952
C	-1.120187	3.206991	2.860089
C	0.921003	3.931830	-3.903952
C	-1.120187	3.206991	-2.860089
H	-2.146642	1.577741	3.793612
H	1.502164	2.871890	5.683274
H	-2.146642	1.577741	-3.793612
H	1.502164	2.871890	-5.683274
H	1.785216	4.590909	3.946176
H	-1.835697	3.260942	2.043027
H	1.785216	4.590909	-3.946176
H	-1.835697	3.260942	-2.043027
C	-0.546682	5.294211	0.725102
C	-0.546682	5.294211	-0.725102
C	1.497254	3.948628	0.729437
C	1.497254	3.948628	-0.729437
C	-1.383568	-1.456024	-5.744088
C	0.990744	-1.418822	-5.363258
C	-1.383568	-1.456024	5.744088
C	0.990744	-1.418822	5.363258
C	-1.407405	-3.949789	-4.151686
C	0.922339	-4.300443	-4.624431
C	0.922339	-4.300443	4.624431
C	-1.407405	-3.949789	4.151686
H	-2.315564	-1.994602	-5.899786
H	1.931457	-1.918796	-5.147336
H	-2.315564	-1.994602	5.899786
H	1.931457	-1.918796	5.147336
H	1.923139	-5.777184	-3.435389
H	-2.245005	-5.108439	2.565979

H	1.923139	-5.777184	3.435389
H	-2.245005	-5.108439	-2.565979
C	1.182222	-5.828254	-0.696165
C	-1.105435	-6.572559	-0.696467
C	-1.105435	-6.572559	0.696467
C	1.182222	-5.828254	0.696165
H	2.069567	-5.476312	-1.216909
H	-2.009586	-6.868792	-1.224193
H	-2.009586	-6.868792	1.224193
H	2.069567	-5.476312	1.216909
H	4.394474	2.167398	-1.256727
H	4.394474	2.167398	1.256727
H	-3.243162	7.353755	-1.252016
H	-3.243162	7.353755	1.252016
C	3.593330	2.659335	-0.708678
C	3.593330	2.659335	0.708678
C	-2.499709	6.771026	0.711731
C	-2.499709	6.771026	-0.711731
H	2.576735	3.227062	2.474644
H	2.576735	3.227062	-2.474644
H	-1.553977	6.049510	2.490992
H	-1.553977	6.049510	-2.490992
C	2.567452	3.264608	1.393694
C	-1.557604	6.045824	-1.403828
C	-1.557604	6.045824	1.403828
C	2.567452	3.264608	-1.393694

Atomic coordinates:  
**Conformer III of**  
**derivative 55**

C	0.012431	-2.016663	5.621438
C	0.012431	-2.016663	-5.621438
C	-0.120169	-5.731402	-1.427686
C	-0.120169	-5.731402	1.427686
C	-0.127758	-3.337587	-4.962565
C	-0.127758	-3.337587	4.962565
C	0.071792	0.829452	-5.747427
C	0.071792	0.829452	5.747427
C	-0.193714	-5.216814	2.815862
C	-0.193714	-5.216814	-2.815862
C	-0.021223	2.186541	5.148347
C	-0.021223	2.186541	-5.148347
C	0.027336	3.918821	2.912389
C	0.027336	3.918821	-2.912389
C	0.171589	4.099747	1.433160
C	0.171589	4.099747	-1.433160
C	1.249320	0.084164	5.523078
C	-1.066310	0.106191	6.168498
C	1.249320	0.084164	-5.523078
C	-1.066310	0.106191	-6.168498
H	2.161682	0.594887	5.225846
H	-1.973949	0.639524	6.443375
H	2.161682	0.594887	-5.225846
H	-1.973949	0.639524	-6.443375
C	0.948402	-5.085458	-3.636877
C	-1.363246	-4.552152	-3.241150
C	-1.363246	-4.552152	3.241150
C	0.948402	-5.085458	3.636877
H	1.907492	-4.033162	5.239148
H	-2.218380	-3.038183	4.482844
H	-2.218380	-3.038183	-4.482844
H	1.907492	-4.033162	-5.239148
C	-1.213422	2.532714	4.475454
C	1.122937	2.963364	4.863276
C	-1.213422	2.532714	-4.475454
C	1.122937	2.963364	-4.863276

C	1.150415	3.807923	3.749646	H	1.849840	-5.646507	-3.399415
C	-1.188359	3.385923	3.374233	H	-2.274828	-4.639523	2.655139
C	1.150415	3.807923	-3.749646	H	1.849840	-5.646507	3.399415
C	-1.188359	3.385923	-3.374233	H	-2.274828	-4.639523	-2.655139
H	-2.131290	1.991682	4.691442	C	1.074450	-5.562483	-0.695940
H	2.044287	2.792325	5.415887	C	-1.267657	-6.111002	-0.696693
H	-2.131290	1.991682	-4.691442	C	-1.267657	-6.111002	0.696693
H	2.044287	2.792325	-5.415887	C	1.074450	-5.562483	0.695940
H	2.094113	4.256250	3.444115	H	1.989175	-5.288941	-1.216194
H	-2.083047	3.492207	2.763526	H	-2.193423	-6.331888	-1.223800
H	2.094113	4.256250	-3.444115	H	-2.193423	-6.331888	1.223800
H	-2.083047	3.492207	-2.763526	H	1.989175	-5.288941	1.216194
C	0.508930	2.912759	0.724744	H	-1.032504	8.550063	-1.249895
C	0.508930	2.912759	-0.724744	H	-1.032504	8.550063	1.249895
C	-0.127130	5.281174	0.728488	H	1.268612	-0.399944	-1.255916
C	-0.127130	5.281174	-0.728488	H	1.268612	-0.399944	1.255916
C	-1.095980	-1.285738	-6.104245	C	-0.781171	7.637291	-0.713236
C	1.220450	-1.305622	-5.461991	C	-0.781171	7.637291	0.713236
C	-1.095980	-1.285738	6.104245	C	1.064269	0.519555	-0.710375
C	1.220450	-1.305622	5.461991	C	1.064269	0.519555	0.710375
C	-1.331134	-3.635727	-4.288430	H	-0.468531	6.489668	2.497268
C	0.980771	-4.168290	-4.685268	H	-0.468531	6.489668	-2.497268
C	0.980771	-4.168290	4.685268	H	0.784832	1.646033	2.483134
C	-1.331134	-3.635727	4.288430	H	0.784832	1.646033	-2.483134
H	-2.024478	-1.803914	-6.334800	C	-0.467069	6.493702	1.409255
H	2.112558	-1.827715	-5.125044	C	0.792558	1.675809	-1.400346
H	-2.024478	-1.803914	6.334800	C	0.792558	1.675809	1.400346
H	2.112558	-1.827715	5.125044				
C	-0.467069	6.493702	-1.409255				

## **4.8 CPP-Based Luminescent Solar Concentrator**

### **4.8.1 Procedure of preparation of [8] CPP and [10]CPP**

These derivatives was obtained in accordance with the literature procedure reported by Jasti in 2012 by our group.<sup>94</sup> Before to produce the slabs, we have performed NMR spectra and UV-Vis and fluorescence spectra were acquired and they were compared with literature.

## Ringraziamenti

La prima persona che mi sento di ringraziare è il prof. **Carmin Gaeta** il quale mi guida dal 13 Febbraio 2012 (giorno della mia prima sintesi) e da allora molto del suo tempo lo ha dedicato a me. Da allora malgrado la mia inesperienza è riuscito ad insegnarmi davvero tanto e non solo come chimico ma anche come persona. Ritengo e ho sempre ritenuto che l'insegnamento va oltre la lettura di una semplice nozione su un libro e Lui ne è la prova certa. Lo ringrazio non solo per quello che mi ha trasmesso ma anche per la fiducia che mi ha accordato giornalmente.

Il prof. **Placido Neri** è la seconda persona che voglio ringraziare, che in modo molto paterno mi ha spesso consigliato e guidato e il quale operato non è passato mai in sordina. Ma indelebili sono i momenti di condivisione di idee, progetti o di esperienze passate... cose che ci portano ad amare il nostro lavoro.

**Carmen Talotta** (detta Carmela) la quale mi ha guidato e affiancato in questo cammino. Mi ha lasciato non solo un bagaglio culturale considerevole ma anche una grande amicizia. Con lei ho condiviso tantissimo in questi anni e senza di lei probabilmente non sarebbero passati in modo così felice.

Un pensiero speciale va a **Stefano Tommasone** il quale è per me un amico e un collega e dal quale è stato difficile staccarsi. È stato al mio fianco per molti anni e per me un punto di riferimento. Nonostante la distanza l'amicizia resta forte.

Inutile dire l'importanza di tutti i dottorandi che si sono succeduti negli anni e che più leggero e piacevole hanno reso questo mio cammino... **Gerardo Concilio, Nicola De Simone, Pellegrino La Manna, Veronica Iuliano, Clotilde Capacchione e Rocco Del Regno.** È stato davvero bello conoscervi e lavorare con voi.

In questi anni tuttavia sono stati essenziali per la mia crescita tutti gli studenti che ho seguito nel loro percorso di tesi. Mi ricordano costantemente che l'insegnamento non è mai a senso unico. Quindi grazie a **Rocco Del Regno (bis), Giuseppina Di Benedetto,**

**Carmela Calabrese, Chiara Laureana, Chiara Nieri, Fabio Fratta, Ilaria Ruberto, Luca Di Marino, Luca Liguori, Ludovica Panico, Mara Milione, Martina Barbuto** e in particolare **Arico Del Mauro, Emanuele Della Rocca e Guglielmo Iannone** con i quali, nonostante la lontananza è viva una grande amicizia.

E ora dato che la vita va oltre il laboratorio... non posso non ringraziare **Nico Picardi** ed **Emilio De Cesare** amici ormai di lunga data e sempre presenti nella mia vita. Grazie di cuore.

Infine, i miei **Genitori** e mio **Fratello**. Quel che è della vita e poca cosa senza una famiglia e senza qualcuno con cui dividerla. Spero un giorno di poter calcare i vostri passi e fare altrettanto bene. Grazie.

Grazie a tutti coloro che ci sono e ci sono stati e che nel bene e nel male mi hanno fatto crescere, facendo sì che oggi io sia la persona che sono. Anche e soprattutto dagli sbagli si impara.

*“...when I die, I want to be remembered for the life I lived -  
not the money I made”*

**Tim Bergling (AVICII)**